Electrochemical and Spectroelectrochemical characterisation of cyano and trifluoromethyl substituted polypyridines and their transition metal complexes

Alexander R. L. Delf

Thesis submitted for the degree of Ph.D.

The University of Edinburgh

May 2011

Declaration

I hereby declare that this thesis has been entirely composed by myself and that the work described herein is my own except where clearly mentioned either in acknowledgement, reference or text. It has not been submitted in whole or in part for any other degree, diploma or other qualification.

Alexander R. L. Delf

May 2011

Acknowledgments

First and foremost I would like to thank Prof. Lesley Yellowlees for all of her help, advice, enthusiasm and bars of Swiss chocolate that she has given me during my time with “the lab rats”. But most of all I would like to thank her for believing in me when even I didn’t.

Thanks have to go to Prof. Eric Mcinnes for the solid phase EPR simulations. I’d also like to thank the University of Edinburgh crystallography service for the crystal structures. For their help with NMR, Mass Spectrometry and CHN analysis thanks must go to Marika DeCremoux, Alan Talyor and Sylvia Williamson respectively. A special thank you has to go to Dr. Patricia Richardson of the EAsT Chem Research Computing Facility for her all her help and advice on all things computational and for long rambling discussions about interesting aspects of spectroscopy.

For helpful discussions about the finer points of electrochemistry I’d like to thank Dr. Andy Mount, Dr. John Henry and Charlotte Brady. Thanks must also go to Dr. Neil Robertson for helping me with my work in those times when Lesley was away from the department.

Thanks to all the members of the Yellowlees “lab rats” over the years; Dr. Lucy Moorcaft, Dr. Salma Al-Musharafi, Ed Nind, Calum Findlay and last but no means least Dr. Paul Murray. Thanks Paul for teaching me the tricks of the trade and letting me take part in some of the Chemical Connections fun.

A thank you of the lab friends wouldn't be complete without mentioning the Robertson group. The "solar girls" Dr. Keri McCall, Dr Charlotte Linfoot, Martina "bella" Congiu, Nina Chadwick and Tracy Hewat. The "materials boys" Dr. Rob Valentine, Dr. Simon Dalgleish, Dr Luca Pilia, Max "Maximus" Reinhardt and Alex Whyte. Thanks for all the banter and assorted baked goods, especially after you left me for pastures new down the corridor. I must single out Nina for special thanks here for managing to get the crystal structure of the 4,4´-$(CF_3)_2$-bpy ligand while doing her Masters project with Yellowlees group. Don't worry your name will go the paper once it's done.

Now to thank the people from outside the chemistry department that have had a hand in creation of my magnum opus. A huge thanks has to go the Kendo club boys in the Hill Square flat for all the nights that they have let me stay on their couch while I was writing up. Also the stress reliving value of getting to beat someone round the head with a bamboo stick cannot be overstated.

Finally I must thank my mum for putting up with me over the last few months while I have been writing up. Thank you for the free food, accommodation and for bank rolling my trips back to Edinburgh. I'll get started on that long list of odd jobs you want done next week.

Abstract

This thesis is concerned with the electrochemical and spectroelectrochemical characterisation of cyano (CN) and trifluoromethyl (CF_3) substituted polypyridine ligands and their metal complexes. The ligands investigated were X-CN-py (X = 3, 4 and 5, py = pyridine), X,X´-$(CN)_2$-bpy) (X,X´ = 3,3´, 4,4´ and 5,5´ bpy = 2,2´-bipyridine) and X,X´-$(CF_3)_2$-bpy (X,X´ = 3,3´, 4,4´ and 5,5´). The Pt(II) complexes of the X-CN-py and X,X´-$(CN)_2$-bpy ligands were studied along with the Fe(II) complexes of the X,X´-$(CN)_2$-bpy and X,X´-$(CF_3)_2$-bpy ligands.

Electrochemical studies of the X-CN-py ligands indicated that 2-CN-py and 4-CN-py have one reversible $1e^-$ reduction and 3-CN-py has one quasi-reversible reduction. 4-CN-py is more easily reduced than 2-CN-py. EPR experiments on $[2\text{-CN-py}]^{1-}$ and $[4\text{-CN-py}]^{1-}$ combined with DFT calculations have indicated that the semi-occupied molecular orbital (SOMO) is delocalised over the entire molecule. The complex $[Pt(4\text{-CN-py})_2Cl_2]$ undergoes two reversible $1e^-$ reductions, attributed to the sequential reduction of the two 4-CN-py ligands. $[Pt(3\text{-CN-py})_2Cl_2]$ was found to exhibit one irreversible reduction.

The electrochemistry of the X,X´-$(CN)_2$-bpy ligands indicated that 3,3´-$(CN)_2$-bpy and 5,5´-$(CN)_2$-bpy have two reversible $1e^-$ reductions while 4,4´-$(CN)_2$-bpy has only one reversible $1e^-$ reduction. The reductions of 5,5´-$(CN)_2$-bpy occur at significantly less negative potentials than those in 3,3´ or 4,4´ analogue. *In-situ* UV/Vis/NIR and EPR experiments on the X,X´-$(CN)_2$-bpy ligands indicate that the reduction electron is delocalised over both the CN-py rings with the SOMO being spread across the entire molecule. $[Pt(3,3´\text{-}(CN)_2\text{-bpy})Cl_2]$ and $[Pt(5,5´\text{-}(CN)_2\text{-bpy})Cl_2]$ undergo two

reversible $1e^-$ reductions, attributed to the sequential reduction of the X,X´-$(CN)_2$-bpy ligand.

4,4´-$(CF_3)_2$-bpy and 5,5´-$(CF_3)_2$-bpy, whose X-ray crystallographically determined structures are reported, both have one reversible $1e^-$ reduction while 3,3´-$(CF_3)_2$-bpy exhibits an irreversible reduction. Again the 5,5´ analogue is the most easily reduced. Spectroelectrochemical results indicate that the reduction electron enters a SOMO that is delocalised over both the CF_3-py rings. Substitution in the 5,5´ positions is determined to be electronically most significant.

Complexes of the general formula [Fe(II)(X_2-bpy)$_3$][BF_4] (where X = CN or CF_3 in the 4,4´ or 5,5´ positions) exhibit three reversible ligand based reduction processes and a metal based oxidation. UV/Vis/NIR and EPR studies have confirmed that the reduction electron in each case enters a molecular orbital that is predominantly based on a bpy ligand.

The redox potentials of 4-CN-py and 5,5´-$(CN)_2$-bpy are solvent dependent with $1e^-$ reduction of 4-CN-py and the two $1e^-$ reductions of 5,5´-$(CN)_2$-bpy moving to less negative potentials as the acceptor number (AN) of the solvent increases.

A computational model has been developed for the study of the electronic properties of substituted bipyridines using DFT methods. This model has been used to aid the analysis of the EPR and UV/Vis/NIR spectra of the X_2-bpys studied.

Contents

Abbreviations

Bpy	2,2´-bipyridine
DCM	dichloromethane
DFT	Density Functional Theory
DMF	dimethylformamide
DMSO	dimethylsulphoxide
E	potential
$E_{½}$	half-wave potential
E_{pa}	anodic peak potential
E_{pc}	cathodic peak potential
EPR	Electron Paramagnetic Resonance
G	Gauss
HOMO	Highest Occupied Molecular Orbital
i_{pa}	anodic peak current
i_{pc}	cathodic peak current
LUMO	Lowest Unoccupied Molecular Orbital
MeCN	acetonitrile
NIR	Near Infra-Red
NMR	Nuclear Magnetic Resonance
py	pyridine
SCE	Saturated Calomel Electrode
SOMO	Semi-Occupied Molecular Orbital
[TBA]	tetrabutylammonium ($[^{n}Bu_4N]^{1+}$)
THF	tetrahydrofuran
UV	Ultra-Violet
ν	scan rate
Vis	Visible

1 Introduction

1.1 2,2´-bipyridine

Bipyridines are a family of hetrocyclic molecules comprising two pyridine ring systems linked by a C-C bond. Six isomers of bipyridine exist, of these the 2,2´ and 4,4´ isomers have been the most extensively studied. The work detailed in this thesis concentrates solely on derivatives of 2,2´-bipyridine (bpy).

The chemical properties of pyridine, the building block of 2,2´-bipyridine can be grouped into three broad categories. Firstly there are properties that are generally similar to those of benzene but modified by the presence of the ring nitrogen. These include electrophilic substitution reactions such as sulfination and halogenation.[1,2] These reactions are much more difficult than the corresponding reactions for benzene and must be carried out under more extreme conditions. Electrophilic susbstitution reactions of pyridines favour the formation of products with the substituent in the 3 position.[1,2]

The low reactivity of pyridine toward electrophilic aromatic substitution is due largely to the fact that the electron density of the ring is decreased by the electron withdrawing inductive effect of the electronegative nitrogen atom. This leads to pyridine having a sizeable dipole moment (μ = 2.26 D).[2] Thus electrophilic attack on the positively polarised carbon atoms is difficult. The reactivity of the pyridine ring towards electrophilic attack is further decreased by interaction of the electrophile with the basic ring nitrogen causing a positive charge distribution across the entire ring.[2]

The second group of properties are those not usually associated with the benzene system. This group includes reactions in which the key step involves the interaction of the pyridine ring system with a base or nucleophilic reagent.[1] In direct comparison to pyridine's lack of reactivity towards electrophilic substitution, halopyridines substituted at the 2 and 4 positions undergo nucleophilic aromatic substitution easily.[1,2] The initial addition step is favoured by the ability of the electronegative nitrogen to stabilize the anion intermediate. In contrast nucleophilic aromatic substitution at the 3 position is unfavoured because it is not possible to localise the negative charge on to the ring nitrogen.[2]

The final group of properties are those that arise from the lone pair of electrons on the ring nitrogen atom. These electrons are available for bonding without disturbing the aromaticity of the ring. The presence of the lone pair allows for the formation of salts, quaternary compounds and N-oxides.[1] The conversion of a pyridine to the N-oxide activates the ring to electrophilic aromatic substitution by helping to overcome the inductive effect of the electronegative nitrogen atom. However substitution reactions will only occur at the 4 position.[2] Thus only 4-substituted pyridines and bipyridines can be made in this fashion. The lone pair of the ring nitrogen can be donated to a metal centre enabling the formation of a strong M-N bond. Thus pyridine and its derivatives can act as ligands for coordination complexes.[3]

2,2´-Bipyridines exhibits similar properties to pyridine, with the two linked pyridine ring units having similar reactivity to nucleophilic substitution and inertness to electrophilic

substitution reactions. Bpy can act as a chelating ligand in coordination complexes, binding to transition metals via a bidentate motif through the two nitrogen atom lone pairs.

X-ray crystallographic studies of bpy have indicated that the two pyridine rings are coplanar, with the nitrogen atoms adopting a *trans* conformation relative to the C(2)-C(2´) bond joining the two pyridine rings.[4] The crystal structure determined by Merritt *et al.* is shown in figure 1.1. The unit cell is monoclinic with a = 5.66 Å, b = 6.24 Å, c = 13.46 Å and β = 118°. The space group is $P2_1/c$ and there are two molecules per unit cell. The average C-C and C-N bond lengths in the pyridine rings are 1.39 Å and 1.36 Å respectively. These bond lengths agree well with the same bonds observed for pyridine. The C(2)-C(2´) bond length is 1.50 Å, which is slight longer than the value of 1.48 Å observed for the equivalent C-C bond in biphenyl.[5]

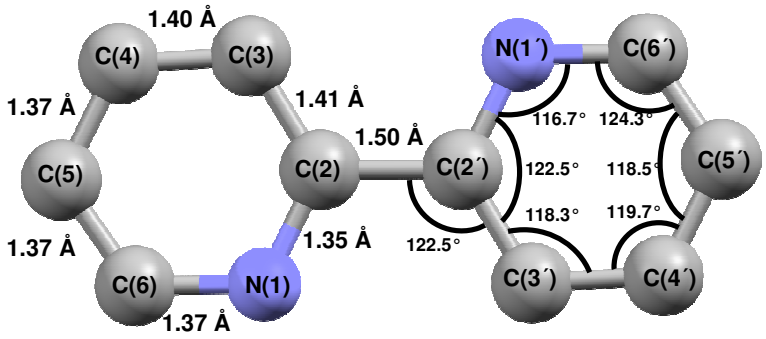

Figure1.1 Crystal structure of 2,2´-bipyridine as determined by Merritt *et al.*[4]

Comparison of the bond angles in the pyridine ring indicates a slight distortion from the expected 120° for a hexagonal ring. This is due to the C-N bonds being shorter than the

C-C bonds. Therefore there must be a distortion of the rings to compensate for this which is corroborated by the angles adjacent to the C-N bonds being larger than 120°. No short intermolecular distances have been observed in the crystal packing structure, therefore intermolecular binding must be due only to weak van der Waals forces. This is supported by the low melting point (69.5 ºC) of bpy and also the tendency of these crystals to slowly sublime in air at the room temperature.

Investigation of the dipole moment of bpy in organic solvents has indicated that the molecule adopts a roughly *trans* conformation with a N(1)-C(2)-C(2´)-N(1´) torsional angle of 152º-170º.[6-8] The resulting angle between the ring planes of 10-28º is significantly smaller than that observed for biphenyl (45º).[9] The *trans* conformation is strongly stabilised by two intramolecular C-H· · ·N, three centre four electron interactions between the C-H units at the 3,3´ positions and the opposing ring nitrogen atoms.

Nakamoto investigated changes in the UV/Vis spectrum of bpy in aqueous solutions at various pH values. It was concluded that in basic solutions the *trans* conformation was favoured, while in acidic solution the *cis* conformation predominates.[10] Stabilisation of the *cis* conformation was attributed to the formation of the protonated mono-cation, resulting in interactions of the positively charged protonated ring nitrogen atom with the unprotonated nitrogen of the other ring. The structure was suggested to be slightly twisted due to the steric hindrance of the hydrogen atoms in the 3,3´ positions. In strong acids the doubly protonated di-cation was formed and it was predicted to adopt a *trans* conformation. Once again the structure was suggested to be slightly twisted due to

repulsive interaction between the hydrogen atoms in the 3,3´ positions and the quaternary hydrogen atoms of the ring nitrogen atoms.

Computational studies of the torsional barrier of bpy have indicated that the molecule possesses a global minimum at 180º and local minima at approximately 40º and 320º.[9,11] Energy maxima are predicted for the perpendicular orientations of the pyridine rings and for 0º conformation. The barrier height at 0º has been found to be particularly sensitive to the computational method used.[11] Hartree-Fock (HF) and Møller-Plesset perturbation theory (MP2) methods give relative energies that are higher by 5 $kJmol^{-1}$ compared to density functional theory (DFT) methods. This has been attributed to use of an insufficiently large basis set for MP2 and to the neglect of electron correlation in HF.[11]

DFT calculations conducted by Göller and Grummt[11] have indicated that the global minima at 180º is stabilised by approximately 27 $kJmol^{-1}$ relative to the twisted *cis* confomers. The energy barrier for the perpendicular orientations are about 31 $kJmol^{-1}$ higher than the global minimum and about 4 $kJmol^{-1}$ higher than the local minima. The 0º barrier is approximately 32 $kJmol^{-1}$ higher than the *trans* conformation and 5 $kJmol^{-1}$ higher than the local minima. A plot of the torsional potential energy of bpy is shown in figure 1.2.

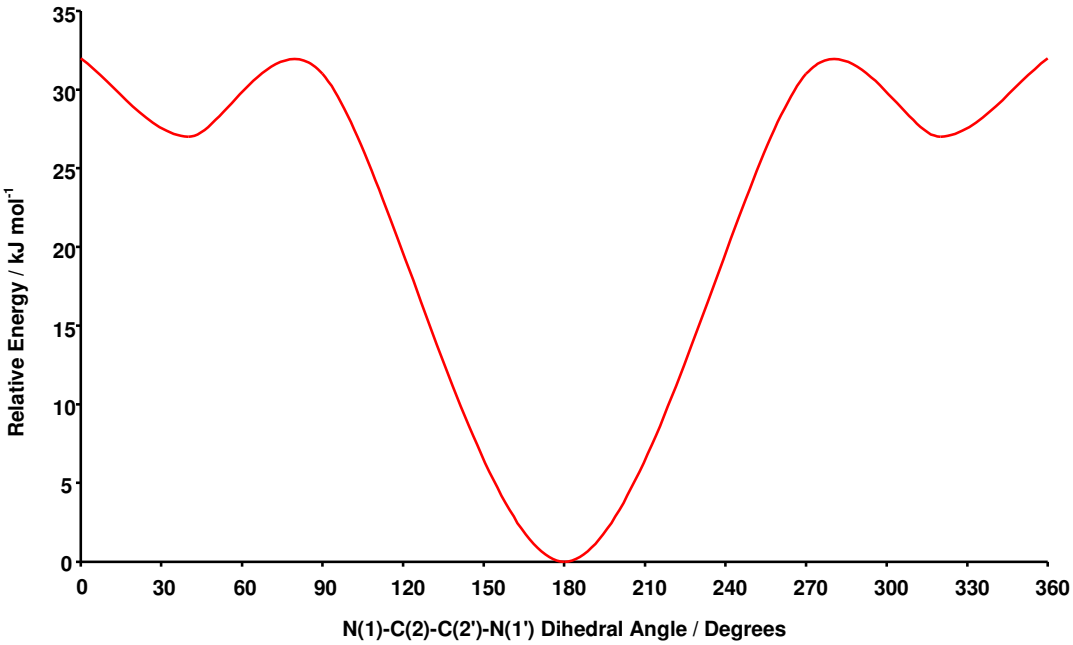

Figure1.2 Torsional potential of 2,2´-bipyridine calculated by Göller and Grummt using B3LYP /6-31+G(d)[11]

The distance between the hydrogen atoms in the 3 and 3´ positions in the 0º structure was determined computationally to be only 2.014 Å. This supports the theory that molecules in the *cis* conformation will experience steric repulsion effects. In contrast the short distance of 2.471 Å between the hydrogen atoms in the 3,3´ positions and the opposing ring nitrogen atoms in the *trans* conformation of bpy favour the formation of three centre four electron interactions that have been suggested to stabilise this conformation.

It was also found that the C(2)-C(2´) bond length between the two ring systems was seen to change length with rotation about the C-C bond. Lengths of 1.492 Å and 1.495 Å were observed for the global and local minima respectively, extending to 1.501 Å at 0º and reaching a maximum of 1.502 Å for the perpendicular conformations. This elongation of

the inter-ring distance was less pronounced than was observed for the equivalent bond in biphenyl.[9]

Castellà-Ventura *et al*. have examined the structure of the $[bpy]^{1-}$ radical in solution through a combination of time-resolved resonance Raman spectroscopy and DFT calculations.[12] Comparison with resonance Raman results for the *cis* form coordinated to Li^+ and the *trans* form in a glassy matrix indicated that solution results were in good agreement with a *trans* conformation. When the experimental data were compared to the theoretical vibrational frequencies for the optimized geometry of the *trans* and *cis* confomers of the anion radical it was determined that, like the neutral species, $[bpy]^{1-}$ favours a *trans* conformation in solution. Comparison of the optimized geometry for $[bpy]^{1-}$ and the geometry of bpy[4,12] indicate a shortening of the C(2)-C(2´) (-0.055 Å) and C(3)-C(4) (-0.015 Å) bonds and lengthening of the N(1)-C(2) (+0.044 Å), C(2)-C(3) (+0.029 Å) and C(4)-C(5) (+0.023 Å) bonds. The shortening of the inter-ring C(2)-C(2´) bond in the reduced species is indicative of an increased amount of double bond character and therefore increased π-conjugation and a favouring of a planar conformation.

1.2 Substituted 2,2´-bipyridine

There has been much interest into the synthesis of derivatives of 2,2´-bipyridine.[13-18] These molecules have found much use as ligands in coordination complexes with a large number of transition metals.[19-30] The electronic properties of the bpy ligands and the complexes as a whole can be tuned by changing the nature and position of the substituent

groups on the bpy. These properties have led to their incorporation into transition metal complexes with uses such as photosensitisers, photocatalysts and catalysts.[31]

Many investigations have concentrated on the study of disubstituted tris-bpy complexes of Ru(II). This is due to the application of these complexes in such areas as display devices[32], water-oxidation catalysts[33] and as luminescent sensors for organic molecules[34], metal cations[35] and lanthanides[36].

Ru(II) bpy complexes have also found uses in the development of Dye-Sensitised Solar Cells (DSSCs).[37] In recent years the development of cheaper more efficient renewable energy sources has become ever more important. This has stimulated increased interest in this research area. DSSCs function is dependent on the ability of the solar dye to absorb light in the visible region of the electromagnetic spectrum. Once excitation has occurred the dye molecule can inject an electron into the conduction band of the semiconductor substrate (e.g. TiO_2). The oxidised dye is then regenerated by electron donation from the electrolyte (e.g. iodide/triiodide). The ability to fine tune the energy levels of the dye molecule by changing the substituent groups on the bpy ligands presents a significant advantage over traditional silicon based solar cells.

One of the most efficient dye molecules that has been developed is $[Ru(4,4´\text{-}(CO_2H)_2\text{-}bpy)_2(NCS)_2]$, known as N719 (figure1.3). N719 is almost universally used when comparing cell parameters and dye performances in liquid electrolyte DSSCs. The popularity of the N719 dye can be attributed to a combination of its good efficiency,

reported at up to 12%[38], and its good stability. The stability of the N719 dye is the result of its ability to rapidly inject electrons from the excited state to the semiconductor substrate.

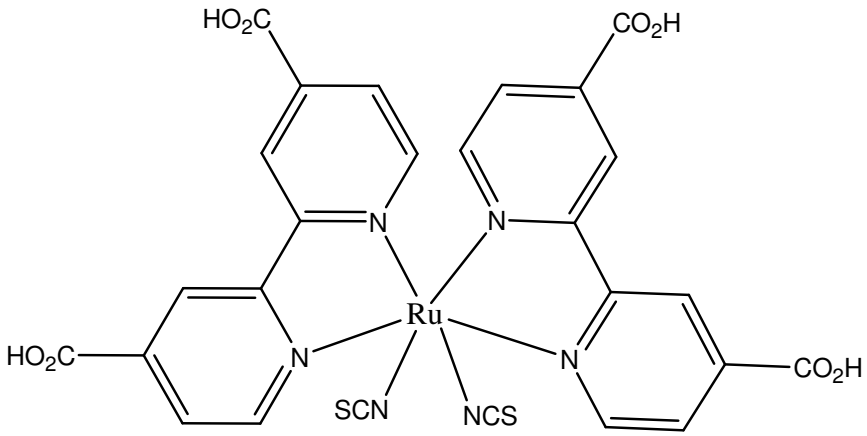

Figure1.3 [Ru(4,4´-$(CO_2H)_2$-bpy)$_2$$(NCS)_2$], N719 DSSC dye

In recent years square planar Pt(II) coordination complexes with bpy ligands have also been studied for their potential use in the area of DSSCs.[39-41] An example of one of the complexes that has been investigated by Geary *et al*.[41] is shown in figure 1.4.

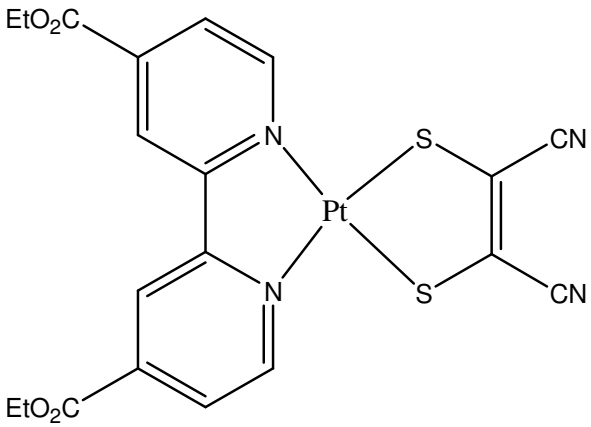

Figure1.4 [Pt(4,4´-$(CO_2Et)_2$-bpy)(mnt)] DSSC dye

Previous work on di-substituted bipyridine ligands has concentrated on the study of the 4,4´ positions.[30] This is likely due to the difficulty in preparation of 3,3´ and 5,5´ substituted compounds. As discussed above derivatives of pyridine are much less susceptible to electrophillic aromatic substitution than their benzene equivalents. Conversion to the N-oxide can activate the ring system to electrophillic attack; however substitution will only occur at the 4 position. Therefore only 4,4´-substituted bipyridines can be made in this fashion. Bipyridine derivatives substituted in the 3,3´ and 5,5´ positions are usually made by the coupling of two substituted pyridine rings in an Ullmann type reaction,[13,42-44] figure 1.5.

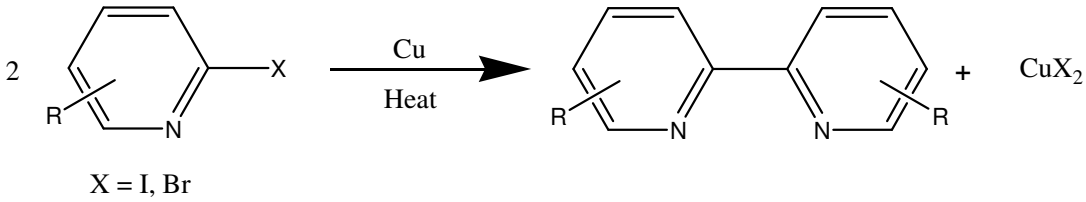

Figure1.5 Reaction scheme for an Ullmann coupling of substituted halopyridines

A number of attempts to correlate the physical properties of disubstituted bipyridines and their transition metal complexes with the Hammett parameter, σ, of the substituent have been made.[20,22,30,32,45,46] The Hammett parameter can be considered to be a measure of the electron withdrawing (positive σ values) or donating (negative σ values) character of a substituent.[47]

The values of the Hammett parameter, σ_x, are empirically derived from the ionization constants of benzoic acid and X-benzoic acid, where X is the substituent under investigation in either the *meta* or *para* position, using equation 1.1.

$$\sigma_X = \log K_X - \log K_H \qquad \textbf{Equation 1.1}$$

K_H is the ionization constant of benzoic acid in water at 25 °C and K_X is the corresponding ionization constant for the substituted X-benzoic acid.

Conner *et al.* reported a linear correlation of σ_p with the absorption and emission maxima of [Mo(4,4´-$(X)_2$-bpy)$(CO)_4$] (X = NMe_2, NH_2, OMe, CMe_3, Me, H, Ph, CO_2H, Cl, CO_2Me and NO_2).[20] Worl *et al.* noted a similar correlation for [Re(4,4´-$(X)_2$-bpy)$(CO)_3Cl$].[22] Pichot *et al.* determined a correlation between the first reduction potentials of a series of 5,5´-$(X)_2$-bpy ligands and the σ_m, however a better fit was achieved with σ_p.[32] McInnes found that the first reduction potential of [Pt(4,4´-$(X)_2$-bpy)Cl_2] (X = NH_2, Me, H, CO_2Me, CO_2Et, OEt, Ph and Cl) displayed a linear correlation with σ_p.[30] A similar correlation was observed by Jack for the first reduction potentials of [Pt(5,5´-$(X)_2$-bpy)Cl_2] and σ_m (X = NH_2, Me, H, CO_2Me, CO_2Et).[45]

Jack also found a linear correlation with σ_m for the first reduction potentials of a series of 5,5´-$(X)_2$-bpy compounds (X= Me, H, CO_2Me and CO_2Et), reporting an R^2 value of 0.9997.[45] Al-Musharafi extended the correlation to include data for X = Ph, Cl and Br. Upon inclusion of this data the quality of the fit dropped significantly with an R^2 value of 0.6335 reported.[46]

The electrochemical data for a range of known disubstituted bpy systems have been collated and are reported in tables 1.1, 1.2 and 1.3 for the 3,3´-, 4,4´- and 5,5´-substituted

bpys respectively. An attempt to determine if there is a correlation between the previously reported first reduction potentials of the 4,4´-$(X)_2$-bpy molecules and σ_p is shown in figure 1.6 (the data for 4,4´-$(NO_2)_2$-bpy is excluded from the linear fit due to its unusual properties, *vide infra*). A fairly good correlation is observed, with the linear fit having $R^2 = 0.9084$. The correlation between the reduction potential of the 5,5´-(X_2)-bpy and σ_m, first observed by Jack,[45] is rexamined in figure 1.7. The correlation observed for the full range of 5,5´ substituted bpys investigated here is much weaker than that reported by Jack, with the linear fit giving a R^2 value of 0.8019. A much improved correlation is achieved when the reduction potentials of 5,5´-$(X)_2$-bpy compounds are plotted against σ_p (figure 1.8), resulting in $R^2 = 0.9419$. This is in line with the correlations found by Pichot.[32] Thus both 4,4´- and 5,5´-disubstituted bpys give better linear correlations of $E_{½}$ *vs*. σ for σ_p rather than σ_m.

3,3´-X_2-bpy							
X	σ_m	σ_p	R	F	$E_{½,(1)}$ / V	$E_{½,(2)}$ / V	Reference
H	0.00	0.00	0.00	0.03	-2.05	-	48
CO_2Et	0.37	0.45	0.11	0.34	-1.84	-	41
NO_2	0.71	0.78	0.13	0.65	-0.79	-1.10	49

Table 1.1 The first and second reduction potentials of a series of 3,3´-$(X)_2$-bpy *vs*. Ag/AgCl and the σ_m, σ_p, R and F parameters of the substituent X (X = H, CO_2Et and NO_2)[50]

4,4´-$(X)_2$-bpy						
X	σ_p	R	F	$E_{½,(1)}$ / V	$E_{½,(2)}$ / V	Reference
OEt	-0.24	-0.50	0.26	-2.33*	-	48
Me	-0.17	-0.18	0.01	-2.13	-	48
Ph	-0.01	-0.13	0.12	-1.79	-	48
H	0.00	0.00	0.03	-2.05	-	48
Cl	0.23	-0.19	0.42	-1.69*	-	48
CO_2Me	0.45	0.11	0.34	-1.48	-1.97	48
CO_2Et	0.45	0.11	0.34	-1.53	-	41
NO_2	0.78	0.13	0.65	-0.65	-0.79	45

Table 1.2 The first and second reduction potentials of a series of 4,4´-$(X)_2$-bpy *vs*. Ag/AgCl and the σ_p, R and F parameters of the substituent X (X = Me, H, Ph, OEt, Cl, CO_2Me, CO_2Et and NO_2).[50]
*** indicates an irreversible reduction process, E_{pc} value is quoted for this process**

5,5´-X_2-bpy							
X	σ_m	σ_p	R	F	$E_{½,(1)}$ / V	$E_{½,(2)}$ / V	Reference
Me	-0.07	-0.17	-0.18	0.01	-2.21	-	45
H	0.00	0.00	0.00	0.03	-2.05	-	48
Ph	0.06	-0.01	-0.13	0.12	-1.75	-	46
Cl	0.37	0.23	-0.19	0.42	-1.74*	-	46
CO_2Me	0.37	0.45	-0.11	0.34	-1.25	-1.64	45
CO_2Et	0.37	0.45	0.11	0.34	-1.23	-1.61	41
Br	0.39	0.24	-0.22	0.45	-1.72*	-	46
NO_2	0.71	0.78	0.13	0.65	-0.61	-0.70	49

Table 1.3 The first and second reduction potentials of a series of 5,5´-$(X)_2$-bpy *vs*. Ag/AgCl and the σ_m, σ_p, R and F parameters of the substituent X (X = Me, H, Ph, Cl, CO_2Me, CO_2Et, Br and NO_2).[50] * indicates an irreversible reduction process, E_{pc} value is quoted for this process

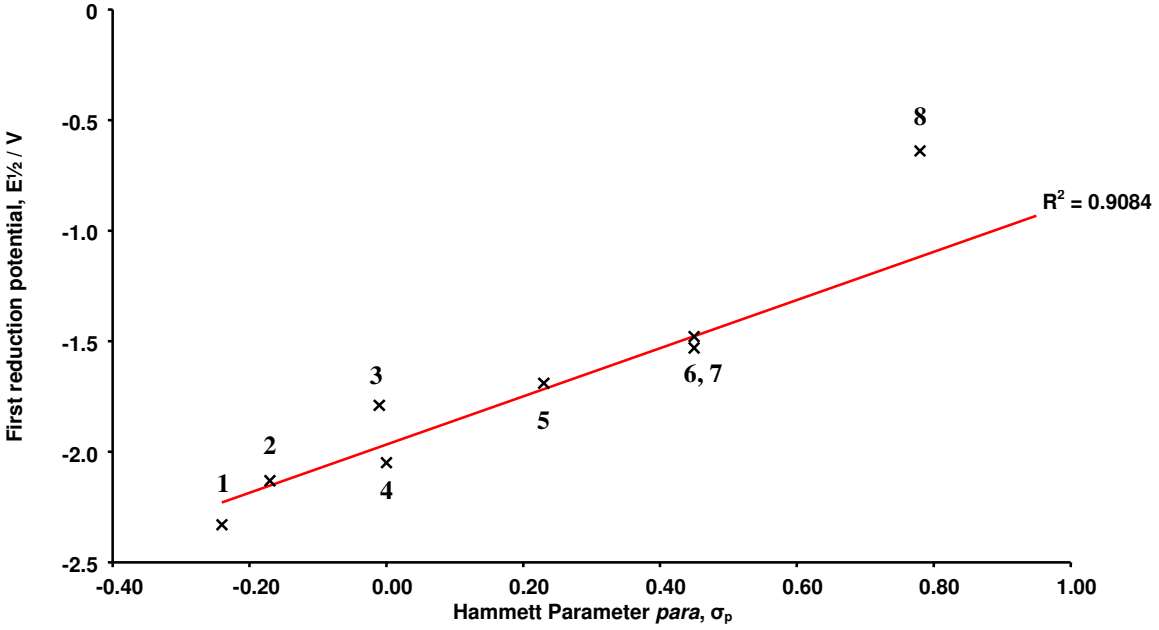

Figure 1.6 Plot of $E_{½}$ of the first reduction of 4,4´-$(X)_2$-bpy *vs. para* Hammett parameter, σ_p of the substituent X, (where X is the substituent under investigation).[50] 1) X = OEt, 2) X = Me, 3) X = Ph, 4) X = H, 5) X = Cl, 6) X = CO_2Me, 7) X = CO_2Et, 8) X = NO_2 (4,4´-($NO_2)_2$-bpy data excluded from the linear fit due to the unusual properties of this compound)

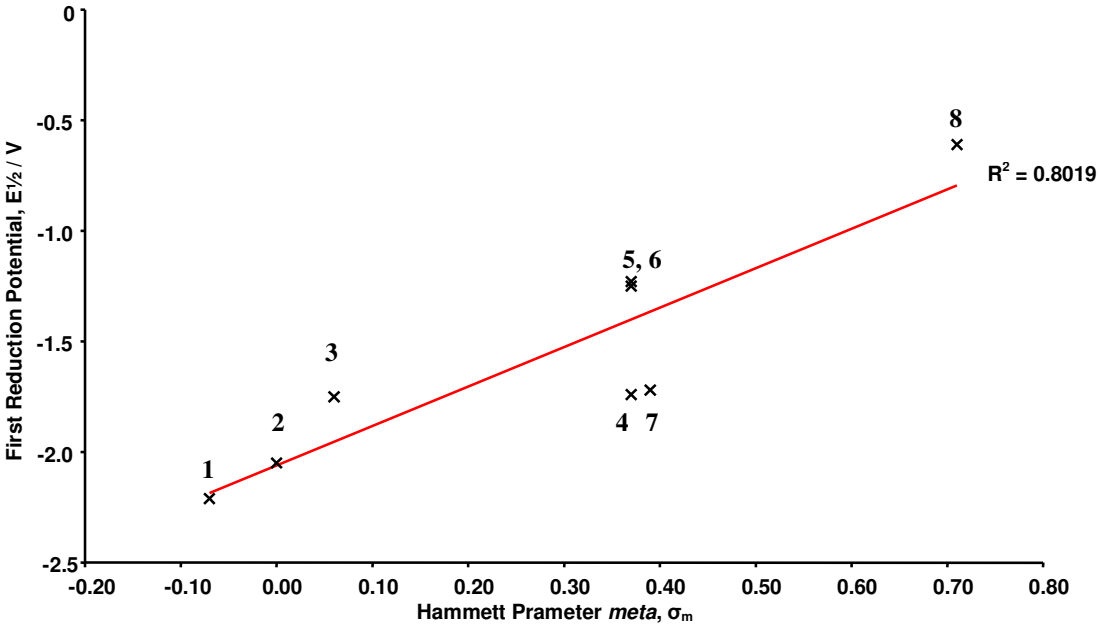

Figure 1.7 Plot of $E_{½}$ of the first reduction of 5,5´-$(X)_2$-bpy *vs. meta* Hammett parameter, σ_m of the substituent X, (where X is the substituent under investigation).[50] 1) X = Me, 2) X = H, 3) X = Ph, 4) X = Cl, 5) X = CO_2Me, 6) X = CO_2Et, 7) X = Br, 8) X = NO_2

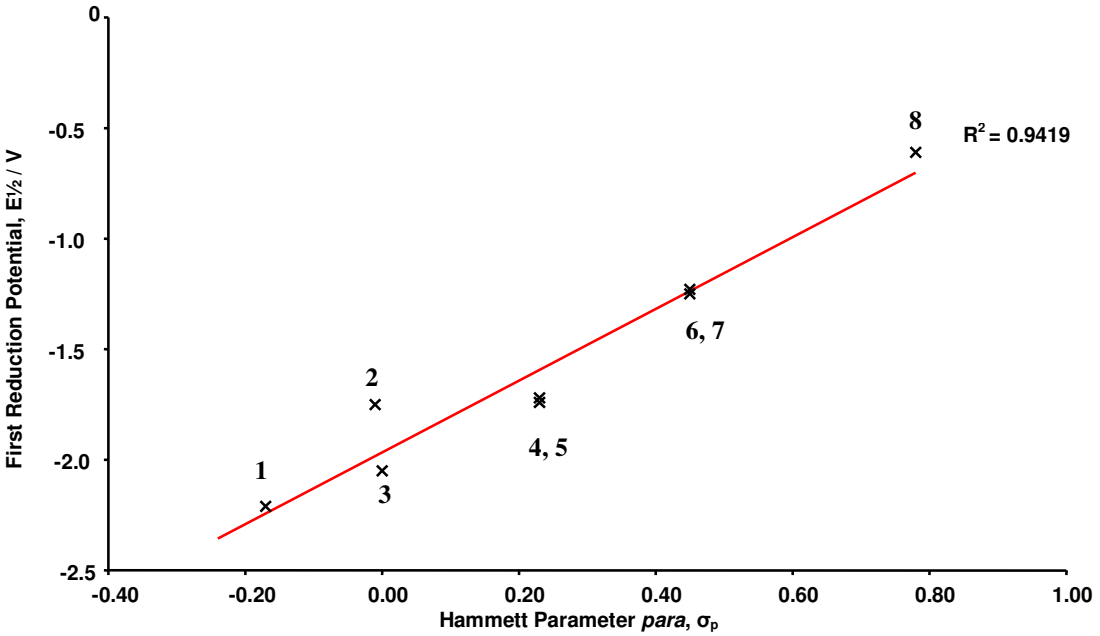

Figure 1.8 Plot of $E_{½}$ of the first reduction of 5,5´-$(X)_2$-bpy *vs. para* Hammett parameter, σ_p of the substituent X, (where X is the substituent under investigation).[50] 1) X = Me, 2) X = Ph, 3) X = H, 4) X = Cl, 5) X = Br, 6) X = CO_2Me, 7) X = CO_2Et, 8) X = NO_2

This surprising result can be rationalised by examining in more detail the effects that contribute to the magnitude of the Hammett parameters. The Hammett parameters can be considered using the inductive, field and resonance effects of the substituent. The inductive effect is a measure of the transmission of charge through the σ bonds between atoms in a molecule due to the difference in electronegativity of the bonded atoms. Field effects arise from through space electrostatic interactions of polar substituents with the reaction site. Resonance effects are a measure of the degree to which a substituent stabilizes or destabilizes the resonance forms of the molecule. In most case the field and induction effects are grouped together to form the field/induction parameter (F) and the resonance effect is represented by the Resonance parameter (R). The relationship between the Hammett parameter, σ and the R and F parameters is defined by equations 1.2 and 1.3 for σ_p and σ_m respectively.[51]

$$\sigma_p = F + R \qquad \textbf{Equation 1.2}$$

$$\sigma_m = F + \tfrac{1}{3}R \qquad \textbf{Equation 1.3}$$

The field/inductive parameter can be empirically derived from the ionization constants of bicycloctane carboxylic acid and X-bicycloctane carboxylic acid, where X is the substituent under investigation in the *para* position, using equation 1.4.

$$F = \log K_X - \log K_H \qquad \textbf{Equation 1.4}$$

K_H is the ionization constant of bicycloctane carboxylic acid in a 50% ethanol solution at 25°C and K_X is the corresponding ionization constant for the substituted X-bicycloctane carboxylic acid. The value of the R parameter can then be determined from equation 1.2. The R and F values for the substituents investigated are listed in tables 1.1 – 1.3.

Comparison of the R and F values for the substituents under investigation shows that these effects vary independently for each substituent. Attempts to draw a correlation between the first reduction potential and the R or F values produce fits with much lower R^2 values than the correlations with the Hammett parameter. This indicates that neither R nor F in isolation are sufficient to account for the observed behaviour.

The degree to which R and F contribute to the Hammett parameter is dependent on the position of the substituent. When the substituent group is in the *para* position of a pyridine molecule the reduction product can adopt the resonance forms shown in figure 1.9. The reduction electron is stabilised by localisation on the electronegative nitrogen atom of the ring. In contrast when the substituent is in the *meta* position the reduction electron cannot be localised to the ring nitrogen atom, figure 1.10, and the reduction product is less stable compared to the *para* substituted analogue. This results in *para* substituted pyridines being more sensitive to the resonance character of the substituent group and therefore σ_p having a greater contribution from R than σ_m.

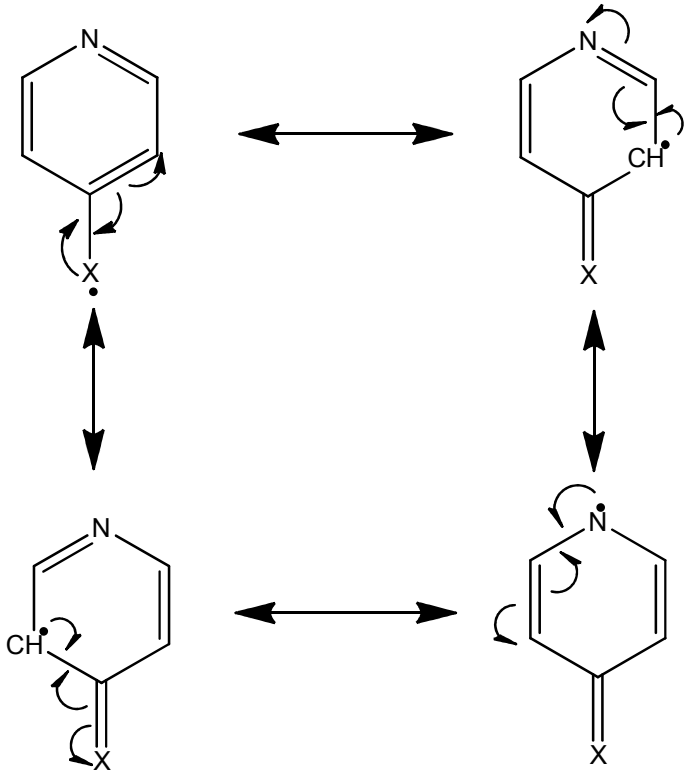

Figure 1.9 The resonance structures adopted by mono-reduced 4-X-py

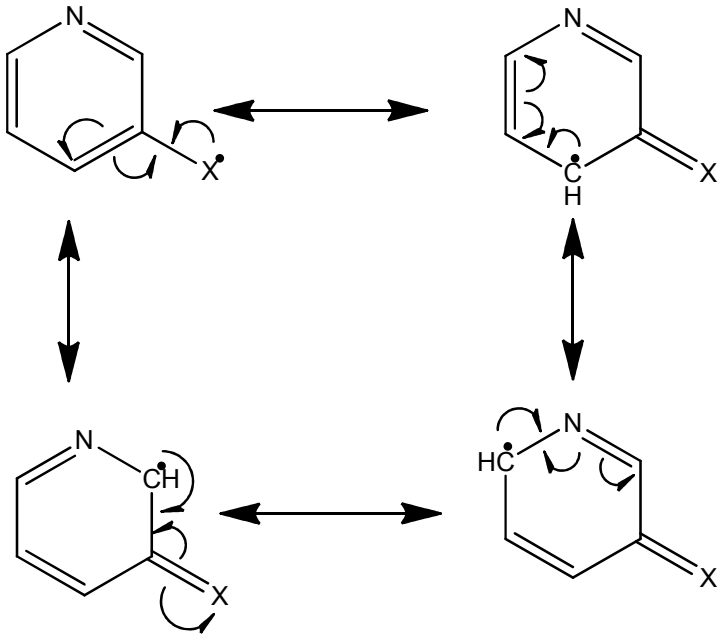

Figure 1.10 The resonance structures adopted by mono-reduced 3-X-py

A similar analysis of the possible resonance forms adopted by the reduction product of the disubstituted bipyridines can also be conducted. When the initial reduction occurs on a substituent in the 4,4´ positions the mono-reduced species can adopt the resonance forms depicted in figure 1.11. Resonance stabilisation can only be achieved around one of the pyridine rings. As with the pyridine analogue the reduction electron is stabilised by localisation onto the nitrogen atom of the pyridine ring.

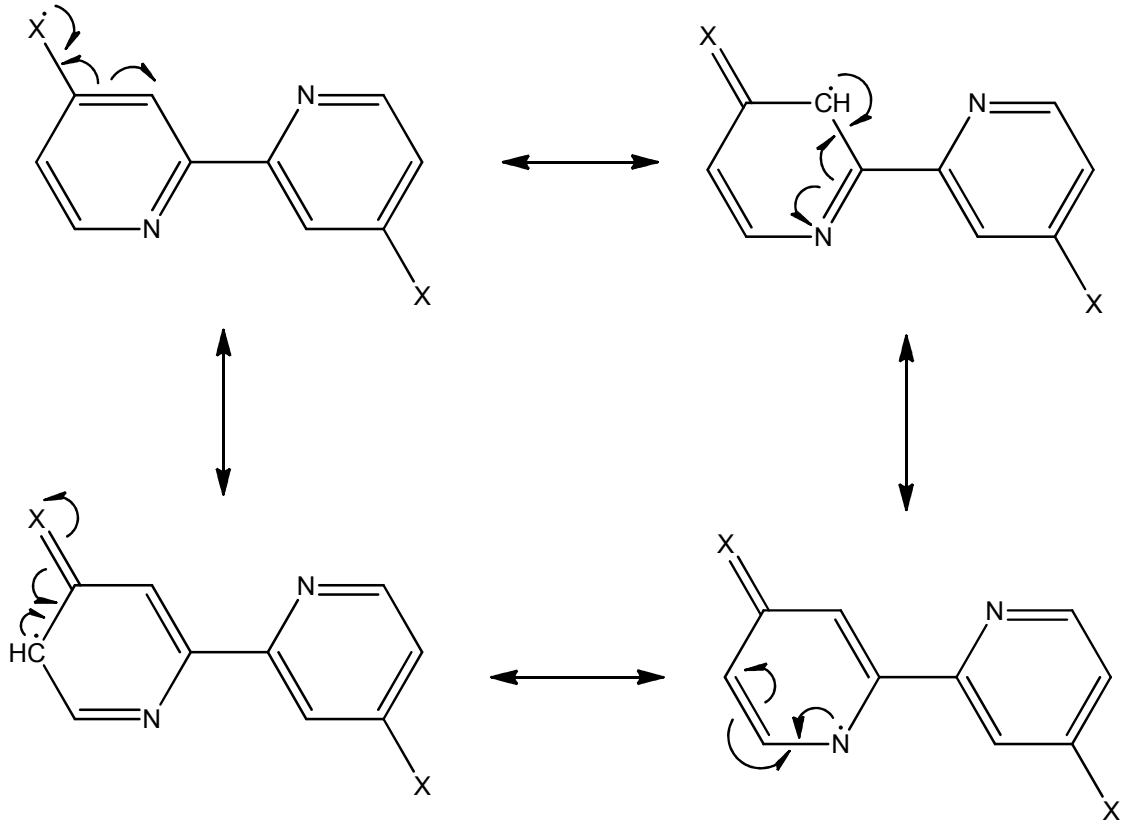

Figure 1.11 The resonance structures adopted by mono-reduced 4,4´-$(X)_2$-bpy

Conversely when the reduction occurs on a substituent in either the 3,3´ or 5,5´ positions the reduction product is stabilised by resonance around both pyridine rings systems, figure 1.12 and 1.13. In addition the reduction electron is localised on the nitrogen atom of the second ring. These increased resonance effects are in direct contrast to the

destabilisation effects experienced by the 3-X-py analogues. This difference in the resonance behaviour can account for the discrepancy observed in the plot of the first reduction potential *vs*. σ_m, figure 1.7. As stated above σ_p has a greater contribution from R. Due to the significant resonance effects experienced by the 3,3´- or 5,5´-substituted bpys it would be expected that σ_p would a better model for the effect of the addition of a substituent in these positions. This is confirmed by the far superior fit observed in figure 1.8 compared to figure 1.7.

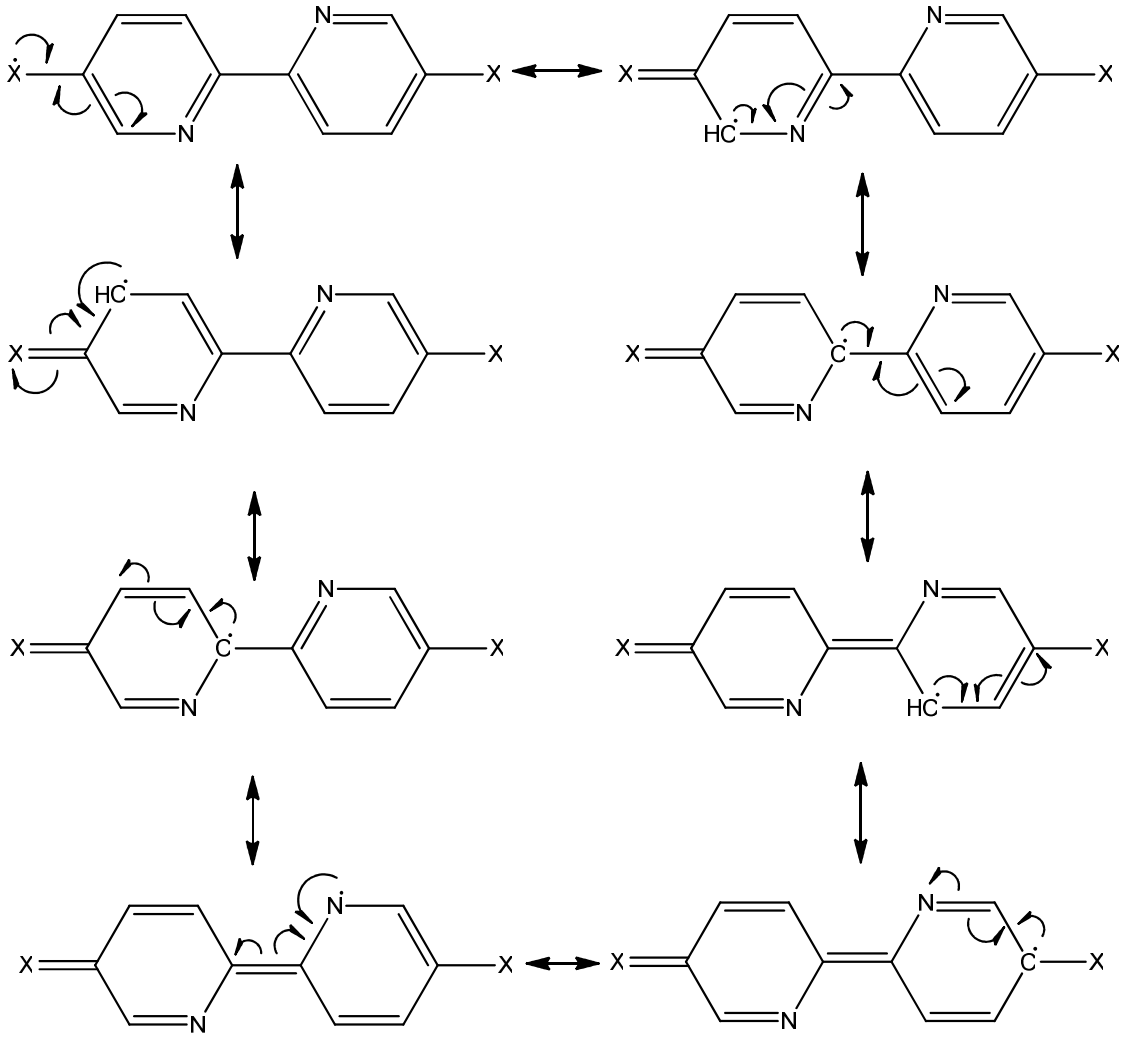

Figure 1.12 The resonance structures adopted by mono-reduced 5,5´-$(X)_2$-bpy

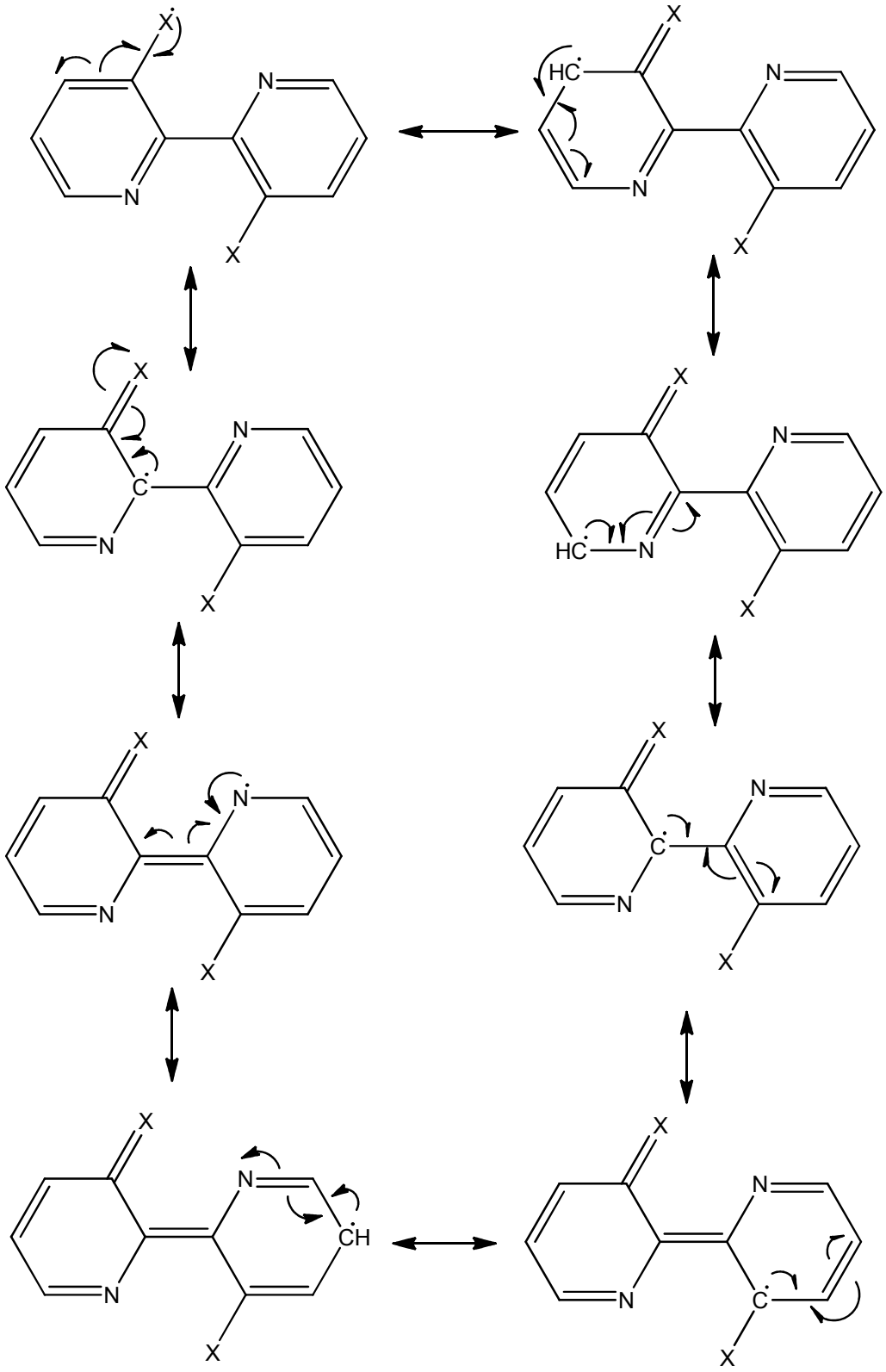

Figure 1.13 The resonance structures adopted by mono-reduced 3,3´-$(X)_2$-bpy

From figures 1.6 and 1.8 it is clear that the electron withdrawing/donating character of the substituent group has a significant effect on the electronic properties of the bpy molecule. The presence of an electron withdrawing substituent results in the bpy molecule being reduced at less negative potentials, while electron donating substituents cause the opposite effect.

Previously it was believed that the 4,4´ positions of the bipyridine ring system were the most important electronically. However, when Baxter and co-workers investigated the electronic character of a series of dicyanobipyridine complexes of Mo and W it was discovered that when the cyano substituent is in the 5,5´ positions it exerts a stronger electron withdrawing effect than when the substituent is placed in the 4,4´ positions.[21]

Takeshita *et al*. have conducted EPR investigations on a series of alkali metal bpy complexes (were M = K, Na and Li).[52] Boersma *et al.* have also studied similar alkylzinc complexes.[53] In both investigations an attempt was made to assign the observable ^{1}H hyperfine coupling constants to the four pairs of hydrogen atoms positioned around the bipyridine ring systems using the McConnell relationship for proton splittings.[54] For all of the complexes studied it was found that the largest observable ^{1}H coupling constants could be assigned to the hydrogen atoms in the 5,5´ positions. The ^{1}H coupling constant assigned to the hydrogen atoms in the 4,4´ positions was observed to be significantly smaller than the coupling to the hydrogen atoms in the 5,5´ positions. The hydrogen atoms in the 3,3´ and 6,6´ positions were found to have couplings of similar magnitude, these were much smaller than the couplings observed for the hydrogen atoms in either the

4,4´ or 5,5´ positions. Comparison of these results enables the ordering of the ring positions in terms of the amount of electron density localised at any given position, 5,5´ > 4,4´ > 3,3´ > 6,6´.

McInnes *et al*. have used EHMO and DFT methods to calculate information about the molecular orbitals of $[Pt(bpy)(CN)_2]$.[55] The contribution to the LUMO of the complex from each of the ring carbon atoms positions was calculated to be in the order 2,2´ > 4,4´ > 6,6´ > 5,5´ > 3,3´ by EHMO and 5,5´ > 2,2´ > 4,4´ > 3,3´ > 6,6´ by DFT. EPR analysis of the mono-reduced $[Pt(bpy)(CN)_2]^{1-}$ species exhibited coupling to two pairs of equivalent ^1H nuclei.[55] This suggests that two of the ring hydrogen bearing carbon atoms have significantly greater unpaired electron density than the remaining two positions.

From these studies it is evident that the 4,4´ and 5,5´ positions have the largest contribution to the electronic properties of the bpy molecule. Comparison of the plots of the first reduction potentials of $[Pt(4,4´\text{-}(X)_2\text{-bpy})Cl_2]$ and $[Pt(5,5´\text{-}(X)_2\text{-bpy})Cl_2]$ *vs*. the Hammett parameters σ_p and σ_m determined by McInnes[30] and Jack[45] indicates that the $[Pt(5,5´\text{-}(X)_2\text{-bpy})Cl_2]$ plot has a steeper gradient. Therefore changing the substituent in the 5,5´ positions has a greater effect on the reduction potential than altering the substituent in the 4,4´ positions. Jack concluded that 5,5´ positions of bpy must therefore be the most electronically important.

By comparison of the electrochemical data for the 4,4´- and 5,5´-substituted bpys presented in tables 1.2 and 1.3 it is possible to examine the nature of the interaction of the

substituent group with the bpy ring system. Analysis of the reduction potentials for the two isomers for a given substituent group and the R and F parameters can establish the relative importance of resonance and field/inductive effects on this interaction.

Examination of a wide range of substituent groups ranging from the electron donating Me group to the strongly electron withdrawing NO_2 have been previously undertaken in the Yellowlees laboratory. It is observed that for Ph, CO_2Me, CO_2Et and NO_2 substituent groups the 5,5´ isomer is reduced at less negative potentials than the 4,4´ isomer. Conversely in the case of the Me and Cl substituent groups the 4,4´ isomer is found to be easier to reduce.

The CO_2R substitution groups have an F parameter of 0.34. These groups can therefore stabilise the reduction electron through relatively strong field/inductive effects. In addition they have an R parameter of 0.11, due to these significant resonance effects it would be expected that the 5,5´ isomer would experience a greater stabilisation effect than the 4,4´ isomer. This is corroborated by the electrochemical results with the 5,5´ isomers of the CO_2Me and CO_2Et substituted bpys being 230 mV and 300 mV easier to reduce than the 4,4´ isomers respectively.

The difference in reduction potential between the 4,4´ and 5,5´ isomers of the NO_2 and Ph substituted bpys is much smaller than that observed for those with the CO_2R substituents. The 5,5´ isomer is only 40 mV more stable than the 4,4´ isomer for both of these substituents. Though the relative stabilities of the two isomers with these

substituent groups are similar the enhanced stability of the 5,5´ isomer arises from very different resonance and field/inductive effects.

Examination of the R and F values for NO_2 show that the substituent has significant resonance stabilisation with an R parameter of 0.13. This is comparable to the R parameter for the CO_2R substituents and would suggest that the 5,5´ isomer should be significantly more stable. However the field/inductive effects are much stronger in this substituent with the F parameter being 0.65. This would suggest that the field/inductive effects dominate for this substituent with the resonance effects only slightly enhancing the stability of the 5,5´ isomer.

In contrast the Ph substituent has an appreciable negative R parameter (R = -0.13) indicating that it will donate electron density into the bpy ring system and therefore destabilise the resonance forms of the reduction product. This destabilisation effect is countered by a positive field/inductive effect (F = 0.12) that acts to stabilise the reduced species. The fact that the 5,5´ isomer is slightly more stable than the 4,4´ isomer suggests that the field/inductive effects play a more prominent role than the destabilising resonance effects in this substituent group.

As mentioned above when the substituent is either Cl or Me the 4,4´ isomer is observed to reduce at less negative potentials than the 5,5´ isomer. For the Cl substituent the 4,4´ isomer was found to be more stable by 50 mV. The Cl group has a substantial negative resonance effect (R = -0.19), indicating a significant destabilisation of the reduced

species due to donation of electron density into the bpy ring system. The field/inductive effects for this substituent are strongly positive giving an F parameter of 0.42. However unlike for the Ph substituent, the field/inductive effects are insufficient to compensate for the destabilisation of the reduction product caused by the negative resonance effects.

For the Me substituent group the relative stability of the 4,4´ isomer increases compared to the Cl substituted bpys. The 4,4´ isomer is more stable than the 5,5´ isomer by 80 mV. As for the Cl substituent the Me group has a considerable negative resonance effect (R = -0.18). Again this will lead to destabilisation of the substituted bpy reduction product. Unlike the Cl group the Me substituent does not have any significant field/inductive effects (F = 0.01). Thus the destabilisation effect caused by the negative resonance effects is not offset. Therefore the due to the higher dependence of resonance effects of the 5,5´ isomer it will be significantly more destabilised compared to the 4,4´ isomer.

Table 1.4 summarises the data. One interesting observation is that there is very little difference between the 4,4´ and 5,5´ reduction potentials for all the substitution groups studied in the Yellowlees group to date apart from the two ester substituents. The question this poses is whether the esters are anomalous or whether other substituents show similar behaviour.

X	$E_{½}$(4,4') / V	$E_{½}$(5,5') / V	$E_{½}$(5,5')-$E_{½}$(4,4') / V	R	F
Me	-2.13	-2.21	-0.08	-0.18	0.01
Ph	-1.79	-1.75	0.04	-0.13	0.12
H	-2.05	-2.05	0.00	0.00	0.03
Cl	-1.69	-1.74	-0.05	-0.19	0.42
CO_2Me	-1.48	-1.25	0.23	0.11	0.34
CO_2Et	-1.53	-1.23	0.30	0.11	0.34
NO_2	-0.65	-0.61	0.04	0.13	0.65

Table 1.4 First reduction potentials for a series of 4,4´-$(X)_2$-bpy and 5,5´-$(X)_2$-bpy compounds (where X = Me, Ph, H, Cl, CO_2Me, CO_2Et and NO_2) in 0.1M [TBA][BF_4]/DMF *vs.* Ag/AgCl. Also shown is the difference in reduction potentials of the 4,4´ and 5,5´ isomers for a given substituent

Spectroelectrochemical investigations using UV/Vis/NIR and EPR spectroscopic techniques have been conducted on a wide range of substituted bpys that exhibit stable reduction products.[41,45,46,49,56] These studies have been conducted to determine the effect that the addition of a substituent group has on the character of the LUMO of the bpy molecule.

The UV/Vis/NIR spectroscopy studies conducted on the mono-reduced $[3,3´\text{-}(CO_2Et)_2\text{-bpy}]^{1-}$, $[4,4´\text{-}(X)_2\text{-bpy}]^{1-}$ (where X = Ph and CO_2Et) and $[5,5´\text{-}(X)_2\text{-bpy}]^{1-}$ (where X = Ph, CO_2Me and CO_2Et) species have resulted in spectra that display a similar pattern of transitions to those observed in the spectrum of mono-reduced unsubstituted bpy.[57] These results suggest that the semi-occupied molecular orbital (SOMO) of these compounds has significant character from the bpy ring system, with little influence from the substituent. In contrast the mono-reduced $[X,X´\text{-}(NO)_2\text{-bpy}]^{1-}$ species (were X,X´ = 3,3´, 4,4´, 5,5´) give spectra that show evidence that the reduction electron is primarily localised on the NO_2 groups of the molecule rather than being delocalised over the extended ring system.

EPR spectroscopy of the paramagnetic mono-reduced $[3,3´\text{-}(NO)_2\text{-bpy}]^{1-}$, $[4,4´\text{-}(CO_2Et)_2\text{-bpy}]^{1-}$ and $[5,5´\text{-}(X)_2\text{-bpy}]^{1-}$ (where X = Ph, CO_2Et and NO_2) species have shown that in each of these compounds the unpaired electron enters a SOMO that is spread across both rings of the bipyridine molecule. The spectra for the Ph and CO_2Et substituted bpys studied show no coupling to the spin active nuclei of the substituent groups. This is in line with the UV/Vis NIR spectroscopy results that suggest that the SOMO for these compounds is predominantly $[bpy]^{1-}$ in character.

In contrast the spectra for the 3,3´ and 5,5´ NO_2 substituted bpys exhibit a large coupling to a pair of ^{14}N nuclei which Murray attributed to the nitrogen atoms of the NO_2 groups.[49] This confirms the analysis from the UV/Vis/NIR spectroscopy that the SOMO has a high degree of character from the NO_2 substituent.

The EPR spectrum of the mono-reduced $[4,4´\text{-}(NO)_2\text{-bpy}]^{1-}$ species displays markedly different character to the other disubstituted bpy compounds investigated to date. Analysis of the spectrum indicates that the unpaired electron enters a SOMO that is located on only one of the 4-NO-py rings of the molecule. The spectrum of this molecule exhibits coupling to two different ^{14}N nuclei. The larger of these was attributed to the NO_2 group nitrogen atom by Al-Musharafi.[46] This is again in accordance with the UV/Vis/NIR results that suggest the SOMO should have a high degree of NO_2 group character.

As shown in tables 1.1 - 1.3 a number of the substituted bpys exhibit a second reduction process. It is noted that a second reduction process is only observed for bpys with substituents that have significant electron withdrawing character. EPR investigations on these compounds have found that the di-reduced species in almost all cases is diamagnetic.[41,46,49] Only in the case of 4,4´-(NO_2)-bpy is the di-reduced species paramagnetic.[45,58] This result is in direct contradiction to the DFT calculations conducted by Duan *et al.* which suggest that the di-radical should be lower in energy for all bpy systems.[59]

Whether the second reduction electron enter the higher energy LUMO+1 or spin pairs with the electron in the SOMO is dependent on the energy gap between the SOMO and LUMO+1 compared to the energy penalty conceded by the spin pairing of the electrons. The first and second reductions of 4,4´-(NO_2)-bpy in 0.1M [TBA][BF_4]/dimethylformamide (DMF) are separated by 140 mV. This is significantly smaller than most of the other substituted bpys that have two observable reductions, with the only exception of 5,5´-(NO_2)$_2$-bpy. 5,5´-(NO_2)$_2$-bpy in 0.1M [TBA][BF_4]/DMF has a very small separation of 90 mV. EPR experiments have confirmed that this is a spin pairing process despite the small energy gap.

1.3 Previous investigations into solvent effects

In many previous investigations the authors have considered the solvent to be inert and have no effect upon the redox process. This had led to the solvent frequently being changed between different studies on the same compound without considering any effects

that this might have on the system.[45] When an extensive search of the literature is conducted a number of papers that describe solvent effects on the electrochemical character of the species studied can be found. The reaction entropies, $\Delta S°_{rc}$, for a series of simple octahedral M(III/II) couples in water using a non-isothermal cell[61] has been investigated by Weaver et al.[61,62] It was determined that the experimental $\Delta S°_{rc}$ values were dependent on the nature of the bound ligands. The dependence observed was much larger than would have been expected from predictions made using the dielectric-continuum Born model.[63] This led Weaver to conclude that the observed effect was due to interactions of the ligand with the surrounding water molecules.

Since the study by Weaver numerous investigations have been conducted into the relation between $\Delta S°_{rc}$ and the nature of the solvent.[64-84] Gutmann has determined a linear correlation between $\Delta S°_{rc}$ and the solvent acceptor number (AN)[85] for a range of simple M(III/II) couples. Hupp and Weaver have proposed an empirical equation for this correlation, Equation 1.5.[86]

$$\Delta S°_{rc} = K_1 + K_2 (AN) + K_3 (Z_{ox}^2 - Z_{red}^2) / r \qquad \textbf{Equation 1.5}$$

Where $\Delta S°_{rc}$ is the reaction entropy of the M(III/II) couple (J K^{-1} mol^{-1}), AN is the acceptor number, Z_{ox} and Z_{red} are the charge numbers of the oxidised and reduced species respectively, r is the effective radius of the couple and K_1, K_2, and K_3 are constants empirically determined to be 91.5 J K^{-1} mol^{-1}, -2.43 J K^{-1} mol^{-1} and 89.6 J K^{-1} mol^{-1} Å respectively.

Jaworski[87] has determined that specific solvation interactions are also important in the electrochemical properties of organic molecules. It was discovered that the $\Delta S°_{rc}$ for the reduction of *p*-dicyanobenzene had a linear correlation with the acceptor number of the solvent used. In comparison the reduction of anthracene was found to be described best by the dielectric continuum approach.[87] The reduction of nitromesitylene was also considered. It was found that a two parameter approach involving the acceptor number and the solvent donor number (DN) described the system best.[87]

The difference between these approaches has been attributed to the differing degrees of delocalisation of the electric charge in each compound. The charge is localised at the cyano groups in *p*-dicyanobenzene but the charge is far more delocalised in anthracene leading to much weaker specific solvation interactions. The correlation equation (Equation 1.5) determined previously for transition metal compounds was not found to hold for organic radicals.[88] This difference can be rationalised by considering the difference in the degree of access of the solvent molecules to the reduction site. In transition metal complexes the redox process is metal localised so the site where the electron transfer occurs is surrounded by ligands. These ligands will prevent solvent molecules from reaching the site of the redox process and thus solvent will have little effect. In comparison organic radicals often have an exposed charge and solvent molecules can gain direct access to it.

Several authors have since investigated the effect of altering the solvent on the half-wave potential, $E_{½}$, of redox couples. A linear correlation between the $E_{½}$ value of $K^{+/0}$ couple

and the solvent donor number was determined by Gritzner.[89] Keita *et al*. have determined that the acceptor number showed the best correlation for the reductions of $[\alpha\text{-}SiW_{12}O_{40}]K_4$ and $[\alpha\text{-}P_2W_{16}O_{62}]K_6$ as the solvent is changed.[90]

Most recently the effect of solvent on the electronic properties of a number of substituted pyridines and 2,2´-bipyridines has been investigated. Moorcraft found that the reduction potentials of X-NO_2-py and X-CO_2Me-py (where X = 2, 3 and 4) were significantly effected by the choice of the solvent.[91] However Moorcraft was unable to draw any correlation between the observed reduction potentials and a number of empirical parameters of the solvents used.[91]

Murray and Al-Musharafi have investigated a series of NO_2 substituted bpy compounds.[46,49] For 4-NO_2-bpy and 5,5´-$(NO_2)_2$-bpy it was found that there was a strong linear correlation between the half-wave potentials of the observed reductions and the solvent acceptor number. Murray has also determined a correlation between increasing acceptor number and decreasing $\Delta E_{½}$ for the two one-electron reductions of 5,5´-$(NO_2)_2$-bpy.[49] Due to the fact that acceptor number is measure of solvent acidity,[83] these effects can be attributed to greater stabilisation of the negatively charged reduction products by more Lewis acidic solvents.

Conversely when 4-NO_2-4´-Cl-bpy and 4,4´-(NO_2)-bpy were studied by Al-Musharafi it was found that the reduction potentials of these molecules exhibit a dependence on the solvent but no correlation with the solvent acceptor number was observed.[46]

Al-Musharafi also investigated 6,6´-$(Cl)_2$-bpy and found that the electrochemistry of this compound was solvent independent.[46]

1.4 2,2´-bipyridine as a ligand for TM complexes

As previously mentioned in section 1.1, 2,2´-bipyridine is known to coordinate to transition metal *via* a bidentate motif through the lone pairs of the two ring nitrogen atoms. This requires the molecule to twist about the C(2)-C(2´) inter ring bond from the *trans* confirmation favoured in solution to the *cis* conformation (figure 1.14).

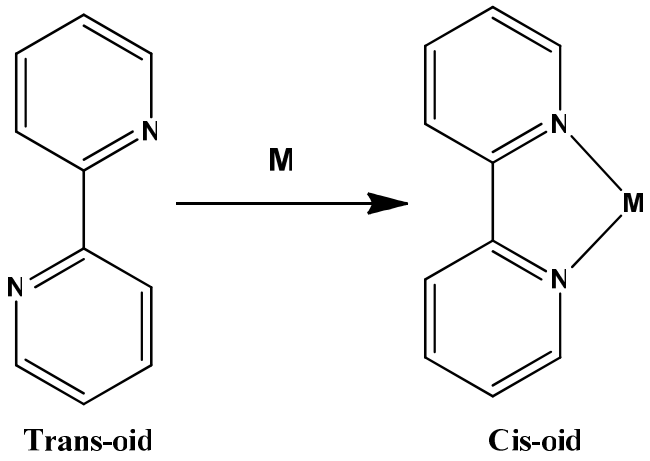

Figure 1.14 The *trans/cis* geometry shift of 2,2´-bipyridine upon complexation to a metal

Substituted bipyridines are known to form complexes with metal ions from throughout the periodic table. This stability arises from the ability to form a stable five membered ring with M^{n+} ion at the centre. Bpy can act as a σ-donor and π-acceptor ligand. The lone pair of electrons on the nitrogen atoms of the ring can form a σ-bond with an unoccupied orbital of appropriate symmetry on the metal ion.

In a similar manor occupied orbitals of the metal centre, commonly d-orbitals, that posses the appropriate symmetry can overlap with the unoccupied orbitals of the delocalised π^* system of the 2,2´-bipyridine. These two interactions are synergistic: σ-donation from the bpy ligand increases the electron density on the metal centre, thus enhancing the ability of the metal to donate electron density to the π^* system of the bpy. This cooperative donation of electron density from the metal centre to the ligand is known as π backdonation, figure 1.15.

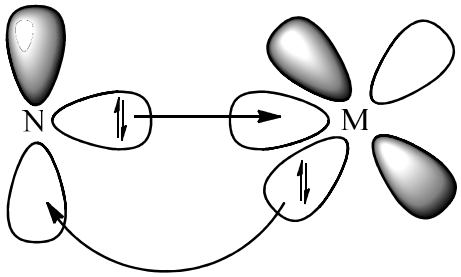

Figure1.15 Schematic of σ-donating and π-accepting character of 2,2´-bipyridine

The N(1)-M-N(1´) angle formed upon chelation of the bpy ligand to the metal centre has been found to be approximately 80°.[48,49] A bite angle of this size leads to octahedral and square planar geometries being favoured, as the coordination angle is closer to optimal angle of 90° for these geometries than 109.5° for a tetrahedral geometry.

1.5 The aims of this Thesis

This thesis is devoted to the study of two further substituted 2,2´-bipyridines; namely X,X´-$(CF_3)_2$-bpy and X,X´-$(CN)_2$-bpy, figure 1.16. Both these substituents are electron withdrawing as both contain electronegative elements, F and N respectively. The CF_3 substituent has no π-character whereas the CN substituent has, which can extend the π-conjugation of the system. Thus both ligand types should be easily reducible and the spin active F and N centres lend themselves to detailed EPR study of the mono-reduced paramagnetic state.

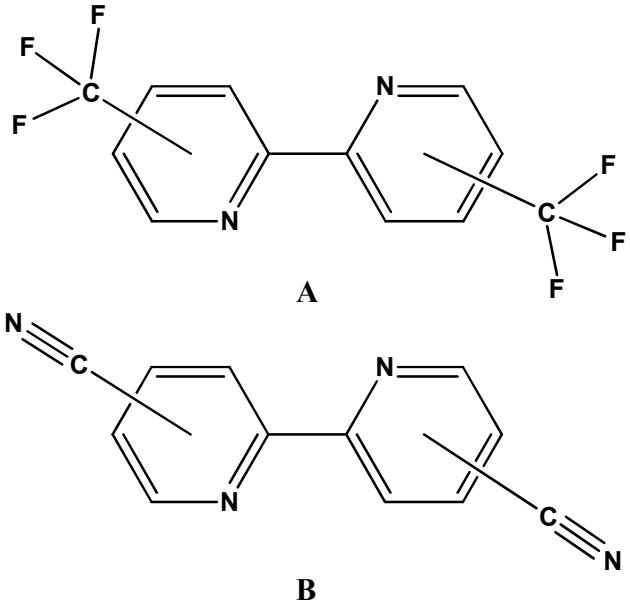

Figure1.16 General structure of the A) X,X´-$(CF_3)_2$-2,2´-bipyridine and B) X,X´-$(CN)_2$-2,2´-bipyridine molecules studied in this work

The aims of this thesis are detailed below:

- To investigate the electronic structure of CN and CF_3 substituted polypyridine compounds using a combination of electrochemical techniques, UV/Vis/NIR

spectroelectrochemistry, EPR spectroelectrochemistry and DFT computational methods.

- To investigate the effect of altering the position of the substituent group on the electronic structure by comparing the electrochemical and spectroelectrochemical results for the three isomers of cyanopyridine and the 3,3´, 4,4´, 5,5´ isomers of dicyanobipyridine and ditrifluoromethylbipyridine.

- To compare the results for the CN and CF_3 substituted bpy compounds to previously investigated substituted bpy molecules to establish if the groups under investigation fits with the trend observed between the reduction potential and the Hammett parameter, σ, of the substituent. Comparison of the results for the cyano and trifluoromethyl groups will enable the relative importance of resonance *vs*. inductive effects to be studied. Additionally, the relative half-wave potentials for the 4,4´ and 5,5´ disubstituted analogues will also be studied to permit comparison with the results in table 1.4.

- To investigate the electrochemical properties of the cyano substituted polypyridines in a range of solvents. Comparison of the results from these solvent studies will determine if the solvent acceptor number (AN) has a similar effect on the electrochemical properties of the dicyanobipyridine molecules investigated as those previously observed for the dinitrobipyridine analogues. Solvent effects on the reduced species will be considered by EPR spectroelectrochemistry.

- To undertake DFT calculations using a variety of basis sets for X,X´-(CF_3)-bpy and X,X´-$(CN)_2$-bpy in order to aid assignment of UV/Vis/NIR transitions and EPR coupling constants in the reduced state and to determine which basis set gives the most acceptable agreement with experiment.

- To prepare complexes with the dicyanobipyridine and ditrifluoromethylbipyridine ligands bound to Fe(II) and Pt(II) metal centres, to study the effect of the metal 2+ centre on the electronic character of the pro-ligands. This will enable an assignment of the nature of the redox processes observed for each the complex to a ligand-based or metal-based process.

1.6 References

1. E. Klingsberg, *Pyridine and its derivatives*, Interscience Publishers, New York, 1960, Vol 14, pt 1.

2. J. McMurry, *Organic chemistry*, 6th ed., Brooks/Cole Thomson Learning, Belmont, 2004.

3. M. J. Winter, *d-block chemistry*, Oxford University Press, Oxford, 1994.

4. L. L. Merritt Jr., E. D. Schroeder, *Acta Cryst.*, 1956, **9**, 801-804.

5. L. Pauling, *The Nature of the chemical bond*, 2nd ed., Cornell University Press, Ithaca, 1948.

6. P. E. Fielding, R. J. W. Le Fèvre, *J. Chem. Soc.*, 1951, 1811-1814.

7. C. W. N. Cumper, R. F. A. Ginman, A. I. Vogel, J. Chem. Soc., 1962, 1188-1192.

8. P. H. Cureton, C. G. Le Fèvre, R. J. W. Fèvre, *J. Chem. Soc.*, 1963, 1736-1739.

9. A. Göller, U.-W. Grummt, *Chem. Phys. Lett.*, 2000, **321**, 399-405.

10. K. Nakamoto, *J. Phys. Chem.*, 1960, **64**, 1420-1425

11. A. Göller, U.-W. Grummt, *Chem. Phys. Lett.*, 2002, **354**, 233-242.

12. M. Castellà-Ventura, E. Kassab, G. Buntinx, O. Poizat, *Phys. Chem. Chem. Phys.*, 2000, **2**, 4682-4689.

13. F. H. Case, *J. Am. Chem. Soc.*, 1946, **68**(12), 2574-2577.

14. G. Maerker, F. H. Case, *J. Am. Chem. Soc.*, 1958, **80**, 2745-2748.

15. W. H. F. Sasse, C. P. Whittle, *J. Chem. Soc.*, 1961, 1347-1350.

16. C. P. Whittle, *J. Heterocycl. Chem.*, 1977, **14**, 191-194.

17. K. D. Bos, J. G. Kraaijkamp, J. G. Noltes, *Synth. Commun.*, 1979, **9**, 497-504.

18. D. Wenkert, R. B. Woodward, *J. Org. Chem.*, 1983, **8**, 283-289.

19. D. C. Craig, H. A. Goodwin, D. Onggo, *Aust. J. Chem.*, 1988, **41**, 1157-1169.

20. J. A. Connor, C. Overton, N.E. Murr, *J. Organomet. Chem.*, 1984, **277**, 277-284.

21. P. N. W. Baxter, J. A. Conner, *J. Organomet. Chem.*, 1988, **355**, 193-196.

22. L. A. Worl, R. Duesing, P. Chen, L. D. Ciana, T. J. Meyer, J. Chem. Soc., *Dalton Trans.*, 1991, 849-858.

23. M. A. Weiner, A. Basu, *Inorg. Chem.*, 1980, **19**, 2797-2800.

24. A. Basu, M. A. Weiner, T. C. Strekas, H. D. Gafney, *Inorg. Chem.*, 1982, **21**, 1085-1092.

25. A. Basu, H. D. Gafney, T. C. Strekas, *Inorg. Chem.*, 1982, **21**, 2231-2235.

26. S. Anderson, E. C. Constable, K. R. Seddon, J. E. Turp, J. E. Baggott, M. J. Pilling, *J. Chem. Soc.*, *Dalton Trans.*, 1985, 2247-2261.

27. R. J. Donohoe, C. D. Tait, M. K. De Armond, D. W. Wertz, *J. Phys. Chem.*, 1986, **90**, 3923, 3927-3930.

28. R. J. Donohoe, C. D. Tait, M. K. DeArmond, D. W. Wertz, *J. Phys. Chem.*, 1986, 90, 3923-3926.

29. M. Furue, K. Maruyama, T. Oguni, M. Naiki, M. Kamachi, *Inorg. Chem.*, 1992, **31**, 3792-3795.

30. E. J. L. McInnes, R. D. Farley, C. C. Rowlands, A. J. Welch, L. Rovatti, L. J. Yellowlees, *J. Chem. Soc.*, *Dalton Trans.*, 1999, 4203-4208.

31. E. C. Consatble, *Adv. Inorg. Chem.*, 1989, **34**, 1-63.

32. F. Pichot, J. H. Beck, C. M. Elliott, *J. Phys. Chem. A*, 1999, **103**, 6263-6267.

33. F. P. Rotzinger, S. Munavalli, P. Comte, J. K. Hurst, M. Gratzel, F.-J. Pern, A. J. Frank, J. Am. Chem. Soc., 1987, **109**(22), 6619-6626.

34. H. F. M. Nelissen, A. F. J. Schut, F. Venema, M. C. Feiters, R. J. M. Nolte, *Chem. Commun*., 2000, 577-578.

35. P. D. Beer, O. Kocian, R. J. Mortimer, C. Ridgway, *Dalton Trans*., 1993, **17**, 2629-2638.

36. V. W.-W. Yam, A. S.-F. Kai, *Inorganica Chemica Acta*, 2000, **300**-**302**, 82-90.

37. B. O'Regan, M. Grätzel, *Nature*, 1991, **353**. 737-739.

38. M. K. Nazeeruddin, A. Kay, I. Rodicio, R. Humphry-Baker, E Mueller, P. Liska, N. Vlachopoulos, M. Graetzel, *J. Am. Chem. Soc*., 1993, **115**(14), 6382-6390.

39. A. Islam, H. Sugihara, K. Hara, L. Pratap Singh, R. Katoh, M. Yanagida, Y. Takahashi, S. Murata, H. Arakawa, *New J. Chem*., 2000, **24**(6), 343-345.

40. A. Islam, H. Sugihara, K. Hara, L. Pratap Singh, R. Katoh, M. Yanagida, Y. Takahashi, S. Murata, H. Arakawa, G. Fujihashi, *Inorg. Chem*., 2001, **40**(21), 5371-5380.

41. E. A. M. Geary, K. L. McCall, A. Turner, P. R. Murray, E. J. L. McInnes, L. A. Jack, L. J. Yellowlees, N. Robertson, *Dalton Trans*., 2008, 3701-3708.

42. F. Calogero, H. S. Freeman, J. F. Esancy, W. M. Whaley, *Dyes and Pigments*, 1987, **8**, 431-447.

43. J. Hassan, V. Penalva, L. Lavenot, C. Gozzi, M. Lemaire, *Tetrahedron*, 1998, **54**(45), 13793-13804.

44. J. Hassan, C. Gozzi, M. Lemaire, *C. R. Acad. Sci*., *Série IIc: Chimie*, 2000, 517-521.

45. L. Jack, Ph.D Thesis, University of Edinburgh, 2003.

46. S. K. Al-Musharafi, Ph.D Thesis, University of Edinburh, 2006.

47. J. March, *Advanced Organic Chemistry* : *reactions*, *mechanisms*, *and structure*, 4th ed., Wiley Interscience publications, New York, 1992.

48. E. J. L. McInnes, Ph.D Thesis, University of Edinburgh, 1995.

49. P. R. Murray, Ph.D Thesis, University of Edinburgh, 2006.

50. C. Hansch, A. Leo, R. W. Taft, *Chem. Rev*., 1991, **91**, 165-195.

51. R. W. Taft, I. C. Lewis, *J. Am. Chem. Soc*., 1958, **80**, 2436-2443.

52. T. Takeshita, N. Hirota, *J. Am. Chem. Soc*., 1971, **93**, 6421-6429.

53. J. Boersma, A. Mackor, J. G. Noltes, *J. Organomet. Chem*., 1975, **99**, 337-341.

54. H. M. McConnell, *J. Chem. Phys*., 1956, **24**(4), 764-766.

55. E. J. McInnes, R. D. Farley, S. A. Macgregor, K. J. Taylor, L. J. Yellowlees, C. C. Rowlands, *J. Chem. Soc*., *Faraday Trans*., 1998, **94**, 2985-2991.

56. L. Yang, F. L. Wimmer, S. Wimmer, J. Zhao, P. S. Braterman, *J. Organomet. Chem*., 1996, **525**, 1-8.

57. E. König, S. Kremer, *Chem. Phys. Lett*., 1970, **5**(2), 87-90.

58. E. J. L. McInnes, A. J. Welch, L. J. Yellowlees, *Chem. Commun*., 1996, **21**, 2393-2394.

59. H. X. Duan, Z. M. Su, Y. Q. Qiu, L. K. Yan, Y. H. Kan, R. S. Wang, *Synth. Met*., 2003, **137**, 1351-1352.

60. C. M. Criss, M. Saloman, *Physical Chemistry of Organic Solvent Systems*, Plenum Press, New York, 1973.

61. E. L. Yee, R. J. Cave, K. L. Guyer, P. D. Tyma, M. J. Weaver, *J. Am. Chem. Soc*., 1979, **101**(5), 1131-1137.

62. E. L. Yee, M. J. Weaver, *Inorg. Chem*., 1980, **19**(4), 1077-1079.

63. K. J. Laidler, Can. J. Chem., 1956, **34**, 1107-1113.

64. N. Sutin, M. J. Weaver, E. L. Yee, *Inorg. Chem.*, 1980, **19**(4), 1096-1098.

65. S. Sahami, M. J. Weaver, *J. Electroanal. Chem. Interfacial Electrochem.*, 1981, **122**, 155-170.

66. S. Sahami, M. J. Weaver, J. Electroanal. Chem. Interfacial Electrochem., 1981, 122, 171-181.

67. M. J. Weaver, *J. Phys. Chem.*, 1979, **83**(13), 1748-1757.

68. M. J. Weaver, *J. Phys. Chem.*, 1980, **84**(6), 568-576.

69. M. J. Weaver, E. L. Yee, *Inorg. Chem.* 1980, **19**(7), 1936-1945.

70. K. M. Kadish, K. Das, D. Schaeper, C. L. Merill, B. R. Welch, L. J. Wilson, *Inorg. Chem.*, 1980, **19**(9), 2816-2821.

71. K. M. Kadish, D. Schaeper, J. Chem. Soc. Chem. Commun., 1980, **24**, 1273-1275.

72. M. P. Youngblood, D. W. Margerum, *Inorg. Chem.*, 1980, **19**(10), 3038-3072.

73. J. M. Anast, A. Hamburg, D. W. Margerum, *Inorg. Chem.*, 1983, **22**(15), 2139-2145.

74. V. T. Taniguchi, N. Sailasuta-Scott, F. C. Anson, H. B. Gray, *Pure Appl. Chem.*, 1980, **52**(10), 2275-2281.

75. N. Sailasuta, F. C. Anson, H. B. Gray, *J. Am. Chem. Soc.*, 1979, **101**(2), 455-458.

76. V. T. Taniguchi, B. G. Malmstrom, F. C. Anson, H. B. Gray, *Proc. Nat. Acad. Sci. U.S.A.*, 1982, **79**(10), 3387-3389.

77. L. S. Reid, V. T. Taniguchi, H. B. Gray, A. G. Mauk, *J. Am. Chem. Soc.*, 1982, **104**(26), 7516-7519.

78. W. Bottcher, G. M. Brown, N. Sutin, *Inorg. Chem.*, 1979, **18**(6), 1447-1451.

79. E. F. Wawrousek, J. V. McArdle, *J. Inorg. Biochem.*, 1982, **17**(3), 169-183.

80. H. Ogino, K. Ogino, *Inorg. Chem.*, 1983, **22**(15), 2208-2211.

81. J. T. Hupp, H. Y. Lui, P. A. Lay, W. H. F. Petri, A. M. Sargeson, M. J. Weaver, *J. Electroanal. Chem. Interfacial Electrochem.*, 1984, **163**(1-2), 371-379.

82. J. T. Hupp, M. J. Weaver, *J. Electrochem. Soc.*, 1984, **131**(3), 619-622.

83. J. T. Hupp, M. J. Weaver, *Inorg. Chem.*, 1984, **23**(2), 256-258.

84. J. T. Hupp, M. J. Weaver, *J. Phys. Chem.*, 1984, **88**(9), 1860-1864.

85. V. Gutmann, *The Donor-Acceptor Aproach to Molecular Interactions*, plenum Press, New York, 1978.

86. J. T. Hupp, M. J. Weaver, *Inorg. Chem.*, 1984, **23**(22), 3639-3644.

87. J. S. Jaworski, *J. Electroanal. Chem.*, 1987, **219**(1-2), 209-219.

88. J. S. Jaworski, *J. Electroanal. Chem.*, 1989, **260**(2),327-333.

89. G. Gritzner, *J. Phys. Chem.*, 1986, **90**(21), 5478-5485.

90. B. Keita, D. Bouaziz, L. Nadjo, *J. Electrochem. Soc.* 1988, **135**(1), 87-91.

91. L. Moorcraft, Ph.D Thesis, University of Edinburgh, 2008.

2 Experimental and Theoretical techniques

2.1 Synthesis

2.1.1 Tetrabutyl ammonium tetrafluroborate $[TBA]^+ [BF_4]^-$ electrolyte

Tetrafluroboric acid (120 ml, 50%) was dissolved in water (500 ml) and tetrabutylammonium hydroxide (40%) was added until neutralisation was achieved (pH 7). More water (1 l) was added to ensure efficient stirring. The white precipitate of $[TBA][BF_4]$ was filtered, recrystallised twice from 1:1 mixture of methanol:water and dried in a vacuum oven at 60°C before use.

2.1.2 5,5´-dibromo-2,2´-bipyridine

The compound was prepared by the method of Bruce *et al.*[1] with modifications. 2,5-Dibromopyridine (8.00 g, 0.338 mol), hexamethylditin (5.53 g, 0.0169 mol) and $[Pd(PPh_3)_4]$ (0.80 g) were heated to relfux in benzene (250 cm^3) for 65 hours under argon. The reaction mixture was cooled and ether (200 cm^3) added. An off-white precipitate was filtered off over a sintered funnel. Yield: 2.480 g (46.7%), ^1H NMR ($CDCl_3$, 250.13 MHz): δ 8.637 (dd, J = 2.325, 0.605 Hz, 2H), 8.217 (dd, J = 8.510, 0.690 Hz, 2H), 7.869 (dd, J = 8.515, 2.355 Hz, 2H) ppm.

2.1.3 5,5´-dicyano-2,2´-bipyridine

The compound was prepared by the method of Veauthier *et al.*[2] with modifications. 5,5´-dibromobipyridine (0.400 g, 1.28 mmol), NaCN (0.124 g, 2.54 mmol), $Pd(OAc)_2$ (0.036 g, 0.16 mmol), dpppe (0.15 g 0.34 mmol), TMEDA (0.13 ml, 0.86 mmol) and mesitylene (5ml) were loaded into a 25 ml round bottomed flask equipped with a stir

bar. The flask was fitted with a reflux condenser and the whole apparatus was purged under Ar for 10 min before initiating reflux. The contents were heated to reflux temperature under Ar for 60 hours, during which time the colour of the reaction mixture became dark brown. The reaction was allowed to cool and yielded a grey gel. HPLC grade water (10 ml) was added to the reaction flask and the slurry was stirred for 10 min. The slurry was then filtered through a medium sintered glass frit providing a grey solid. Due to the partial solubility of the product in mesitylene the aqueous slurry from the filtration was extracted with CH_2Cl_2 (2 x 15 ml) and this was combined with the undissolved portion. The solution was then filtered through a medium sintered frit to remove any undissolved solid. The solvent was then removed under vacuum using a rotary evaporator and the powder was rinsed with pentane (3 x 20 ml) on a sintered glass frit and dried under vacuum for 12 hours to yield a white powder. Yield: 0.0630 g (24.1%), ^{1}H NMR ($CDCl_3$, 250.13 MHz): δ 8.898 (dd, J = 2.085, 0.805 Hz, 2H), 8.571 (dd, J = 8.305, 0.825 Hz, 2H), 8.069 (dd, J = 8.310, 2.120 Hz, 2H) ppm.

2.1.4 4,4´-trifluromethyl-2,2´-bipyridine

The compound was prepared by the method of McFarland *et al*.[3] with modifications. Activated zinc powder was prepared by washing ground zinc powder with 0.5 M HCl followed by water, ethanol and diethyl either. The washed zinc was subsequently subjected to vacuum at 120°C overnight. Tetraethylammonium iodide was dried under vacuum at 110°C for 8 h and then stored in a vacuum dessicator containing phosphorous pentoxide for 16 hours. The tetraethylammonium iodide (4.0 g, 20 mmol), and activated zinc (1.96 g, 30 mmol) were then combined with dibromobis(triphenylphosphine)-nickel(II) (4.46 g, 6 mmol) under argon. Argon-

purged dry THF (70 ml) was added via cannula and the mixture was stirred at room temperature for 30 minutes. 2-chloro-4-trifluromethyl-pyridine (3.6 g, 20 mmol) was injected into the mixture which was subsequently stirred at 50°C for 48 hours.

The resulting black slurry was added to 200 ml 2 M ammonium hydroxide and mixed with 200 ml of chloroform and allowed to stir for 15 min. The reaction mixture was then filtered. The organic layer was separated, dried with anhydrous $NaSO_4$ and evaporated to dryness *in vacuo*. Purification of the brown residue was achieved by silica gel column chromatography using 0.5% ethyl acetate in hexane, yielding the desired product as light yellow crystals. Yield: 0.283 (9.7%). mp = 81°C (lit. = 81.5-82°C[3]). ^{1}H NMR (250.13 MHz, $CDCl_3$): δ 8.67 (s, 2H), 8.825 (d, J = 5.05 Hz, 2H), 7.52, (d, J = 5.05 Hz, 2H) ppm; ^{19}F NMR (250.13 MHz, $CDCl_3$) δ 65.7 (s, 6F) ppm. CHN analysis for $C_{12}H_6N_2F_6$: Calculated: C, 49.33%; H, 2.07%; N, 9.59%. Found: C, 49.73%; H, 1.86%; N, 9.24%. +ve ESI-MS: m/z = 292.04 (M^+).

2.1.5 5,5´-trifluromethyl-2,2´-bipyridine

Synthesis was achieved from 2-chloro-5-trifluoromethyl-pyridine as per the method for 4,4´-Ditrifluoroemthyl-2,2´-bipyridine (Section 2.1.4). The product was isolated as a white powder. Yield: 0.9430 g (32.3%) ^{1}H NMR (250.13 MHz, CDCl3) δ 9.07 (s, 2H), 8.675 (d, J = 8.72 Hz, 2H), 8.275 (d, J = 8.72 Hz, 2H) ppm; ^{19}F NMR (250.13 MHz, $CDCl_3$) δ 64.0 (s, 6F) ppm. CHN analysis for $C_{12}H_6N_2F_6$: Calculated: C, 49.35%; H, 2.07%; N, 9.59%. Found: C, 55.12%; H, 2.80%; N, 7.49%. +ve ESI-MS: m/z = 292.04 (M^+).

2.1.6 3,3´-trifluromethyl-2,2´-bipyridine

Synthesis was achieved from 2-chloro-3-trifluoromethyl-pyridine as per the method for 4,4´-Ditrifluoroemthyl-2,2´-bipyridine (Section 2.1.4). The product was isolated as a brown solid. Yield: 0.320 g (11.0%). ^{1}H NMR (250.13 MHz, CDCl3) δ 8.776 (dd, J = 4.82, 1.44 Hz, 2H), 8.063 (dd, J = 8.08, 1.57 Hz, 2H), 7.488 (dd, J = 8.08, 4.82 Hz, 2H) ppm; ^{19}F NMR (250.13 MHz, $CDCl_3$) δ 59.6 (s, 6F) ppm.

2.1.7 [Pt(II)(4-cyanopyridine)$_2$(Cl)$_2$]

$K_2[PtCl_4]$ 0.0875 g (2.11 mmol) was added to a 25 ml round bottomed flask. The $K_2[PtCl_4]$ was then dissolved in distilled 5 ml H_2O. A solution of 4-cyanopyridine 0.0439 g (0.422 mmol) dissolved in 5 ml H_2O was then added to the aqueous solution of $K_2[PtCl_4]$, yielding an orange solution. The reaction mixture was allowed to stir for 48 hours. The yellow/green precipitate formed was filtered under vacuum and washed with distilled H_2O. The product was dried overnight in a vacuum oven. Yield 0.0763 g (76.3%), CHN analysis for $C_{12}H_8N_4Cl_2Pt$: Calculated: C, 30.39%; H, 1.70%; N, 11.81%. Found: C, 30.41%; H, 1.60%; N, 11.60%.

2.1.8 [Pt(II)(3-cyanopyridine)$_2$(Cl)$_2$]

$K_2[PtCl_4]$ 0.0875 g (2.11 mmol) was added to a 25 ml round bottomed flask. The $K_2[PtCl_4]$ was then dissolved in distilled 5 ml H_2O. A solution of 3-cyanopyridine 0.0439 g (0.422 mmol) dissolved in 5 ml H_2O was then added to the aqueous solution of $K_2[PtCl_4]$, yielding an orange solution. The reaction mixture was allowed to stir for 4 days. The yellow precipitate formed was filtered under vacuum and washed with distilled H_2O. The product was dried overnight in a vacuum oven. Yield 0.0526 g

(52.6%), CHN analysis for $C_{12}H_8N_4Cl_2Pt$: Calculated: C, 30.39%; H, 1.70%; N, 11.81%. Found: C, 30.35%; H, 1.58%; N, 11.41%.

2.1.9 [Pt(II)(3,3´-dicyano-2,2´-bipyridine)(Cl)$_2$]

$K_2[PtCl_4]$ 0.0882 g (0.212 mmol) was added to a 50 ml round bottomed flask. The $K_2[PtCl_4]$ was then dissolved in distilled 10 ml H_2O. A solution of 3,3´-dicyano-2,2´-bipyridine 0.0440 g (0.213 mmol) dissolved in 5 ml MeCN was then added to the aqueous solution of $K_2[PtCl_4]$. The reaction mixture was then heated to reflux for 48 h. The reaction mixture was then cooled, filtered under vacuum and washed with distilled H_2O. The orange product was dried overnight in a vacuum oven. Yield 0.0725 g (72.4%), ^{1}H NMR ($(CD_3)_2SO$, 250.13 MHz): δ 9.3125 (dd, J = 6.52 Hz, 2H), 8.705 (dd, J = 9.52 Hz, 2H), 7.942 (dd, J = 14.22 Hz, 2H) ppm. CHN analysis for $C_{12}H_6N_4Cl_2Pt$: Calculated: C, 30.52%; H, 1.28%; N, 11.87%. Found: C, 29.63%; H, 1.21%; N, 11.32%. IR (KBr, cm^{-1}): 2238 (s) (C≡N stretch).

2.1.10 [Pt(II)(5,5´-dicyano-2,2´-bipyridine)(Cl)$_2$]

$K_2[PtCl_4]$ 0.0880 g (0.212 mmol) was added to a 50 ml round bottomed flask. The $K_2[PtCl_4]$ was then dissolved in distilled 10 ml H_2O. A solution of 5,5´-dicyano-2,2´-bipyridine 0.0449 g (0.218 mmol) was dissolved in 10 ml MeCN was then added to the aqueous solution of $K_2[PtCl_4]$. The reaction mixture was then heated to reflux for 96 h. The reaction mixture was then cooled, filtered under vacuum and washed with distilled H_2O. The black powder product was dried overnight in a vacuum oven. Yield: 0.0545 g (54.4%), ^{1}H NMR ($(CD_3)_2SO$, 500 MHz): δ 9.770 (dd, J = 1.42 Hz, 2H), 9.047 (dd, J = 10.3 Hz, 2H), 8.8952 (dd, J = 8.19 Hz, 2H) ppm. CHN analysis for

$C_{12}H_6N_4Cl_2Pt$: Calculated: C, 30.52%; H, 1.28%; N, 11.87%. Found: C, 24.82%; H, 1.13%; N, 7.95%. IR (KBr, cm^{-1}): 2238 (s) (C≡N stretch)

2.1.11 [Fe(II) (5,5´-dicyano-2,2´-bipyridine)$_3$].(BF$_4$)$_2$

[Fe(II)$(BF_4)_2$].$6H_2O$ 0.0398 g (0.118 mmol) and 5,5´-dicyano-2,2´-bipyridine 0.0729 g (0.354 mmol) were added to a 25 ml round bottomed flask. 10 ml of MeCN was then added to the solids. Upon dissolution of the solids a deep purple coloured solution was formed instantaneously. The reaction mixture was then left to stir for 90 mins to ensure complete formation of the desired product. The mixture was then concentrated by removing most of the MeCN on a rotary evaporator. Diethyl ether was then added to crash the product out of solution. The resulting purple/black precipitate was filtered off and dried overnight in a vacuum oven. Yield: 0.0592 g (58.8%), ^{1}H NMR (CD_3CN, 500 MHz): δ 8.766 (d, J = 8.35 Hz, 2H), 8.562 (dd, J = 10.09 Hz, 2H), 7.642 (d, J = 1.10 Hz, 2H) ppm. CHN analysis for $C_{36}H_{18}N_{12}B_2F_8Fe$: Calculated: C, 50.98%; H, 2.14%; N, 19.82%. Found: C, 41.08%; H, 2.20%; N, 14.80%.

2.1.12 [Fe(II) (4,4´-ditrifluoromethyl-2,2´-bipyridine)$_3$].(BF$_4$)$_2$

Synthesis of [Fe(II)(4,4´-ditrifluoromethyl-2,2´-bipyridine)$_3$].$(BF_4)_2$ was achieved using the same methods as for [Fe(II)(5,5´-dicyano-2,2´-bipyridine)$_3$].$(BF_4)_2$ with the exception that 0.103 g (0.353 mmol) 4,4´-ditrifluoromethyl-2,2´-bipyridine was used. Yield: 0.0729 g (72.9%) CHN analysis for $C_{36}H_{18}N_6B_2F_{26}Fe$: Calculated: C, 39.09%; H, 1.64%; N, 7.60%. Found: C, 35.31%; H, 1.68%; N, 6.86%.

2.1.13 [Fe(II) (5,5´-ditrifluoromethyl-2,2´-bipyridine)$_3$].(BF$_4$)$_2$

Synthesis of [Fe(II)(5,5´-Ditrifluoromethyl-2,2´-bipyridine)$_3$].(BF$_4$) was achieved using the same methods as for [Fe(II)(5,5´-dicyano-2,2´-bipyridine)$_3$].(BF$_4$) with the exception that 0.103 g (0.353 mmol) 4,4´-ditrifluoromethyl-2,2´-bipyridine was used. Yield: 0.0792 g (79.2%) CHN analysis for $C_{36}H_{18}N_6B_2F_{26}Fe$: Calculated: C, 39.09%; H, 1.64%; N, 7.60%. Found: C, 39.13%; H, 1.68%; N, 8.46%.

2.1.14 Purification of solvents

DCM (environmental grade) was stored over KOH pellets for a minimum of two weeks before being distilled three times from P_2O_5. It was freshly distilled from P_2O_5 before use.

Acetonitrile (HPLC grade) was heated to reflux over aluminium chloride (15 g/l) for 1 hour and then distilled. The distillate was refluxed over alkaline potassium permanganate (10 g potassium permanganate and 10g lithium carbonate per litre) for 15 minutes followed by distillation. The distillate was refluxed over potassium bisulfate (15 g/l) for 1 hour followed by distillation. The distillate was then refluxed over calcium hydride (2 g/l) for 1 hour followed by a careful fractionation from a helice packed column at a high reflux ratio. The middle 80 % fraction was retained and distilled three times from phosphorus pentoxide (1 % w/v). The now purified and dried acetonitrile was freshly distilled from phosphorus pentoxide before use.

All other solvents were purchased *puriss* (>99.5 %) and used with no further purification.

2.1.15 Purchased Compounds

Samples of 2-CN-py, 3-CN-py and 4-CN-py were purchased from Aldrich in 98% purity. Samples of 3,3´-Dicyano-2,2´-bipyridine were purchased from Combi-Blocks Inc in 98% purity. Samples of 4,4´-Dicyano-2,2'-bipyridine were purchased from HetCat.

2.2 Electrochemical Techniques

Electrochemical data were captured on a DELL Pentium IV desktop PC with General Purpose Electrochemistry system (GPES) version 4.9 connected to a µAutolab TYPE III potentiostat.

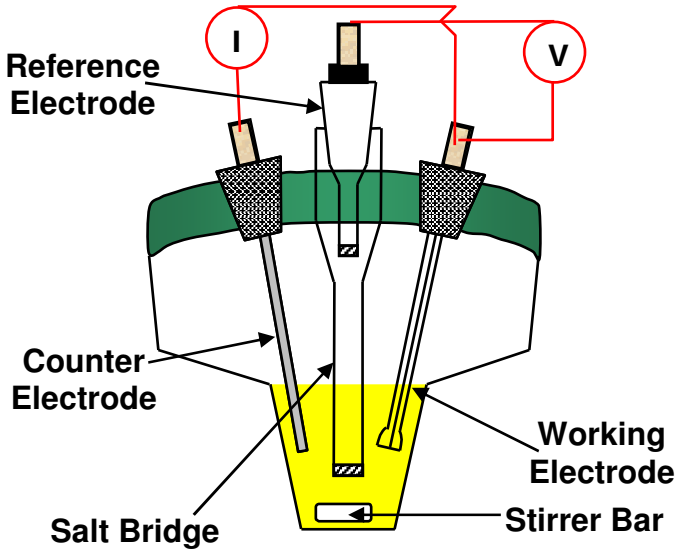

Figure 2.1 The three electrode electrochemistry cell

The electrochemical studies were conducted using a standard three electrode system depicted in Figure 2.1 above.

The electrode of primary interest is the working electrode (WE) as this is the site where the redox reaction takes place. Platinum was used for the WE in these studies.

It was decided to use Pt due to several favourable properties: Pt has good malleability, is ductile, is relatively inert and is stable over a wide potential and temperature range. The combination of these properties enables the reproducible manufacture of electrodes of various shapes and sizes that are resistant to chemical and thermal degradation, allowing for their repeated use in multiple studies. The flat disc shaped Pt electrode used in these studies had a diameter of 0.25mm.

The reference electrode (RE) for the system was Ag/AgCl in DCM/0.45 M $[TBA][BF_4]$ + 0.05 M [TBA][Cl]. The potential of the system is measured with respect to this electrode. Current is passed round the loop containing the working electrode and a counter electrode (CE), which is commonly a Pt rod. A minimal amount of current flows around the working electrode/reference electrode loop.

There are two main reasons for the use of a three electrode system. The potential applied across the working electrode/reference electrode system (V_T) can be broken down into two components; the potential across the WE/solvent interface (V_w) and the potential across the RE/solvent interface (V_r). However there is a further complication, as any solvent used will have an intrinsic resistance and thus from Ohm's law (equation 2.1) will cause a "potential drop" (V_R) to be experienced across the cell.

$$\mathbf{V_R = iR} \qquad \textbf{Equation 2.1}$$

Thus the total potential across the system is a combination of these three terms (equation 2.2).

$$V_T = V_w + V_r + V_R \qquad \text{Equation 2.2}$$

Due to the fact that no current flows between the WE and RE, V_R is equal to zero (since i = 0 in equation 2.1). The value of V_r remains constant for the system and therefore any potential change at the WE/solvent interface can be monitored.

All of the solutions studied were purged of O_2 gas by bubbling with N_2 prior to investigation. This was done to prevent masking of sample signals by the highly active O_2 electrochemical signal. In addition reduction of O_2 can yield H_2O_2 which may react with the species under investigation. [TBA][BF_4] was used as the inert electrolyte in order to increase the conductivity of the solution due to good charge mobility properties. This also ensured the reaction was purely diffusion controlled with respect to reactants and products. 0.3 M [TBA][BF_4] concentrations were used for all the solvents unless stated otherwise.

2.2.1 Cyclic Voltammatory

In this technique the potential is scanned linearly from an initial potential E_1 to a second potential E_2, at which point the direction of sweep is reversed and the potential is scanned back to E_1, Figure 2.2.

Shown in Figure 2.3 is the typical shape of the current *vs.* potential plot (voltammogram) for this technique. The signal can be broken down into four main regions. Initially when the potential is first applied, [Figure 2.3 region (a)], there is insufficient potential to cause an electron transfer reaction and therefore no current flows. When the applied potential reaches the redox potential for the system under investigation the reaction occurs and the current begins to increase exponentially

[region (b)]. The example shown here is of a reduction process, and thus by electrochemical convention the initial current is negative.

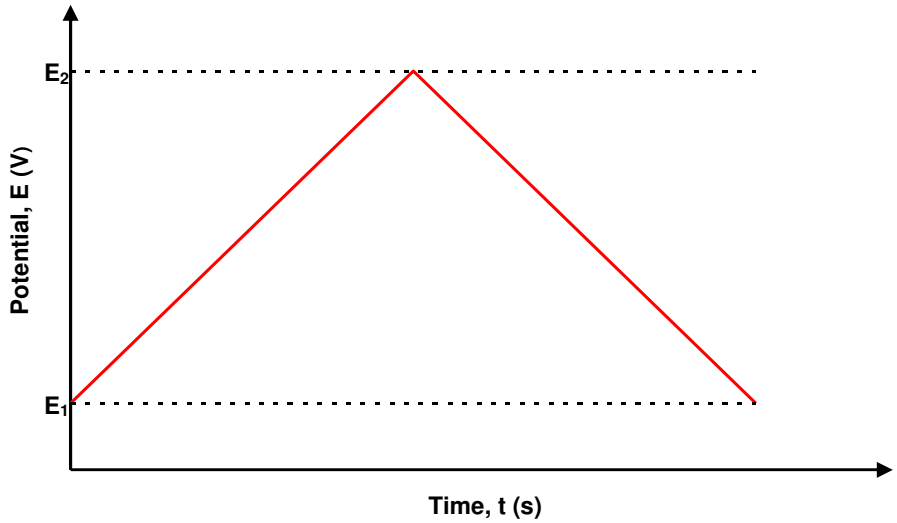

Figure 2.2 Variation in potential as a function of time in a cyclic voltammetry experiment

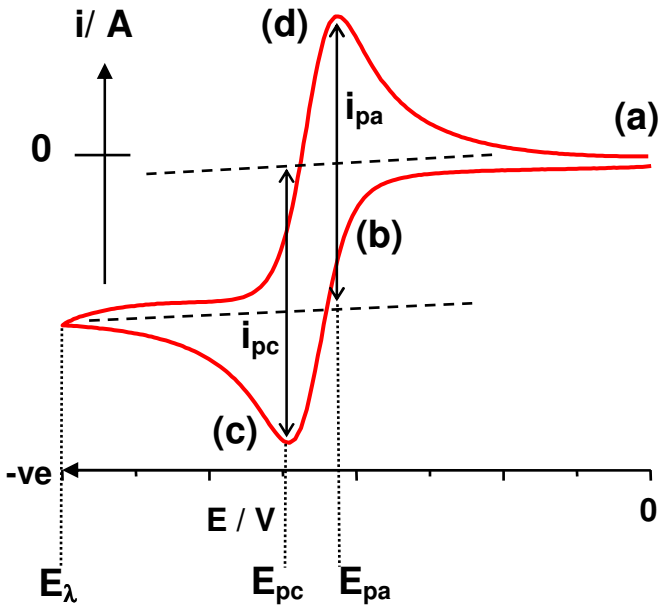

Figure 2.3 Typical cyclic voltammogram for a reversible redox process

As the potential is swept to increasingly negative values the rate at which the current increases starts to slow and ultimately a maximum is reached (i_{pc} at potential E_{pc}), known as the peak current. This maximum in current is caused by a balance between the increasing rate of reduction, k_{red}, and a decrease in the surface concentration of

reactant, $[O]_0$. After the peak current has been reached the current then begins to decrease [region (c)].

In this region the observed current is governed by the rate at which fresh reactant can diffuse from the bulk to the electrode surface. The decrease in current is due to the formation of an increasingly thick diffusion layer of reacted material for fresh reactant to pass through before reaching the electrode surface. Eventually a steady-state diffusion layer thickness, δ_d, evolves which is controlled by the extent of natural convection in the sample solution. At this point a diffusion limited current, i_L, is reached, the magnitude of which is given by equation 2.3.

$$\mathbf{i_L = \frac{D_O F A [O]_{bulk}}{\delta_d}} \qquad \textbf{Equation 2.3}$$

Where D_O is the diffusion coefficient of the diffusing species, F is the Farday constant (9.648×10^4 $Cmol^{-1}$), A is the area of the electrode surface and $[O]_{bulk}$ is the reactant concentration in the bulk solution.

As soon as the maximum potential (E_λ) is reached, the potential is immediately scanned back to the starting potential. If the reaction is reversible then the opposite electron transfer reaction will occur [region (d)]. The separation between the forward and reverse peaks for a reversible redox process is given by Equation 2.4.

$$\mathbf{\left|E_{pc} - E_{pa}\right| = 2.303 \frac{RT}{nF}} \qquad \textbf{Equation 2.4}$$

Where E_{pc} and E_{pa} are the cathodic and anodic peak potentials respectively, and *n* is the number of electrons being transferred during the reaction. For a redox process at room temp (298 K) the equation can be simplified to Equation 2.5. Thus for a $1e^-$ redox process the separation is approximately 59 mV. This value is independent of scan rate.

$$\left|E_{pc} - E_{pa}\right| = \frac{0.0592}{n} \qquad \textbf{Equation 2.5}$$

In addition, for a reversible electrochemical process the peak current (i_{pa}, i_{pc}) increases linearly as a function of the square root of the scan rate (ν). Therefore, the reversibility of a process can be established by ensuring that the plot of i_{pa} vs. $\sqrt{\nu}$ is linear. For a chemically reversible electron transfer reaction process the half-wave potential, $E_{½}$, for the redox couple is given by the equation 2.6.

$$E_{½} = \frac{E_{pa} + E_{pc}}{2} \qquad \textbf{Equation 2.6}$$

In the case where the electron transfer reaction is not chemically reversible (*i.e.* the newly reduced/oxidised compound is unstable and decomposes, or undergoes a subsequent reaction), then a reverse wave is not observed (Figure 2.4). However, by increasing the scan rate and/or decreasing the temperature it is possible in some cases, to complete a reverse scan before the oxidised/reduced species decomposes.

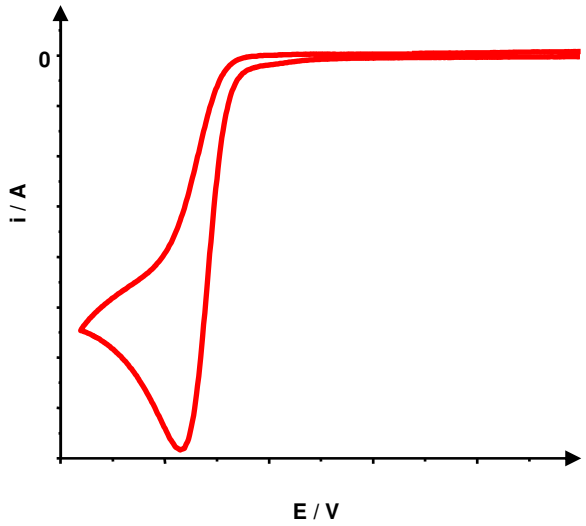

Figure 2.4 Typical cyclic voltammogram for an irreversible redox process

For a redox process that is electrochemically irreversible the peak separation will be larger than 59 mV, and this separation will increase with increasing scan rate.

The experimental values for this method can be calibrated by the addition to the sample system of a small amount of a reference material with a known $E_{½}$ value. The reference chosen for use in this study was ferrocene. This was due to ferrocene possessing several favourable properties; it is cheap, stable in a wide range of solvents and has a reversible $1e^-$ oxidation at +0.54 V *vs*. saturated Ag/AgCl in DMF.[4] A scan is conducted over a range that includes the ferrocene redox process and the experimental value, $E_{½,\,exp}$, is compared to the literature value, $E_{½,\,lit}$, to determine the correction factor for the apparatus (equation 2.7).

$$\mathbf{E_{½,exp} - E_{½,lit} = correction\ \ factor} \qquad \textbf{Equation 2.7}$$

2.2.2 Differential Pulse Voltammetry

Pulse voltammetry (PV), methods can be considered to be a derivative of linear sweep voltammetry (LSV) methods. In LSV the potential is applied as a continuously increasing/decreasing value with time. In contrast, in differential pulse voltammetry

(DPV), the potential is applied in a series of discreet pulses, with the base potential increasing after each pulse.

The typical shape of the variation in the applied potential with time during a DPV experiment is shown in Figure 2.5. The current is sampled twice for each pulse. The first measurement is taken just before the pulse starts at time τ´ and second at time τ late in the pulse.

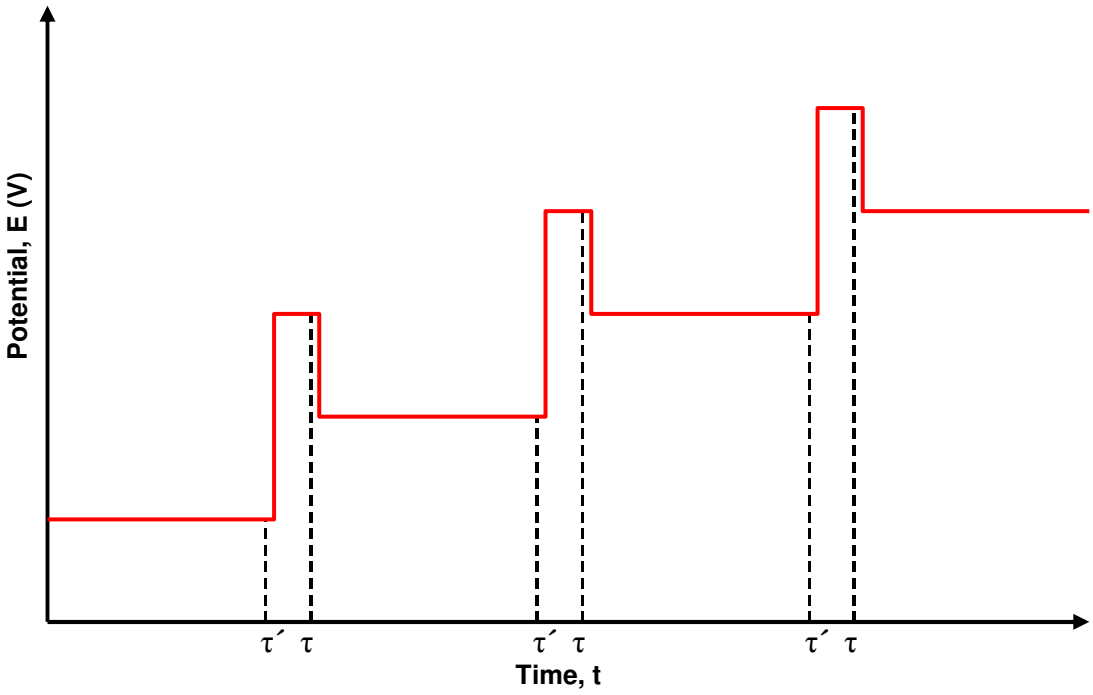

Figure 2.5 The waveform for differential pulse voltammetry

Figure 2.6 shows the structure of one pulse in more detail. The period before the first pulse and between subsequent pulses is known as the waiting time and is typically in the range of 0.5 and 4 s. The increase in potential upon application of the pulse is know as the potential step and ranges between 10 and 100 mV. The pulse duration is 5 to 100 ms, with a value of 50 ms being typical.

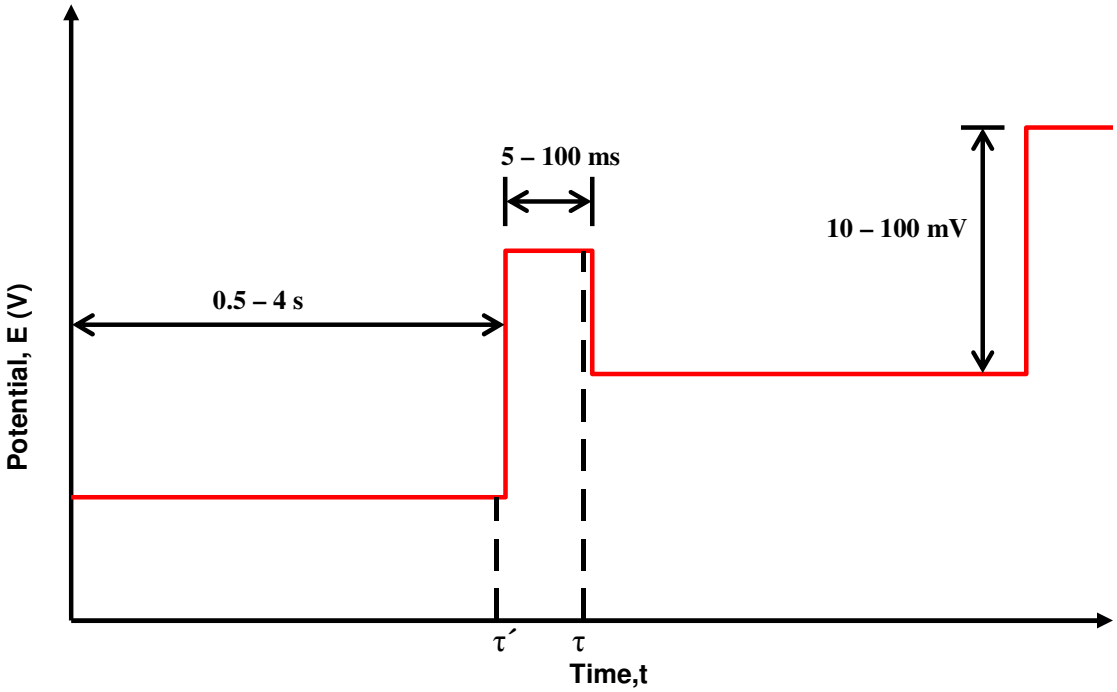

Figure 2.6 Detail of one differential pulse voltammetry pulse

The results are presented as a plot of the current difference, δ_i (Equation 2.8), versus the base potential (Figure 2.7). The use of a differential technique gives a peaked output in contrast to the wave-like response for other electrochemical techniques.

$$\delta_i = i(\tau') - i(\tau) \qquad \textbf{Equation 2.8}$$

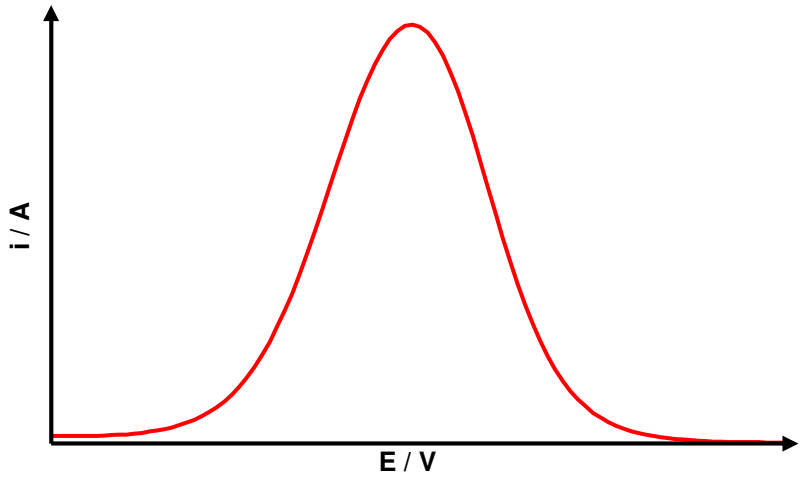

Figure 2.7 Typical shape of a differential Pulse Voltammogram

In the early part of the experiment the base potential is much less than that required to cause the redox process to occur. Hence no current flows before the pulse and the change in potential during the pulse is insufficient to cause an electron transfer, thus the δ_i is virtually zero. Late in the experiment when the base potential is far beyond the standard potential, E^e, for the redox couple, the species at the electrode surface reacts during the waiting period at the maximum rate. The increase in potential caused by the pulse cannot increase this rate further as the reaction is now governed by the diffusion of new material to the electrode surface and not electrode kinetics, leading to δ_i being small once again. Thus it is only in a region where a small potential difference can make a sizeable difference in current flow that the differential pulse technique shows a response.

At potentials close to the redox potential for the species under investigation an appreciable difference in current is observed. In this region the base potential causes the species at the electrode surface to react during the waiting period at a rate less than the maximum, since the reaction is not yet diffusion controlled. Application of the pulse serves to increase the rate of the reaction due to the increased over-potential being applied and thus an increase in the current is observed, leading to a significant δ_i.

The maximum potential, E_{max}, for a given peak in a differential pulse experiment is given by equation 2.9, where ΔE is the step potential. It can be seen that E_{max} precedes $E_{1/2}$ by $\Delta E/2$ for a reduction, and follows $E_{1/2}$ by $\Delta E/2$ for an oxidation. The average of E_{max} for the oxidation and reduction peaks will give $E_{1/2}$ for the redox couple.

$$\mathbf{E_{max} = E_{1/2} - \frac{\Delta E}{2}} \qquad \textbf{Equation 2.9}$$

The maximum current during the experiment, $(\delta_i)_{max}$, will occur at E_{max} and is given by equation 2.10. Where the term σ is defined by equation 2.11. A negative ΔE will result in a negative (cathodic) current, while a positive ΔE will result in a positive (anodic) current.

$$(\delta i)max = -\frac{nFAD_O^{1/2}[O]}{\pi^{1/2}(\tau - \tau')^{1/2}} \cdot \left(\frac{1-\sigma}{1+\sigma}\right) \qquad \textbf{Equation 2.10}$$

$$\sigma = \exp\left(\frac{nF}{RT} \cdot \frac{\Delta E}{2}\right) \qquad \textbf{Equation 2.11}$$

If a redox couple shows electrochemically irreversible behaviour due to slow kinetics a differential response will still be observable, but the peak will be shifted from the redox potential to more extreme potentials by an activation overpotential. The peak width will also be broader than for a reversible system.

The time scales in differential pulse experiments are much shorter than in cyclic voltammetry. As a consequence, the degree of reversibility of reactions in pulse methods may differ from that observed in linear sweep methods. A process that is found to be chemically irreversible in CV may appear as quasi-reversible or even fully reversible in DPV due the timescale of measurement being short compared to the kinetics of the chemical decomposition process.

2.3 Spectroelectrochemical Techniques

Electrochemical techniques can be used to gain information about the potential at which a redox process will occur and the reversibility of the electron transfer process involved but it is not possible to identify the nature of the redox species produced from electrochemical methods alone. By combining electrochemistry with various

spectroscopic techniques the electronic structure of the redox species generated can be probed.

Electrochemical methods have a significant advantage over chemical methods for the generation of redox species. The use of chemical reducing or oxidising agents can lead to the production of redox products in a range of unknown oxidation states. In contrast the careful selection of the generation potential used in electrochemical methods can enable the isolation of compounds in specific oxidation states.

Ex-situ generation of redox species for spectroscopic analysis can be conducted in a standard electrochemical cell. The relative ease of generation is offset by the need to transfer the redox product to the spectrometer. During the transfer process the redox species can decompose as it passes through the air. Therefore a more efficient method is to generate the compound in a spectroelectrochemical cell placed inside the spectrometer. In addition the apparatus is kept at low temperature to increase the stability of the generated redox species.

One of the most commonly used spectroelectrochemical techniques is the combination of *in-situ* electrogeneration with Ultra Violet/Visible/Near Infra-Red (UV/Vis/NIR) spectroscopy. This method has a relatively simple experimental set up and gives a great deal of information about the electronic transitions in the species under investigation.

A relatively under used spectroelectrochemical technique that has been used extensively in this work is Electron Paramagnetic Resonance (EPR) spectroscopy.

EPR spectroscopy is a very sensitive technique that is well suited to the investigation of the radical compounds that are common products of electrogeneration. These techniques will be discussed in greater detail in following sections.

2.3.1 Ultra Violet/Visible/Near Infra-Red spectroelectrochemistry

UV/Vis/NIR spectroscopy involves the promotion of electrons from the ground state energy level (GS) of a molecule to an excited state energy level (ES), where the energy of the electronic transition between the GS and ES correspond to frequencies ranging from the Ultra Violet to the Near Infra-Red region of the electromagnetic spectrum.

There are two important parameters to be obtained from the electronic spectra collected. Firstly the position of the absorption peaks, and secondly the intensity of the band. From the intensity and concentration of the sample it is possible to calculate the extinction coefficient, ε, for each peak using the Beer-Lambert law (Equation 2.12).

$$\mathbf{A = \log_{10}(I_0 / I) = \varepsilon c l} \qquad \textbf{Equation 2.12}$$

Were A is the absorbance, I_0 is the intensity of the incident light at a given wavelength, I is the transmitted intensity, c is the molar concentration and l is the path length in centimetres. The magnitude of the extinction coefficient for a given peak can be used to determine the nature of the electronic transition that the absorption signal corresponds to. Some typical extinction coefficient ranges for different types of electronic transitions are given in Table 2.1.

Electronic Transition	ε_{max} (mol^{-1} cm^{-1})
Spin forbidden d-d	< 1
Laporte forbidden d-d	20 - 100
Laporte allowed d-d	200 - 250
Charge Transfer	1000 - 50000
π-π*	10000 - 25000

Table 2.1 Typical extinction coefficient values for some electronic transitions[5,6]

An optically transparent thin layer electrode (OTTLE) cell was used to collect the UV/Vis/NIR spectra of the compound studied. The basic design of this cell is given in figure 2.8. The OTTLE cell comprises a quartz cell with a path length of 0.5 mm with a quartz extension fitted to the cell which acts as a reservoir for the sample solution. A scaled down three electrode system is fitted into the cell to enable *in-situ* electrogenereation. The WE comprises a Pt gauze with the wire that extends into the reservoir covered by a Teflon sleeve to minimise undesired bulk electrolysis in the reservoir rather than in the flat part of the cell. A Pt wire is used as a CE and the RE is a Ag/AgCl electrode. The CE and RE are separated from the reaction solution by sintered frits.

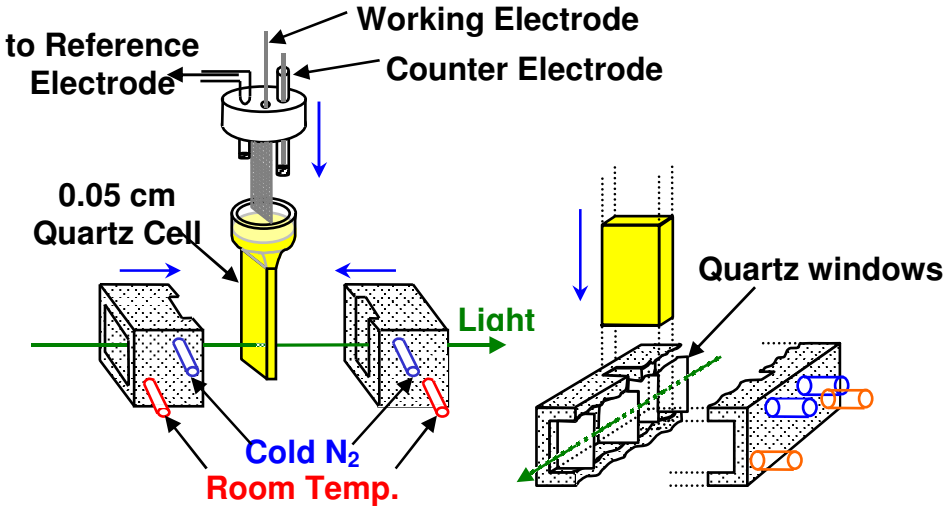

Figure 2.8 Experimental set-up for *in-situ* UV/Vis/NIR spectoelectrochemistry

The OTTLE cell is placed in a PTFE block containing two pairs of quartz windows. Cooled N_2 gas is passed between the OTTLE cell and the inner set of quartz windows to cool the sample. Room temperature dry nitrogen is passed between the inner and outer set of quartz windows to prevent the cell and windows from frosting up, giving erroneous absorbance signals. The temperature of the sample is monitored using a thermocouple connected to a digital thermometer, and the temperature is regulated by adjusting the flow of cooled nitrogen into the system.

An initial scan is conducted to determine the absorbance character of the initial species. A fixed potential is then applied to the system to generate the reduced/oxidised species desired. The UV/Vis/NIR spectrum of the system is taken every ten minutes and the changes in the signal are monitored. The reaction is continued until the spectrum stops changing and the current flow ceases. Once this point has been reached the potential is reversed to regenerate the original species and check that the reaction is fully reversible.

The spectra were collected on a Perkin-Elmer Lambda 9 spectrophotometer that was connected to a Datalink Pentium desktop PC running UV Winlab software, version 2.70.01.

2.3.2 Electron Paramagnetic Resonance Spectroscopy

Electron paramagnetic resonance (EPR) spectroscopy can be considered to be analogous to the more familiar nuclear magnetic resonance (NMR) technique. Both techniques deal with the interaction of electromagnetic radiation with magnetic

moments. In EPR the magnetic moment arises from the spin of one or more unpaired electrons, rather than the spin of nuclei as in NMR spectroscopy.

An electron has a spin quantum number of S = ½ and a magnetic moment, with spin angular momentum components of m_s = +½ and m_s = -½. In the absence of an external magnetic field these two energy confirmations are degenerate. When a magnetic field is applied to a system containing an unpaired electron the magnetic moment will align either parallel or anti-parallel to the applied field and the degeneracy will be removed, figure 2.9. The energy of a given alignment is described by equation 2.13, where μ_B is the Bohr magneton (9.274×10^{-24} JT^{-1}), B is the magnetic field (T) and g_e is the Zeeman factor for a free electron (2.0023).The energy difference between the two states ΔE, is given by the equations 2.14.

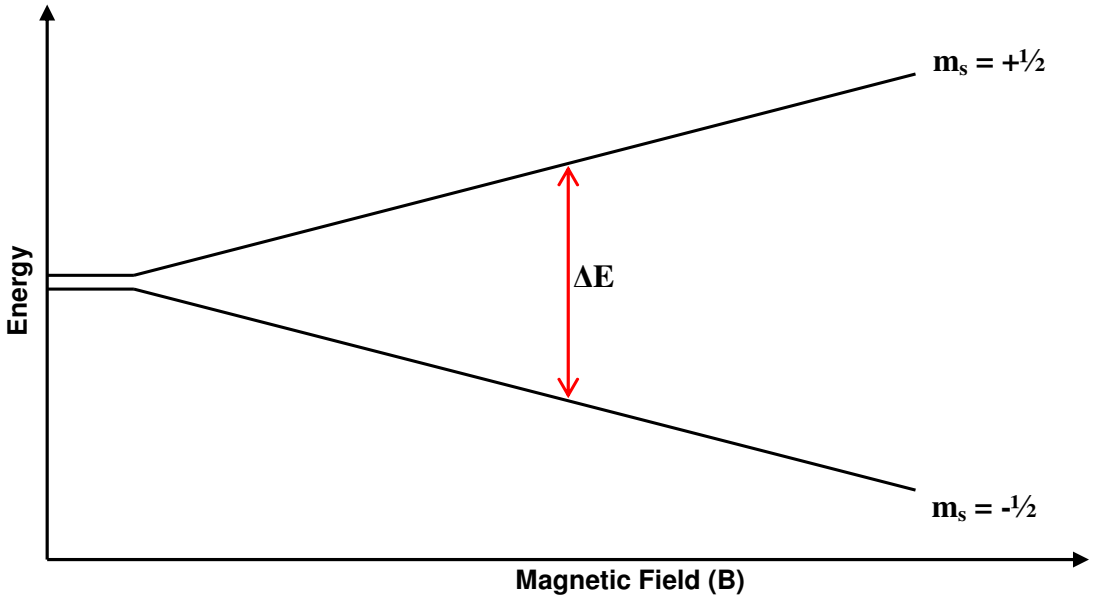

Figure 2.9 Energy levels of a free electron in the presence of external magnetic field

$$E = g_e \mu_B B m_S \qquad \textbf{Equation 2.13}$$

$$\Delta E = E_{upper} - E_{lower} \qquad \textbf{Equation 2.14 a}$$

$$\Delta E = g_e \mu_B B \qquad \textbf{Equation 2.14 b}$$

A transition from the lower energy state to the upper energy state can be induced by the absorption of electromagnetic radiation of frequency ν such that the photon energy, hν, matches the energy difference between the two levels, ΔE, equations 2.15, where ν corresponds to radiation in the microwave region of the electromagnetic spectrum for EPR spectroscopy.

$$\Delta E = h\nu \qquad \textbf{Equation 2.15 a}$$

$$h\nu = g_e \mu_B B \qquad \textbf{Equation 2.15 b}$$

Thus an EPR experiment can be conducted by holding a fixed magnetic field and scanning the frequency of radiation applied to the system. However it is technically difficult to obtain a microwave source that will scan over a wide range. It is therefore more common for a single frequency of applied radiation to be chosen and the magnetic field to be scanned.

The EPR resonance signal is detected by a field modulation technique. An oscillating magnetic field is applied to the sample *via* coils placed either side of the cavity. This oscillating magnetic field is at a fixed frequency and is applied throughout the experiment. Due to this mode of operation EPR spectra are recorded as first derivatives of the more usual absorption peak; these two waveforms are shown in figure 2.10.

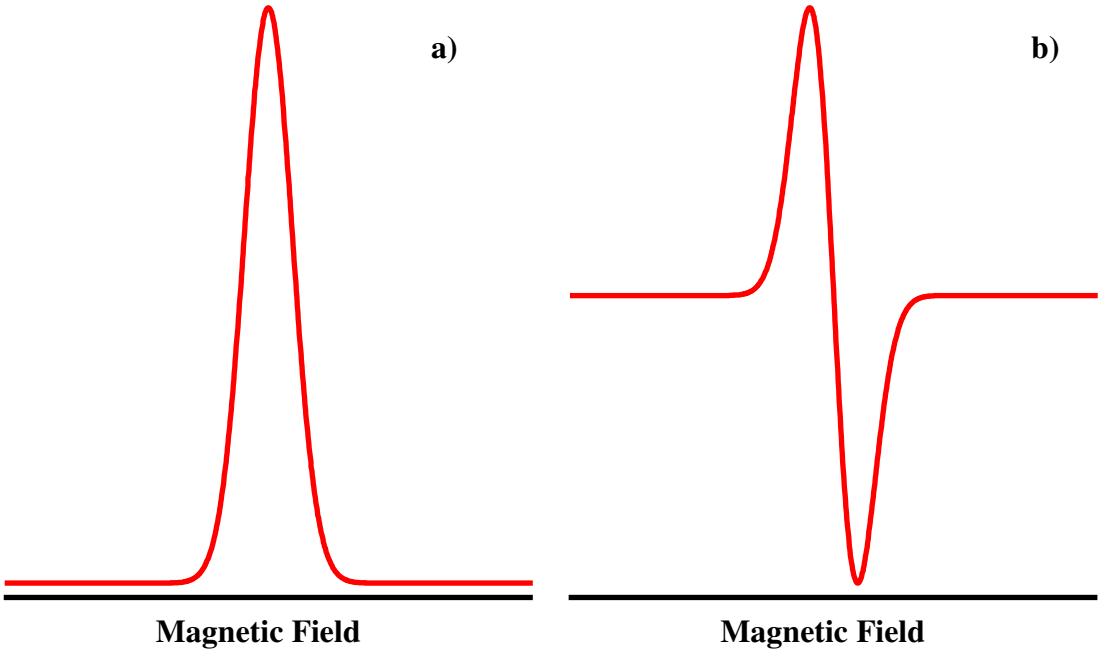

Figure 2.10 Typical shapes of an absorption peak (a) and its first derivative (b)

The magnetic field experienced by an unpaired electron in an atom or molecule may be modified by local magnetic field effects, B_{local}, that add vectorially to the external magnetic field to produce the total effective field, B_{eff}, equation 2.16.

$$\mathbf{B_{eff} = B + B_{local}} \qquad \textbf{Equation 2.16}$$

In practice it is more convenient to retain the external magnetic field and replace g_e with an effective experimental g-factor, g_{exp}, that deviates from g_e according to the strength of B_{local}. Thus the degree of variation of g_{exp} from the g_e value is an indication of the local environment on the unpaired electron. Many organic radicals have $g_{exp} \approx g_e$, inorganic radicals have g_{exp} in the range 1.9 to 2.1 and paramagnetic d-metal complexes have g_{exp} in a much wider range, 0 to 4.[7] The experimental g-factor can be determined using equation 2.17, where m_e is the electron rest mass and e is elementary charge of the electron.

$$\mathbf{g_{exp} = \frac{4\pi m_e}{e} \cdot \frac{\nu}{B}} \qquad \textbf{Equation 2.17}$$

In practice it is possible to gain more information about the environment of the unpaired electron from hyperfine coupling effects. Just as in NMR spectroscopy it is possible for one nuclear spin to interact with another nuclear spin, so it is also possible for the spin of the electron to interact with the spin of neighbouring nuclei.

The simplest system exhibiting nuclear hyperfine interaction is the hydrogen atom. Since the proton has a spin of I = ½, m_I has two possible values $m_I = \pm ½$. The electron will experience one of two possible local field contributions by the magnetic moment of the proton. The nuclear hyperfine interaction splits each of the electron Zeeman levels into two levels. The resulting four energy levels are shown in figure 2.11 and the energy of each state is given by equations 2.18, where g_n is the nuclear Zeeman factor, μ_n is the nuclear magneton (5.051×10^{-27} JT^{-1}) and A is the hyperfine coupling constant.

$$E_{m_S=+½,m_I=+½} = +\frac{1}{2}g_e\mu_B B - \frac{1}{2}g_n\mu_n B + \frac{1}{4}A \qquad \textbf{Equation 2.18 a}$$

$$E_{m_S=+½,m_I=-½} = +\frac{1}{2}g_e\mu_B B + \frac{1}{2}g_n\mu_n B - \frac{1}{4}A \qquad \textbf{Equation 2.18 b}$$

$$E_{m_S=-½,m_I=+½} = -\frac{1}{2}g_e\mu_B B - \frac{1}{2}g_n\mu_n B - \frac{1}{4}A \qquad \textbf{Equation 2.18 c}$$

$$E_{m_S=-½,m_I=-½} = -\frac{1}{2}g_e\mu_B B + \frac{1}{2}g_n\mu_n B + \frac{1}{4}A \qquad \textbf{Equation 2.18 d}$$

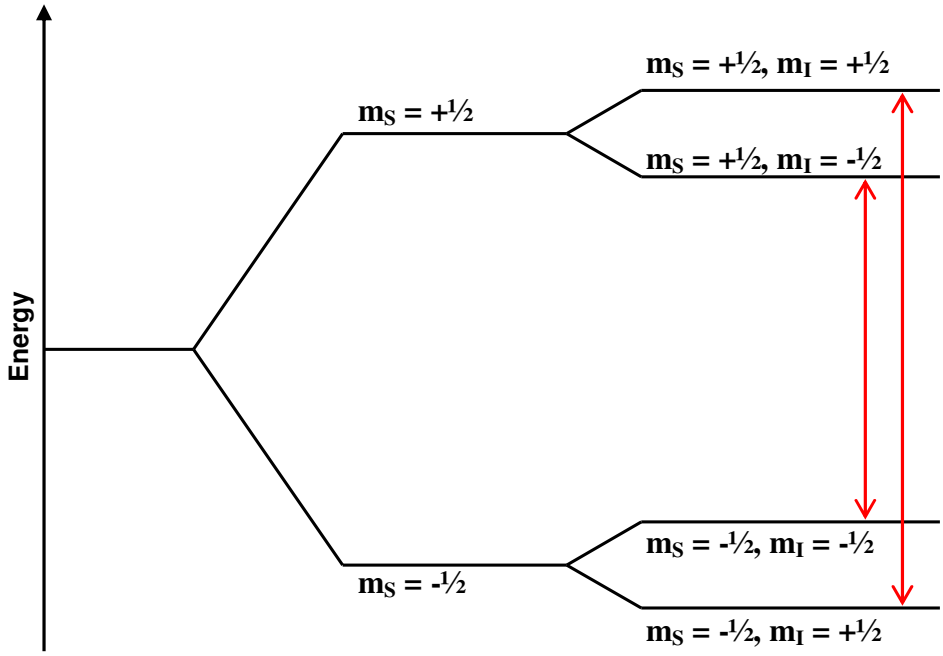

Figure 2.11 Energy level diagram for coupling of an unpaired electron to one nucleus with I = ½

An allowed transition will cause a change in the angular momentum of the electron but no change in angular momentum of the nucleus, in accordance with the selection rules $\Delta M_S = \pm 1$ and $\Delta M_I = 0$. It can be seen for the system described above that there will be two allowed transitions, indicated by the red arrows in figure 2.11. The energy separations are now given by equation 2.19.

$$\Delta E = g_e \mu_B B + m_I A \qquad \textbf{Equation 2.19}$$

For a system of I = ½ nuclei the intensity distribution of the lines follow a binomial distribution just as coupling patterns do in NMR spectroscopy. The EPR spectrum for an unpaired electron coupling to a ^{1}H nucleus is shown below in figure 2.12.

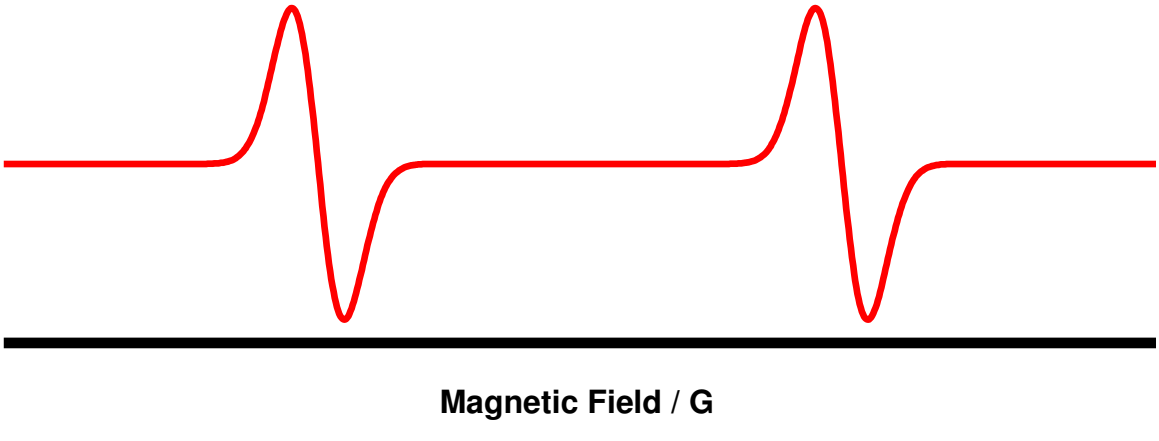

Figure 2.12 Typical EPR spectrum for coupling of an unpaired electron to one ^{1}H nucleus

Coupling can also occur to quadrupolar nuclei, i.e. nuclei with a spin greater than I = ½. For example the EPR spectrum for the coupling of an unpaired electron to a ^{14}N nucleus is shown in figure 2.13. The spectrum exhibits three peaks in a 1:1:1 ratio arising from coupling to the I = 1 ^{14}N nucleus. In general if the electron is surrounded by n equivalent spin active nuclei each with a spin quantum number of I, then a signal comprising of 2nI+1 lines will be observed.

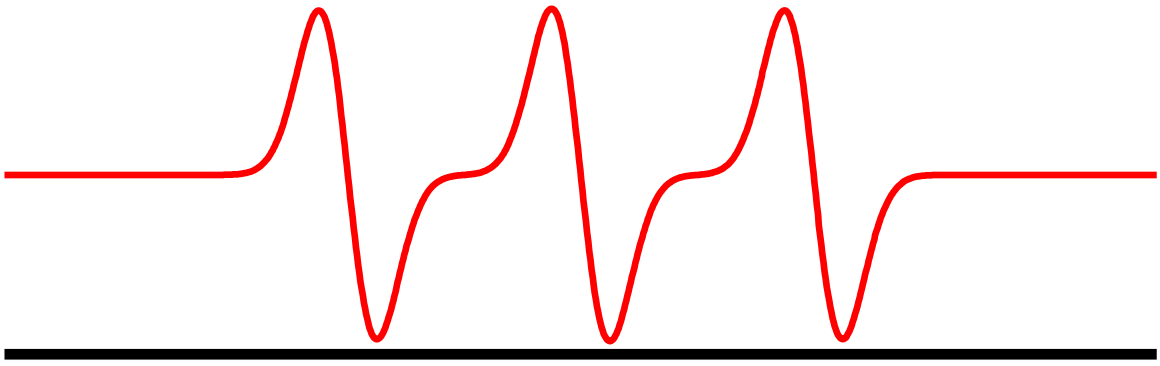

Figure 2.13 Typical EPR spectrum for coupling of an unpaired electron to one ^{14}N nucleus

As previously discussed above the key requirement for the EPR technique is that the species under investigation must contain an unpaired electron. However the majority of compounds are diamagnetic and therefore do not possess the required unpaired electron and thus will not give an EPR spectrum. A solution to this problem is to generate a paramagnetic redox product of the species under investigation using chemical or electrochemical methods. As discussed in section 2.3 there are several problems related with chemical and *ex-situ* generation. Variable temperature *in-situ* EPR by comparison is ideally suited to the study of unstable radicals.

One difficulty experienced with EPR is that solvents absorb the applied microwaves. To minimise this unwanted absorption a solvent with a lower dielectric constant

should be used. This is not always practical so the undesired absorption can be reduced by placing the sample in a flat EPR cell. The flat cell is aligned so as to maximise the magnetic field component while minimising the electric field component.

Line broadening effects are another factor that must be taken into consideration when choosing a suitable solvent for an EPR experiment. In more viscous solvents the molecules tumble more slowly. This leads to line broadening in the EPR signal. The viscosity of a solvent is dependent upon its melting point. It is therefore an important property to consider when EPR active species are generated at low temperature. For example, if an EPR active species is generated in DMF (mp = 212 K) at 233 K, a temperature where the viscosity of DMF is increased, then it is possible for much of the fine structure to be obscured by line broadening effects. Dichloromethane (DCM) is ideally suited as it has a significantly lower melting point and dielectric constant compared to DMF. However solubility problems may arise with many compounds in this solvent.

A specifically designed variable temperature *in-situ* EPR cell was used in these studies and is shown in figure 2.14.[8] The cell consists of a high grade quartz flat cell onto which two quartz side arms have been attached. The WE consists of a Pt gauze with a Pt wire welded to it. The gauze is placed in the flat section of the cell with the wire running the length of the cell to allow for connection to the potentiostat. The WE wire is sheathed in a Teflon sleeve to prevent bulk electrolysis of material out-with the flat part of the cell. A second piece of Pt wire is used as the counter electrode and

a Ag/AgCl reference electrode is placed in the reservoir at the top of the cell. The cell is then placed in a specifically designed quartz holder in the EPR cavity.

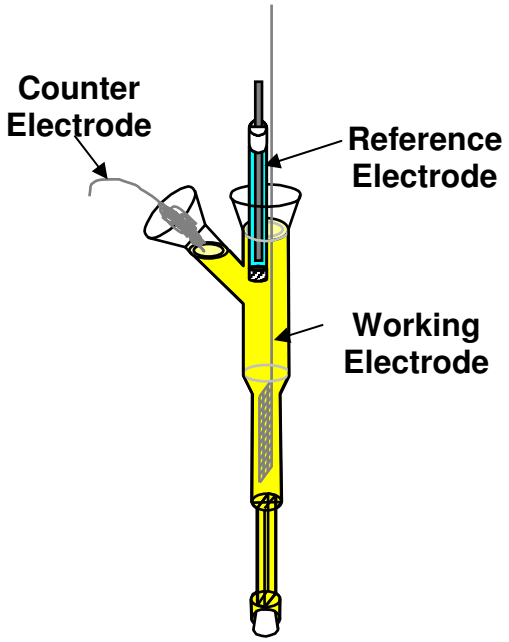

Figure 2.14 *In-situ* EPR spectroelectrochemistry cell

The EPR apparatus is cooled to the desired temperature using a sealed dewar containing liquid nitrogen and a heating unit that is connected to the quartz cell holder by a transfer dewar. Increasing the heater power causes nitrogen to evaporate and pass from the dewar to the cell holder cooling the sample. The temperature is monitored via a thermocouple that is inserted into the bottom of the cell holder into near proximity of the EPR cell. To prevent the EPR cell from frosting up room temperature nitrogen is blown into the cavity and around the EPR cell.

In-situ EPR spectrocelectrochemical experiments were only carried out once the reversibility of the system had been verified using UV/Vis/NIR spectroelctrochemsitry. X-band (ν = 9.5 GHz) EPR data were recorded on an X-band Bruker ER 200-D SRC spectrometer connected to a datalink 486DX desktop PC running EPR acquisition System version 2.42. Electro-generation was performed

using a Potentiostat BASCV-27 Voltammograph. Variable temperature work was carried out using the Bruker ER4111 VT Unit. All experimental g-values were calibrated against the reference g-value of 2,2´-diphenyl-1-picrylhydrazyl (DPPH) which is 2.0036 ± 0.0002.

Simulations were performed using a combination of the WIN EPR Simfonium program and the EasySpin[9] toolbox for MATLAB.

2.4 Computational Methods

The continued development of increasingly powerful computers and the wider availability of the relevant software and hardware have led to computational chemistry methods rapidly becoming standard techniques to aid the research of experimental chemists. Computational modelling of a molecular system under experimental investigation can aid in the understanding of observed chemical properties. In addition calculations can be used to estimate the properties of molecular systems that cannot be studied using current experimental techniques.

2.4.1. Fundamental Theory

Computational chemistry methods aim to solve the time-independent Schrödinger equation to obtain information about the structure and properties of the molecules being studied. However the most complex system for which the Schrödinger equation can be solved exactly is the hydrogen atom. To be able to solve the equation for larger systems it is necessary to make approximations.

The first attempt that is made to simplify the many-body problem is the Born-Oppenheimer approximation. This approximation makes use of the fact that the electrons in a system are much lighter than the nuclei and therefore move much faster. Due to this the electrons can respond almost instantaneously to any change in the locations of the nuclei. Thus the distribution of electrons about the molecule depends only on the positions of the nuclei and not their motions. The Schrödinger equation can then be solved for the electrons in a static electric potential arising from the nuclei in a given arrangement. This approximation holds well for most systems, however for systems where the nuclear and electronic motions are not easily separable the approximation does not hold, for example, in the case of large amplitude molecular vibrations or the motion of light nuclei.

Taking into account the Born-Oppenheimer approximation, the time-independent, electronic Schrödinger equation for a fixed set of nuclear positions is given by equation 2.20.

$$\mathbf{H\Psi(r:R) = E(R)\Psi(r:R)} \qquad \textbf{Equation 2.20}$$

Where E(R) is the electronic energy and $\Psi(r{:}R)$ is the electronic wavefunction, where r denotes the electronic positions and R the dependence of the wavefunction on the nuclear coordinates. The Hamiltonian operator is then given by equation 2.21

$$\mathbf{H} = \frac{-\hbar^2}{\mathbf{2m_e}}\sum_{\mathbf{i}}^{\mathbf{n}}\nabla_{\mathbf{i}}^2 - \sum_{\mathbf{i}}^{\mathbf{n}}\sum_{\mathbf{I}}^{\mathbf{N}}\frac{\mathbf{Z_I e^2}}{\mathbf{4\pi\varepsilon_0 r_{Ii}}} + \frac{\mathbf{1}}{\mathbf{2}}\sum_{\mathbf{ij}}^{\mathbf{n}}\frac{\mathbf{e^2}}{\mathbf{4\pi\varepsilon_0 r_{ij}}} \qquad \textbf{Equation 2.21}$$

The first term in the Hamiltonian describes the kinetic energy of the system of electrons, the second describes the nuclear-electron potential and the third term

contains the electron-electron interactions. By convention the nuclear-nuclear repulsion energy is added as a classical term at the end of the calculation.

The greatest problem in solving the electronic Schrödinger equation arises from the third term. The presence of electron-electron interactions prevents $\Psi(r{:}R)$ from being represented as a simple linear combination of one-electron functions. The coupling of electron motions arises due to two related effects, exchange and correlation.

The exchange effect derives from the Pauli principle, which states that the total wavefunction of a system must be anti-symmetric with respect to the exchange of any two identical fermions (such as a pair of electrons). This requirement results in electrons of the same spin being forbidden from occupying the same region of space.

The correlation effect is the combination of Fermi and Coulomb correlation. Fermi correlation also arises from the Pauli principle. The condition that electrons with parallel spin must avoid each other leads to a quasi-repulsive force that couples their motions and acts to keep them apart. The Coulomb correlation describes the Coulombic repulsion effect experienced by an electron moving in a cloud comprised of all the other electrons in the system.

The exchange and correlation effects result in electrons being spatially separated, to determine the exact energy of a system these effects must be accounted for. The exchange term can be included in computational techniques relatively simply by ensuring that the wavefunctions employed are suitably anti-symmetrised. A useful way of accomplishing this is to write the multi-electron wavefunction in the form of a

Slater determinant of the spinorbitals, ϕ, for electrons. A spinorbital is a product of the spatial and spin functions for an electron.

In contrast the correlation effect is harder to account for and its correct inclusion in computational chemistry methods is an on-going problem. Some of the main methods of dealing with this problem are discussed below.

2.4.2. Hartree-Fock

In the Hartree-Fock method each electron is considered to be moving in a field comprised of the electrostatic field of the nuclei and an average field of the other n-1 electrons. Thus electron correlation effects are completely neglected by this method. This enables the multi-electron wavefunction to be separated into a sum of the spinorbitals. The Hartree-Fock equation for a spinorbital $\phi_a(i)$ is given by equation 2.22.

$$\hat{\mathbf{f}}_i \boldsymbol{\phi}_a(\mathbf{i}) = \boldsymbol{\varepsilon}_a \boldsymbol{\phi}_a(\mathbf{i}) \qquad \textbf{Equation 2.22}$$

Where ε_a is the spinorbital energy and $\hat{f}_i$ is the Fock operator given by equation 2.23.

$$\hat{\mathbf{f}}_i = \hat{\mathbf{h}}_i + \sum_{\mathbf{u}} \{\mathbf{J}_\mathbf{u}(\mathbf{i}) - \mathbf{K}_\mathbf{u}(\mathbf{i})\} \qquad \textbf{Equation 2.23}$$

$\hat{h}_i$ is the core Hamiltonian for electron *i* moving in the field of a bare nucleus. The summation is over all the other spinorbitals, *u*. $\hat{J}_u$ is the Coulomb operator, which takes into account the Coulombic repulsion between electrons. $\hat{K}_u$ is the exchange

operator, which accounts for the electron spin effects. $\hat{J}_u$ and $\hat{K}_u$ are be defined by equations 2.24 and 2.25 respectively.

$$\hat{J}_u(1)\phi_a(1) = \left\{\int \phi_u^*(2)\left(\frac{e^2}{4\pi\varepsilon_0 r_{12}}\right)\phi_u(2)\,dx_2\right\}\phi_a(1) \qquad \textbf{Equation 2.24}$$

$$\hat{K}_u(1)\phi_a(1) = \left\{\int \phi_u^*(2)\left(\frac{e^2}{4\pi\varepsilon_0 r_{12}}\right)\phi_a(2)\,dx_2\right\}\phi_u(1) \qquad \textbf{Equation 2.25}$$

2.4.3. Density Functional Theory

An alternative to Hartree-Fock based methods is the use of density functional theory (DFT). At the core of this method is the concept that the total electronic energy of a system of electrons can be written in terms of the electron probability density, ρ. For a system of n electrons the total electron density of a given point in space, r, is denoted by $\rho(r)$. The total electronic energy of a system, E, can be written as a function of the electron density, $E[\rho]$. Knowledge of the electron density of a system enables determination of the ground-state energy and also gives information about all the other ground state electronic properties. The exact ground state electronic energy, E, for a system of n electrons is given by equation 2.26.

$$E[\rho] = -\frac{\hbar^2}{2m_e}\sum_{i=1}^{n}\int \psi_i^*(r_1)\nabla_1^2\psi_i(r_1)dr_1 - \sum_{I=1}^{M}\int \frac{Z_I e^2}{4\pi\varepsilon_0 r_{I1}}\rho(r_1)dr_1 + \frac{1}{2}\int \frac{\rho(r_1)\rho(r_2)e^2}{4\pi\varepsilon_0 r_{12}}dr_1 dr_2 + E_{XC}[\rho]$$

Equation 2.26

Where ψ_i are the Khon-Sham (KS) orbitals. The first term in equation 2.26 describes the kinetic energy of the n electrons, the second term the electron-nuclear interactions,

the third term represents the electron-electron Coulomb interaction, and the last term is the exchange-correlation energy. The exact form of the exchange-correlation energy is still unknown. However given that the total energy of a system is a functional of the electron density the exchange-correlation energy must also be a functional of the electron density of the system.

The exact ground state, ρ, at a point r is given by equation 2.27. Where the summation is over all the occupied Kohn-Sham (KS) orbitals.

$$\rho(\mathbf{r}) = \sum_{i=1}^{n} |\psi_i(\mathbf{r})|^2 \qquad \textbf{Equation 2.27}$$

In DFT methods, calculation of the energy is dependent on the electron density rather than the wavefunction, as in the other *ab initio* methods discussed. This difference results in DFT methods being less reliant on the size of basis set used compared to HF based methods. For DFT calculations the main source of errors arises from the choice of functional used to model the exchange-correlation term.

A wide range of functionals to model the exchange-correlation dependence have been developed. The simplest of these is based of the Local Density Approximation (LDA). The LDA uses a homogeneous electron gas as a model. This system has been extensively studied and its exchange-correlation energy is known. This approximation has proved remarkably successful for periodic systems but less so for extended molecular systems. The LDA model has been improved by adding non-local, or gradient, corrections to the exchange-correlation energy to account for the inhomogeneity of true molecular electron density. These corrections are known as

generalised gradient approximations (GGA) and have been developed by Perdew[10] and Becke[11], amongst others.

In addition to LDA and GGA functionals a class of approximations known as hybrid functionals have been developed. These hybrid functionals incorporate a portion of the exact exchange from Hartree-Fock theory into the exchange-correlation functional. One of the most successful hybrid functionals is the B3LYP functional[12] which contains the Becke three-parameter (B3) exact exchange functional,[11] and the Lee-Yang-Parr (LYP) functional[13] to account for the correlation. The expanded form of this functional is shown in equation 2.28. Where $a_0 = 0.20$, $a_x = 0.72$ and $a_c = 0.81$ are three empirical parameters determined by fitting the predicted values to a set of atomisation energies, ionisation potentials, proton affinities and atomic energies.[11] E_x^{GGA} is the Becke 88 exchange functional[14], E_c^{GGA} is the Lee-Yang-Parr correlation functional[13] and E_c^{LDA} is the Voska-Wilk-Nusair (VWN) local-density approximation to the correlation functional.[15] This functional has been shown to perform well for molecular systems, and is used in the DFT calculations performed in this thesis.

$$\mathbf{E_{xc}^{B3LYP} = E_{xc}^{LDA} + a_0\left(E_x^{HF} - E_x^{LDA}\right) + a_x\left(E_x^{GGA} - E_x^{LDA}\right) + a_c\left(E_c^{GGA} - E_c^{LDA}\right)}$$

Equation 2.28

2.4.4. Self-Consistent Field method

To solve the HF equation (equation 2.22) for a given spinorbital requires the Fock operator to be known. However the Fock operator depends on the spinorbitals of all the other n-1 electrons in the system. Therefore to solve the HF equation the answer must already be known. A similar problem is experienced in DFT. The KS orbitals

required to solve the KS equations are dependent on the electron density, but the electron density itself is calculated from the KS orbitals (equation 2.27).

This problem is tackled by using an iterative process to obtain the solution and stopping when the answer converges to within a preset tolerance. This iterative approach is known as the self-consistent field (SCF) method.

For the HF method an initial guess at the approximate form of the spinorbitals is made. This initial guess is then used to construct the Fock operator. The HF equations are solved using this Fock operator and a new set of spinorbitals is obtained. These new spinorbitals can be used to form a new Fock operator and so the process continues until the termination conditions are achieved.

For the DFT method an initial guess is made for the electron density. This is frequently a superposition of the atomic densities of the atoms comprising the molecular system under investigation. The initial density is used to calculate a set of KS orbitals that can then be used to compute an improved density.

Calculating the spinorbitals or electron density at each stage in the calculation would incur a significant computational cost. The process is simplified by approximating the spinorbitals or KS orbitals to a linear combination of known basis functions, θ_j, equation 2.29.

$$\psi_i = \sum_j^M c_{ij}\theta_j \qquad \textbf{Equation 2.29}$$

Where c_{ij} are a set of unknown coefficients. The complex problem of calculating the spinorbitals or KS orbitals has now become one of finding the coefficients that best describe the orbitals. The accuracy of the calculation is thus dependent on the basis set of basis functions chosen to describe the orbitals.

2.4.5. Choice of Basis Set

The choice of basis set can have a large effect on the accuracy of a calculation. Therefore the selection of an appropriate basis set must be done carefully. To model the molecular orbital of a system as accurately as possible it is desirable to choose the largest possible basis set incorporating the largest number of basis functionals. However this must be offset against the increased computational cost incurred in using increasingly large basis sets. In practice careful consideration of the number of basis functionals required to model the unknown function and reference to literature material on similar systems can inform the choice of basis set and minimise computational costs.

There are two main types of functions used as basis functions in computational chemistry. These are Slater type orbitals, STOs and Gaussian type orbitals, GTOs.
STOs were determined by fitting analytical exponential functions to numerical atomic wavefunctions and thus provide a good representation of atomic orbitals. However, STOs have the severe shortcoming that most of the required intergrals needed in the course SCF procedure must be calculated numerically which drastically increases the speed of a calcualtion. An alternative to STOs was preposed by Boys in 1950. This was the Gaussian type function.

Gaussian functions have the advantage that the product of two Gaussian functions is itself a Guassian function centred at a point between the centres of the two contributing functions. This reduces the complex two-electron four-centre integrals to two centre integrals. Integrals of this form are much easier to calculate than STOs. However Guassian functions do have a significant disadvantage which is that they give a less realistic description of atomic wavefunctions. The hydrogenic 1s orbital and STOs have a cusp (discontinuous derivative) at the nucleus, whereas a GTO does not. A basis set comprised of a larger number of GTOs compared to STOs must therefore be used in order to model the correct behaviour of the atomic orbitals near the nucleus. This problem can be partially resolved by the use of a linear combination of primitive Gaussian functions (PGF), which are centred on the nucleus, to form a contracted Gaussian function (CGF). Although a greater number of GTOs have to be used than STOs to simulate the atomic orbitals, there is still a significant reduction in the computational cost incurred due to the comparative ease with which GTOs can be integrated.

The simplest type of basis set is a minimal basis set and comprises one PGF for each of the atomic orbitals used. The minimal basis set for a carbon atom would comprise one PGF for each of the 1s, 2s orbitals and the three 2p orbitals. Minimal basis sets do not tend to describe the wavefunction very accurately therefore they find use only in systems that are relatively large or as a starting point for progressively more accurate calculations.

An improvement in accuracy can be achieved by doubling the number of basis functions used, known as a double zeta basis set. Tripling the number of basis

functions relative to the minimal basis set gives a triple zeta basis set. Both of these types of basis set incur a significantly increased computational cost compared to the minimal basis set but give significantly increased accuracy. A solution to offset the size *vs.* computational cost problem is the use of a split valence (SV) basis set.

In the majority of cases the chemical properties of a molecular system arise from interactions with the valence electrons. In a SV basis set the core orbitals are modelled by one CGF, while the valence orbitals are represented separately by several contracted functions. By restricting the number of functions used to describe the core orbitals a significant reduction in computational cost can be achieved. An example of a SV basis set is the Pople 6-31G basis set. The notation indicates that the core orbitals are described by a CGF of 6 PGFs, the valence shell orbital is modelled by two functions (one a CGF of 3 PGFs and the other a single PGF).

The quality of a basis set can be further improved by the inclusion of polarization functions. The formation of chemical bonds in molecules causes the distortion of the atomic orbitals of the contributing atoms. This distortion can be modelled by including basis functions with higher angular momentum values, for example, adding d-type functions to carbon atoms. The addition of a * or (d) to the basis set name indicates the inclusion of six d-type functions to each non H atom. A second * or a (p) indicates the addition of a set of three p-type functions to each H atom.

To enable the accurate modelling of higher excited states or systems with loosely bound electrons the addition of diffuse functions into the basis set may be required. Diffuse functions have a higher principle quantum number but the same value of

angular momentum. In the case of carbon the highest filled orbital is a 2p orbital, therefore suitable diffuse functions to use would be 3p or 4p. The inclusion of diffuse functions in a SV basis set is denoted by the addition of a + to the name.

Pople type basis sets are widely used and give good agreement with a large range of experimental parameters. However, due to GTOs inherently poor description of the electrons near the nucleus they do not model EPR hyperfine coupling interactions well. Early in the development of basis sets for the calculation of EPR hyperfine coupling constants it was observed that adding additional s-type functions with large exponents in the region close to the nucleus leads to a significant improvement in the results.[16] Barone *et al.* have developed two basis sets, EPR-II and EPR-III, that are specifically tailored to the calculation of magnetic properties of radicals.[17,18] Calculations using these basis sets in combination with the B3LYP functional have been observed to accurately model the experimental hyperfine coupling constants for ^{1}H, ^{13}C, ^{14}N and ^{19}F nuclei in a number of radicals.[18-20] Although in some cases no improvement over the 6-31G(d) basis set was observed for the ^{1}H coupling constants.[21]

2.4.6. Time-dependent density functional theory

Time-dependent density functional theory (TD-DFT) can be used to generate a theoretical absorption spectrum for the molecular species under investigation. From comparison of the theoretical and experimental spectra identification of the nature of the transitions which make up absorption bands can be made. The TD-DFT method is based on the response of the ground-state electron density to an external potential, such as an oscillating electromagnetic field. By observing how the ground-states

wavefunction changes over time under the influence of the electromagnetic field it is possible to determine between which orbitals the transition occurred.

2.4.7. Solvent Models

The starting point for many calculation systems is the investigation of isolated molecules in the gas phase. This does not reflect many experimental systems. A more accurate representation of the molecular system under investigation can be obtained with the inclusion of a solvent medium.

Methods for including the effect of solvent can be divided into two general types: explicit solvation and implicit solvation. Explicit solvation involves the use of atomistically represented solvent molecules. Implicit solvation treats the solvent as a continuum with homogenous properties. A combination of these approaches is also possible by considering the first solvation sphere in an explicit manor and treating subsequent spheres with a continuum model.

Explicit solvation effects can be modelled by the addition of solvent molecules around the solute molecule in orientations that are likely to lead to solvent-solute interactions, such as hydrogen bonding. Implicit solvation effects can be modelled using a polarizable continuum model (PCM).

2.4.8. Development of a computational model for EPR analysis

One aim of this study was to develop a computational model that would aid in the assignment of the features observed in the EPR spectroelectrochemical investigations

of the reduced cyano and trifluoromethyl substituted polypyridines considered in this work.

The 4,4´-$(CF_3)_2$-bpy molecule was selected as a model system for this study. The B3LYP functional was chosen for use due to its reported accuracy in calculating EPR hyperfine coupling constants (HFCCs).[18-20] The success of this functional in predicting the HFCCs for organic radicals has been attributed to the inclusion of the exact exchange term in the overall expression for the exchange-correlation energy.

Initial studies were conducted to evaluate the ability of Pople type basis sets to accurately determine the HFCCs. The 6-31G basis set was selected as a starting point and progressively improved with addition of polarisation functions, diffuse functions and valence functions. The HFCCs determined from these basis sets are presented in table 2.2 along with the experimentally determined data recorded in this work.

	Coupling Constant (G)				
Basis Set	**A2 ^{14}N**	**A6 ^{19}F**	**A2 ^{1}H**	**A2 ^{1}H**	**A2 ^{1}H**
6-31G	5.05	6.50	7.13	1.48	0.19
6-31G(d,p)	3.28	4.42	6.51	1.10	0.62
6-31+G(d,p)	3.22	3.41	6.26	1.01	0.48
6-311+G(d,p)	1.96	2.67	5.70	0.91	0.43
EPR-III*	2.53	2.81	6.00	0.98	0.48
Experimental	3.03	2.98	5.25	0.99	0.56

Table 2.2 Computationally determined hyperfine coupling constants of [4,4´-$(CF_3)_2$-bpy]$^{1-}$. * EPR-III calculations conducted using the 6-31+G(d,p) optimised geometry

Examination of the results from table 2.2 indicate that the 6-31G basis set significantly overestimates the ^{14}N, ^{19}F and the two larger ^{1}H coupling constants. Conversely the smallest ^{1}H coupling is significantly underestimated. The addition of polarisation functions to all of the atoms causes a dramatic increase in the accuracy of

the calculations. Subsequent addition of diffuse functionals to the basis set in an attempt to better model delocalisation effects led to a further improvement of all the calculated coupling constants except the smallest ^{1}H couplings. When additional valence functionals are added to the model the ^{19}F coupling constant and the largest ^{1}H coupling were in better agreement with experiment but the coupling constants for the other spin active nuclei, in particular the ^{14}N coupling, were in worse agreement with experiment.

The percentage errors between the calculated and the experimental HFFCs for each of the Pople type basis sets are reported in figure 2.15. From these results it is clear that of the four Pople basis sets the most accurate is the 6-31+G(d,p). This basis set was thus selected for use with the other substituted polypyridines studied in this work.

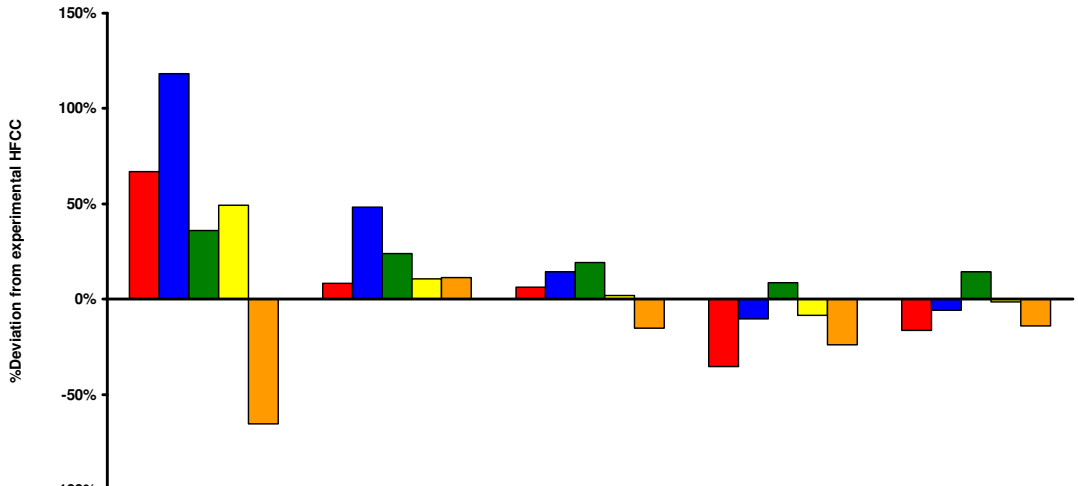

	6-31G	6-31G(d,p)	6-31+G(d,p)	6-311+G(d,p)	EPR-III*
A2 14N	66.8%	8.2%	6.3%	-35.4%	-16.4%
A6 19F	118.2%	48.3%	14.4%	-10.4%	-5.9%
A2 1H	35.9%	24.0%	19.3%	8.6%	14.3%
A2 1H	49.3%	10.6%	1.9%	-8.6%	-1.4%
A2 1H	-65.4%	11.3%	-15.2%	-23.9%	-13.9%

Figure 2.15 Percentage error in calculated hyperfine coupling constants for $[4,4'\text{-}(CF_3)_2\text{-bpy}]^{1-}$. * EPR-III calculations conducted using the 6-31+G(d,p) optimised geometry

Due to Pople basis sets less accurate modelling of electron interactions close to nuclei it has been observed that these basis sets are less efficient at calculating EPR HFCCs. Thus the EPR-III basis set developed by Barone *et al.*[18] for the calculation of HFCCs has also been evaluated.

Comparison of the optimised geometries from the Pople type basis sets showed little variation in the structure with increased quality of the basis set. Therefore it was decided that no meaningful increase in the determined structure would be achieved by repeating the geometry optimisation with the EPR-III basis set. The optimised geometry using the 6-31+G(d,p) basis set was selected for the EPR calculation. The HFCCs calculated for this geometry using the EPR-III basis set are reported in table 2.2 and the % error from the experimental values is shown in figure 2.15.

It can be seen that the error in the hyperfine coupling constants decrease for the ^{19}F coupling and all of the ^{1}H couplings. However, rather unexpectedly the error in the ^{14}N coupling constant increases. Despite this observation, it was concluded that using the EPR-III basis set to calculate the hyperfine couplings constants did result in an improvement overall.

The calculations described thus far considered the molecules to be in the gas phase. In an attempt to more accurately reflect the experimental system three different solvation models were investigated. Firstly the 4,4´-$(CF_3)_2$-bpy molecule was placed in a DMF Polarised Continuum Model (PCM)[22] in an attempt to model implicit solvent effects. The second system investigated used specific solvent molecules in an attempt to

model solvation effects explicitly. The final model developed was a combination of these two approaches.

The optimised geometry from the 6-31+G(d,p) gas phase calculation was taken as the starting point for the solvent calculations. The HFCCs for the three solvation models using the 6-31+G(d,p) basis set are reported in table 2.3 and the % error from the experimental values is shown in figure 2.16. Comparison of the data in figure 2.16 clearly shows that the quality of the calculation is highly dependent on the solvation model used.

	Coupling Constant (G)				
Solvation Model	**A2 ^{14}N**	**A6 ^{19}F**	**A2 ^{1}H**	**A2 ^{1}H**	**A2 ^{1}H**
6-31+G(d,p)	3.22	3.41	6.26	1.01	0.48
6-31+G(d,p) in PCM	3.37	2.85	6.22	1.08	0.65
6-31+G(d,p) & DMF explicit sol.	3.24	3.48	6.15	1.04	0.55
6-31+G(d,p) & DMF explicit sol. in PCM	3.33	2.82	6.21	1.07	0.65
Experimental	3.03	2.98	5.25	0.99	0.56

Table 2.3 Computationally determined hyperfine coupling constants of 4,4´-$(CF_3)_2$-bpy using series of solvation models

Placing the 4,4´-$(CF_3)_2$-bpy molecule in a DMF PCM results in a significant increase in the accuracy of the ^{19}F coupling constant. In contrast the other HFCCs are less accurately calculated, with a significant decrease in accuracy observed for the ^{14}N coupling and the secondary ^{1}H coupling. From these results it was concluded that the PCM was insufficient to represent the solvation of this molecule.

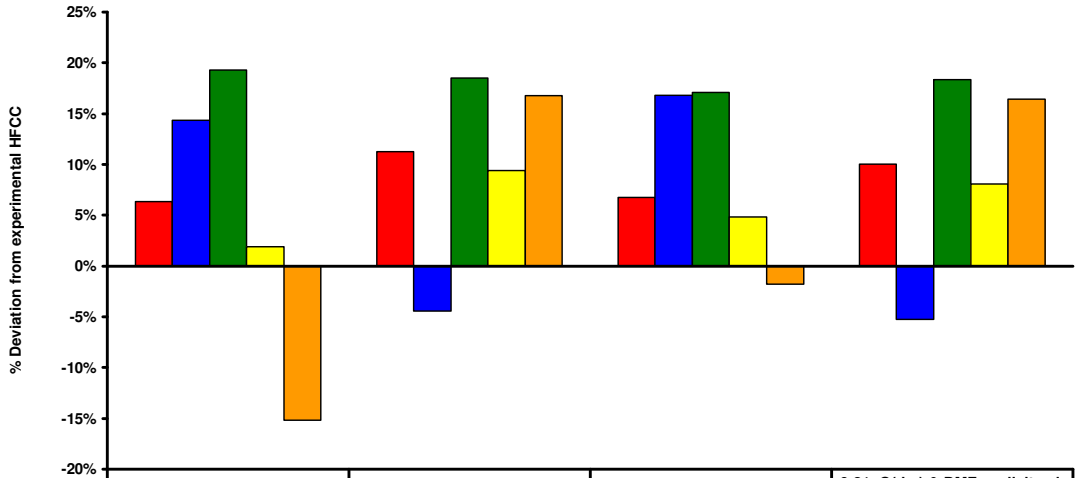

	6-31+G(d,p)	6-31+G(d,p) in PCM	6-31+G(d,p) & DMF explicit sol.	6-31+G(d,p) & DMF explicit sol. in PCM
A2 14N	6.3%	11.3%	6.8%	10.0%
A6 19F	14.4%	-4.4%	16.8%	-5.2%
A2 1H	19.3%	18.5%	17.1%	18.3%
A2 1H	1.9%	9.4%	4.8%	8.1%
A2 1H	-15.2%	16.8%	-1.8%	16.4%

Figure 2.16 Percentage error in calculated hyperfine coupling constants for $[4,4'\text{-}(CF_3)_2\text{-bpy}]^{1-}$ using a series of solvation models

The explicit solvation model was constructed by calculating the electrostatic potential maps for the solvent and solute, then placing the solvent molecules at the most likely positions for electrostatic interactions to occur. Four DMF molecules were initially used to model these explicit solvent interactions, with two molecules placed near the ring nitrogen atoms and the remaining DMF molecules placed near the trifluoromethyl substituent groups. Geometry optimisation of this starting structure using B3LYP/6-31+G(d,p) resulted in the DMF molecules at the trifluoromethyl groups shifting away from these position to coordinate to the DMF molecules placed near the ring nitrogen atoms. This indicates that these DMF molecules are not incorporated into the first solvation sphere. It was therefore decided to neglect these solvents molecules and use only the DMF molecules that coordinate to the ring nitrogen atoms. The structure was then reoptimised with B3LYP/6-31+G(d,p) and the HFCCs calculated.

When specific solvent molecules were placed around the molecule a marked change in the accuracy of the theoretical HFCCs was observed. The error in the ^{19}F coupling constant increased in this solvation model. A decrease in the accuracy of the theoretical values was observed for the ^{14}N coupling and the secondary ^{1}H coupling. A slight improvement in the calculated HFCC for the primary ^{1}H coupling is observed. The only significant improvement over the gas phase HFCCs was observed for the tertiary ^{1}H coupling. This is attributed to explicit hydrogen bonding effects to the DMF molecules.

When the combination of specific DMF molecules and a DMF PCM was investigated the HFCCs obtained from these calculations were almost identical to the values for the PCM model (figure 2.16). This suggests that the PCM dominates in this solvation scheme with the effects from the specific DMF molecules either being overwhelmed or being disrupted by the presence of the continuum.

An attempt to further refine the three solvation models was made by using the EPR-III basis set to calculate the HFCCs for each of the optimised geometries from the 6-31+G(d,p) basis set calculations. The HFCCs determined for these systems are reported in table 2.4 and the % error from the experimental values is shown in figure 2.17.

	Coupling Constant (G)				
Solvation Model	**A2^{14}N**	**A6^{19}F**	**A2^{1}H**	**A2^{1}H**	**A2^{1}H**
EPR-III	2.53	2.81	6.00	0.98	0.48
EPR-III in PCM	2.66	2.20	5.96	1.03	0.65
EPR-III & DMF explicit sol.	2.58	2.94	5.90	1.00	0.55
EPR-III & DMF explicit sol. in PCM	2.66	2.25	5.96	1.03	0.65
Experimental	3.03	2.98	5.25	0.99	0.56

Table 2.4 Computationally determined hyperfine coupling constants of [4,4´-$(CF_3)_2$-bpy]$^{1-}$ in a series of solvation models using the EPR-III basis set starting from the 6-31+G(d,p) optimised geometry

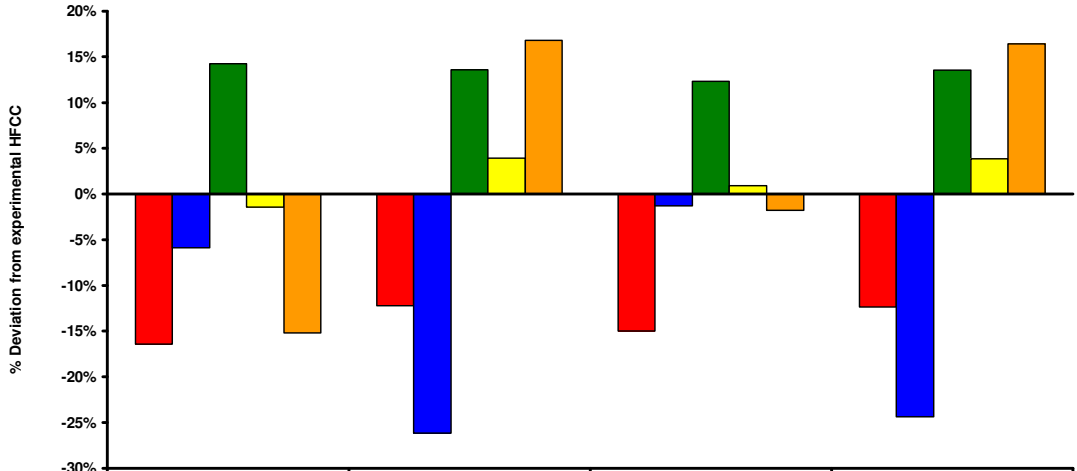

	EPR-III	EPR-III in PCM	EPR-III & DMF explicit sol.	EPR-III & DMF explicit sol. in PCM
A2 14N	-16.4%	-12.2%	-15.0%	-12.3%
A6 19F	-5.9%	-26.1%	-1.3%	-24.4%
A2 1H	14.3%	13.6%	12.3%	13.6%
A2 1H	-1.4%	3.9%	0.9%	3.8%
A2 1H	-15.2%	16.8%	-1.8%	16.4%

Figure 2.17 Percentage error in calculated hyperfine coupling constants for [4,4´-$(CF_3)_2$-bpy]$^{1-}$ in a series of solvation models using the EPR-III basis set starting from the 6-31+G(d,p) optimised geometry

Comparison of the data in figure 2.17 clearly indicates that specific solvent molecules more accurately model the solvation than a PCM. Again the PCM is seen to dominate over the specific solvent effects when the two solvation methods are combined. From this analysis it is clear that the optimal system to be used would be the use of specific DMF molecules coupled to the EPR-III basis set. However the computational cost incurred by this method is prohibitive for even these relative small systems. Comparison of the results for the solvent models with the gas phase calculation data indicates that little improvement is achieved for any of solvent models tested. In addition the considerable increase in computational time and memory required for the inclusion of solvent outweighs any improvement in modelling the experimental data.

Given these findings the calculations carried out on the other polpyridine systems reported in this work were conducted using the 6-31+G(d,p) basis set to obtain an

optimised geometry for use in the systems under investigation. These geometries were used in calculation of the HFFCs using the EPR-III basis set. Possible solvent interactions were neglected due to the prohibitive computational cost.

2.4.9. TD-DFT for UV/Vis/NIR spectroelectrochemistry analysis

TD-DFT calculations were conducted to aid the assignment of the features observed in the UV/Vis/NIR spectroelectrochemical studies of the non-reduced and mono-reduced cyano and trifluoromethyl substituted polypyridines studied in this work.

The 4,4´-$(CF_3)_2$-bpy was again selected as a test system to evaluate the ability of the method to predict the absorption spectra of the non-reduced species and the anion radical. The gas-phase optimised geometry calculated using the 6-31+G(d,p) basis set described above was selected as the geometry for these calculations. The major transitions observed in the calculated and experimental spectra for the non-reduced and mono-reduced species are reported in table 2.5.

	Calculation		Experimental	
	Wavenumber (cm^{-1})	Osc. Strength	Wavenumber (cm^{-1})	Extinction Coefficient ($M^{-1}cm^{-1}$)
4,4'-$(CF_3)_2$-bpy	36400	0.4459	34800	15200
$[4,4'\text{-}(CF_3)_2\text{-bpy}]^{1-}$	37300	0.0377	36100	6400
	28500	0.4371	25600	35600
	19700	0.1672	17200	11400
	7200	0.0315	7200	680

Table 2.5 Computationally determined electronic transitions of 4,4´-$(CF_3)_2$-bpy and $[4,4'\text{-}(CF_3)_2\text{-bpy}]^{1-}$

From these results it is clear that this method efficiently predicts the position of the single band observed in the spectrum of the non-reduced species, with a 4.6% error.

The gas-phase calculation for the mono-reduced species predicts the position of the most intense peak in each of the four absorption band fairly well, with a maximum error of 14.5%. Of particular note is the transition in the NIR region which is predicted exactly. However, the calculation fails to predict the fine structure observed for each of these peaks. This is attributed to the calculations inability to predict vibronic coupling effects accurately.

It is noted that for the mono-reduced species the energy of several of the transitions has been overestimated. This is indirect contrast to what is seen in many other TD-DFT studies on charged species and for charge transfer transitions where an underestimation of the energy of the transitions is more commonly observed.[23]

It is known that the inclusion of a PCM solvation model can improve the agreement between calculated and experimental spectra.[24-26] This has been rationalised to the ability of a PCM to more accurately model the localisation of charge within a solvated molecule compared to and isolated gas-phase molecule calcualtion. To this end TD-DFT calculations were run on the optimised 6-31+G(d,p) structure in a DMF continuum. The transitions observed in the calculated spectrum are reported in table 2.6.

	Calculation		Experimental	
	Wavenumber (cm^{-1})	Osc. Strength	Wavenumber (cm^{-1})	Extinction Coefficient ($M^{-1}cm^{-1}$)
4,4'-$(CF_3)_2$-bpy	35500	0.5357	34800	15200
$[4,4'\text{-}(CF_3)_2\text{-bpy}]^{1-}$	37500	0.0377	36100	6400
	28000	0.4371	25600	35600
	20000	0.1672	17200	11400
	7200	0.0315	7200	680

Table 2.6 Computationally determined electronic transitions of 4,4´-$(CF_3)_2$-bpy and $[4,4'\text{-}(CF_3)_2\text{-bpy}]^{1-}$ in DMF PCM solvation model

Comparison of these values indicates that the fit for the neutral species has improved with the error decreasing to 2%. For the mono-reduced species a slight decrease in the accuracy of the first and third bands is observed but this is off set by an improved agreement for the large intensity second band.

Taking these result into account it was decided that the TD-DFT calculations carried out on the other polpyridine systems reported in this work would be conducted using the 6-31+G(d,p) basis set with the molecules solvated using a PCM solvation model.

However, it is noted that the energy of several of the transitions in the mono-reduced species are still overestimated. It is suggested that this overestimation is due to the PCM being an insufficient description of solvation effects experienced by the charged species.

2.5 References

The background theory for the electrochemical, spectroelectrochemical and computational methods discussed in this work was adapted from the following sources:

Electrochemistry:

A. C. Fisher, *Electrode Dynamics*, Oxford University Press, Oxford, 1996.

A. J. Bard, L. R. Faulkner, *Electrochemical methods. Fundamentals and applications*, 2ed., Wiley, New York, 2000.

Spectroelectrochemistry:

A. C. Fisher, *Electrode Dynamics*, Oxford University Press, Oxford, 1996.

A. K. Brisdon, I*norganic spectroscopic methods*, Oxford University Press, Oxford, 1998.

P. W. Atkins, *Physical Chemistry*, 6th ed., Oxford University Press, Oxford, 1998.

W. Kaim, A. Klein, *Spectroelectrochemistry*, RSC publishing, Cambridge, 2008.

J. A. Weil, J. R. Bolton, J. E. Wertz, *Electron Paramagnetic Resonance : Elementary Theory and Practical Applications*, Wiley. New York, 1994.

Computational:

G. H. Grant, W. G. Richards, *Computational chemistry*, Oxford University Press, Oxford, 1995.

P. Atkins, R. Friedman, *Molecular Quantum Mechanics*, Oxford University Press, Oxford, 2005.

F. Jensen, *Introduction to Computational Chemistry*, Wiley, New York, 1999.

1. J. I. Bruce, J.-C. Chambron, P. Kolle, J.-P. Sauvage, *J. Chem. Soc., Perkin Trans. 1*, 2002, 1226-1231.

2. J. M. Veauthier, C. N. Carlson, G. E. Collis, J. L. Kiplinger, K. D. John, *Synthesis*, 2005, **16**, 2683-2686.

3. S. A. McFarland, F. S. Lee, K. A. W. Y. Cheng, F. L. Cozens, N. P. Schepp, *J. Am. Chem. Soc.*, 2005, **127**(19), 7065-7070.

4. I. Noviandri, K. N. Brown, D. S. Fleming, P. T. Gulyas, P. A. Lay, A. F. Masters, L. Phillips, *J. Phys. Chem. B*, 1999, **103**, 6713-6722.

5. A. K. Brisdon, I*norganic spectroscopic methods*, Oxford University Press, Oxford, 1998.

6. J. McMurry, *Organic chemistry*, 6th ed., Brooks/Cole Thomson Learning, Belmont, 2004.

7. P. W. Atkins, *Physical Chemistry*, 6th ed., Oxford University Press, Oxford, 1998.

8. W. Kaim, A. Klein, *Spectroelectrochemistry*, RSC publishing, Cambridge, 2008.

9. S. Stoll, A. Schweiger, *J. Magn. Reson.* 2006, **178**(1), 42-55.

10. J. P. Perdew, K. Burke, Y. Wang, *Phys. Rev. B*, 1996, **54**(23), 16533-16539.

11. A. D. Becke, *J. Chem. Phys.*, 1993, **98**, 5648-5652.

12. P. J. Stephens, F. J. Delvin, C. F. Chabalowski, M. J. Frisch, *J. Phys. Chem.*, 1994, **98**, 11623-11627.

13. C. Lee, W. Yang, R. G. Parr, *Phys. Rev. B*, 1988, **37**, 785-789.

14. A. D. Becke, *Phys. Rev. A*, 1988, **38**(6), 3098-3100.

15. S. H. Vosko, L. Wilk, M. Nusair, *Can. J. Phys.*, 1980, **58**, 1200-1211.

16. K. Morokuma, H. Konishi, *Chem Phys. Lett.*, 1971, **12**(2), 408-413.

17. V. Barone, *Recent advances in density functional methods*, World Scientific, Singapore, 1995.

18. N. Rega, M. Cossi, V. Barone, *J. Chem Phys*. 1996, **105**, 11060-11067.

19. S. M. Mattar, A. H. Emwas, A. D. Stephens, *Chem. Phys. Lett*., 2002, **363**, 152-160.

20. A. R. Rakitin, D. Yff, C. Trapp, *J. Phys. Chem. A*, 2003, **107**, 6281-6292.

21. P. Lahorte, F. De Proft, F. Callens, P. Geerlings, W. Mondelaers, *J. Phys. Chem. A*, 1999, **103**, 11130-11135.

22. E. S. Böes, P. R. Livotto, H. Stassen, *Chem. Phys*., 2006, **331**, 142-158.

23. E. A. M. Geary, K. L. McCall, A. Turner, P. R. Murray, E. J. L. McInnes, L. A. Jack, L. J. Yellowlees, N. Robertson, *Dalton Trans*., 2008, 3701-3708.

24. A. Vlček Jr., S. Záliš, *J. Phys. Chem. A*, 2005, **109**, 2991-2992.

25. M.-F. Charlot, A. Aukauloo, *J. Phys. Chem. A*, 2007, **111**, 11661-11672.

26. S. R. Stoyanov, J. M. Villegas, D. P. Rillema, *Inorg. Chem. Comm*., 2004, **7**, 838-841.

3 Electrochemical and Spectroelectrochemical Characterisation of 2-CN-py, 3-CN-py and 4-CN-py and their Pt complexes

3.1 Introduction

Substituted pyridines have been investigated in this work since they form the building blocks of 2,2´-bipyridine molecules. Analysis of the electronic character of these building blocks can aid in the understanding of the properties of their substituted bipyridine analogues.[1] In this chapter the electronic effect of the cyano substituent group on pyridine is considered. The compounds investigated are shown in figure 3.1.

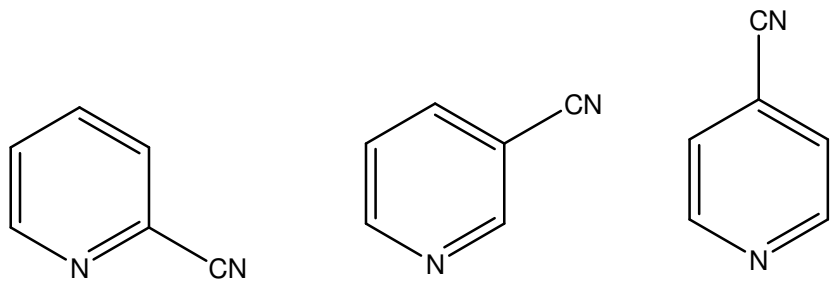

2-CN-py 3-CN-py 4-CN-py

Figure 3.1 Structure of 2-cyanopyridine, 3-cyanopyridine and 4-cyanopyridine

The electronic character of a number of substituted pyridines has been investigated previously by electrochemical and spectroelectrochemical methods.[1-4] The substituent groups studied to date have ranged from weakly electron donating phenyl to the highly electron withdrawing nitro group. Shown in table 3.1 are the reduction potentials for a number of these substituted pyridines. It can be clearly seen that as the strength of electron withdrawing character of the substituent increases the reduction process moves to less negative potentials.

Substituent X	$E_{½}$ / V			Ref.		
	2-X-py	3-X-py	4-X-py	2-	3-	4-
Ph	-2.25	-2.33	-2.09	4	4	4
CHO	-1.53	-1.69*	-1.45*	4	4	4
CO_2Me	-1.88	-2.15	-1.69	4	4	4
NO_2	-0.93	-0.94	-0.74	4	3	2

Table 3.1 Half wave reduction potentials for 2-X-py, 3-X-py and 4-X-py (X = Ph, CHO, CO_2Me and NO_2) *vs*. Ag/AgCl. * indicates an irreversible process, E_{pc} value is quoted for this process

In addition it has been observed that substitution at different positions around the pyridine ring has a significant effect upon the electronic character of the molecule.[2-4] Comparison of the reduction potentials for the 2-, 3- and 4-substituted isomers of the compounds reported in table 3.1 indicate that the 4-substituted analogues are the easiest reduce in each case. This is in line with the theory that pyridines substituted *para* to the ring nitrogen atom should experience a greater resonance stabilisation effect from the substituent, as discussed in section 1.2.

The effect of the substituent group has also been probed by UV/Vis/NIR and EPR spectroelectrochemical methods. Shown in tables 3.2 and 3.3 are the UV/Vis/NIR spectroscopic data collected for 4-CO_2Me-py and 4-NO_2-py in their neutral and mono-reduced states respectively. These compounds give broadly similar spectra, with the transition in the NO_2 substituted species moving to lower energy due to the increased electron withdrawing nature of the substituent group.

	Wavenumber (cm^{-1})	Extinction Coefficient ($M^{-1}cm^{-1}$)	Ref.
4-CO_2Me-py	36500	2700	4
4-NO_2-py	35100	1700	2

Table 3.2 Peak positions and extinction coefficients for signals in the UV/Vis/NIR spectra of 4-CO_2Me-py and 4-NO_2-py

	Wavenumber (cm^{-1})	Extinction Coefficient ($M^{-1}cm^{-1}$)	Ref.
$[4\text{-}CO_2Me\text{-}py]^{1-}$	32300 24000	11500 6000	4
$[4\text{-}NO_2\text{-}py]^{1-}$	33000 31500 21800	5500 6600 2400	2

Table 3.3 Peak positions and extinction coefficients for signals in the UV/Vis/NIR spectra of $[4\text{-}CO_2Me\text{-}py]^{1-}$ and $[4\text{-}NO_2\text{-}py]^{1-}$

EPR investigation of the $[4\text{-}CO_2Me\text{-}py]^{1-}$ and $[4\text{-}NO_2\text{-}py]^{1-}$ species have enabled analysis of the distribution of electron density in the frontier orbitals of these compounds. The hyperfine coupling constants observed for these species are reported in table 3.4 along with data for the ^{15}N labelled analogue of the nitro compound.[3-5] Analysis of the coupling constants indicates that there is significant delocalisation onto the functional group with the contribution being large for the NO_2 substituent due to its stronger electron withdrawing character.

	$[4\text{-}CO_2Me\text{-}py]^{1-}$	$[4\text{-}NO_2\text{-}py]^{1-}$	$[4\text{-}^{15}NO_2\text{-}py]^{1-}$
$A(3 \times {}^1H)/G$	1.05	—	—
$A(1 \times {}^{14}N)/G$ ($^{14}NO_2$)	—	8.43	—
$A(1 \times {}^{15}N)/G$ ($^{15}NO_2$)	—	—	12.3
$A(1 \times {}^{14}N)/G$ (ring)	5.09	2.43	2.55
$A(2 \times {}^1H)/G$	2.99	3.04	3.00
$A(2 \times {}^1H)/G$	0.85	0.45	0.53
g_{iso}	2.0028	2.0055	—
$\Delta H_{pp}/G$	0.35	0.30	—

Table 3.4 EPR hyperfine coupling constants of $[4\text{-}CO_2Me\text{-}py]^{1-}$, $[4\text{-}NO_2\text{-}py]^{1-}$ and $[4\text{-}^{15}NO_2\text{-}py]^{1-}$ [3-5]

Electrochemical analysis of the three isomers of cyanopyridine has been reported previously using polargraphic methods.[6] However, no spectroelectrochemical analysis has been conducted to date. Therefore in this work electrochemistry of the three X-CN-py compounds will be repeated using CV and DPV methods and spectroelectrochemical (UV/Vis/NIR and EPR) studies will be conducted to

determine the nature of the frontier orbitals. In addition the ability of these compounds to act as ligands to transition metals will be investigated.

3.2 Electrochemistry

3.3.1 Cyanopyridines

3.2.1.1 Cyclic Voltammetry

The electrochemical studies were initiated by measuring the cyclic voltamogram of 3-CN-py in 0.3 M [TBA][BF_4]/DMF. The results indicate that the system comprises of one irreversible one-electron reduction with an E_{pc} value of –1.90 V. The cyclic voltammogram for this system is shown in figure 3.2.

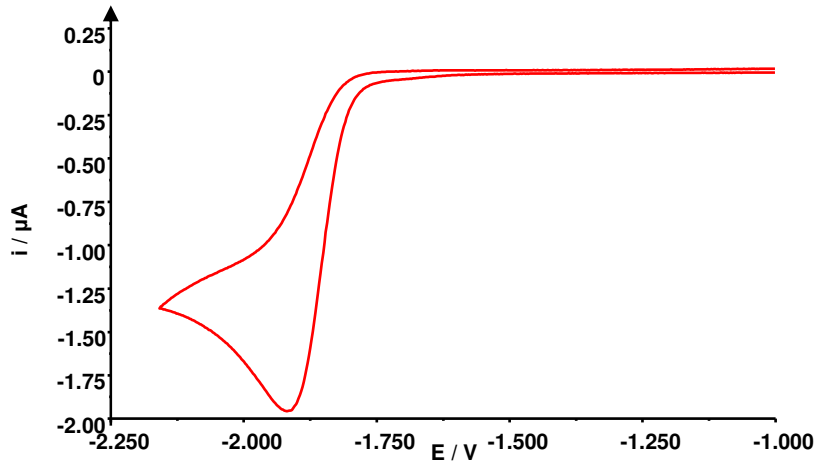

Figure 3.2 Cyclic Voltammetry of 3-CN-py *vs*. Ag/AgCl in 0.3 M [TBA][BF_4]/DMF at 298 K, v = 100 mVs^{-1}

The scan rate was increased sequentially from 0.1 Vs^{-1} to 1.0 Vs^{-1} in an attempt to investigate the irreversible nature of the reaction. The solution was also cooled to 233 K in an attempt to stabilise any reduced species formed. It was determined that even at the highest scan rate and lowest temperature studied that the reaction remained irreversible. This indicates a rapid decomposition process is occurring following electron transfer. The scan rate dependence study of 3-CN-py is shown in figure 3.3 and a linear plot of i_{pc} *vs*. $\nu^{½}$ indicates that the electron transfer process is diffusion controlled.

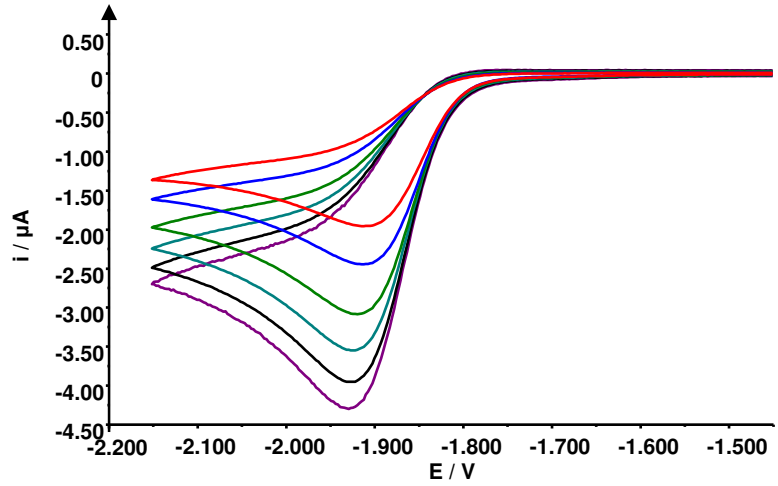

Figure 3.3 Scan rate study of 3-CN-py in 0.3 M [TBA][BF_4]/DMF T=233 K at scan rate of 0.1 Vs^{-1}(red), 0.2 Vs^{-1} (blue), 0.4 Vs^{-1} (green), 0.6 Vs^{-1} (cyan), 0.8 Vs^{-1} (black) and 1.0 Vs^{-1} (violet).

When the cyclic voltammogram for 4-CN-py in 0.3 M [TBA][BF_4]/DMF system was recorded one reversible reduction reaction was observed see figure 3.4 below. The $E_{½}$ value for the system is -1.66 V.

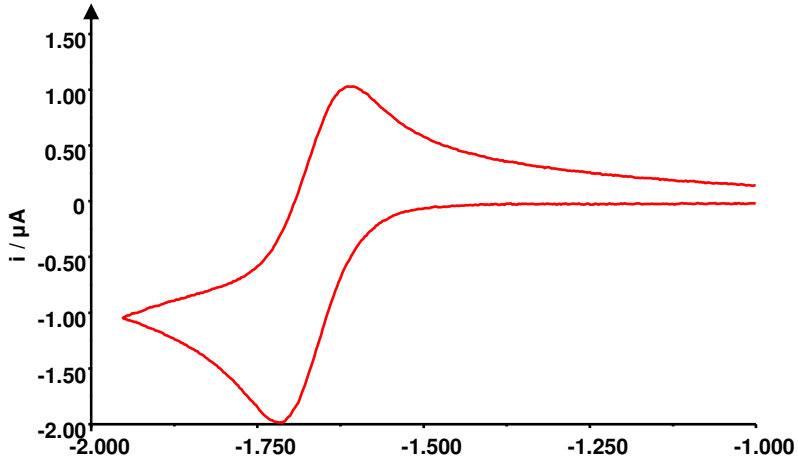

Figure 3.4 Cyclic Voltammogram of 4-CN-py *vs*. Ag/AgCl in 0.3 M [TBA][BF4]/DMF at 298 K, ν = 100 mVs^{-1}

A plot of i_p vs $\nu^{½}$ for the reduction reaction of 4-CN-py reveals a linear relationship. This indicates that the reduction is diffusion controlled see figure 3.5.

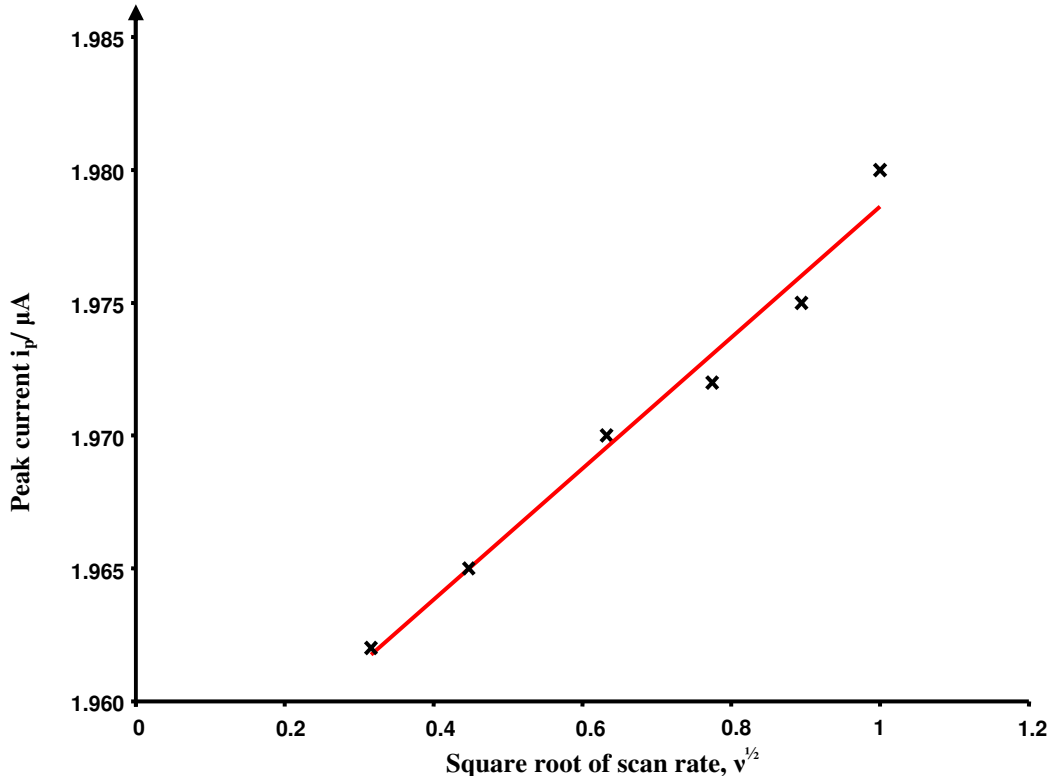

Figure 3.5 Plot of i_p *vs* $v^{½}$ for the reduction of 4-CN-py in 0.3 M [TBA][BF_4]/DMF

The cyclic voltamogram for 2-CN-py in 0.3 M $TBABF_4$/DMF indicated that it also had one reversible reduction process, with an $E_{½}$ value of -1.85 V. The reduction potentials observed in the CV investigations of the three cyanopyridines are shown in table 3.5.

	$E_{½}$ / V
2-CN-py	-1.85
3-CN-py	-1.90*
4-CN-py	-1.66

Table 3.5 Half wave reduction potentials for 2-CN-py, 3-CN-py and 4-CN-py *vs*. Ag/AgCl. * indicates an irreversible process, E_{pc} value is quoted for this process

Comparison of these results clearly shows that the 4-CN-py is the most easily reduced. The 2- and 3- substituted analogues are significantly harder to reduce, with the reduction processes occurring at similar potentials. In 2-CN-py the electron withdrawing substituent group is directly adjacent to the electron rich ring nitrogen

atom, thus leading to potential electronic repulsions between the two groups making it more difficult to reduce compared to 4-CN-py.

The 3-CN-py isomer is the hardest to reduce, with the reduction resulting in an unstable redox product. This instability can be attributed to the decreased resonance stabilisation effects experienced by *meta* substituted pyridines as discussed in section 1.2. These findings are in line with the results reported for a number of other substituted pyridines, see table 3.1.

3.2.1.2 Differential Pulse Voltammetry

The differential pulse voltammograms for the three cyanopyridines were also recorded to compare with the results of the cyclic voltammetry experiments. The differential pulse voltammograms for 2-CN-py and 4-CN-py confirmed the findings of the cyclic voltammetry, indicating that both compounds have one reversible reduction at -1.84 V and -1.67 V respectively. The voltammogram of 4-CN-py is shown in figure 3.6.

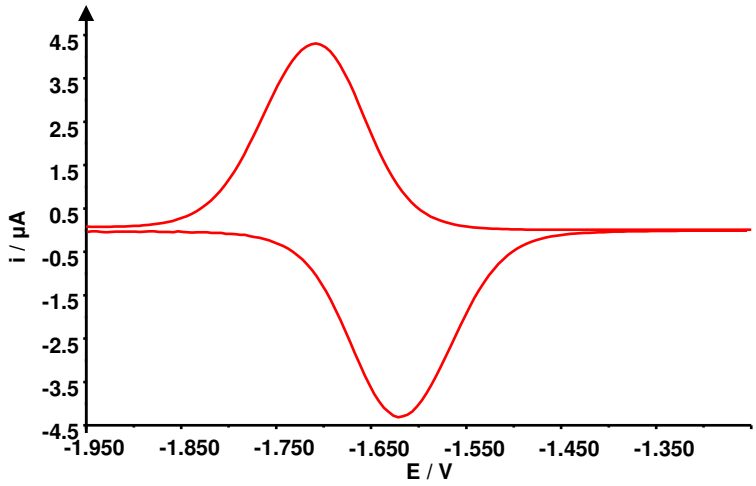

Figure 3.6 Differential Pulse of 4-CN-py *vs*. Ag/AgCl in 0.3 M [TBA][BF_4]/DMF at 298 K

When the differential pulse voltammetry of the 3-CN-py compound was conducted it indicated that the reaction was quasi-reversible, figure 3.7, in contrast to the findings from the CV experiment.

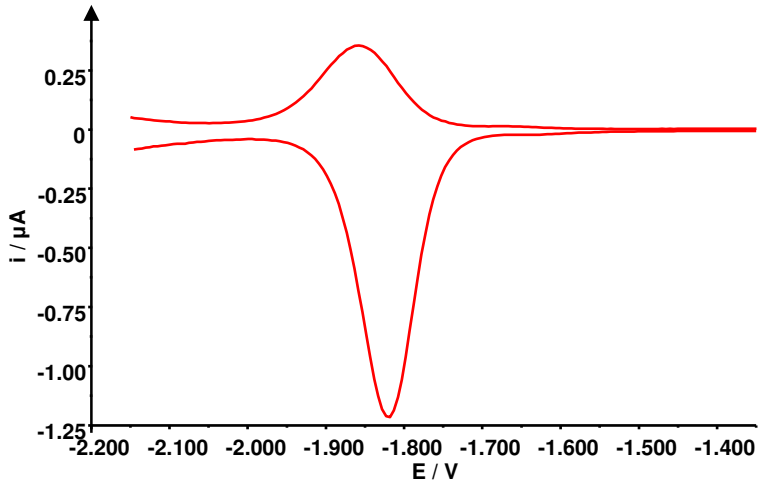

Figure 3.7 Differential Pulse of 3-CN-py *vs*. Ag/AgCl in 0.3 M [TBA][BF_4]/DMF at 298 K

This observation of a small return wave in the DPV experiment compared to the lack of return wave in the cyclic voltammogram can be put down to the increased sensitivity of the differential pulse technique. Unlike in the CV it is possible to detect small amount of the reduced species being oxidised back to the neutral ligand before the unstable reduced species decomposes. The quasi-reversible peak has an $E_{½}$ value of -1.85 V. The electrochemical results from the DPV experiments for the three cyanopyridines are shown in table 3.6. Comparison of the $E_{½}$ values for the three compounds indicate that the 2- and 3- substituted cyanopyridines are reduced at very similar potentials that are significantly more negative than for the 4-CN-py analogue.

	$E_{½}$ / V
2-CN-py	-1.84
3-CN-py	-1.85
4-CN-py	-1.67

Table 3.6 Half wave reduction potentials for 2-CN-py, 3-CN-py and 4-CN-py *vs*. Ag/AgCl.

3.2.2 $[Pt(X\text{-}CN\text{-}py)_2Cl_2]$ complexes

3.2.2.1 Cyclic Voltammetry

Cyclic voltammertric studies of $[Pt(4\text{-}CN\text{-}py)_2Cl_2]$ in 0.1 M $[TBA][BF_4]$/DMF at 298 K revealed an irreversible reduction with E_{pc} = -1.12 V and one reversible reduction at $E_{½}$ = -1.23 V. The cyclic voltammogram for this system is shown in figure 3.8.

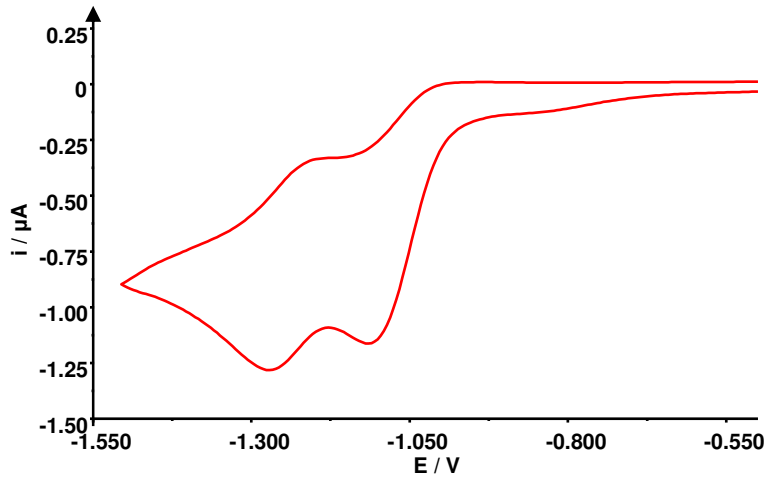

Figure 3.8 Cyclic Voltammogram of $[Pt(4\text{-}CN\text{-}py)_2Cl_2]$ *vs*. Ag/AgCl in 0.1 M $[TBA][BF_4]$/DMF at 298 K, ν = 100 mVs^{-1}

The scan rate was increased sequentially from 0.1 Vs^{-1} to 1.0 Vs^{-1} in an attempt to investigate the irreversible nature of the first redox process of $[Pt(4\text{-}CN\text{-}py)_2Cl_2]$. An overlaid plot of the cyclic voltammograms at different scan rates is shown in figure 3.9. It is clear from this plot that even a slight increase in scan rate to 0.2 Vs^{-1} causes the first reduction to become more reversible at 298 K with a $E_{½}$ = -1.07 V. This indicates that the decomposition process occurring after electron transfer is slow.

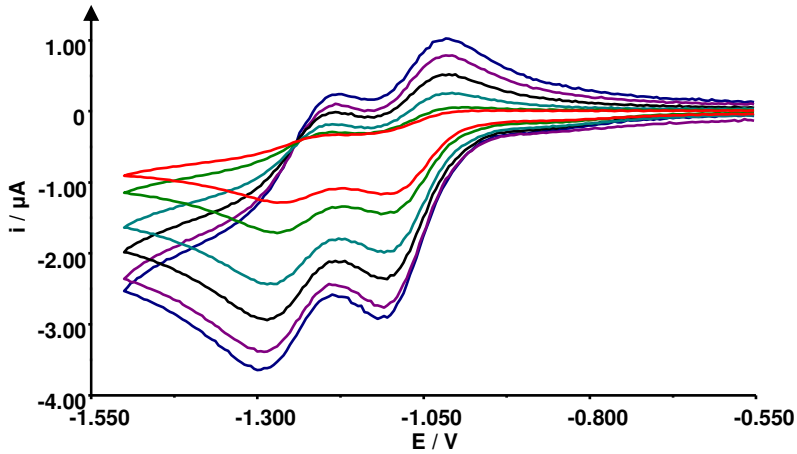

Figure 3.9 Scan rate study of $[Pt(4\text{-}CN\text{-}py)_2Cl_2]$ in 0.1 M $[TBA][BF_4]$/DMF T=283 K at scan rate of 0.1 Vs^{-1}(red), 0.2 Vs^{-1} (green), 0.4 Vs^{-1} (cyan), 0.6 Vs^{-1} (black), 0.8 Vs^{-1} (violet) and 1.0 Vs^{-1} (blue)

The temperature dependence of the redox processes of $[Pt(4\text{-}CN\text{-}py)_2Cl_2]$ was also investigated. Figure 3.10 shows the cyclic voltammogram recorded at 0.1 Vs^{-1} and 233 K. It clearly shows that the first reduction is fully reversible at 233 K.

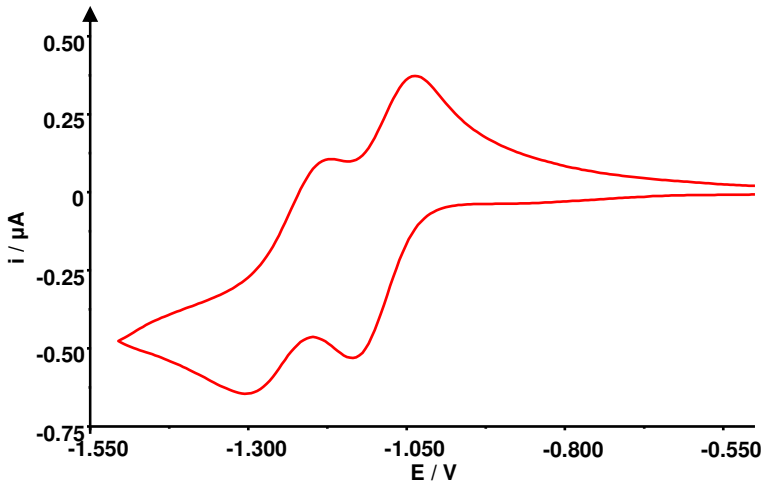

Figure 3.10 Cyclic Voltammogram of $[Pt(4\text{-}CN\text{-}py)_2Cl_2]$ *vs*. Ag/AgCl in 0.1 M $[TBA][BF_4]$/DMF at 233 K, v = 100 mVs^{-1}

The two one-electron reductions peaks for $[Pt(4\text{-}CN\text{-}py)_2Cl_2]$ are assigned to the sequential reduction of the two 4-CN-py ligands. This is in accordance with the reduction patterns observed for other Pt complexes of substituted pyridines.[4]

When the cyclic voltammogram of $[Pt(3\text{-}CN\text{-}py)_2Cl_2]$ in 0.1 M $[TBA][BF_4]$/DMF was conducted one irreversible reduction with E_{pc} = -1.32 V was observed, shown in figure 3.11. A scan rate study and a temperature study were conducted to investigate the irreversible nature of the reduction process. It was determined that even at 1.0 Vs^{-1} at 233 K the redox process remained irreversible. This indicates that the decomposition process occurring after the electron transfer is more rapid than for $[Pt(4\text{-}CN\text{-}py)_2Cl_2]$.

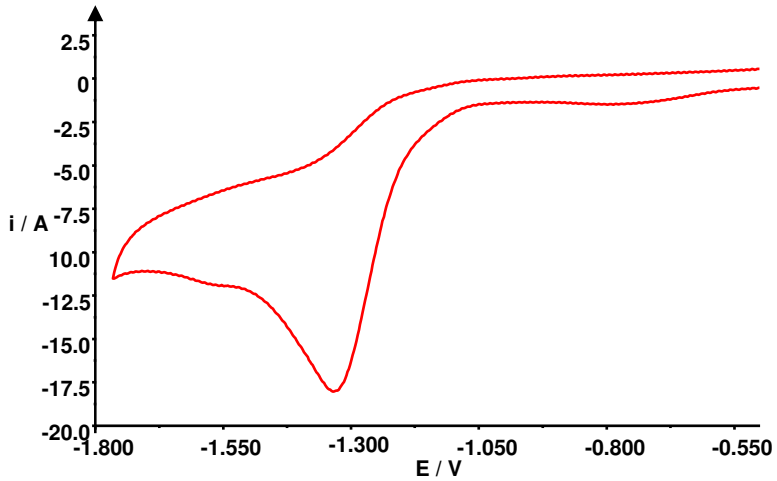

Figure 3.11 Cyclic Voltammogram of $[Pt(3\text{-}CN\text{-}py)_2Cl_2]$ *vs.* Ag/AgCl in 0.1 M $[TBA][BF_4]$/DMF at 298 K, ν = 100 mVs^{-1}

Attempts to synthesis the $[Pt(2\text{-}CN\text{-}py)_2Cl_2]$ analogue were unsuccessful, presumably because substitution in the 2 position of pyridine causes steric hinderance on binding to the Pt(II) centre.

The two Pt compounds studied both exhibited easier (less negative potential) reductions than the equivalent free ligands (-1.07 V cf. -1.66 V for 4-CN-py and -1.32 V cf. -1.90 V for 3-CN-py). This shift may be attributed to the electronic influence of the Pt(II) metal centre.

Shown in table 3.7 is the electrochemical data for a series of $[Pt(4\text{-}X\text{-}py)_2Cl_2]$ complexes (where X = CO_2Me, CO_2Et and NO_2) along with the data for the $[Pt(4\text{-}CN\text{-}py)_2Cl_2]$ complex investigated in this work. Comparison of the reduction potentials indicates that, as was found for the free ligands, the addition of electron withdrawing groups to the pyridine ligands results in the observed reductions moving to less negative potentials. The stronger the electron withdrawing effect of the substituent, the greater the degree of stabilisation experienced by the LUMO of the complex.

Substituent X	σ_p	[Pt(4-X-py)$_2$Cl$_2$]			Ref.
		$E_{½(1)}$ / V	$E_{½(2)}$ / V	$E_{½(1)}$-$E_{½(2)}$ / mV	
CO_2Me	0.45	-1.15	-1.32	170	4
CO_2Et	0.45	-1.14	-1.32	180	4
CN	0.66	-1.07	-1.23	160	-
NO_2	0.78	-0.44	-0.48	40	4

Table 3.7 Half wave reduction potentials for a series of [Pt(4-X-py)$_2$Cl$_2$] complexes (where X = CO_2Me, CO_2Et, CN and NO_2)

When the separation between the first and second reductions of the complexes are examined it is noted that for the ester and cyano substituted pyridine complexes the separation remains roughly constant, ranging between 160 – 180 mV. The difference in the potentials of the two ligand based reductions can be ascribed to the varying influence of the Pt(II) metal centre. Reduction of the first ligand shields the positive charge of the metal centre, resulting in the reduction of second ligand requiring a more negative potential.

In contrast the reductions observed for [Pt(4-NO_2-py)$_2$Cl$_2$] are separated by only 40 mV. Moorcraft attributed this to the reduction electrons entering MOs that are located primarily on the NO_2 substituent groups of the pyridine ligands. The localisation of the first reduction electron onto the nitro group of the ligand results in little shielding of the Pt(II) metal centre. Thus the metal centre's ability to stabilise the reduction of the second nitropyridine ligand is relatively unaffected by the presence of the [4-NO_2-py]$^{1-}$ ligand.

3.2.2.2 Differential Pulse Voltammetry

The differential pulse voltammograms for the two Pt complexes under investigation were also recorded. The results obtained for [Pt(4-CN-py)$_2$Cl$_2$] confirmed the findings

from the cyclic voltammerty indicating that the complex had two reversible reduction processes at -1.06 V and -1.24 V respectively.

When the differential pulse voltammerty of the $[Pt(3\text{-}CN\text{-}py)_2Cl_2]$ complex was conducted it showed a quasi-reversible reduction at $E_{½}$ = -1.28 V. The observation of a small anodic peak in the differential pulse voltammogram matches the response observed for the 3-CN-py free ligand, figure 3.7.

3.3 Spectroelecrochemsirty

3.3.1 Cyanopyridines

3.3.1.1 Ultra Violet/Visible/Near Infra-Red Spectrolelectrochemistry

The UV/Vis/NIR spectrum of 4-CN-py before the generation potential was applied is shown in figure 3.12. From the spectrum it is clear that the compound has one strong absorbance signal at approximately 36500 cm^{-1} (ε = 3300 M^{-1} cm^{-1}), corresponding to a HOMO-LUMO π-π^* transition.

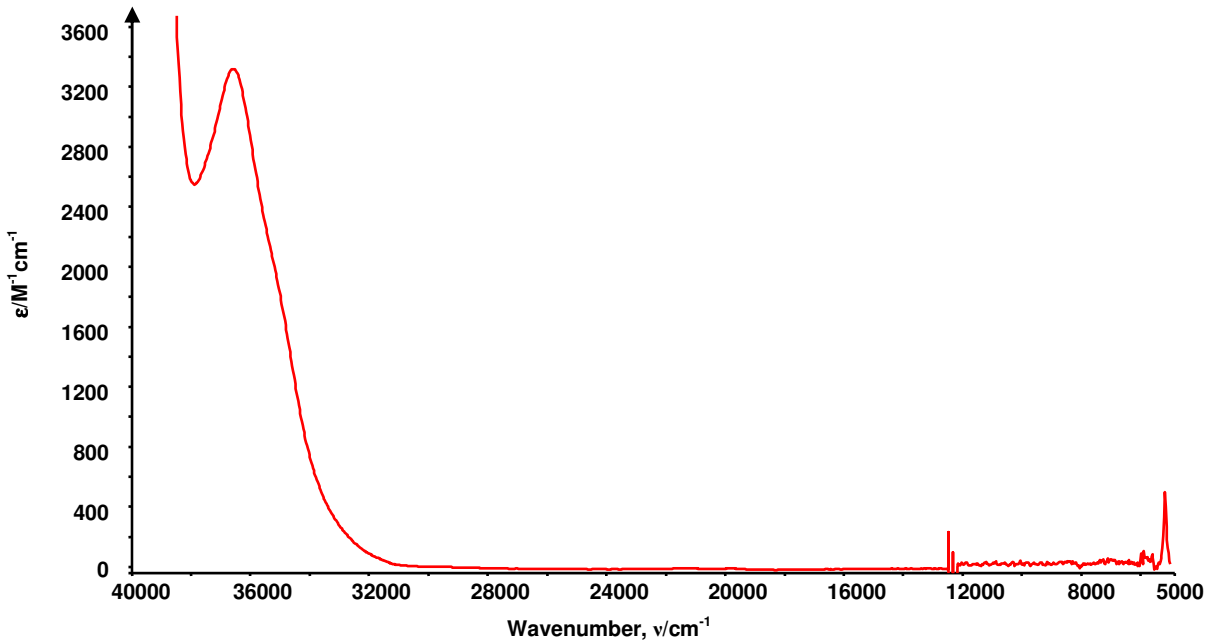

Figure 3.12 UV/Vis/NIR of 4-CN-py in 0.1 M $[TBA][BF_4]$/DMF at 233 K

A potential of -2.0 V was then applied to the system to generate the mono-reduced $[4\text{-CN-py}]^{1-}$ species. Figure 3.13 shows the spectrum of the system during the 70 minute reduction period.

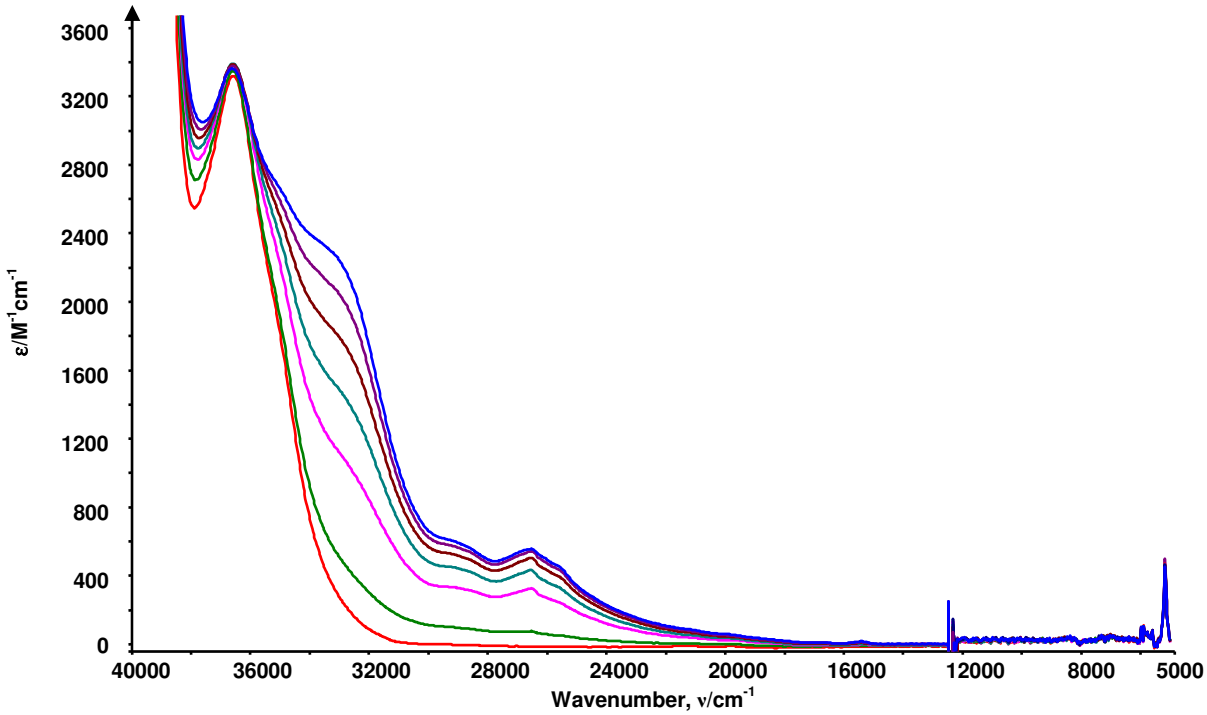

Figure 3.13 UV/Vis/NIR of 4-CN-py in 0.1 M [TBA][BF_4]/DMF at 233 K 70 minutes after a potential of -2.0 V *vs*. Ag/AgCl was applied. $[4\text{-CN-py}]^0$ red spectrum, $[4\text{-CN-py}]^{1-}$ blue spcetrum

During the one-electron reduction process the strong absorbance signal that was present in the initial spectrum remained relatively constant and a series of new peaks grow in. The position and extinction coefficient of these peaks are given in table 3.8.

	Wavenumber (cm^{-1})	Extinction Coefficient ($M^{-1}cm^{-1}$)
4-CN-py	36500	3300
$[4\text{-CN-py}]^{1-}$	36600	3400
	33100	2300
	29000	600
	26500	560
	25600	450
	20000	60
	15600	20

Table 3.8 Peak positions and extinction coefficients for signals in the UV/Vis/NIR spectra of 4-CN-py and $[4\text{-CN-py}]^{1-}$

The lower energy peaks in the spectrum are not present in the initial scan before the potential is applied and continue to increase until the point of maximum growth. This a clear indication that these peaks correspond to the $[4\text{-CN-py}]^{1-}$ species. These bands were assigned to intraligand transitions involving the partially filled π^* orbital. On reversal of the electrogeneration potetntial to 0 V the spectrum of the mono-reduced $[4\text{-CN-py}]^{1-}$ collapsed and the spectrum of the neutral species was regenerated.

3.3.1.2 Electron Paramagnetic Resonance Spectroelectrochemistry

In-situ electrochemical reduction was used to generate the EPR active $[2\text{-CN-py}]^{1-}$ and $[4\text{-CN-py}]^{1-}$ species. It was not possible to generate $[3\text{-CN-py}]^{1-}$ as the reduction of 3-CN-py is irreversible. A potential of -2.2 V and -1.8 V were used to generate the $[2\text{-CN-py}]^{1-}$ and $[4\text{-CN-py}]^{1-}$ species respectively.

The EPR spectrum recorded for $[2\text{-CN-py}]^{1-}$ shown in figure 3.14 consists of 34 lines. The large number of lines observed can be attributed to the presence of many inequivalent spin-active nuclei in the molecule which the unpaired electron can couple to. Simulation of the experimental spectrum was achieved by including coupling to two different ^{14}N nuclei and coupling to four different ^{1}H nuclei see figure 3.14. The simulation corresponds very well with the experimentally observed EPR spectrum. The results show that the unpaired electron is delocalised across the entire ring system rather than localised on one particular position. The largest coupling of 6.68 G is to a ^{1}H. Examination of the two nitrogen couplings reveals that the larger coupling of 4.48 G is more than twice the size of the smaller coupling of 2.22 G. An assignment of which ^{14}N coupling is due to the CN group nitrogen or the ring nitrogen is not possible from these experimental results alone. The third largest coupling of 3.09 G is

a ^{1}H coupling. The remaining two ^{1}H coupling are of a similar size having values of 0.72 G and 0.53 G.

The EPR spectrum obtained for the $[4\text{-CN-py}]^{1-}$ species is shown in figure 3.15, it consists of 27 lines. Simulation of the experimental spectrum was achieved by including coupling to two different ^{14}N nuclei and coupling to two pairs of equivalent ^{1}H nuclei, and shows excellent agreement with experiment (figure 3.15). As with the $[2\text{-CN-py}]^{1-}$, the observed coupling pattern indicates that the unpaired electron is spread across the whole ring system. In comparison to the $[2\text{-CN-py}]^{1-}$ the largest coupling (5.70 G) in the $[4\text{-CN-py}]^{1-}$ spectrum is due to coupling to a ^{14}N nuclei. The coupling to the remaining ^{14}N is again much smaller at 2.34 G. The two ^{1}H couplings have coupling constants of 2.58 G and 1.55 G. As in the $[2\text{-CN-py}]^{1-}$ case one of these couplings is larger than the smaller nitrogen coupling. The EPR results do not give any indication of which nuclei correspond with which coupling constant. DFT calculations have be conducted to aid in the assignment of the observed coupling constants (*vide infra*).

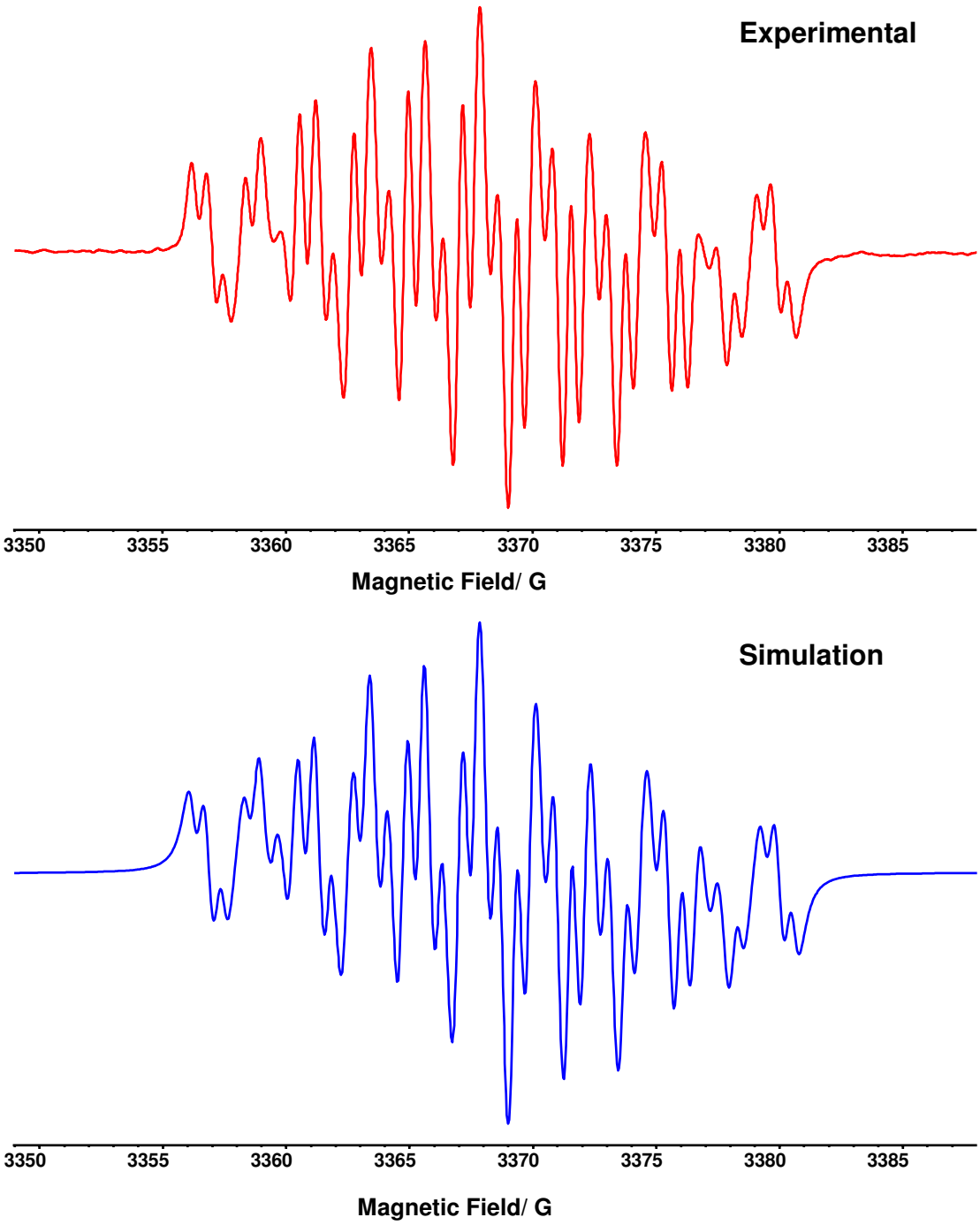

$A_{1\ ^{14}N}$ = 4.48 G
$A_{1\ ^{14}N}$ = 2.22 G
$A_{1\ ^{1}H}$ = 6.68 G
$A_{1\ ^{1}H}$ = 3.09 G
$A_{1\ ^{1}H}$ = 0.72 G
$A_{1\ ^{1}H}$ = 0.53 G
ΔH_{pp} = 0.49 G
L/G = 0
g_{iso} = 2.00372

Figure 3.14 Experimental and simulated EPR of $[2\text{-CN-py}]^{1-}$ generated *in-situ* at -2.2 V *vs*. Ag/AgCl at 233 K in 0.1 M $[TBA][BF_4]$/DMF

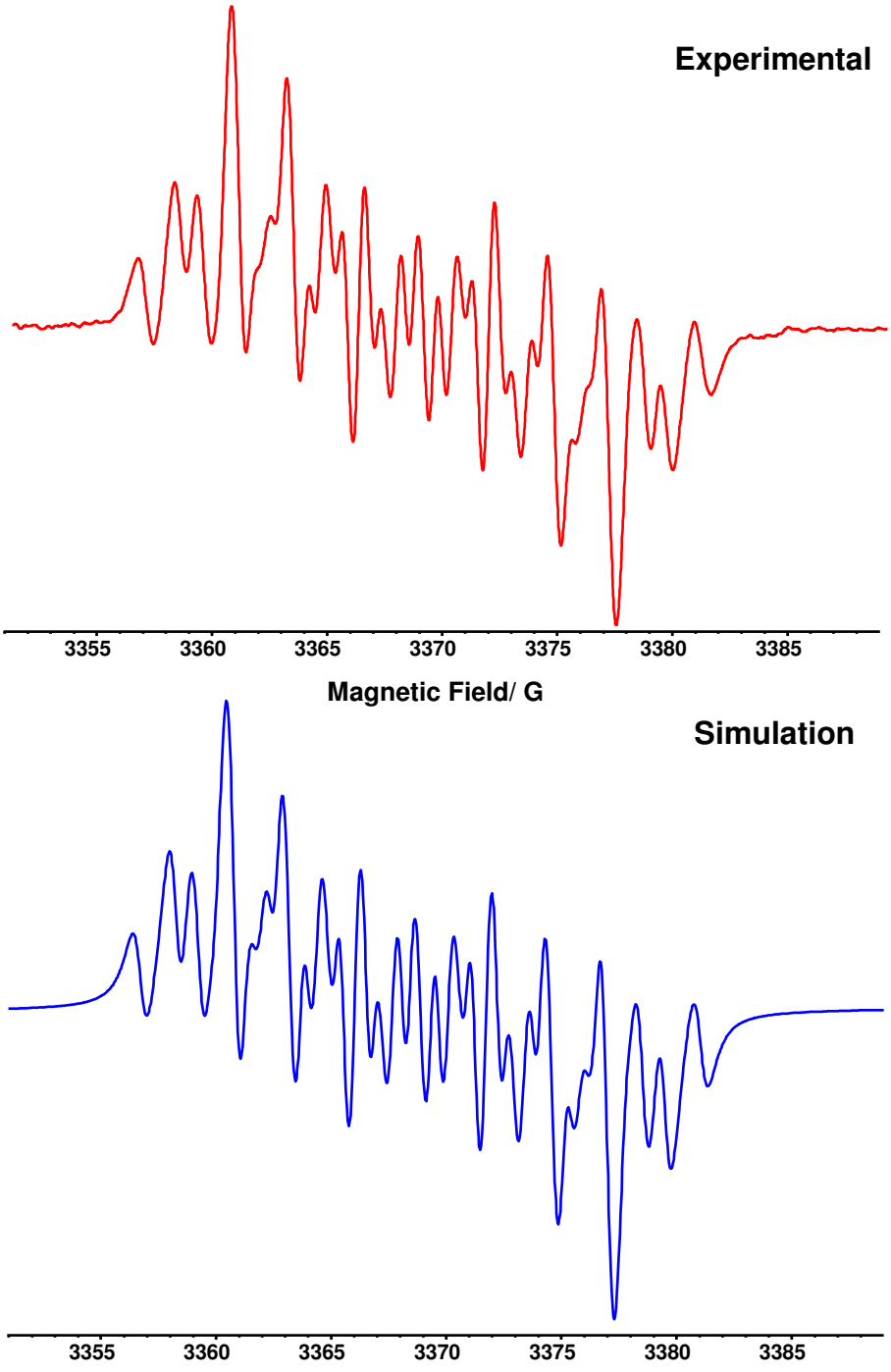

Figure 3.15 Experimental and simulated EPR of $[4\text{-CN-py}]^{1-}$ generated *in-situ* at -1.8 V *vs*. Ag/AgCl at 233 K in 0.1 M $[TBA][BF_4]$/DMF

3.3.2.1 Ultra Violet/Visible/Near Infra-Red Spectroelectrochemistry

The spectrum of the neutral complex $[Pt(4\text{-}CN\text{-}py)_2Cl_2]$ in 0.1 M $[TBA][BF_4]$/DMF at 233 K is shown in figure 3.16 and has two strong absorption bands at 35100 cm^{-1} (ε = 10700 M^{-1} cm^{-1}) and 30000 cm^{-1} (ε = 6700 M^{-1} cm^{-1}). The higher energy band is assigned to a π-π^* intraligand transition (shifted to lower energy upon bonding to the Pt(II) metal centre) and the lower energy band is attributed to a MLCT transition.

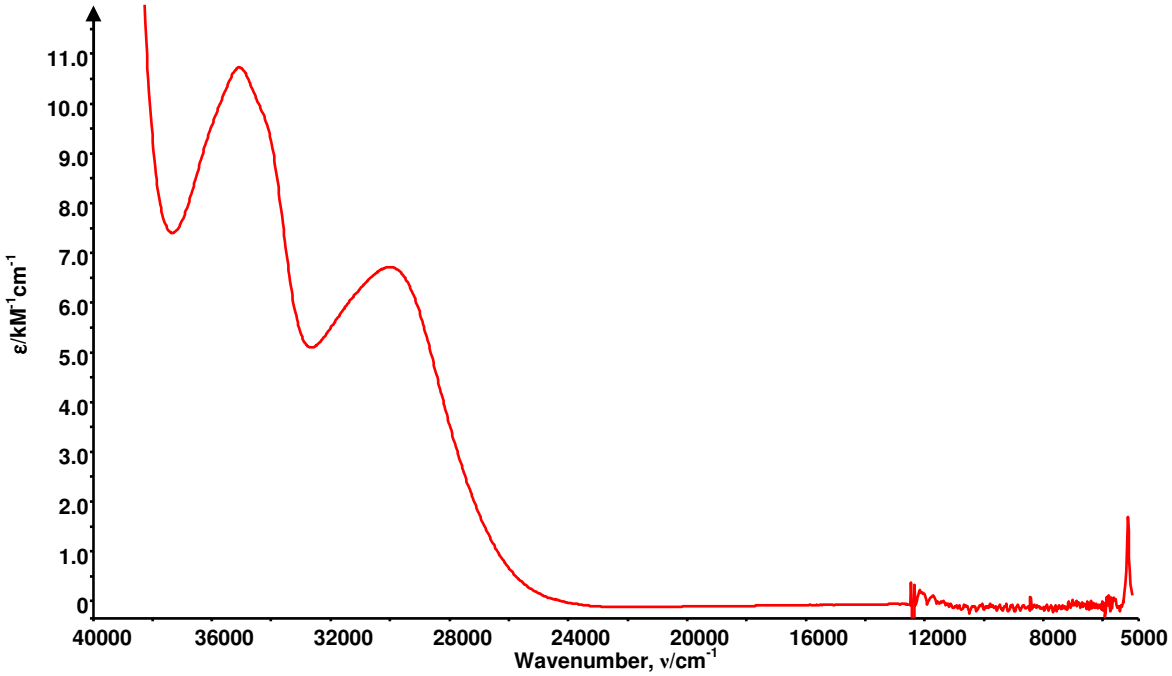

Figure 3.16 UV/Vis/NIR of $[Pt(4\text{-}CN\text{-}py)_2Cl_2]$ in 0.1 M $[TBA][BF_4]$/DMF at 233 K

A potential of -1.1 V was then applied to generate the mono-reduced compound $[Pt(4\text{-}CN\text{-}py)_2Cl_2]^{1-}$. The spectra collected during application of the generation potential for 140 minutes are shown in figure 3.17. The observed transitions for the non-reduced and mono-reduced species are summarised in table 3.9. Two strong bands are observed in the spectrum of $[Pt(4\text{-}CN\text{-}py)_2Cl_2]^{1-}$ at 36200 cm^{-1} (ε = 10900 M^{-1} cm^{-1}) and 31800 cm^{-1} (ε = 8800 M^{-1} cm^{-1}). The spectrum of the $[Pt(4\text{-}CN\text{-}py)_2Cl_2]^{1-}$ shows similarities to the spectrum of $[4\text{-}CN\text{-}py]^{1-}$ suggesting that the reduction electron enters a MO with a significant degree of character from the

4-CN-py ligand. In addition peaks associated with the neutral species, namely a π-π^* transition and a MLCT can also be observed. Thus the spectrum of $[Pt(4\text{-}CN\text{-}py)_2Cl_2]^{1-}$ supports the assignment of the reduced species as $[Pt(4\text{-}CN\text{-}py)^{1-}(4\text{-}CN\text{-}py)Cl_2]^{1-}$.

	Wavenumber (cm^{-1})	Extinction Coefficient ($M^{-1}cm^{-1}$)
$[Pt(4\text{-}CN\text{-}py)_2Cl_2]$	35100 30000	10700 6700
$[Pt(4\text{-}CN\text{-}py)_2Cl_2]^{1-}$	36000 31800	10900 8800

Table 3.9 Peak positions and extinction coefficients for signals in the UV/Vis/NIR spectra of $[Pt(4\text{-}CN\text{-}py)_2Cl_2]$ and $[Pt(4\text{-}CN\text{-}py)_2Cl_2]^{1-}$

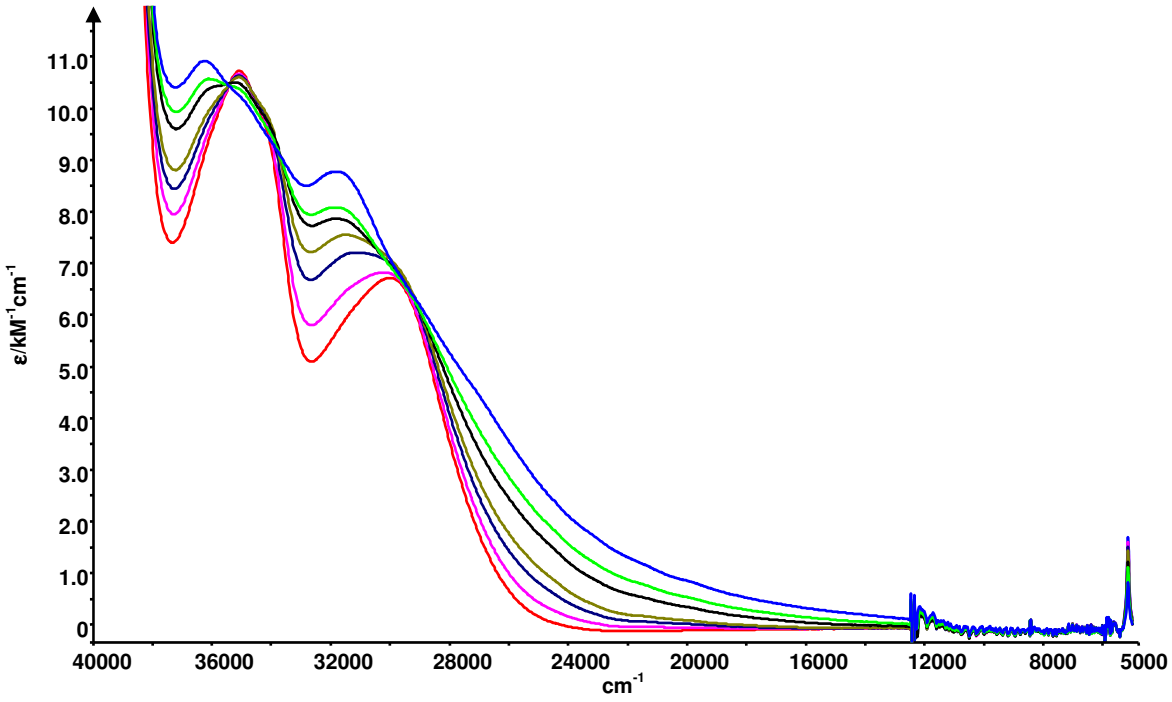

Figure 3.17 UV/Vis/NIR of $[Pt(4\text{-}CN\text{-}py)_2Cl_2]$ in 0.1 M $[TBA][BF_4]$/DMF at 233 K 140 minutes after a potential of -1.1 V *vs*. Ag/AgCl was applied. $[Pt(4\text{-}CN\text{-}py)_2Cl_2]$ red spectrum, $[Pt(4\text{-}CN\text{-}py)_2Cl_2]^{1-}$ blue spectrum

3.3.2.2 Electron Paramagnetic Resonance Spectroelectrochemistry

The EPR active $[Pt(4\text{-}CN\text{-}py)_2Cl_2]^{1-}$ species was generated *in-situ* with a generation potential of -1.35 V. The EPR spectrum recorded for the mono-reduced complex is

shown in figure 3.18. The spectrum consists of three main peaks, with the central peak being significantly more intense.

Simulation of the experimental spectrum was achieved by considering coupling to a single Pt nucleus. The two smaller intensity peaks arise from coupling of the unpaired electron to a ^{195}Pt nucleus with I = ½. The greater intensity central peak is due to molecules that contain one of the five isotopes of Pt that have I = 0, which comprise approximately 66% of the natural abundance. No coupling to any of the ligand nuclei is observed. This is likely to be due to the broad nature of the spectrum. The linewidth of 21.0 G would lead to any couplings to the lighter ligand nuclei being obscured. Attempts to further resolve the spectrum were unsuccessful. The observed ^{195}Pt hyperfine coupling constant of 53.0 G is in agreement with other analogous mono-reduced substituted pyridine Pt complexes.[4]

The ^{195}Pt coupling constants observed for a series of $[Pt(4\text{-}X\text{-}py)_2Cl_2]^{1-}$ complexes are given in table 3.10. Comparison of these values shows that as the electron withdrawing nature of the substituent group increases the magnitude of the ^{195}Pt coupling constant decreases. Therefore more electron density is being drawn away from the metal centre and onto the $[4\text{-}X\text{-}py]^{1-}$ lignad.

Substituent X	$[Pt(4\text{-}X\text{-}py)_2Cl_2]^{1-}$		Ref.
	g_{iso}	A_{iso} ^{195}Pt / cm^{-1}	
CO_2Me	2.0003	51.8×10^{-4}	4
CN	1.9997	49.5×10^{-4}	-
NO_2	2.0055	31.8×10^{-4}	4

Table 3.10 EPR hyperfine coupling constants for a series of $[Pt(4\text{-}X\text{-}py)_2Cl_2]^{1-}$ (where X = CO_2Me, CN and NO_2)

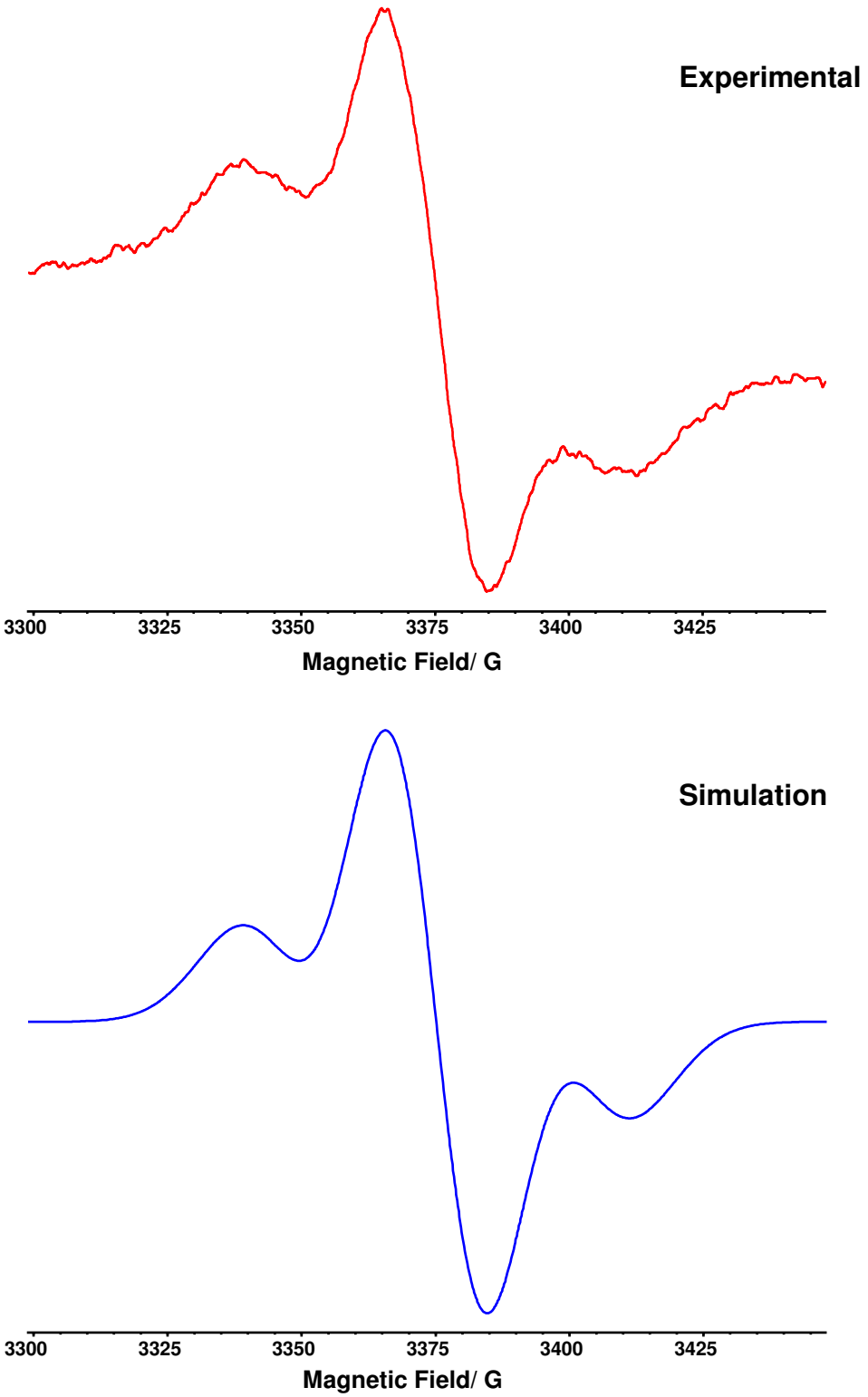

$A_{^{195}Pt}$ = 53.0 G

ΔH_{pp} = 21.0 G

L/G = 1

g_{iso} = 1.9997

Figure 3.18 Experimental and simulated EPR of $[Pt(4\text{-}CN\text{-}py)_2Cl_2]^{1-}$ generated *in-situ* at -1.35 V *vs*. Ag/AgCl at 233 K in 0.1 M [TBA][BF_4]/DMF

3.4 Calculations

In an attempt to gain a greater understanding of the electronic properties of the cyanopyridine compounds investigated in this work DFT calculations were conducted.

The optimised geometries calculated for the three cyanopyridines in their mono-reduced states are shown in figures 3.19-3.21. Also shown are the calculated SOMOs for each of these compounds. Examination of these orbitals can aid in the interpretation of the experimental results obtained from spectroelctrochemcial investigation of the mono-reduced species.

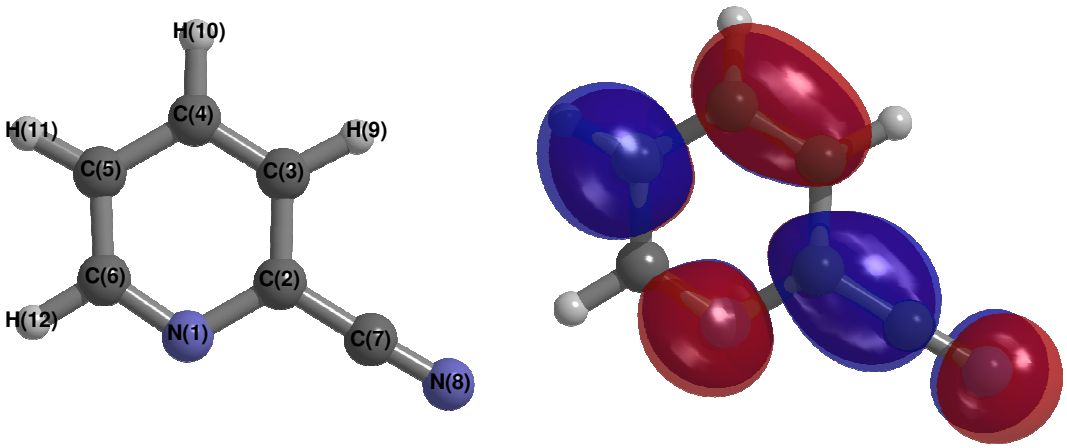

Figure 3.19 Optimised geometry and calculated SOMO of $[2\text{-CN-py}]^{1-}$

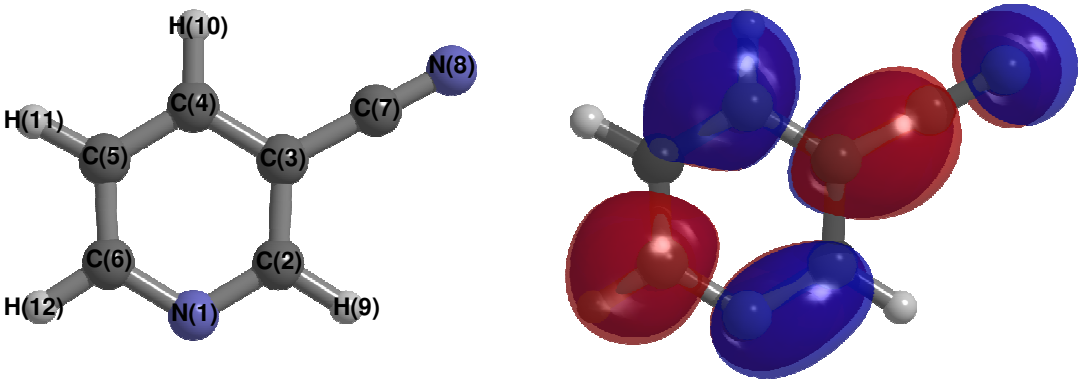

Figure 3.20 Optimised geometry and calculated SOMO of [3-CN-py]$^{1-}$

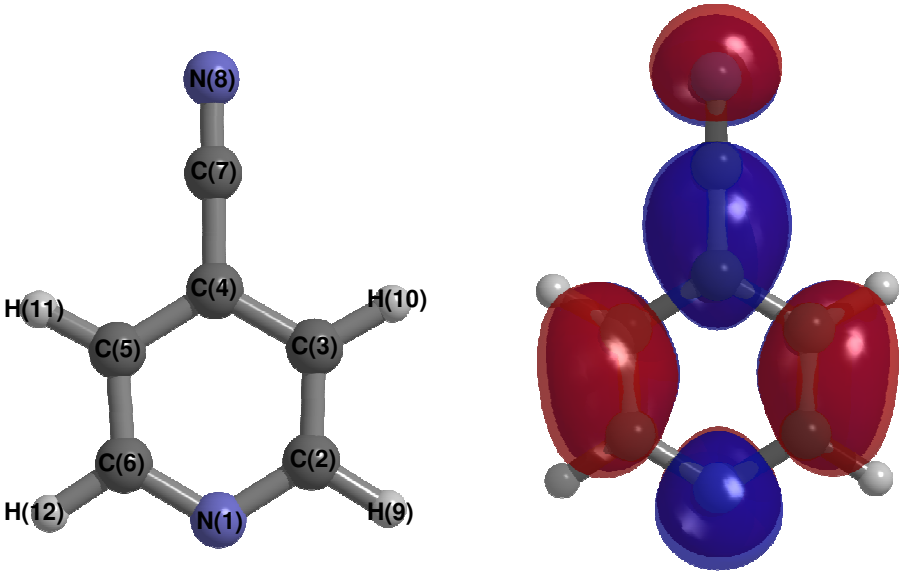

Figure 3.21 Optimised geometry and calculated SOMO of [4-CN-py]$^{1-}$

A quick comparison of the orbitals clearly shows that altering the positions of the cyano substituent has a significant effect on the distribution of electron density about the pyridine ring system. Given in table 3.11 are the breakdowns of the % occupations by atom for the SOMOs of the three mono-reduced cyanopyridines.

$[2\text{-CN-py}]^{1-}$ SOMO	
Atom	%
N(1)	13.40
C(2)	20.76
C(3)	3.17
C(4)	16.83
C(5)	30.48
C(6)	1.41
C(7)	3.79
N(8)	10.10
H(9)	0.01
H(10)	0.02
H(11)	0.04
H(12)	0.00

$[3\text{-CN-py}]^{1-}$ SOMO	
Atom	%
N(1)	7.91
C(2)	4.14
C(3)	25.57
C(4)	22.26
C(5)	0.84
C(6)	26.86
C(7)	3.36
N(8)	8.98
H(9)	0.00
H(10)	0.03
H(11)	0.00
H(12)	0.05

$[4\text{-CN-py}]^{1-}$ SOMO	
Atom	%
N(1)	14.97
C(2)	3.76
C(3)	10.63
C(4)	44.29
C(5)	10.63
C(6)	3.76
C(7)	6.08
N(8)	5.85
H(9)	0.01
H(10)	0.01
H(11)	0.01
H(12)	0.01

Table 3.11 The % occupations by atom for the SOMOs of 2-CN-py, 3-CN-py and 4-CN-py

It is observed that the amount of electron density localised onto the cyano substituent is affected by the positions of the group. It is noted that in each of the SOMOs there is a node between the carbon and nitrogen atoms of the cyano group.

This is suggestive of limited delocalisation within the substituent group. It is therefore of interest to examine the amount of electron density localised on the nitrogen atom of the substituent. It is noted that for the cyanopyridines the nitrogen atom contributes 5.85% - 10.10% to the SOMOs, with the largest contribution observed for the 2-cyanopyridine molecule.

As discussed in section 1.2, the most electronically important position in the pyridine ring system is the nitrogen atom. Accordingly it is of interest to study how altering the position of the substituent effects the distribution of electron density on this position. Comparison of the SOMOs for the three cyanopyridines indicates that the ring nitrogen contributes 7.91% - 14.97%, with the largest contribution observed for the 4-cyanopyridine.

Time-dependent density functional theory (TD-DFT) calculations were conducted in an attempt to gain further information about the UV/Vis/NIR spectroelectrochemical data collected for the 4-cyanopyridine compound. Shown in figure 3.22 is an overlay of the calculated and experimental UV/Vis/NIR spectra of 4-CN-py.

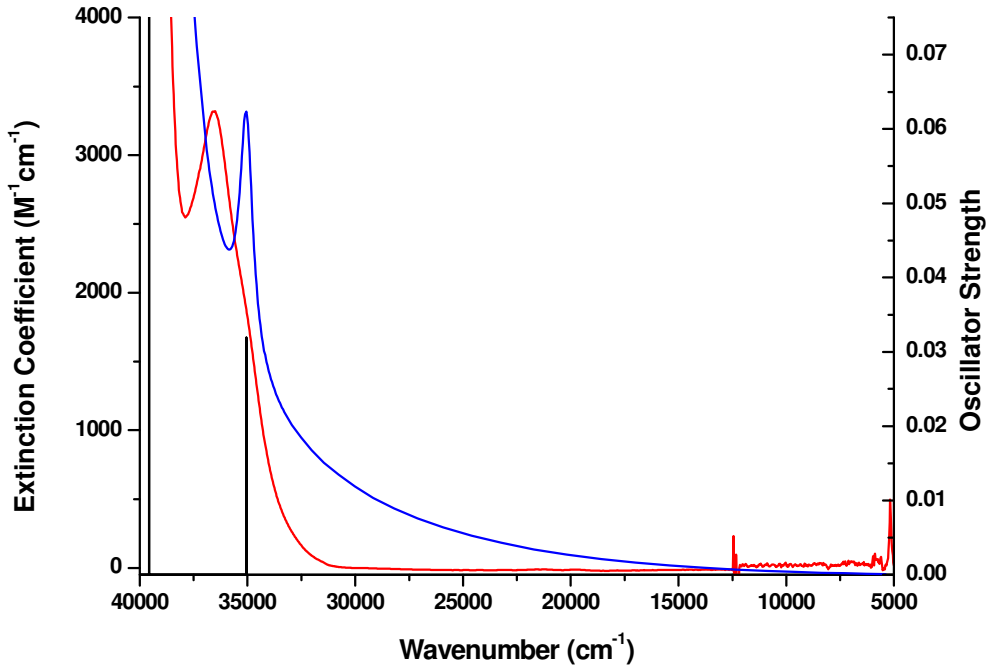

Figure 3.22 Overlay of the experimental UV/Vis/NIR spectrum (red) and the TD-DFT calculated spectrum (blue) of 4-CN-py. Calculated transitions are shown as black columns

When the spectra are compared it can be seen that the while the calculated spectrum matches the overall shape of the experimental data, there is a discrepancy in the energy of the transition. The calculated transition occurs at lower energy than observed in experiment. The experimental and calculated transitions observed in the UV/Vis/NIR spectrum of 4-CN-py are reported in table 3.12. Analysis of the transition in the calculated spectrum show that it is due to the HOMO-LUMO transition.

	Experimental		Calculation	
	Wavenumber (cm^{-1})	Extinction Coefficient ($M^{-1}cm^{-1}$)	Wavenumber (cm^{-1})	Osc. Strength
4-(CN)-py	36500	3300	35000	0.0029
$[4\text{-(CN)-py}]^{1-}$	36600	3400	38900	0.3308
	33100	2300	33900	0.1719
	29000	600	29600	0.0247
	26500	560	26600	0.0298
	25600	450		
	20000	60	18600	0.0052
	15600	20	13700	0.0005

Table 3.12 Transitions in the experimental and calculated UV/Vis/NIR spectra of 4-CN-py and $[4\text{-CN-py}]^{1-}$

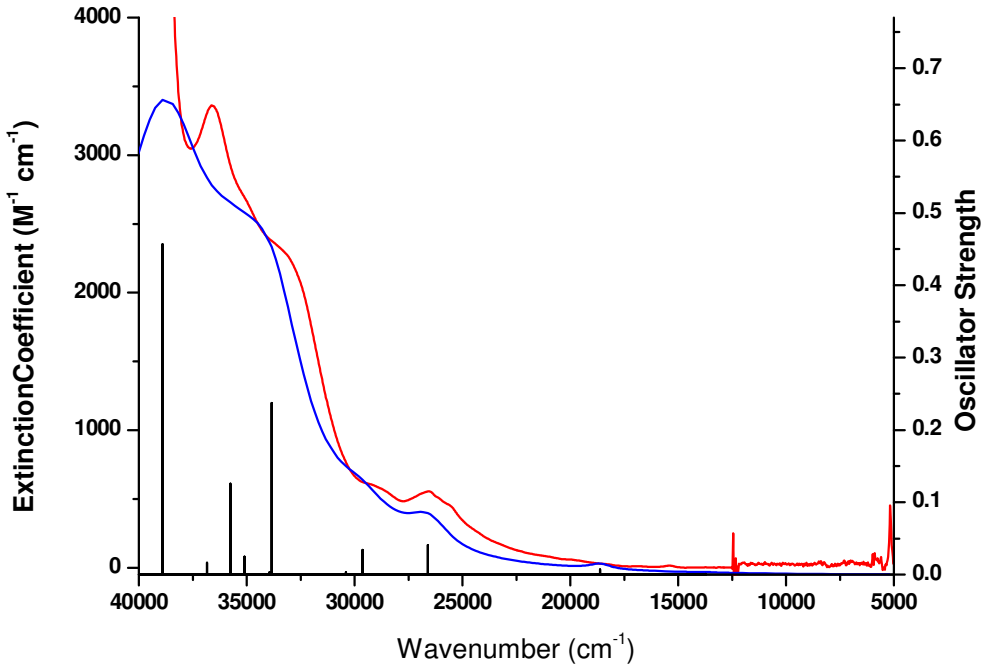

Figure 3.23 Overlay of the experimental UV/Vis/NIR spectrum (red) and the TD-DFT calculated spectrum (blue) of $[4\text{-CN-py}]^{1-}$. Calculated transitions are shown as black columns

Of more interest is the information that can be gained by applying this technique to the more complicated spectrum of the mono-reduced $[4\text{-CN-py}]^{1-}$ species. Shown in figure 3.23 is an overlay of the experimental and calculated spectra for this species.

Again comparison of the spectra indicates that the calculated spectrum matches the overall pattern of transitions observed in the experimental spectrum. However, it is noted that the calculation overestimates the energy of all the transitions. Shown in table 3.12 are the experimental and calculated transitions observed in the UV/Vis/NIR spectrum of the $[4\text{-CN-py}]^{1-}$ species.

Though the overall structure features of the experimental spectrum are reproduced accurately by the calculation is has failed to replicate the fine structure observed in some of the experimental peaks. This is possibly due to these features arising from vibrational coupling effects which cannot be accounted for in the TD-DFT calculation.

Analysis of the composition of the transitions in the calculated spectrum allows for the assignment of the bands observed in the experimental spectrum. It is of interest to note that the SOMO→LUMO transition can be assigned to the very low intensity band at 15600 cm^{-1} in the experimental spectrum. The first features in the experimental spectrum with any significant intensity are the bands around 26000 cm^{-1}. These features can be attributed to transitions from the SOMO to higher lying empty π^* orbitals. The intense band observed at 33100 cm^{-1} can be assigned to a transition from the HOMO-1→SOMO. This equates to the HOMO→LUMO transition in the 4-cyanopyridine species moving to lower energy upon reduction. The highest energy band at 36600 cm^{-1} can be assigned to transitions from the SOMO to very high energy π^* orbitals.

Calculations can be used in the same way to aid in the assignment of experimental EPR hyperfine coupling constants to specific nuclei in the paramagnetic species under investigation.

Shown in tables 3.13–3.15 are the hyperfine coupling constants calculated for the $[2\text{-CN-py}]^{1-}$, $[3\text{-CN-py}]^{1-}$ and $[4\text{-CN-py}]^{1-}$ species respectively.

$[2\text{-CN-py}]^{1-}$			
Coupling constant	**Experimental**	**Calculated**	**Assignment**
A(1 x ^{14}N) / G	**4.48**	**3.31**	**Ring ^{14}N**
A(1 x ^{14}N) / G	**2.22**	**2.12**	**Cyano ^{14}N**
A(1 x ^{1}H) / G	**6.68**	**7.76**	**5 position ^{1}H**
A(1 x ^{1}H) / G	**3.09**	**2.93**	**4 position ^{1}H**
A(1 x ^{1}H) / G	**0.72**	**0.99**	**6 position ^{1}H**
A(1 x ^{1}H) / G	**0.53**	**0.70**	**3 position ^{1}H**

Table 3.13 Experimental and calculated EPR hyperfine coupling constants for $[2\text{-CN-py}]^{1-}$

$[3\text{-CN-py}]^{1-}$		
Coupling constant	**Calculated**	**Assignment**
A(1 x ^{14}N) / G	**0.36**	**Ring ^{14}N**
A(1 x ^{14}N) / G	**1.85**	**Cyano ^{14}N**
A(1 x ^{1}H) / G	**10.48**	**6 position ^{1}H**
A(1 x ^{1}H) / G	**7.48**	**4 position ^{1}H**
A(1 x ^{1}H) / G	**1.68**	**5 position ^{1}H**
A(1 x ^{1}H) / G	**1.15**	**2 position ^{1}H**

Table 3.14 Calculated EPR hyperfine coupling constants for $[3\text{-CN-py}]^{1-}$

$[4\text{-CN-py}]^{1-}$			
Coupling constant	**Experimental**	**Calculated**	**Assignment**
A(1 x ^{14}N) / G	**5.70**	**4.49**	**Ring ^{14}N**
A(1 x ^{14}N) / G	**2.34**	**1.64**	**Cyano ^{14}N**
A(2 x ^{1}H) / G	**2.58**	**2.59**	**3,5 position ^{1}H**
A(2 x ^{1}H) / G	**1.55**	**1.61**	**2,6 position ^{1}H**

Table 3.15 Experimental and calculated EPR hyperfine coupling constants for $[4\text{-CN-py}]^{1-}$

Comparison of the experimental and calculated coupling constants for the $[2\text{-CN-py}]^{1-}$ and $[4\text{-CN-py}]^{1-}$ species indicate that the calculations have been able to effectively replicate the pattern of coupling constants observed experimentally. By comparing the

magnitude of the calculated and experimental hyperfine coupling constants it is possible to make assignment of coupling to specific nuclei.

Though no experimental results are available for the $[3\text{-CN-py}]^{1-}$ species due to the instability of the mono-reduced species, calculations can be used to get an idea of the what the hyperfine coupling constants would be like if they could be observed.

Through analysis of these calculations it is possible to solve the problem of differentiating the two observed ^{14}N couplings, which is not possible from experimental data alone. For the $[4\text{-CN-py}]^{1-}$ compound the calculations indicate that the larger of the ^{14}N couplings is due the ring nitrogen atom rather than nitrogen of the electron withdrawing cyano substituent. This in accordance with what was found when the SOMO of the species was examined. This suggests that while the electron withdrawing substituent affects the electronic character of the molecule the electronics are still dominated by the pyridine ring system.

Examination of the ^{1}H couplings constants indicates that the larger of the two couplings is due to the hydrogen atoms in the 3 and 5 positions of the pyridine ring while the smaller coupling is due to the hydrogen atoms in the 2 and 6 positions. This indicates that while the ring nitrogen remains more electronically important than the nitrogen of the cyano group a significant amount of electron density is drawn to the other side of the ring system by the electron withdrawing nature of the cyano substituent.

While the pattern of couplings observed for the $[2\text{-CN-py}]^{1-}$ species is more complicated due to the fewer number of equivalent nuclei, useful information about

the distribution of electron density can be obtained from the calculations. As with the $[4\text{-CN-py}]^{1-}$ species the calculations can be used to differentiate between the two ^{14}N couplings. Once again the calculations show that the larger of the two couplings arises from the ring nitrogen and the smaller from the cyano group nitrogen.

The largest coupling observed in this species is due to coupling to a ^{1}H nucleus. The calculations can be used to assign this to the hydrogen atom in the 5 position in the pyridine ring. The second largest of the ^{1}H couplings can be assigned to the hydrogen atom in the 4 position. Assignment of the remaining two ^{1}H couplings proves more difficult. When a comparison of the experimental and calculated coupling constants for the two remain ^{1}H nuclei is conducted it is noted that the difference in magnitude is small. A rough assignment based upon these coupling are that the larger of the two is due to the hydrogen atom in the 6 position and the smaller the hydrogen atom in the 3 position.

When the calculated coupling constants for the $[3\text{-CN-py}]^{1-}$ species are examined it can be seen that the calculated couplings differ quite dramatically from the patterns observed in the other two species. One of the ^{14}N couplings calculated for this species is significantly smaller than observed in the other species. In this species the smaller of the two ^{14}N couplings is due to the ring nitrogen atom rather than the cyano group nitrogen. The coupling constant observed for the cyano group nitrogen is of a similar size to those predicted for the other two species.

The ^{1}H couplings observed in this species are much larger then for either of the other two species. The largest coupling of 10.48 G is assigned to the hydrogen atom in the 6

position of the pyridine ring. This is in direct contrast to the other species which have very little electron density on the 6 position of the ring. Thus the very different electronic character of the $[3\text{-CN-py}]^{1-}$ compared to 2- and 4- analogues may explain the chemical instability of the $[3\text{-CN-py}]^{1-}$ species.

3.5 Conclusion

It has been determined in this study that substitution with the cyano group at different positions around the pyridine ring has a significant effect on the electrochemical properties of the ligands studied. The evidence suggest that substitution at the two and four positions, *ortho* and *para* to the ring nitrogen respectively, stabilises the reduction of the ligand, making it less negative compared to py and 3-CN-py. The substitution at the 4 position is more favoured due to its reduction being much less negative than that for 2-CN-py. The separation between these two reductions is approximately 0.18 V. In comparison, substitution at the 3 position, *meta* to the ring nitrogen is not stabilised. This leads to the ligand having a quasi-reversible reduction at a more negative potential than the other ligands studied.

The Pt complex $[Pt(4\text{-CN-py})_2Cl_2]$ may be reduced at less negative potentials than the free ligand, and the UV/Vis/NIR spectroelectrochemical study of the mono-reduced species indicates that the reduction electron is sited on one 4-CN-py ligand. TD-DFT calculations are in agreement with experiment and aid in the assignment of the electronic transitions in the UV/Vis/NIR spectra. EPR parameters from the DFT calculations are qualitatively in good agreement with experiment and can be used to assign coupling constants to specific nuclei.

3.6 References

1. P. R. Murray, L. Jack, E. J. L. McInnes, L. J. Yellowlees, *Dalton Trans.*, 2010, **39**, 4179-4185

2. L. Jack, Ph.D Thesis, University of Edinburgh, 2003.

3. P. R. Murray, Ph.D Thesis, University of Edinburgh, 2006.

4. L. P. Moorcraft, Ph.D Thesis, University of Edinburgh, 2008.

5. M. Itoh, T. Okamoto, S. Nagakura, *Bull. Chem. Soc. Jpn.*, 1963, **36**, 1665-1672.

6. R. O. Loutfy, R. O. Loutfy, *Can. J. Chem.*, 1973, **51**, 1169-1171.

4 Electrochemical and Spectroelectrochemical Characterisation Of 3,3´-$(CN)_2$-bpy, 4,4´-$(CN)_2$-bpy and 5,5´-$(CN)_2$-bpy

4.1 Introduction

Previous investigations into the effect of substitution on the electronic properties of bpy have concentrated mainly on weakly electron withdrawing groups such as CO_2Et.[1] It was found that substitution with these groups did not perturb the overall electronic structure of the bpy ring system significantly. UV/Vis/NIR and EPR spectroelectrochemical investigations determined that the frontier orbital of these compounds is primarily based on the bpy rings of the molecule.

In contrast when the highly electron withdrawing NO_2 substituent was investigated it was found that the electronic properties of the molecule was dominated by the nature of the substituent. UV/Vis/NIR and EPR spectroelectrochemical investigations of 3,3´-$(NO_2)_2$-bpy and 5,5´-$(NO_2)_2$-bpy determined that the frontier orbital of these compounds is primarily based on the nitro substituent groups.[2] Of particular note is the unusual character exhibited by 4,4´-$(NO_2)_2$-bpy. UV/Vis/NIR and EPR spectroelectrochemical investigations of this compound indicated that the frontier orbital was localised to a single NO_2-py ring.[3,4] Upon di-reduction the electron entered a higher energy orbital to form a paramagnetic triplet state, with each electron localised to a NO_2-py unit, rather than spin pairing to form a diamagnetic di-reduced species like all other substituted bpy investigated.[3,4]

It is therefore of interest to examine what effect a substituent group with electron withdrawing properties between the two groups studied to date would have upon the electronic character of the bpy ring system. The cyano group is a prime candidate for such an investigation. Shown in table 4.1 are the Hammett parameters for these three groups along with the corresponding Resonance and Field/Inductive parameters. When the F parameters are compared it can be seen that these increase significantly going from the CO_2Et to NO_2. In contrast there is little change in the R parameter with the cyano substituent having the strongest effect.

	σ_m	σ_p	F	R
CO_2Et	**0.37**	**0.45**	**0.34**	**0.11**
CN	**0.56**	**0.66**	**0.51**	**0.15**
NO_2	**0.71**	**0.78**	**0.65**	**0.13**

Table 4.1 Hammett parameters, Field/Inductive parameters and Resonance parameters for CO_2Et, CN and NO_2 substituent groups[5]

This chapter details the electrochemical and spectroelectrochemical (UV/Vis/NIR, EPR) study of the dicyano substituted bpy ligands, 3,3´-$(CN)_2$-bpy, 4,4´-$(CN)_2$-bpy and 5,5´-$(CN)_2$-bpy.

The X-ray crystal structure of 3,3´-$(CN)_2$-bpy determined by Baxter *et al.* is shown in figure 4.1.[6] The unit cell is triclinic with a = 3.82 Å, b = 10.14 Å, c = 12.78 Å, α = 99.1° β = 91.0° and γ = 98.4°. The space group is $P\bar{1}$ and there are two molecules per unit cell. The 3,3´-$(CN)_2$-bpy molecule can be seen to adopt a roughly *trans* conformation. The C(2)-C(2´) bond length is 1.48 Å which is slight shorter than the value of 1.50 Å observed for the equivalent C-C bond in bipyridine.[7]

The two substituted pyridine rings are twisted away from coplanarity, with a N(1)-C(2)-C(2´)-N(1´) torsional angle of 156.4°.[6] The resulting angle between the ring planes of 23.6° is significantly larger than that observed for unsubstituted bpy.[7]

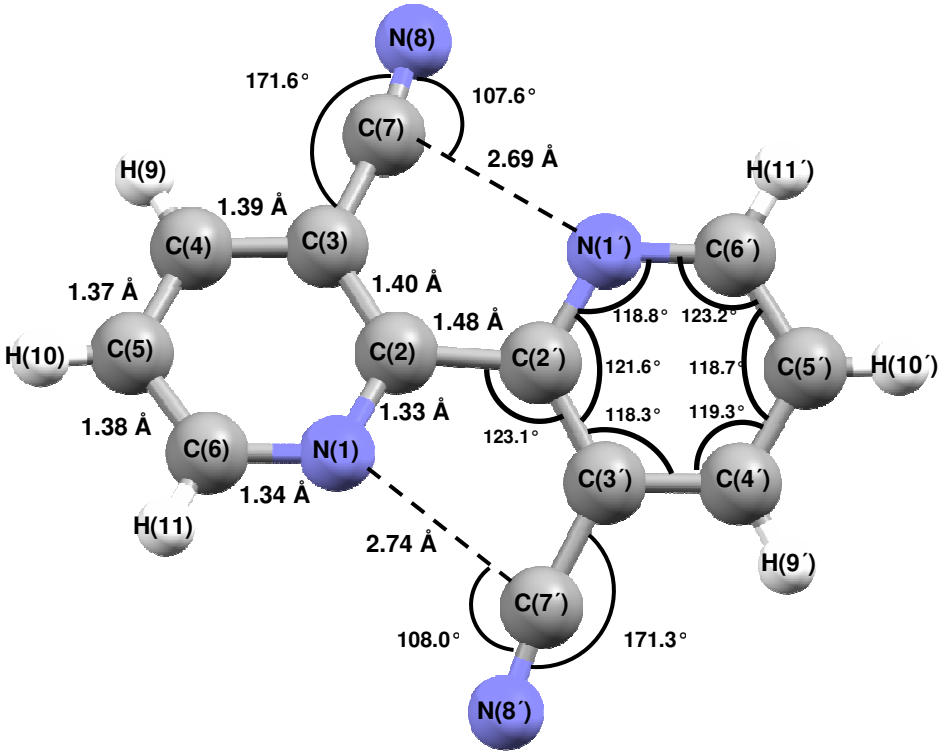

Figure 4.1 Crystal structure of 3,3´-$(CN)_2$-bpy as determined by Baxter *et al.*[6]

Baxter *et al*. attributed this to attractive N· · ·C interactions between the pyridine ring nitrogen atoms and the carbon atoms of the cyano group on the opposing ring. The N(1) · · ·C(7´) and N(1´) · · ·C(7) distances (2.74 Å and 2.69 Å respectively) are considerably shorter than the sum of the corresponding van der Waals radii (3.2 Å).[6] These interactions cause the C-C≡N groups to bow away from linearity by approximately 8.5° such that the central sp carbon atom is moved closer to the opposing ring nitrogen atom.

The N(1)-C(7´)-N(8´) and N(1´)-C(7)-N(8) angles are both very close to 108°. Baxter *et al*. proposed that this angle is the most favourable mutual orientation for these groups and that the 3,3´-$(CN)_2$-bpy molecule adopts a structure that optimises the angle of approach of the pyridine nitrogen atom to the cyano group.[6]

4.2 Electrochemistry

4.2.1 Cyclic Voltammetry

The cyclic voltammogram of 3,3´-$(CN)_2$-bpy in 0.1 M [TBA][BF_4]/DMF at 298 K, shown in figure 4.2, has two sequential one-electron reversible reductions with $E_{½}$ = -1.34 V and -1.97 V. A plot of i_p *vs*. $v^{½}$ gives a linear relationship for both of the redox processes. This indicates that both of the electron transfer processes are diffusion controlled.

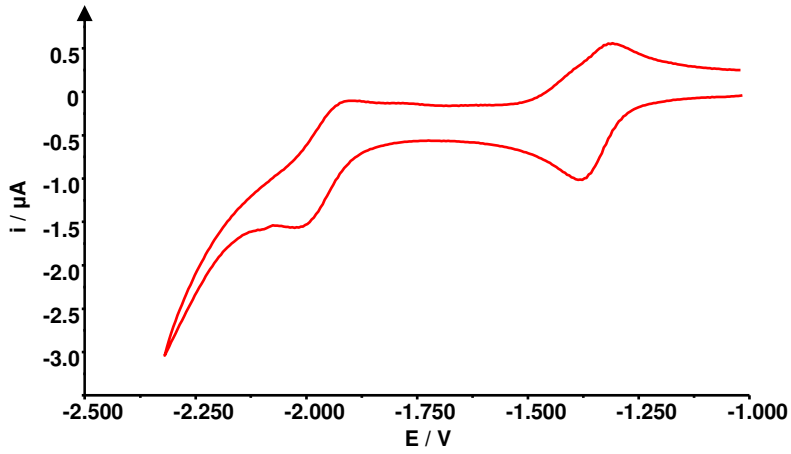

Figure 4.2 Cyclic Voltammetry of 3,3´-$(CN)_2$-bpy *vs*. Ag/AgCl in 0.1 M [TBA][BF_4]/DMF at 298 K, v = 100 mVs^{-1}

The separation between the two redox processes in 3,3´-$(CN)_2$-bpy, $\Delta E_{½}$, was found to be 630 mV. A value of this size indicates that the second reduction is a spin pairing process. This is corroborated by the EPR spectrocelectrochemistry results for this system (see section 4.3.2), with the first reduction giving rise to a paramagnetic

species whereas addition of the second reduction electron leads to collapse of the EPR signal and generation of a diamagnetic dianion.

By contrast when the cyclic voltammogram of 4,4´-$(CN)_2$-bpy in 0.1 M [TBA][BF_4]/DMF at 298 K was conducted, one fully reversible reduction was observed, figure 4.3. The $E_{½}$ value for the process is -1.48 V. A plot of i_p *vs*. $v^{½}$ for the redox process reveals a linear relationship, indicating that the electron transfer reaction is diffusion controlled. No second reduction process could be observed in the solvent window.

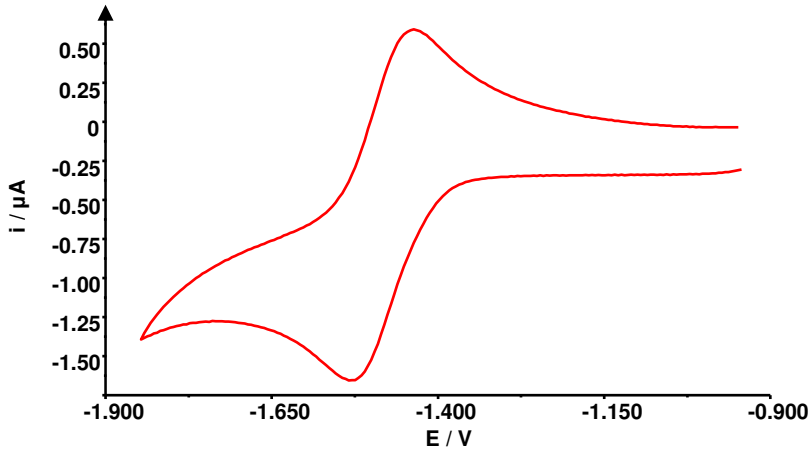

Figure 4.3 Cyclic Voltammetry of 4,4´-$(CN)_2$-bpy *vs*. Ag/AgCl in 0.1 M [TBA][BF_4]/DMF at 298 K, ν = 100 mVs^{-1}

The cyclic voltammogram for 5,5´-$(CN)_2$-bpy in 0.3 M [TBA][BF_4]/DMF at 298 K shown in figure 4.4 indicates that it also had two reversible reduction peaks, with $E_{½}$ values of -1.08 V and -1.61 V. A plot of i_p *vs*. $v^{½}$ for both redox processes gives linear relationships. This indicates that both of the redox processes are diffusion controlled.

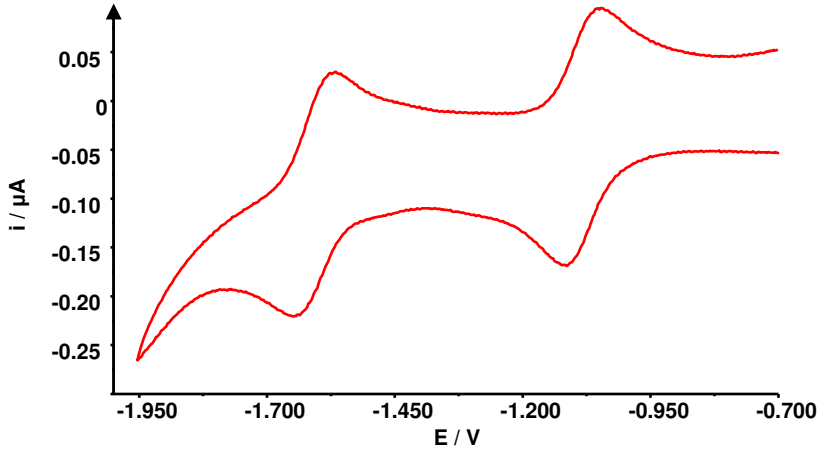

Figure 4.4 Cyclic Voltammetry of 5,5´-$(CN)_2$-bpy *vs*. Ag/AgCl in 0.3 M [TBA][BF_4]/DMF at 298 K, ν = 100 mVs^{-1}

The separation between the two reduction reactions in 5,5´-$(CN)_2$-bpy, $\Delta E_{½}$, was found to be 530 mV. Again a value of this size indicates that the second reduction is a spin pairing process. EPR spectroelectrochemical investigations of this compound support these findings (see section 4.3.2), with a paramagnetic monoanion and a diamagnetic dianion.

The reduction potentials observed in the cyclic voltammetric investigation of the three dicyanobipyridine ligands are shown in table 4.2. Comparison of the potentials for the first reductions in each of the compounds clearly shows that the 5,5´-$(CN)_2$-bpy ligand is reduced at significantly less negative potentials than either the 3,3´- or 4,4´-substituted analogs. The 4,4´-$(CN)_2$-bpy ligand exhibits the most negative reduction potential and thus substitution in this position results in the least stabilisation of the reduction electron.

	$E_{½,(1)}$ / V	$E_{½,(2)}$ / V
3,3´-$(CN)_2$-bpy	**-1.34**	**-1.97**
4,4´-$(CN)_2$-bpy	**-1.48**	–
5,5´-$(CN)_2$-bpy	**-1.08**	**-1.61**

Table 4.2 Half wave reduction potentials for 3,3´-$(CN)_2$-bpy, 4,4´-$(CN)_2$-bpy and 5,5´-$(CN)_2$-bpy

The second reduction process for the 5,5´-$(CN)_2$-bpy ligand is again at significantly less negative potential than the corresponding process in 3,3´-$(CN)_2$-bpy. In addition the $\Delta E_{½}$ for the first and second reduction of 5,5´-$(CN)_2$-bpy is approximately 100 mV smaller than the $\Delta E_{½}$ value for the 3,3´ ligand. These two findings support the assumption that reduction of the 5,5´ substituted ligand is the most stabilised.

Plots of the Hammett parameter $\sigma_{p,}$ *vs*. the first reduction potential of a series of substituted bipyridines including the 4,4´ and 5,5´ dicyanobipyridines investigated during these studies, are shown in figure 4.5 and figure 4.6, in order to establish if the

cyano substitution group follows the previously determined correlation observed for the 4,4´-$(X)_2$-bpy and 5,5´-$(X)_2$-bpy ligands (see section 1.2).

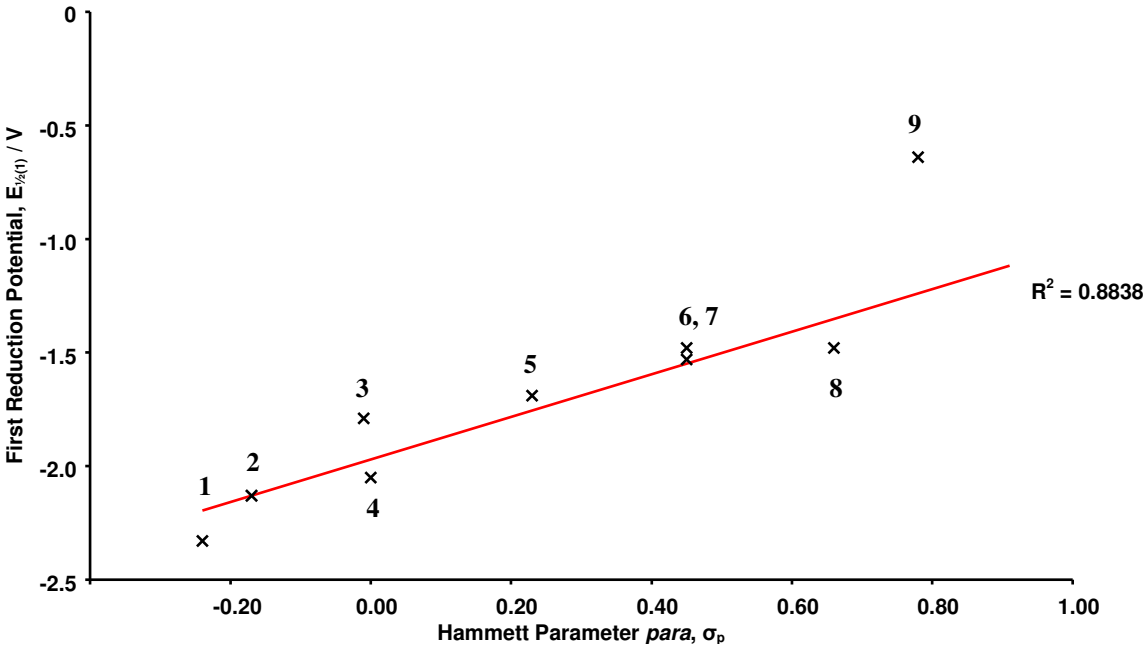

Figure 4.5 Plot of $E_{½}$ of the first reduction of 4,4´-$(X)_2$-bpy *vs.* para Hammett parameter, σ_p of the substituent X, (were X is the substituent under investigation). 1) X = OEt, 2) X = Me, 3) X = Ph, 4) X = H, 5) X = Cl, 6) X = CO_2Me, 7) X = CO_2Et, 8) X = CN, 9) X = NO_2 (4,4´-($NO_2)_2$-bpy data excluded from the linear fit due to the unusual properties of this compound)[3]

From figure 4.6 it can be seen that the $E_{½,(1)}$ of the 5,5´-$(CN)_2$-bpy ligand gives a good agreement with the predicted correlation with σ_p, the linear fit having a R^2 value of 0.9363. This value is reduced slightly from the plot in figure 1.8 but does not represent a marked departure from the previously observed correlation.

Conversely the 4,4´-$(CN)_2$-bpy ligand gives a significantly poorer agreement with the predicted correlation with σ_p; the R^2 value for the linear fit has reduced from 0.9084 in figure 1.6 to 0.8838 in figure 4.5. This indicates that the cyano substituent group does not play such a prominent role in stabilising the LUMO of the 4,4´-$(CN)_2$-bpy ligand as previous investigations would suggest.

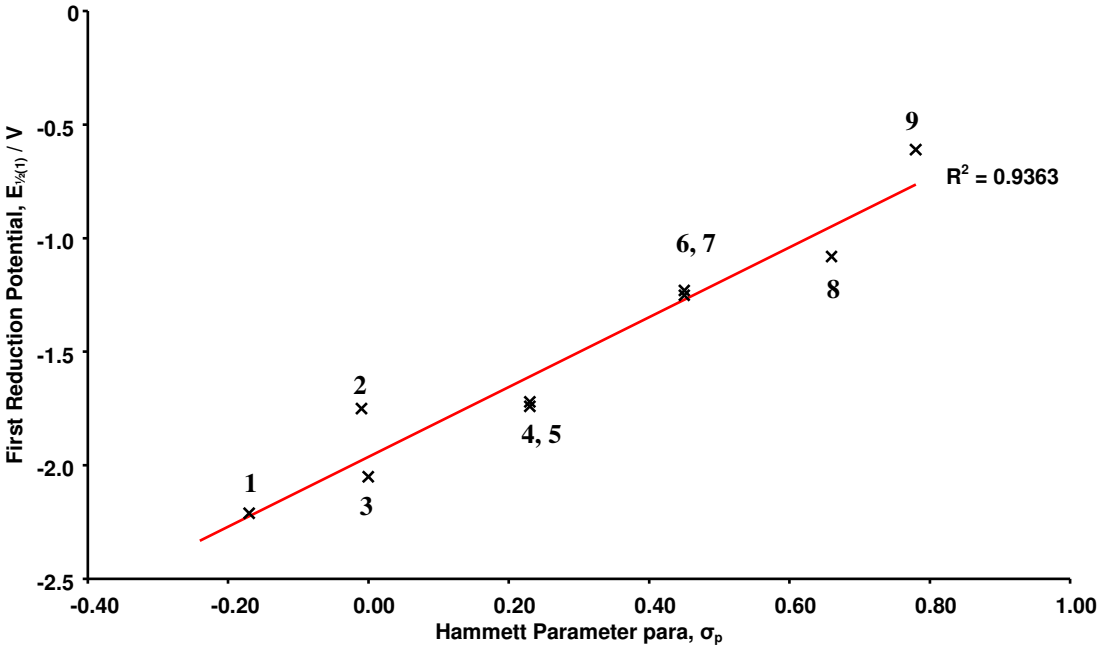

Figure 4.6 Plot of $E_{½}$ of the first reduction of 5,5´-$(X)_2$-bpy *vs.* para Hammett parameter, σ_p of the substituent X, (were X is the substituent under investigation). 1) X = Me, 2) X = Ph, 3) X = H, 4) X = Cl, 5) X = Br, 6) X = CO_2Me, 7) X = CO_2Et, 8) X = CN, 9) X = NO_2

4.2.2 Differential Pulse Voltammetry

As with the analogous X-CN-py ligand the three X,X´-$(CN)_2$-bpy ligands were also investigated by differential pulse voltammetry to corroborate the findings from the CV investigation. The differential pulse voltammograms for 3,3´-$(CN)_2$-bpy and 5,5´-$(CN)_2$-bpy confirmed the findings from the cyclic voltammatry, indicating that both compounds had two reversible reductions. The reduction potentials for these processes and the $\Delta E_{½}$ values are given in table 4.3 The DP voltammogram of 5,5´-$(CN)_2$-bpy is shown in figure 4.7.

	$E_{½,(1)}$ / V	$E_{½,(2)}$ / V
3,3´-$(CN)_2$-bpy	**-1.34**	**-1.97**
4,4´-$(CN)_2$-bpy	**-1.48**	**–**
5,5´-$(CN)_2$-bpy	**-1.08**	**-1.61**

Table 4.3 Half wave reduction potentials for 3,3´-$(CN)_2$-bpy, 4,4´-$(CN)_2$-bpy and 5,5´-$(CN)_2$-bpy

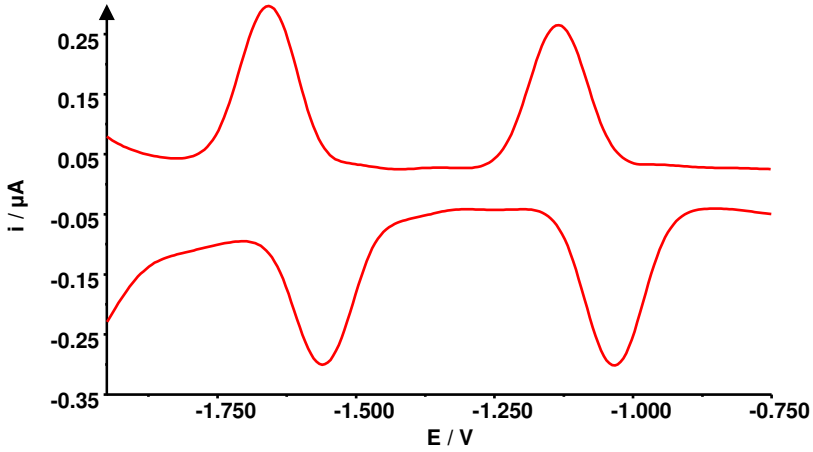

Figure 4.7 Differential Pulse Voltammogram of 5,5´-$(CN)_2$-bpy in 0.3M [TBA][BF_4]/DMF at 298 K

When the differential pulse voltammetry of 4,4´-$(CN)_2$-bpy was conducted it was observed that in addition to the one reduction peak expected, $E_{½}$ = -1.51 V, there were two additional redox processes observed with $E_{½}$ values of -0.94 V and -1.79 V. It is proposed that these peaks are due to the decomposition of the 4,4´-$(CN)_2$-bpy compound in DMF. In an attempt to confirm this, the experimental set up was left for thirty minutes and the differential pulse voltammogram run again. The overlay of these two scans is shown if figure 4.8. From this it is clear that the peak corresponding to the reduction in the DP voltammogram decreases in intensity with time while the two new peaks increase in intensity. Thus it is concluded that the 4,4´-$(CN)_2$-bpy ligand is unstable in DMF over a relatively long time scale and therefore a different solvent would be needed for spectroelectrochemical investigations. No attempts were made to identify the species responsible for the additional peaks in the differential pulse voltammogram.

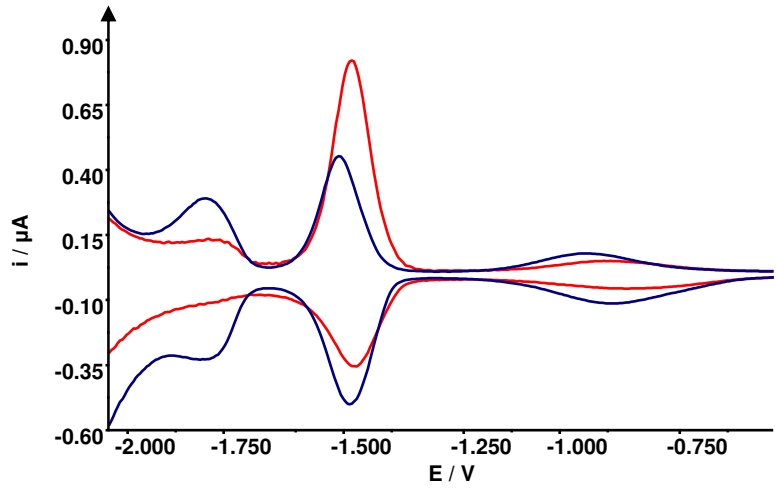

Figure 4.8 Differential Pulse Voltammogram of 4,4´-$(CN)_2$-bpy in 0.1M [TBA][BF_4]/DMF at 298 K (red t= 0 min, blue t = 30 min)

Accordingly the DPV scan of 4,4´-$(CN)_2$-bpy was repeated in 0.3 M [TBA][BF_4]/THF. Initial scans of the system gave a single reduction peak at $E_{½}$ -1.54 V. After ninety minutes the DPV scan was repeated and no additional peaks were observed. It was concluded that the 4,4´-$(CN)_2$-bpy ligand was sufficiently stable in this solvent system for it to be used for spectroelctrochemical investigations.

4.3 Spectroelectrochemistry

4.3.1 Ultra Violet/Visible/Near Infra-Red Spectroelectrochemistry

The UV/Vis/NIR spectrum of 3,3´-$(CN)_2$-bpy in 0.3 M [TBA][BF_4]/DMF at 233 K before a potential was applied is shown in figure 4.9. From the spectrum it can be seen that there is one broad shoulder at approximately 36000 cm^{-1} ($\varepsilon \approx 6200$ $M^{-1}cm^{-1}$) that traverses the solvent background. The peak is assigned to a HOMO-LUMO π-π^* transition.

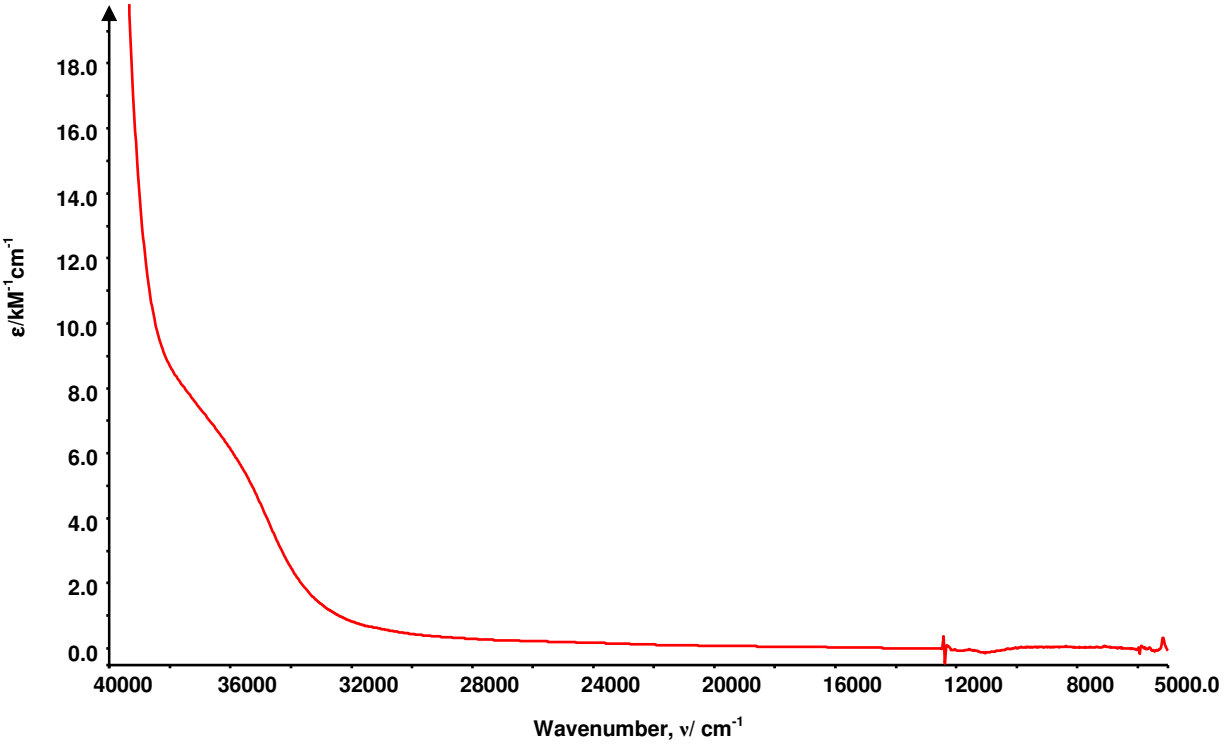

Figure 4.9 UV/Vis/NIR of 3,3´-$(CN)_2$-bpy in 0.3 M [TBA][BF_4]/DMF at 233 K

A potential of -1.5 V was then applied to the system to generate the mono-reduced $[3,3´\text{-}(CN)_2\text{-bpy}]^{1-}$ species. Figure 4.10 shows the spectra of the system during the reduction at -1.5 V.

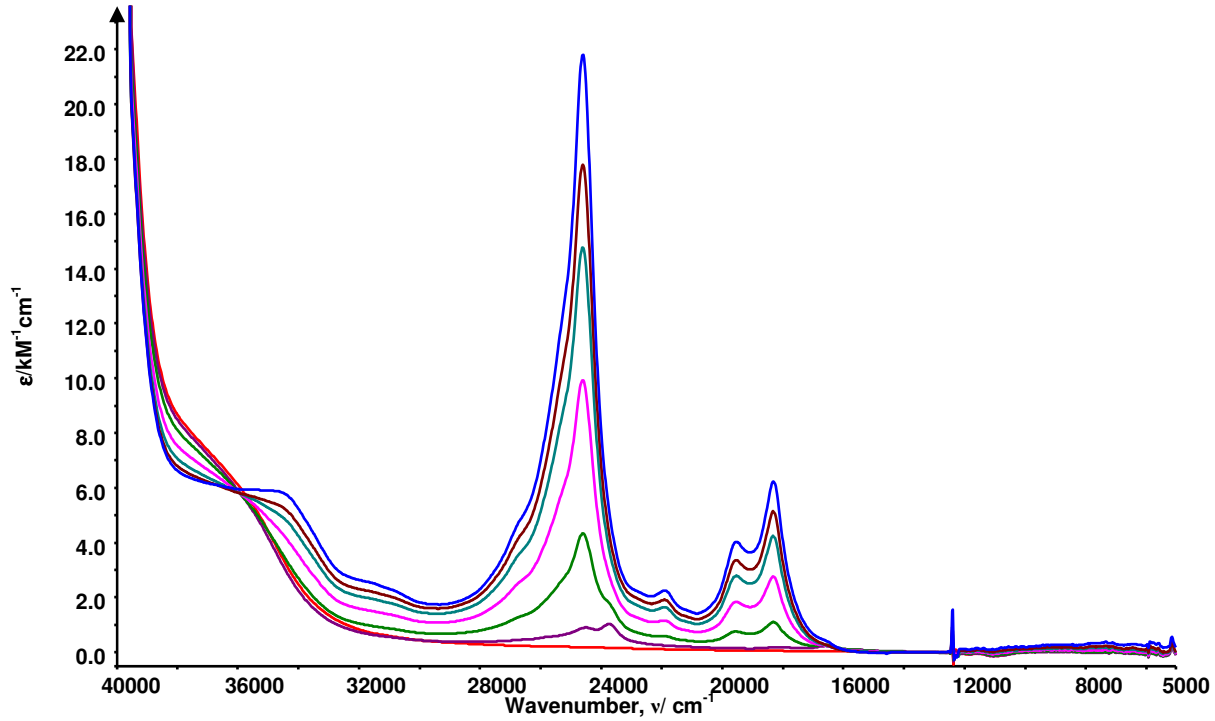

Figure 4.10 UV/Vis/NIR of 3,3´-$(CN)_2$-bpy in 0.1 M [TBA][BF_4]/DMF at 233 K 120 minutes after a potential of -1.5 V *vs*. Ag/AgCl was applied. Initial spectrum red, final spectrum blue

By comparing figure 4.9 and figure 4.10 the changes in absorption character of the compound can be clearly seen. The broad absorbance signal that was present in the initial spectrum loses intensity and a series of new peaks grow in during the electrogeneration experiment. The position and extinction coefficient of these peaks are given in table 4.4. That these peaks are not present in the initial spectrum before the potential is applied and continue to increase until the point of maximum growth is a clear indication that these peaks correspond to the $[3,3´\text{-}(CN)_2\text{-}bpy]^{1-}$ species. When the generation potential was switched back to 0 V the original spectrum was regenerated, indicating that the reduction is reversible. Note the isosbestic point at 35900 cm^{-1} indicating a clean conversion of the neutral starting material to the monoanion.

	Wavenumber (cm^{-1})	Extinction Coefficient ($M^{-1}cm^{-1}$)
3,3'-$(CN)_2$-bpy	**36000**	**6200**
$[3,3'\text{-}(CN)_2\text{-}bpy]^{1-}$	**34600**	**5800**
	26600	**4900**
	24600	**21800**
	21900	**2200**
	19500	**4000**
	18300	**6200**
	16600	**450**
	10700	**250**
	7300	**300**
	6400	**300**
	5700	**300**

Table 4.4 Peak positions and extinction coefficient for signals in the UV/Vis/NIR spectra of $3,3´\text{-}(CN)_2\text{-}bpy$ and $[3,3´\text{-}(CN)_2\text{-}bpy]^{1-}$

Previous studies on the UV/Vis absorption spectrum of reduced bpy ligands indicate that the reduction electron enters a molecular orbital based across both pyridine rings.[8] The observed spectra all have the following features; a weakish near-IR band around 10000 cm^{-1}, a doublet band around 20000 cm^{-1} and a more intense band at approximately 25000 cm^{-1}.[8] These bands have been assigned to intraligand charge

transfers involving the semi-occupied lowest energy π^* orbital.[8] The spectra of $[3,3'\text{-}(CN)_2\text{-bpy}]^{1-}$ also shows such transitions and therefore the LUMO of 3,3´-$(CN)_2$-bpy is primarily based on the bpy rings, with only a minor contribution coming from the substituent.

The spectrum of 4,4´-$(CN)_2$-bpy in 0.3 M [TBA][BF_4]/THF at 233 K is shown in figure 4.11. The spectrum has two main strong absorption bands. Their positions and extinction coefficients are give in table 4.4. The band at 33600 cm^{-1} (ε = 14100 $M^{-1}cm^{-1}$) is assigned to a HOMO-LUMO π-π^* transition. The other band is assigned to a higher energy π-π^* transitions from lower energy π orbitals.

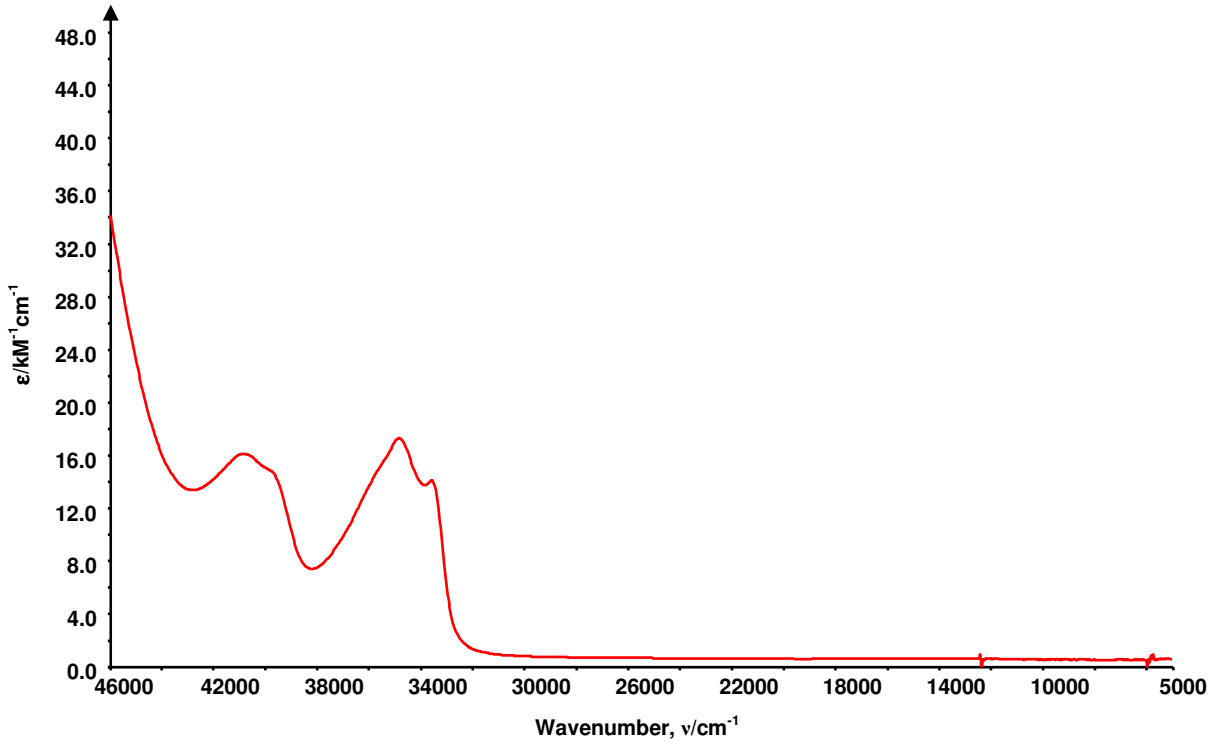

Figure 4.11 UV/Vis/NIR of 4,4´-$(CN)_2$-bpy in 0.3 M [TBA][BF_4]/THF at 233 K

A potential of -1.8 V was then applied to generate the mono-reduced $[4,4'\text{-}(CN)_2\text{-bpy}]^{1-}$ species. The spectra collected during the application of the generation potential for 260 minutes is shown in figure 4.12. The initial broad peaks

have decreased in intensity and a series of new peaks have grown in during the course of the experiment.

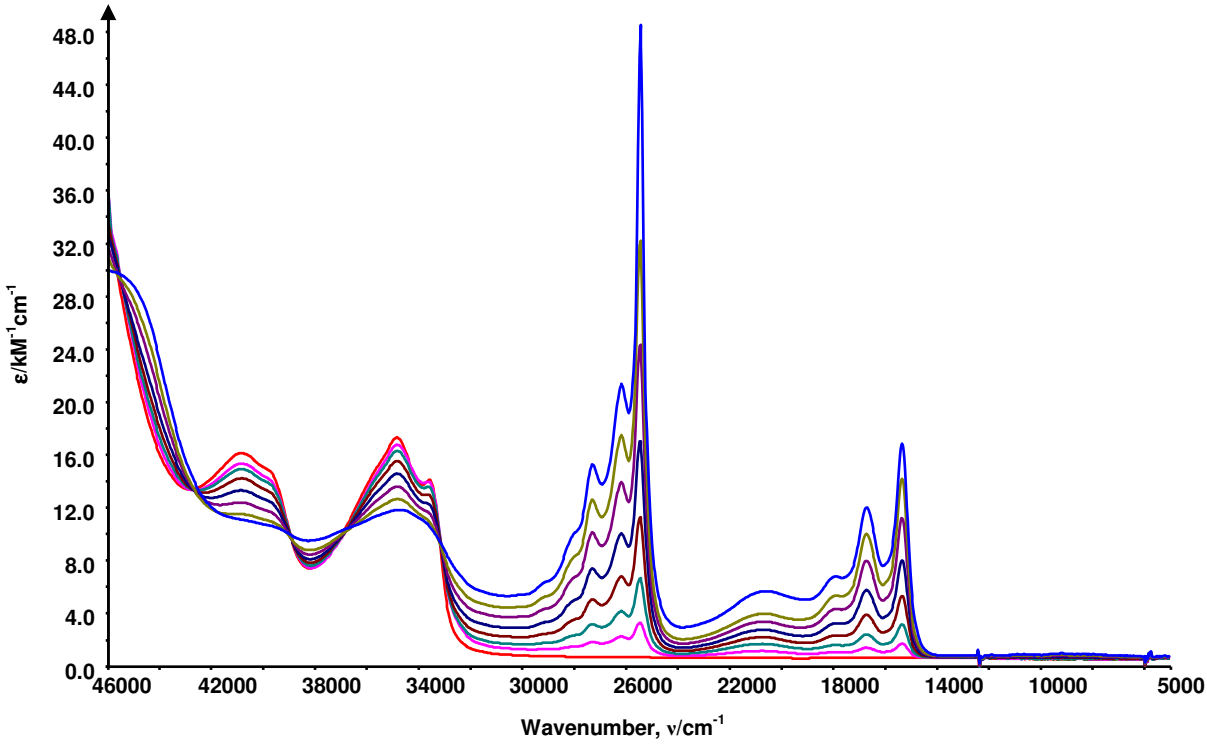

Figure 4.12 UV/Vis/NIR of 4,4´-$(CN)_2$-bpy in 0.3 M [TBA][BF_4]/THF at 233 K 260 minutes after a potential of 1.8 V *vs*. Ag/AgCl was applied. Initial spectrum red, final spectrum blue

The position and extinction coefficient of the peaks are given in table 4.4. The spectral features between 30000 – 5000 cm^{-1} are not in the initial scan before the application of the generation potential. This again is a clear indication that these peaks are due to the [4,4´-$(CN)_2$-bpy]$^{1-}$ species, with isosbestic points observed at 42700 cm^{-1}, 38900 cm^{-1}, 36800 cm^{-1} and 33100 cm^{-1}. Once again the peaks characteristic of mono-reduced X_2-bpy can be observed and the LUMO of 4,4´-$(CN)_2$-bpy is deduced to be primarily located across the bpy ligand. The bands were assigned to intraligand transitions involving the partially filled lowest energy π^* orbital in the reduced 4,4´-$(CN)_2$-bpy.

	Wavenumber (cm^{-1})	Extinction Coefficient ($M^{-1}cm^{-1}$)
4,4'-$(CN)_2$-bpy	40800	16100
	39800	14800
	34800	17300
	33600	14100
$[4,4'-(CN)2-bpy]^{1-}$	45400	29600
	39500	10500
	34700	11900
	27300	15300
	26200	21400
	25500	48500
	20600	5700
	17900	6800
	16700	12000
	15400	16800
	10700	900
	9200	1000
	8000	900
	6600	800

Table 4.5 Peak positions and extinction coefficient for signals in the UV/Vis/NIR spectra of 4,4´-$(CN)_2$-bpy and $[4,4´-(CN)_2-bpy]^{1-}$

The UV/Vis/NIR spectrum of the neutral 5,5´-$(CN)_2$-bpy in 0.1 M [TBA][BF_4]/DMF at 233 K is shown in figure 4.13. The spectrum shows one strong absorption signal at approximately 32700 cm^{-1} (ε = 13200 $M^{-1}cm^{-1}$) corresponding to a HOMO-LUMO π-π^* transition.

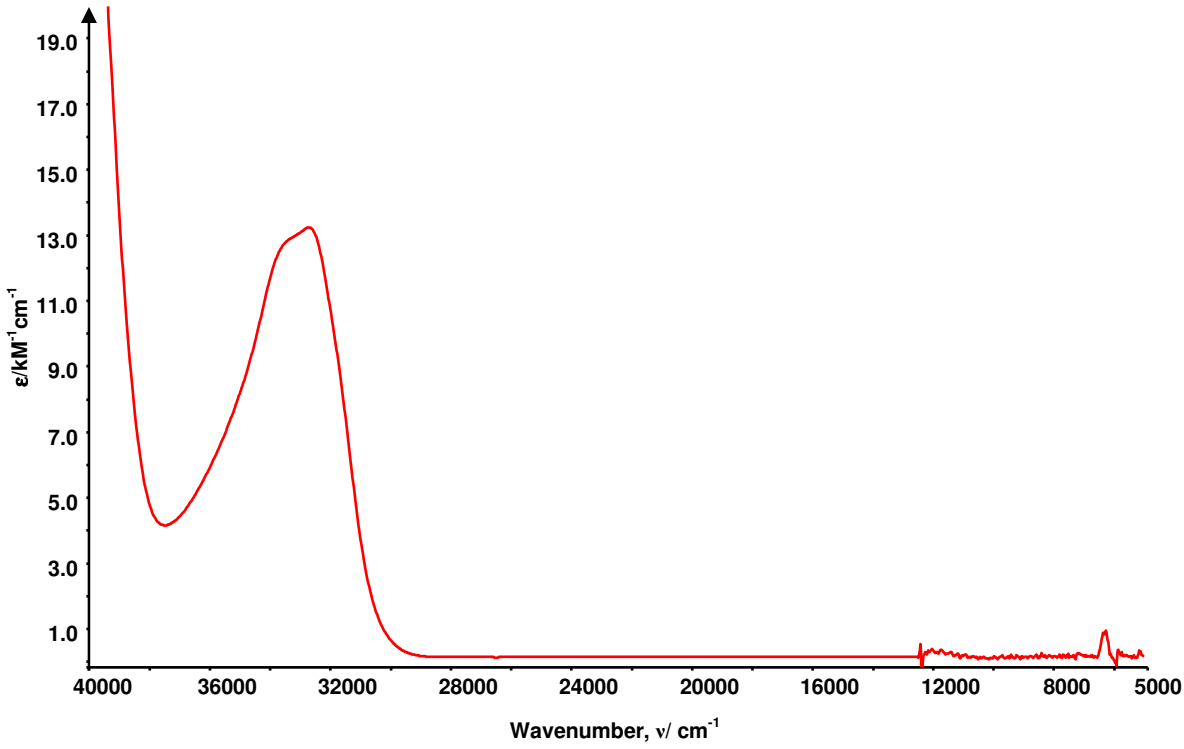

Figure 4.13 UV/Vis/NIR of 5,5´-$(CN)_2$-bpy in 0.3 M [TBA][BF_4]/DMF at 233 K

A generation potential of -1.2 V was applied to the system to generate the $[5,5'\text{-}(CN)_2\text{-bpy}]^{1-}$ species. The spectra during the reduction process (110 minutes) is shown in figure 4.14.

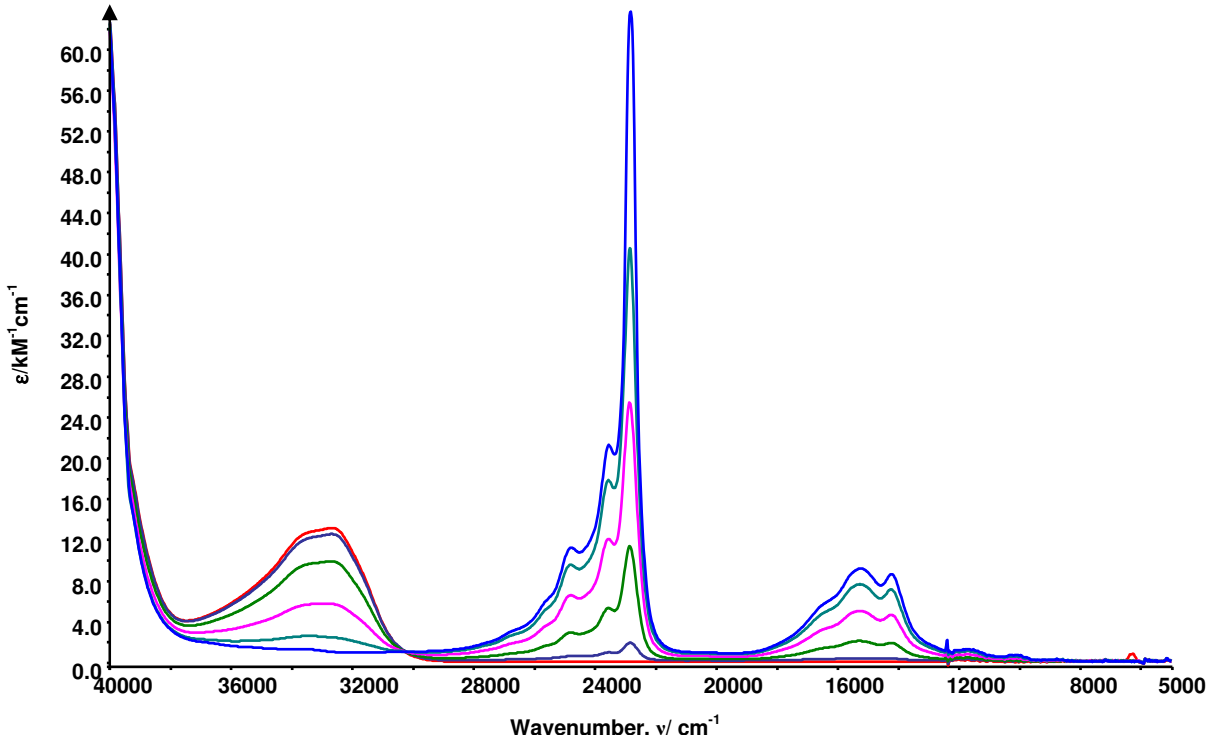

Figure 4.14 UV/Vis/NIR of $5,5'\text{-}(CN)_2\text{-bpy}$ in 0.3 M $[TBA][BF_4]$/DMF at 233 K 110 minutes after a potential of -1.2 V *vs*. Ag/AgCl was applied. Initial spectrum red, final spectrum blue

It is clear from this spectrum that the strong absorption band at 32700 cm^{-1} due to the $5,5'\text{-}(CN)_2\text{-bpy}$ species has completely collapsed. A number of new peaks have appeared during the experiment. The position and extinction coefficient for these peaks are given in table 4.5. The peaks below 30000 cm^{-1} do not appear in the initial spectrum before the generation potential is applied, thus it can be inferred that these are due to the mono-reduced $[5,5'\text{-}(CN)_2\text{-bpy}]^{1-}$ species. This finding is supported by the isosbestic point at 30300 cm^{-1}. Once again the spectrum of the neutral species is regenerated in full on application of an electrogeneration potential of 0 V. The three sets of peaks characteristic of reduced bpy ligands may once again be observed although the lowest energy set of peaks is considerably blue shifted in this case.

Figure 4.15 shows the spectral response of the di-reduced species $[5,5'\text{-}(CN)_2\text{-bpy}]^{2-}$ produced at -1.6 V. The band at 16400 – 8900 cm^{-1} collapses and low intensity features appear at 17100 cm^{-1} (ε = 2300 $M^{-1}cm^{-1}$) and 14200 cm^{-1} (ε = 900 $M^{-1}cm^{-1}$). The very high intensity band around 23000 cm^{-1} also collapses with a series of new peaks growing in between 24600 – 21100 cm^{-1}.

In their study of the electronic spectra of $[bpy]^{1-}$ and $[bpy]^{2-}$ König and Kremer assigned the spectrum of $[bpy]^{2-}$ as comprising of two bands; one at *ca.* 16400 cm^{-1} and a second very intense band at *ca.* 26800 cm^{-1}.[8] These bands have been assigned to intraligand transitions involving the now doubly occupied SOMO to higher energy π^* orbital.[8] The spectra of $[5,5'\text{-}(CN)_2\text{-bpy}]^{2-}$ also shows such transitions but moved to lower energy due to electron withdrawing nature of the cyano substituent.

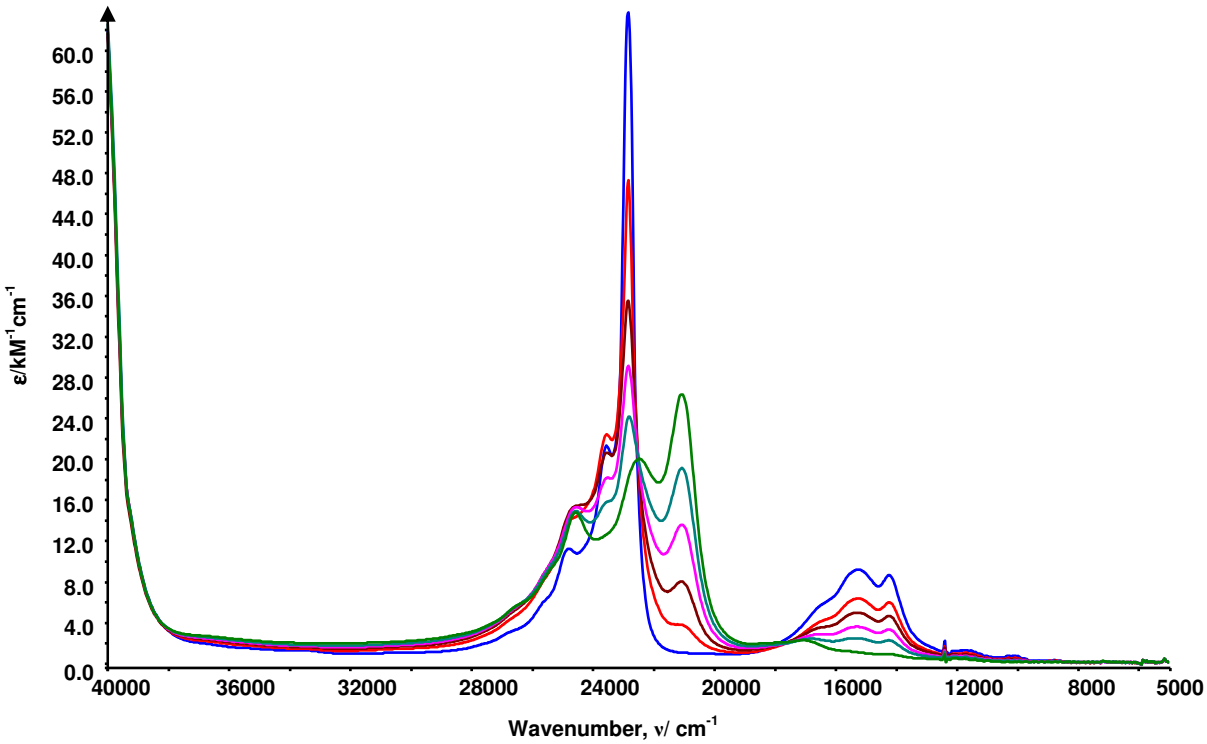

Figure 4.15 UV/Vis/NIR of $5,5'\text{-}(CN)_2$-bpy in 0.3 M [TBA][BF_4]/DMF at 233 K 150 minutes after a potential of -1.6 V *vs*. Ag/AgCl was applied. Initial spectrum blue, final spectrum green

	Wavenumber (cm^{-1})	Extinction Coefficient ($M^{-1}cm^{-1}$)
5,5'-$(CN)_2$-bpy	32700	13200
$[5,5'\text{-}(CN)2\text{-}bpy]^{1-}$	24800 23600 22900 16400 15300 14200 11600 10200 8900	11300 21300 63800 5900 9200 8700 1000 650 200
$[5,5'\text{-}(CN)2\text{-}bpy]^{2-}$	24600 22500 21100 17100 14200	14800 20100 26400 2300 900

Table 4.6 Peak positions and extinction coefficient for signals in the UV/Vis/NIR spectra of 5,5´-$(CN)_2$-bpy, $[5,5'\text{-}(CN)_2\text{-}bpy]^{1-}$ and $[5,5'\text{-}(CN)_2\text{-}bpy]^{2-}$

4.3.2 EPR Spectroelectrochemistry

In-situ electrogeneration was used to generate the EPR active mono-reduced species $[3,3'\text{-}(CN)_2\text{-}bpy]^{1-}$, $[4,4'\text{-}(CN)_2\text{-}bpy]^{1-}$ and $[5,5'\text{-}(CN)_2\text{-}bpy]^{1-}$. A potential of -1.75 V was used to generate the $[4,4'\text{-}(CN)_2\text{-}bpy]^{1-}$ species and a potential of -1.4 V was used to generate both the 3,3´ and 5,5´ analogues.

The EPR spectrum recorded for the $[3,3'\text{-}(CN)_2\text{-}bpy]^{1-}$ species shown in figure 4.16 consists of 14 lines. Simulation of the experimental spectrum was achieved by including coupling to two pairs of equivalent ^{14}N nuclei and coupling to two pairs of equivalent ^{1}H nuclei. This pattern of couplings can only be possible if the unpaired electron is delocalised over the entire molecule rather than being localised on one of the CN-py rings. As for the X-CN-py pro-ligands, it is not possible to assign the observed ^{14}N couplings to either the nitrogen atoms of the CN group or the ring nitrogen atoms from these experimental results alone.

The two largest couplings result from coupling to ^{1}H nuclei. The largest coupling of 2.60 G is more than twice the size of the smaller coupling of 1.20 G. Coupling to the two pairs of ^{14}N nuclei give rise to the smallest couplings observed. They have similar coupling constants of 1.05 G and 0.95 G indicating that a comparable amount of electron density is localised on these atoms

The EPR spectrum obtained for the $[4,4´\text{-}(CN)_2\text{-bpy}]^{1-}$ species is shown in figure 4.17, it consist of 25 lines. Simulation of the experimental spectrum was achieved by considering coupling to two pairs of equivalent ^{14}N nuclei and coupling to two pairs of equivalent ^{1}H nuclei. Though the overall coupling pattern is similar to that of the $[3,3´\text{-}(CN)_2\text{-bpy}]^{1-}$ species the size of the coupling constants corresponding to each pair of nuclei are wildly different. Again the largest coupling is due to a pair of ^{1}H nuclei but in this system it is much larger at 7.00 G. One of the nitrogen couplings is also much larger with a value of 2.09 G. The other nitrogen coupling is much smaller with a value of 0.18 G. It is noted that the larger coupling is more than ten times the size of the smaller; indicating that there is a significantly larger amount of electron density localised to one of the pairs of nitrogen atoms. The remaining ^{1}H coupling is much smaller in this species with coupling constant of 0.85 G.

The EPR spectrum obtained for the $[5,5´\text{-}(CN)_2\text{-bpy}]^{1-}$ species is shown in figure 4.18, it consists of 13 lines. Simulation of the experimental spectrum was achieved using a similar coupling pattern to those determined for the 3,3´ and 4,4´ analogues. This species also exhibited coupling to two pairs of equivalent ^{14}N nuclei and three pairs of equivalent ^{1}H nuclei. The largest coupling is again to a pair of ^{1}H nuclei with a coupling constant of 1.43 G. The largest of the ^{14}N couplings is of a similar size to

this coupling with a coupling constant of 1.20 G. A similar relationship is found between the other ^{14}N coupling and the middle ^{1}H coupling with coupling constants being 0.95 G and 1.32 G respectively. The final ^{1}H coupling in this system is small with a coupling constant of only 0.22 G.

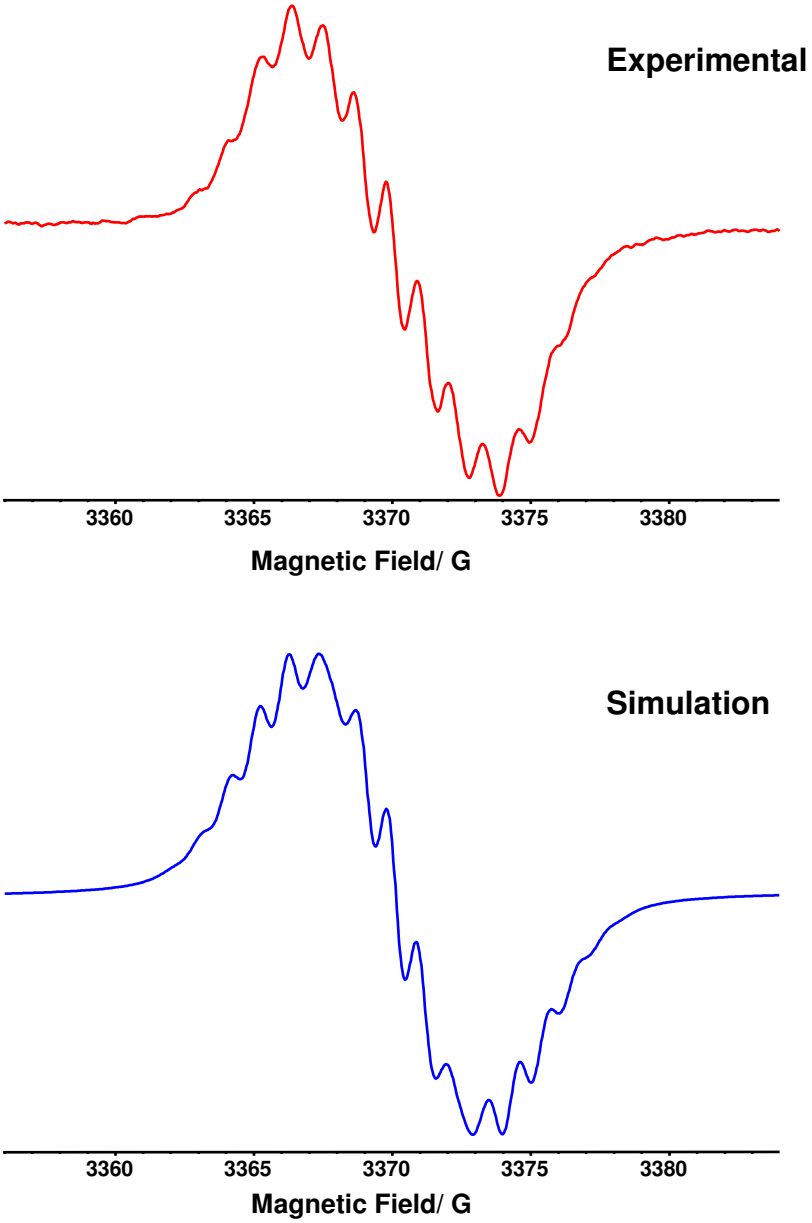

$A_{2\ ^{14}N} = 1.05$ G

$A_{2\ ^{14}N} = 0.95$ G

$A_{2\ ^{1}H} = 2.60$ G

$A_{2\ ^{1}H} = 1.20$ G

$\Delta H_{pp} = 0.81$ G

$L/G = 0$

$g_{iso} = 2.0027$

Figure 4.16 Experimental and simulated EPR of $[3,3'\text{-}(CN)_2\text{-bpy}]^{1-}$ generated *in-situ* at -1.4 V *vs*. Ag/AgCl at 233 K in 0.1 M $[TBA][BF_4]$/DMF

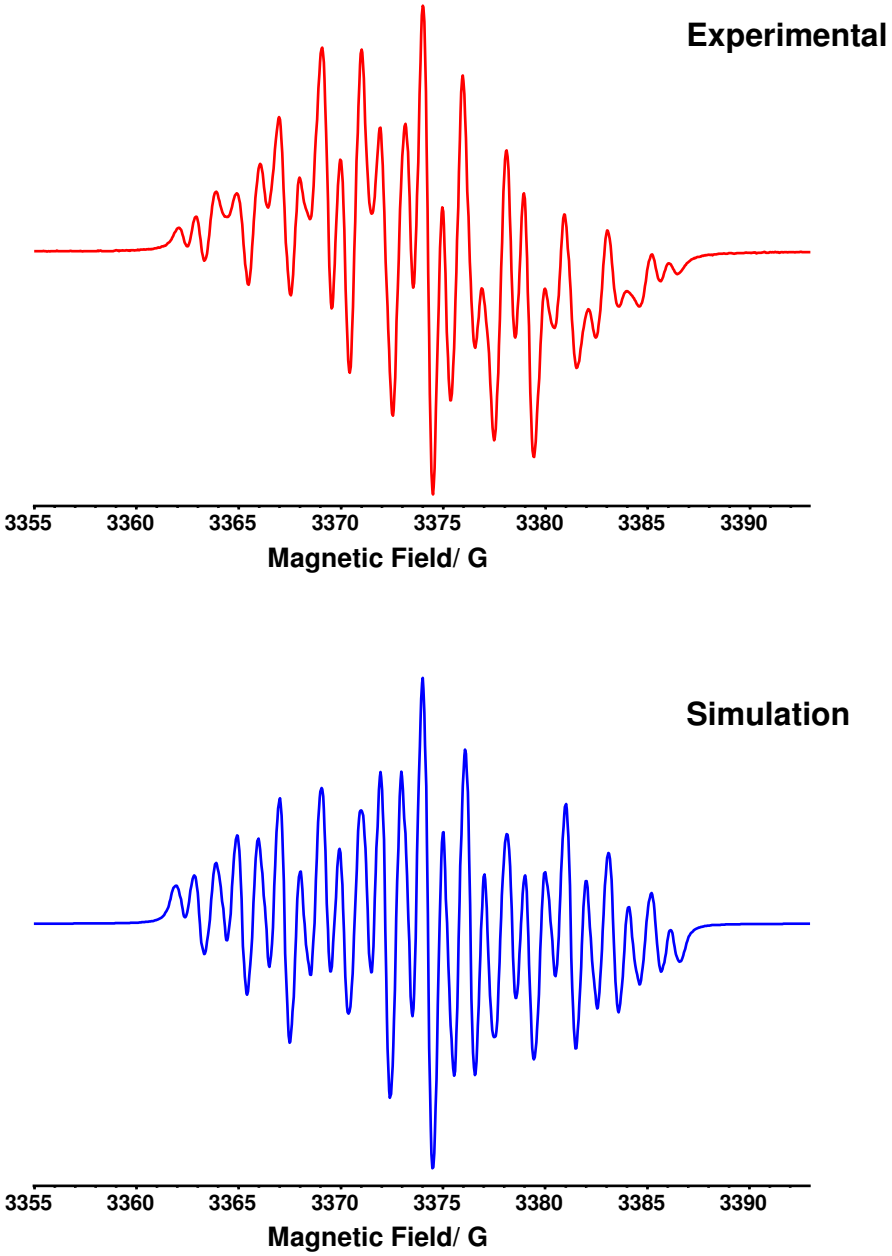

$A_{2\ ^{14}N} = 2.09$ G

$A_{2\ ^{14}N} = 0.18$ G

$A_{2\ ^{1}H} = 7.00$ G

$A_{2\ ^{1}H} = 0.85$ G

$\Delta H_{pp} = 0.42$ G

$L/G = 0$

$g_{iso} = 2.00235$

Figure 4.17 Experimental and simulated EPR of $[4,4'\text{-}(CN)_2\text{-bpy}]^{1-}$ generated *in-situ* at -1.75 V *vs*. Ag/AgCl at 233 K in 0.3 M $[TBA][BF_4]$/THF

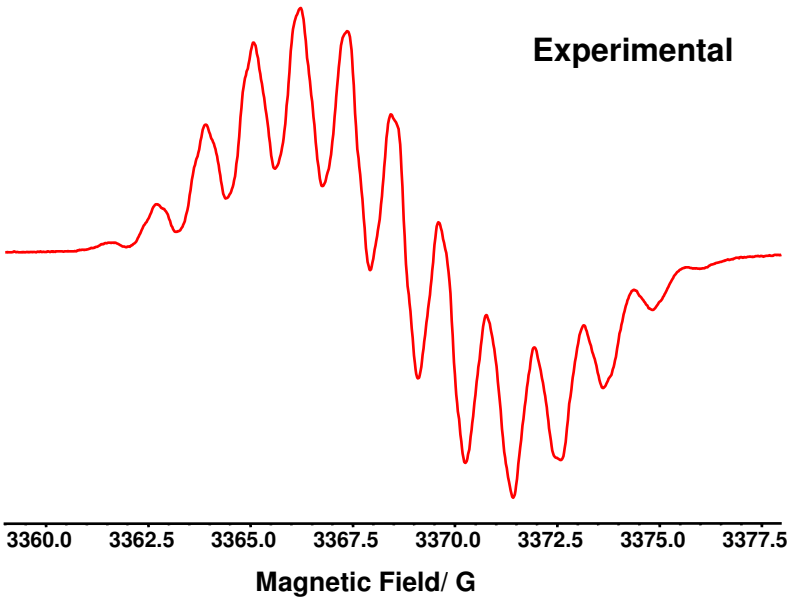

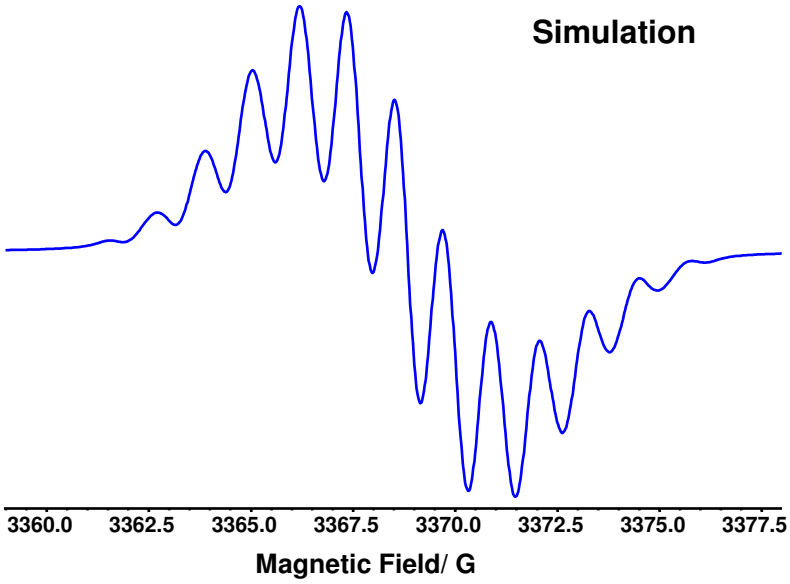

$A_{2\ ^{14}N} = 1.20$ G

$A_{2\ ^{14}N} = 0.95$ G

$A_{2\ ^{1}H} = 1.43$ G

$A_{2\ ^{1}H} = 1.32$ G

$A_{2\ ^{1}H} = 0.22$ G

$\Delta H_{pp} = 0.41$ G

$L/G = 0$

$g_{iso} = 2.00135$

Figure 4.18 Experimental and simulated EPR of $[5,5'\text{-}(CN)_2\text{-bpy}]^{1-}$ generated *in-situ* at -1.4 V *vs.* Ag/AgCl at 233 K in 0.1 M $[TBA][BF_4]$/DMF

4.4 Calculations

DFT calculations were undertaken in an attempt to gain a greater understanding of the electronic properties of the dicyanobipyridine compounds and to aid in the assignment of EPR couplings.

Shown in figure 4.19 is the optimised geometry calculated for 3,3´-$(CN)_2$-bpy. By comparison of the calculated structure with the crystal structure determined by Baxter *et al*., discussed previously is section 4.1, it is possible to assess the accuracy of the calculations in predicting the structural properties of the substituted bipyridines studied in this work.

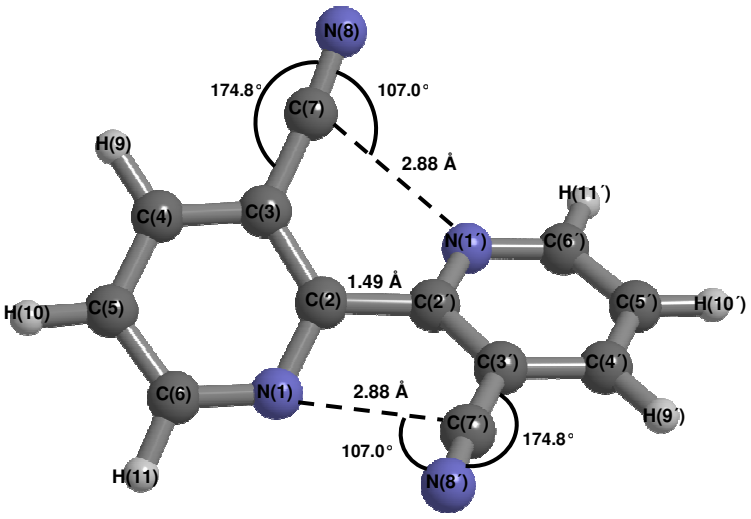

Figure 4.19 Optimised geometry of 3,3´-$(CN)_2$-bpy

When figure 4.1 and figure 4.19 are compared it can be seen that the overall structural properties of the molecule from the crystal structure have been replicated well but that there are some discrepancies. Most notably the calculated structure is significantly more twisted than in the crystal structure, with a N(1)-C(2)-C(2´)-N(2´) torsional angle of 138.1°. In addition the C(2)-C(2´) inter-ring distance is slightly longer.

Of more interest are the changes in the N· · ·C interactions between the ring nitrogen atoms and the cyano group carbon atoms. In the calculated structure these interactions are 0.15 Å longer and the N(1)-C(7´)-N(8´) and N(1´)-C(7)-N(8) angles are slightly smaller. In addition the degree of distortion from linearality in the C-C≡N groups is less, with the groups bowing by only 5.2°. The changes in these properties are in line with what Baxter *et al*. predicted for an increase in the tortional angle in the 3,3´-$(CN)_2$-bpy molecule. Thus the computational model can be considered to be fairly accurate with the discrepancies resulting from the calculation being run in the gas phase.

The optimised geometries calculated for 4,4´-$(CN)_2$-bpy and 5,5´-$(CN)_2$-bpy are shown in figures 4.20 and 4.21. There have been no crystal structures previously reported for these molecules. In both compounds the pyridine rings are coplanar with the N(1)-C(2)-C(2´)-N(2´) torsional angle reported to be 180°. Comparison of the C(2)-C(2´) bond length between the rings for the three X,X´-$(CN)_2$-bpy structures shows that all are approximately 1.49 Å, with variance as little as 0.004 Å. The C(7)-N(8) and C(7´)-N(8´) bond lengths in the cyano groups have also been examined and have been found to be approximately 1.163 Å in all three compounds.

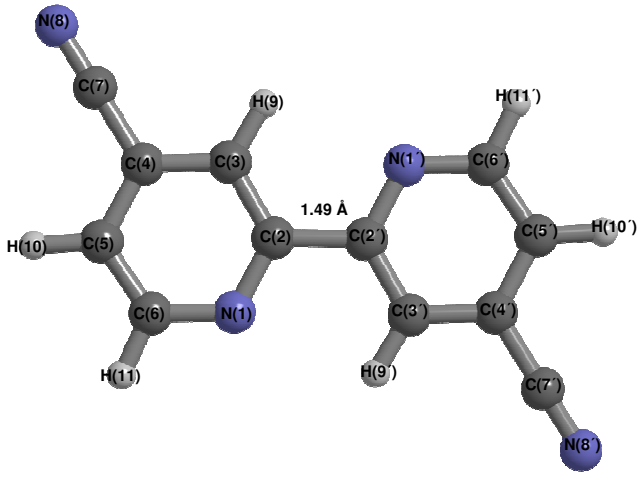

Figure 4.20 Optimised geometry of 4,4´-$(CN)_2$-bpy

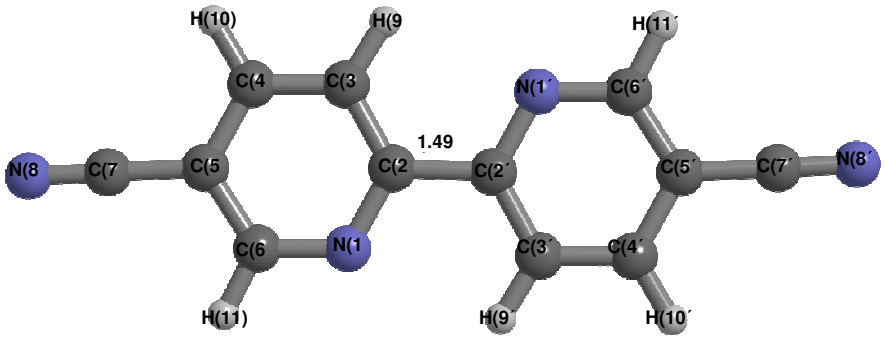

Figure 4.21 Optimised geometry of 5,5´-$(CN)_2$-bpy

The effect of the addition of a substituent group on the torsional barrier of the bpy ring system was also studied. To this end the structure of 5,5´-$(CN)_2$-bpy was recalculated varying the N(1)-C(2)-C(2´)-N(2´) torsional angle. A plot of the torsional potential energy of 5,5´-$(CN)_2$-bpy *vs*. the dihedral angle is shown in figure 4.22.

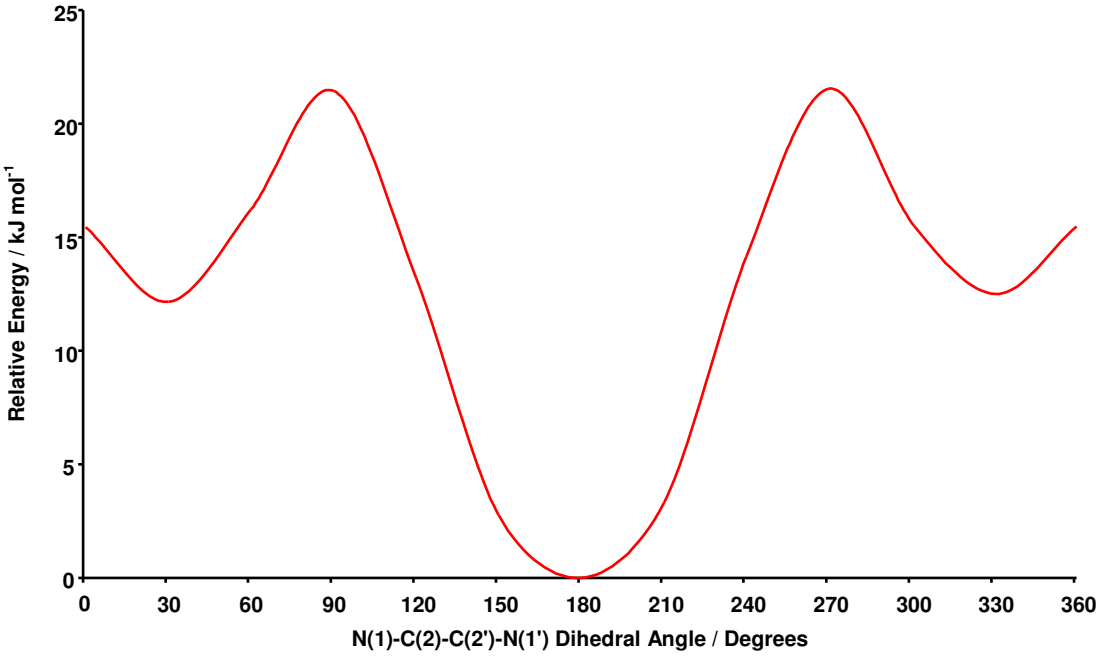

Figure 4.22 Torsional potential of 5,5´$(CN)_2$-bpy calculated using B3LYP/6-31+G(d,p)

The computational study indicates that the molecule possesses a global minima at 180° and local minima at approximately 30° and 330°. Energy maxima are predicted for the perpendicular orientations of the pyridine rings and for 0°. The global minimum at 180° is stabilised by approximately 12 $kJmol^{-1}$ relative to the twisted *cis* confomers. The energy barrier for the perpendicular orientations are about 21.5 $kJmol^{-1}$ higher than the global minimum and about 9.5 $kJmol^{-1}$ higher than the local minima. The 0° barrier is approximately 15 $kJmol^{-1}$ higher than the *trans* conformation and 3 $kJmol^{-1}$ higher than the local minima.

Comparison of these results with the study conducted by Göller and Grummt on unsubstituted bpy[9] indicates that the coplanar conformation of 5,5´-$(CN)_2$-bpy is less stabilised with respect to rotation about the C(2)-C(2´) bond. In addition the local minima are found to be more stable with respect to the perpendicular conformations

than in bpy, while the energy barrier to the 0° conformation remains roughly unchanged for the local minima.

It is noted that the C(2)-C(2´) bond length between the two pyridine rings changes length with rotation about the C-C bond. Lengths of 1.488 Å and 1.492 Å are observed for the global and local minima respectively, extending to 1.497 Å at 0° and reaching a maximum of 1.501 Å for the perpendicular conformations. This elongation of the inter-ring distance is slightly larger than that observed for bpy.[9]

The optimised geometries calculated for the three dicyanobipyridines in their mono-reduced states are shown in figures 4.24-4.26. Comparison of these geometries with those calculated for non-reduced species enables examination of the effect of adding an additional electron to the structure of the molecule.

The largest change observed is clearly for the $[3,3´\text{-}(CN)_2\text{-bpy}]^{1-}$ anion. The N(1)-C(2)-C(2´)-N(2´) torsional angle has increased to 180°, bringing the pyridine rings into coplanarity. The N(1)· · ·C(7´) distance has decreased by 0.141 Å, while the N(1)- C(7´)- N(8´) angle has increased to 110.0°. The stronger N· · ·C interaction causes the C-C≡N group to bend further away from linearity with the angle decreasing to 170.0°. In addition some changes are observed in the bond lengths: a shortening of the C(2)-C(2´) (-0.062 Å) and N(1)-C(6) (-0.062 Å) bonds and lengthening of the N(1)-C(2)(+0.033 Å), C(2)-C(3)(+0.043 Å) and C(5)-C(6)(+0.017 Å) bonds. The shortening of the inter-ring C(2)-C(2´) bond in the reduced species is indicative of an increased amount of double bond character and therefore an increased π-conjugation and a favouring of a planar conformation.

The change in structure upon reduction is less obvious for the 4,4´ and 5,5´ analogues. Both molecules do not deviate from the coplanar structure of the non-reduced state. Once again there are some changes observed in the bond lengths of each of the compounds. For $[4,4´\text{-}(CN)_2\text{-bpy}]^{1-}$ there is a shortening of the C(2)-C(2´) (-0.042 Å) and lengthening of the N(1)-C(2)(+0.038 Å), C(2)-C(3)(+0.012 Å) and C(4)-C(5)(+0.027 Å) bonds. For $[5,5´\text{-}(CN)_2\text{-bpy}]^{1-}$ there is a shortening of the C(2)-C(2´) (-0.052 Å), N(1)-C(6)(-0.011 Å) and C(3)-C(4) (-0.016 Å) bonds and lengthening of the N(1)-C(2)(+0.032 Å), C(2)-C(3)(+0.026 Å) and C(5)-C(6)(+0.012 Å) bonds.

Further comparison of the effect of the reduction upon the structural properties of the dicyanobipyridines was achieved by conducting a study of the tortional barrier of the mono-reduced $[5,5´\text{-}(CN)_2\text{-bpy}]^{1-}$ species. As with the non-reduced species the global minima is at 180°. There is only one local minimum this time at 0°. Energy maxima are predicted for the perpendicular orientations of the pyridine rings.

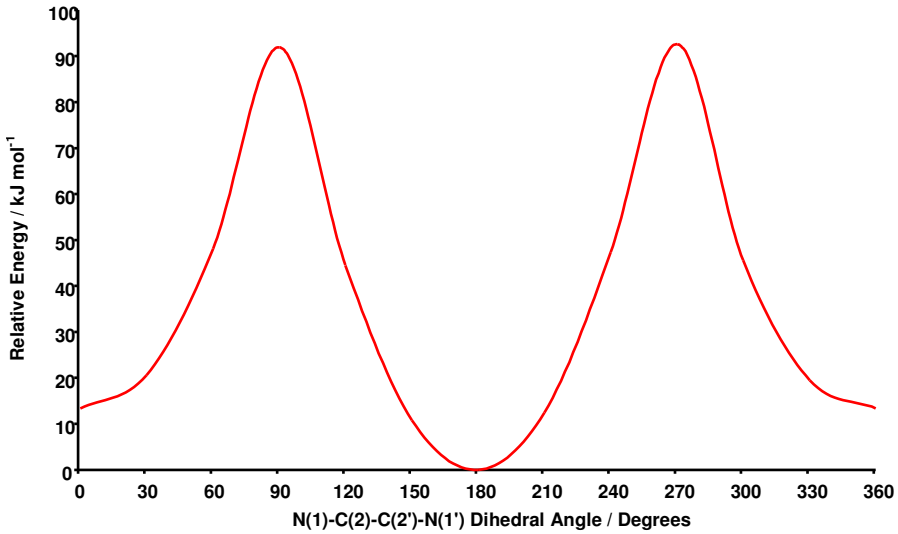

Figure 4.23 Torsional potential of $[5,5´\text{-}(CN)_2\text{-bpy}]^{1-}$ calculated using B3LYP/6-31G+(d,p)

A plot of the torsional potential energy *vs*. the dihedral angle of $[5,5'\text{-}(CN)_2\text{-bpy}]^{1-}$ is shown in figure 4.23. The global minima at 180° is stabilised by approximately 13 $kJmol^{-1}$ relative to the *cis* conformer. The energy barrier for the perpendicular orientations are about 92 $kJmol^{-1}$ higher than the global minimum and about 79 $kJmol^{-1}$ higher than the local minimum. These large energy barrier for rotation are indicative of a high degree of double bond character in the C(2)-C(2´) inter-ring bond and therefore increased π-conjugation when the molecule is in either the *trans* or *cis* conformations.

Also shown in figure 4.24-4.26 are the calculated SOMOs for each of the mono-reduced dicyanobipyridine compounds. Examination of these orbitals can aid in the interpretation of the experimental results obtained from spectroelctrochemcial investigation of the mono-reduced species.

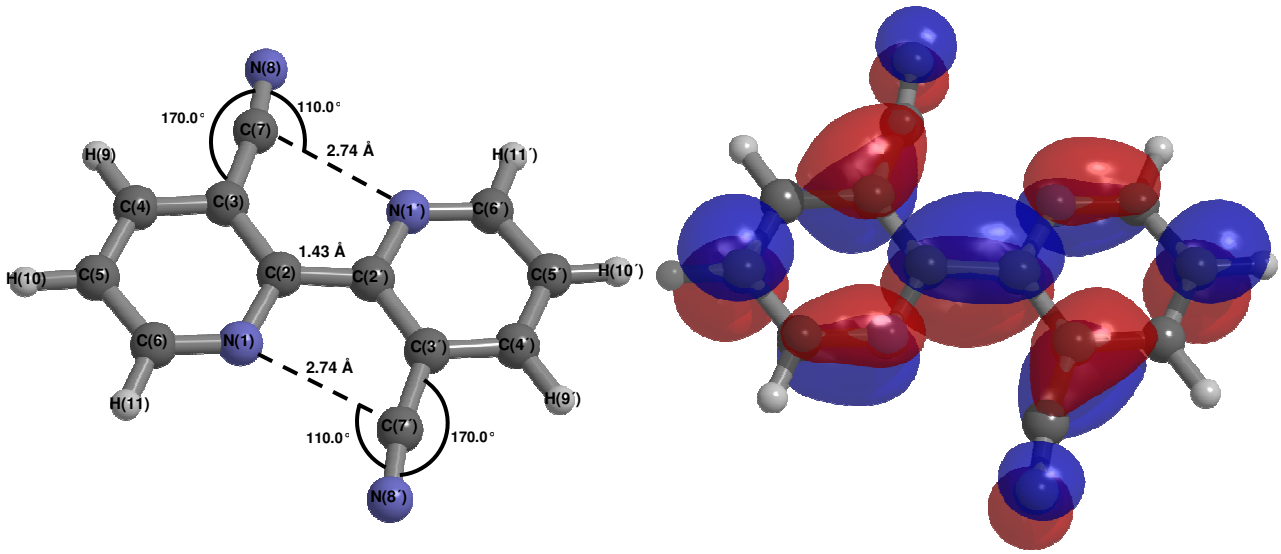

Figure 4.24 Optimised geometry and calculated SOMO of $[3,3'\text{-}(CN)_2\text{-bpy}]^{1-}$

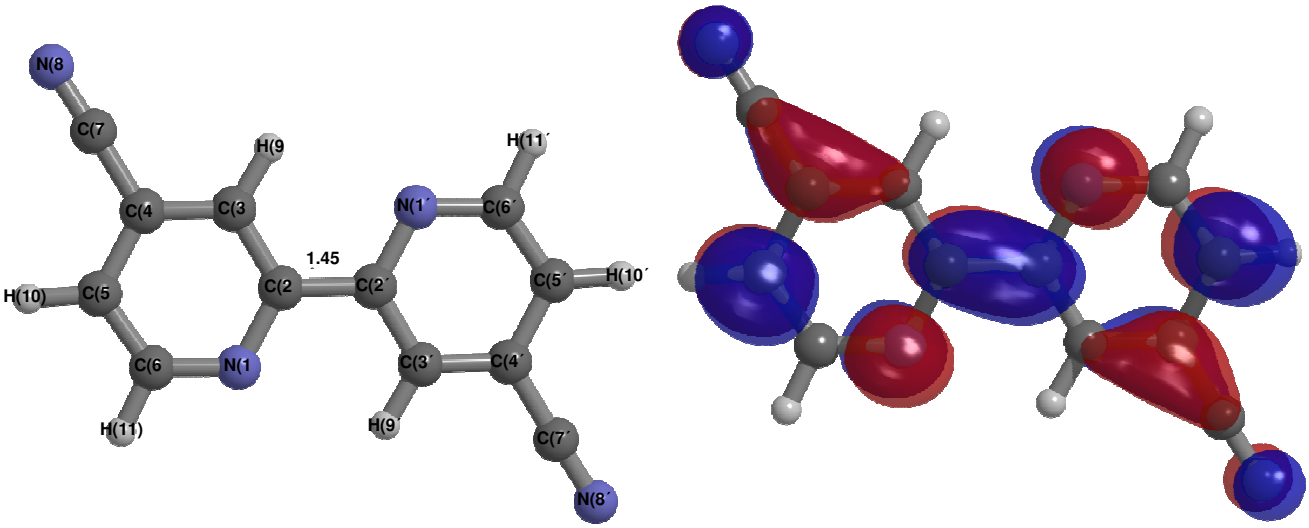

Figure 4.25 Optimised geometry and calculated SOMO of [4,4´-$(CN)_2$-bpy]$^{1-}$

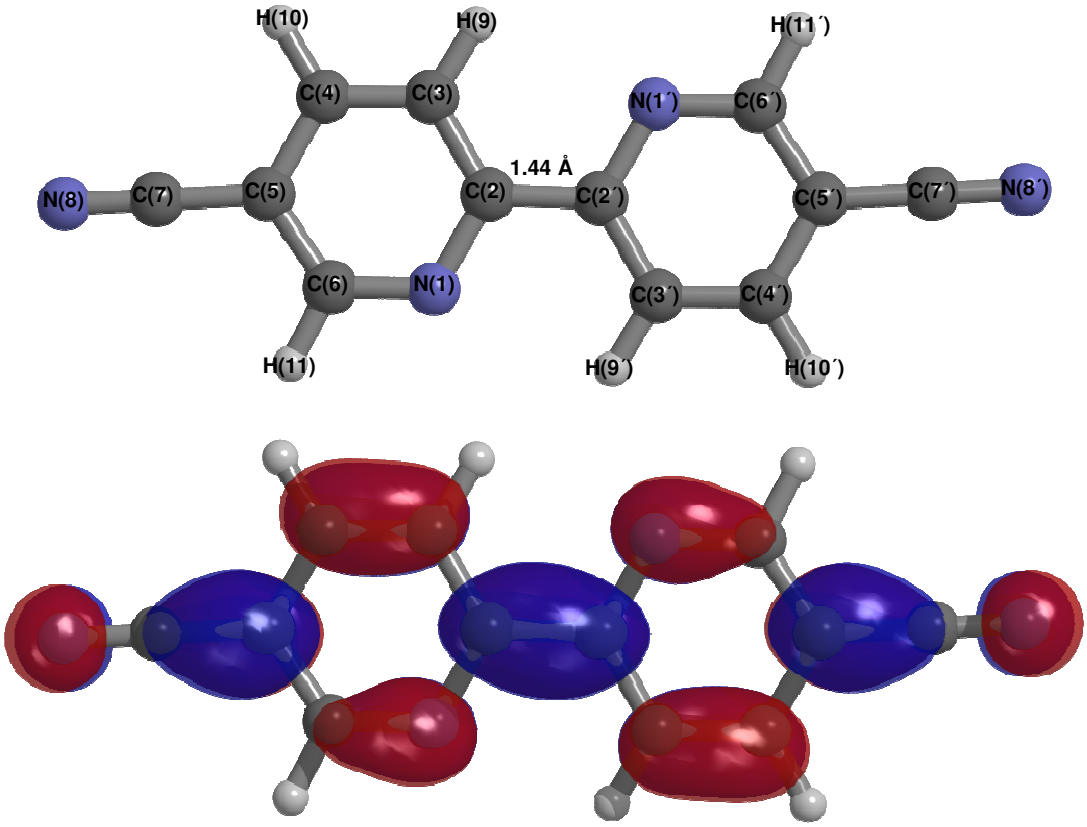

Figure 4.26 Optimised geometry and calculated SOMO of [5,5´-$(CN)_2$-bpy]$^{1-}$

Comparison of the orbitals clearly shows that altering the positions of the cyano substituents has a significant effect on the distribution of electron density about the bipyridine rings. Given in table 4.7 are the breakdowns of the % occupations by atom for the SOMOs of the three mono-reduced dicyanobipyridines.

It is observed that the amount of electron density localised onto the cyano substituent is affected by the positions of the group. It is noted that in each of the SOMOs there is a node between the carbon and nitrogen atoms of the cyano groups.

$[3,3'\text{-}(CN)_2\text{-bpy}]^{1-}$ SOMO	
# Atom	%
N(1)	4.79
C(2)	12.77
C(3)	11.37
C(4)	0.47
C(5)	13.02
C(6)	2.84
C(7)	0.96
N(8)	3.75
H(9)	0.00
H(10)	0.02
H(11)	0.00
N(1´)	4.79
C(2´)	12.77
C(3´)	11.37
C(4´)	0.47
C(5´)	13.02
C(6´)	2.84
C(7´)	0.96
N(8´)	3.75
H(9´)	0.00
H(10´)	0.02
H(11´)	0.00

$[4,4'\text{-}(CN)_2\text{-bpy}]^{1-}$ SOMO	
# Atom	%
N(1)	11.24
C(2)	9.23
C(3)	0.69
C(4)	9.34
C(5)	15.83
C(6)	0.21
C(7)	0.86
N(8)	2.56
H(9)	0.00
H(10)	0.03
H(11)	0.00
N(1´)	11.24
C(2´)	9.23
C(3´)	0.69
C(4´)	9.34
C(5´)	15.83
C(6´)	0.21
C(7´)	0.86
N(8´)	2.56
H(9´)	0.00
H(10´)	0.03
H(11´)	0.00

$[5,5'\text{-}(CN)_2\text{-bpy}]^{1-}$ SOMO	
# Atom	%
N(1)	6.05
C(2)	11.65
C(3)	4.06
C(4)	5.97
C(5)	14.17
C(6)	1.60
C(7)	1.20
N(8)	5.27
H(9)	0.01
H(10)	0.01
H(11)	0.00
N(1´)	6.05
C(2´)	11.65
C(3´)	4.06
C(4´)	5.97
C(5´)	14.17
C(6´)	1.60
C(7´)	1.20
N(8´)	5.27
H(9´)	0.01
H(10´)	0.01
H(11´)	0.00

Table 4.7 The % occupations by atom for the SOMOs of $[3,3'\text{-}(CN)_2\text{-bpy}]^{1-}$, $[4,4'\text{-}(CN)_2\text{-bpy}]^{1-}$ and $[5,5'\text{-}(CN)_2\text{-bpy}]^{1-}$

This is suggestive of limited delocalisation within the substituent group. It is therefore of interest to examine the amount of electron density localised to the nitrogen atom of the substituent. It is noted that for the dicyanobipyridines the nitrogen atom contributes 5.12 - 10.54% to the SOMOs, with the largest contribution observed for the 5,5´-$(CN)_2$-bpy molecule.

As discussed in section 1.2, the most electronically important position in the pyridine ring system is the nitrogen atom. Accordingly it is of interest to study how altering the position of the substituent effects the distribution of electron density on this position. Comparison of the SOMOs for the three dicyanobipyridines indicates that the ring nitrogen atoms contribute 9.58-22.48%, with the largest contribution observed for the $[4,4´\text{-}(CN)_2\text{-bpy}]^{1-}$ species.

Time-dependent density functional theory (TD-DFT) calculations were conducted in an attempt to gain further information about the UV/Vis/NIR spectroelectrochemical data collected for the dicyanobipyridine compounds.

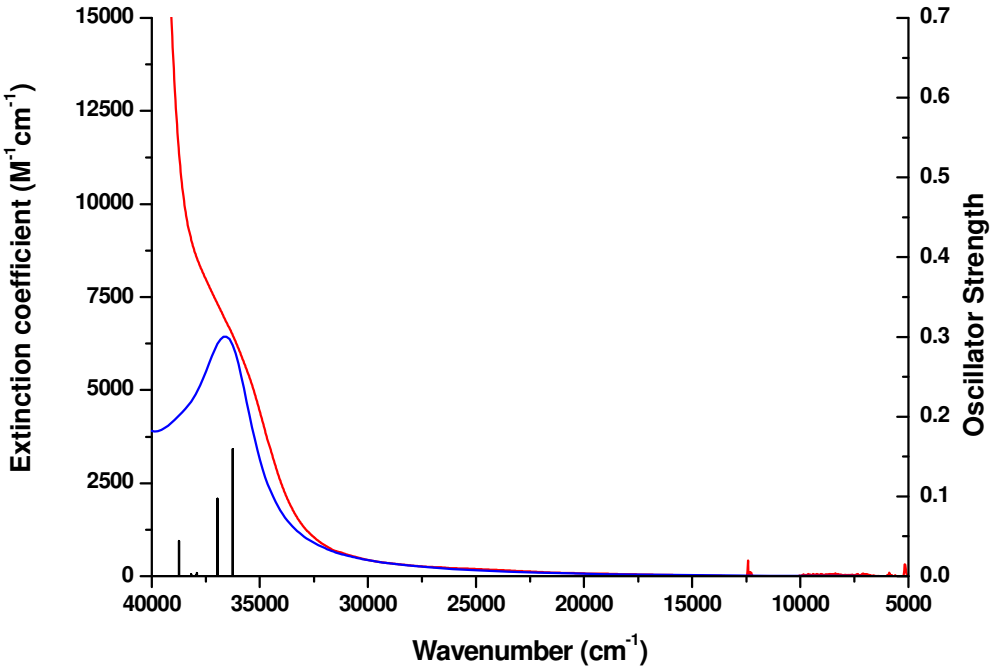

Figure 4.27 Overlay of the experimental UV/Vis/NIR spectrum (red) and the TD-DFT calculated spectrum (blue) of 3,3´-$(CN)_2$-bpy. Calculated transitions are shown as black columns

Shown in figure 4.27 is an overlay of the calculated and experimental UV/Vis/NIR spectra of 3,3´-$(CN)_2$-bpy.

When the spectra are compared it can be seen that the calculated spectrum matches the overall shape of the experimental data well. The experimental and calculated transitions observed in the UV/Vis/NIR spectrum of 3,3´-$(CN)_2$-bpy are reported in table 4.8. Analysis of the transition in the calculated spectrum show that it is due to the HOMO-LUMO transition.

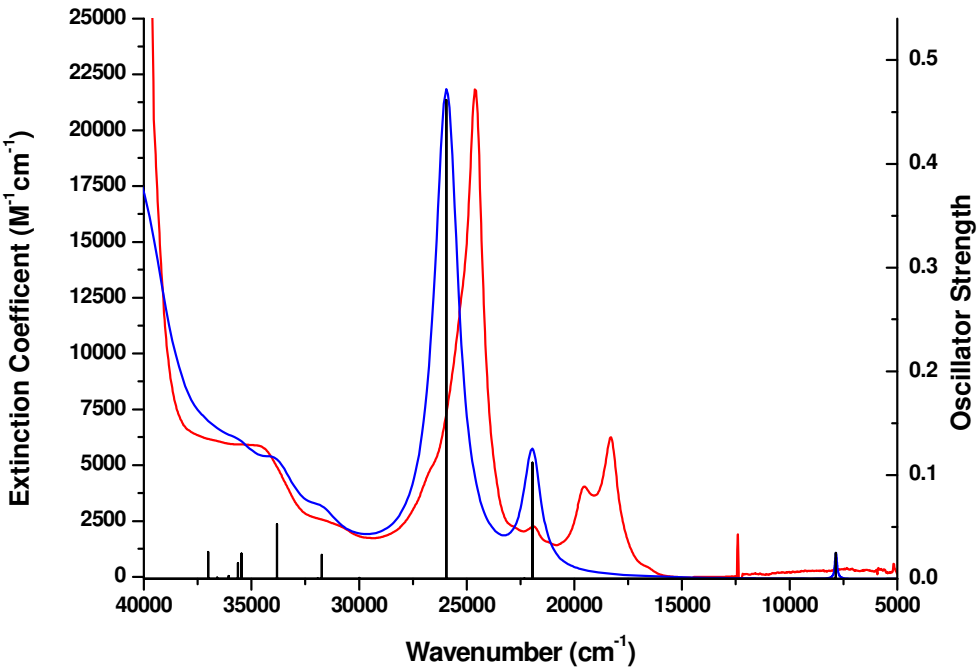

Figure 4.28 Overlay of the experimental UV/Vis/NIR spectrum (red) and the TD-DFT calculated spectrum (blue) of $[3,3'\text{-}(CN)_2\text{-bpy}]^{1-}$. Calculated transitions are shown as black columns

Of more interest is the information that can be gained by applying this technique to the more complicated spectrum of the mono-reduced $[3,3'\text{-}(CN)_2\text{-bpy}]^{1-}$ species. Shown in figure 4.28 is an overlay of the experimental and calculated spectra for this species.

	Experimental		Calculation	
	Wavenumber (cm^{-1})	Extinction Coefficient ($M^{-1}cm^{-1}$)	Wavenumber (cm^{-1})	Osc. Strength
$3,3'\text{-}(CN)_2\text{-bpy}$	36000	6200	36900	0.2015
$[3,3'\text{-}(CN)_2\text{-bpy}]^{1-}$	34600	5800	33800	0.0509
	31500	2500	31700	0.0225
	26600	4900	25900	0.4439
	24600	21800		
	21900	2200		
	19500	4000	22000	0.1079
	18300	6200		
	16600	450		
	10700	250		
	7300	300	7800	0.0241
	6400	300		
	5700	300		

Table 4.8 Transitions in the experimental and calculated UV/Vis/NIR spectra of $3,3'\text{-}(CN)_2\text{-bpy}$ and $[3,3'\text{-}(CN)_2\text{-bpy}]^{1-}$

Again comparison of the spectra indicates that the calculated spectrum matches the overall pattern of transitions observed in the experimental spectrum. However, it is noted that the calculation overestimates the energy of many of the transitions. Shown in table 4.8 are the experimental and calculated transitions observed in the UV/Vis/NIR spectrum of the $[3,3´\text{-}(CN)_2\text{-bpy}]^{1-}$ species.

Though the overall structural features of the experimental spectrum are reproduced accurately by the calculation it has failed to replicate the fine structure observed in some of the experimental peaks. This is possibly due to these features arising from vibrational coupling effects which cannot be accounted for in the TD-DFT calculation.

Analysis of the composition of the transitions in the calculated spectrum allows for the assignment of the bands observed in the experimental spectrum. It is of interest to note that the SOMO→LUMO transition can be assigned to the very low intensity band of peaks between 10700 - 5700 cm^{-1} in the experimental spectrum. The first features in the experimental spectrum with any significant intensity are the bands around 19000 cm^{-1}. These features can be attributed to transitions from the SOMO to higher lying empty π^* orbitals. The intense band observed at 24600 cm^{-1} can be assigned to a transition from the HOMO-1→SOMO. This equates to the HOMO→LUMO transition in the $3,3´\text{-}(CN)_2$-bpy species moving to lower energy upon reduction. The high energy bands at 34600 cm^{-1} and 31500 cm^{-1} can be assigned to transitions from the SOMO to very high energy π^* orbitals.

A similar approach can be adopted for the analysis of the spectra of the 4,4´-$(CN)_2$-bpy and 5,5´-$(CN)_2$-bpy compounds. Shown in figure 4.29 is an overlay of the calculated and experimental UV/Vis/NIR spectra of 4,4´-$(CN)_2$-bpy. The experimental and calculated transitions observed in the UV/Vis/NIR spectrum are reported in table 4.9.

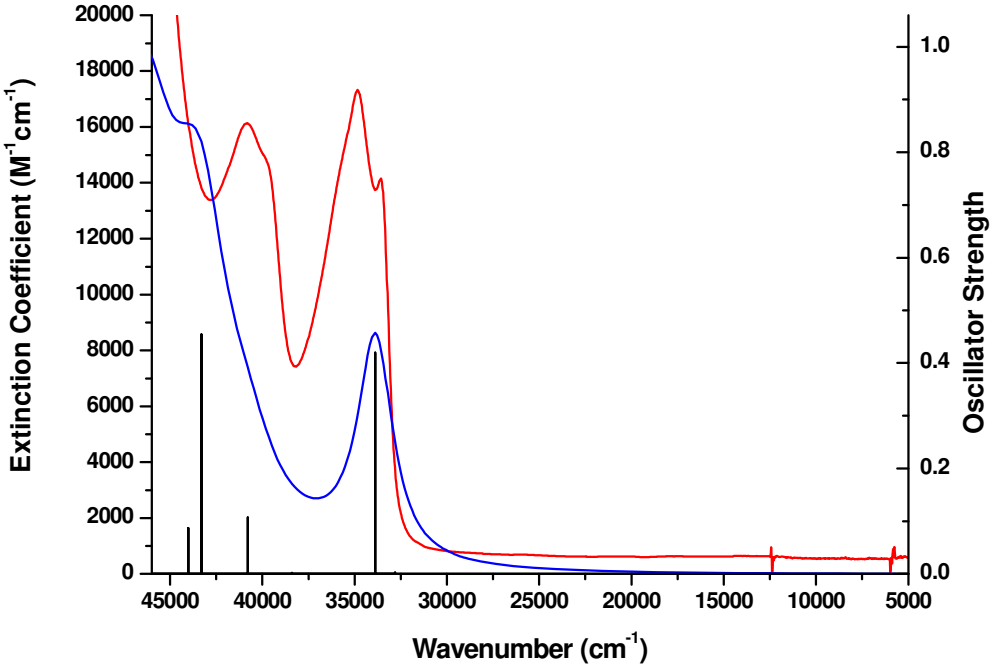

Figure 4.29 Overlay of the experimental UV/Vis/NIR spectrum (red) and the TD-DFT calculated spectrum (blue) of 4,4´-$(CN)_2$-bpy. Calculated transitions are shown as black columns

Analysis of the transitions in the calculated spectrum show that the lowest energy transition is due to the HOMO-LUMO transition, while the higher energy band around 40000 cm^{-1} is due to transition to higher lying π^* orbitals.

Shown in figure 4.30 is an overlay of the experimental and calculated spectra for the mono-reduced $[4,4´\text{-}(CN)_2\text{-bpy}]^{1-}$ species. As was found for $[3,3´\text{-}(CN)_2\text{-bpy}]^{1-}$ species, the calculation overestimates the energy of many of the observed transitions and has failed to replicate the fine structure observed in some of the experimental peaks. The experimental and calculated transitions are given in table 4.9.

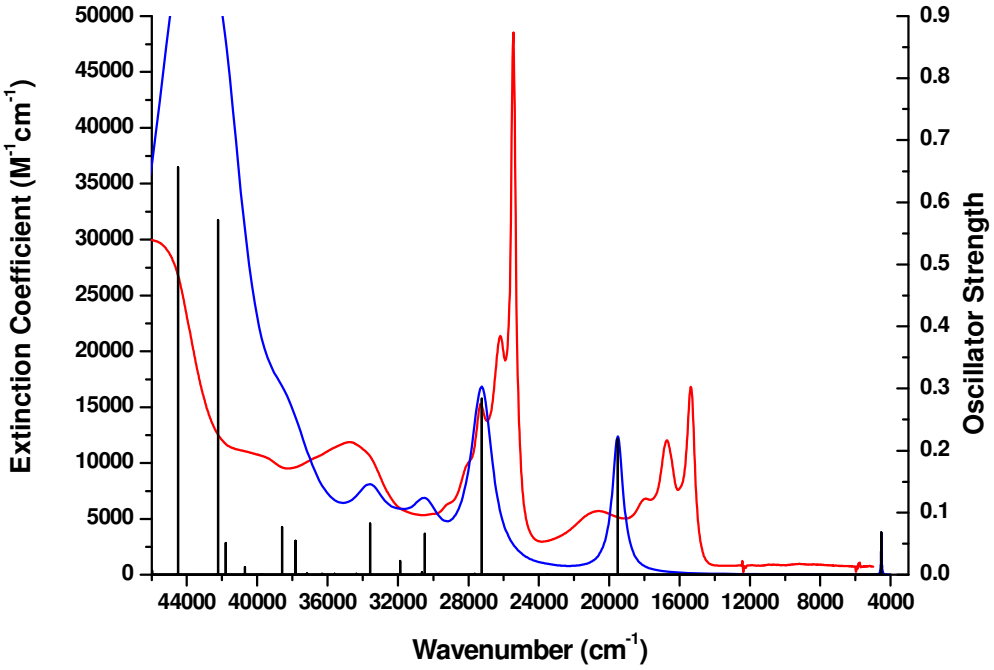

Figure 4.30 Overlay of the experimental UV/Vis/NIR spectrum (red) and the TD-DFT calculated spectrum (blue) of [4,4´-$(CN)_2$-bpy]$^{1-}$. Calculated transitions are shown as black columns

Analysis of the composition of the transitions in the calculated spectrum allows for the assignment of the bands observed in the experimental spectrum. Once again the SOMO→LUMO transition can be assigned to the very low intensity band of peaks between 10700 - 6600 cm^{-1} in the experimental spectrum. It is noted that the calculation has significantly underestimated the energy of this transition; with the peak appearing at 4500 cm^{-1}. The features between 20600 – 15400 cm^{-1} in the experimental spectrum can be attributed to transitions from the SOMO to higher lying empty π^* orbitals. The intense band observed at 25500 cm^{-1} can be assigned to a transition from the HOMO-1→SOMO. This equates to the HOMO→LUMO transition in the 4,4´-$(CN)_2$-bpy species moving to lower energy upon reduction. The high energy bands at 45400 cm^{-1}, 39500 cm^{-1} and 34700 cm^{-1} can be assigned to transitions from the SOMO to very high energy π^* orbitals.

	Experimental		Calculation	
	Wavenumber (cm^{-1})	Extinction Coefficient ($M^{-1}cm^{-1}$)	Wavenumber (cm^{-1})	Osc. Strength
4,4'-$(CN)_2$-bpy	40800	16100	43300	0.5074
	39800	14800	40800	0.1195
	34800	17300	33900	0.4682
	33600	14100		
$[4,4'\text{-}(CN)_2\text{-bpy}]^{1-}$	45400	29600	42200	0.5901
	39500	10500	38600	0.0795
	34700	11900	33600	0.0854
	27300	15300		
	26200	21400	27200	0.2931
	25500	48500		
	20600	5700		
	17900	6800	19500	0.2257
	16700	12000		
	15400	16800		
	10700	900		
	9200	1000	4500	0.0706
	8000	900		
	6600	800		

Table 4.9 Transitions in the experimental and calculated UV/Vis/NIR spectra of 4,4´-$(CN)_2$-bpy and $[4,4'\text{-}(CN)_2\text{-bpy}]^{1-}$

Shown in figure 4.31 is an overlay of the calculated and experimental UV/Vis/NIR spectra of 5,5´-$(CN)_2$-bpy. The experimental and calculated transitions observed in the UV/Vis/NIR spectrum are reported in table 4.10. The observed transition is again attributed to the HOMO-LUMO transition.

Shown in figure 4.32 is an overlay of the experimental and calculated spectra for the mono-reduced $[5,5'\text{-}(CN)_2\text{-bpy}]^{1-}$ species. In line with the findings for the other dicyanobipyridines the calculation overestimates the energy of many of the observed transitions and has failed to replicate the fine structure observed in some of the experimental peaks. The experimental and calculated transitions are given in table 4.10.

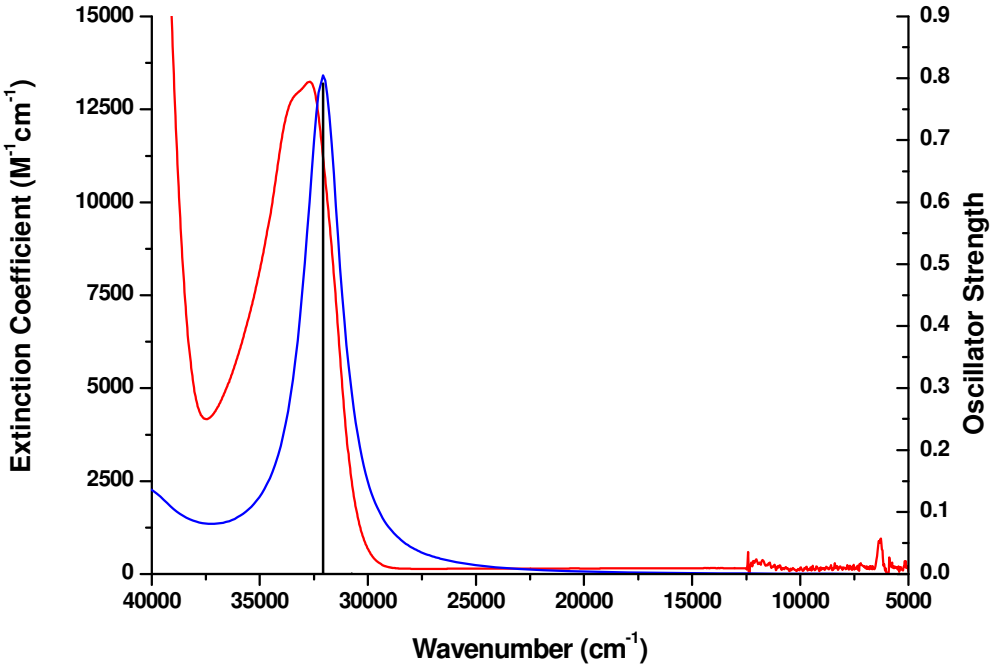

Figure 4.31 Overlay of the experimental UV/Vis/NIR spectrum (red) and the TD-DFT calculated spectrum (blue) of 5,5´-$(CN)_2$-bpy. Calculated transitions are shown as black columns

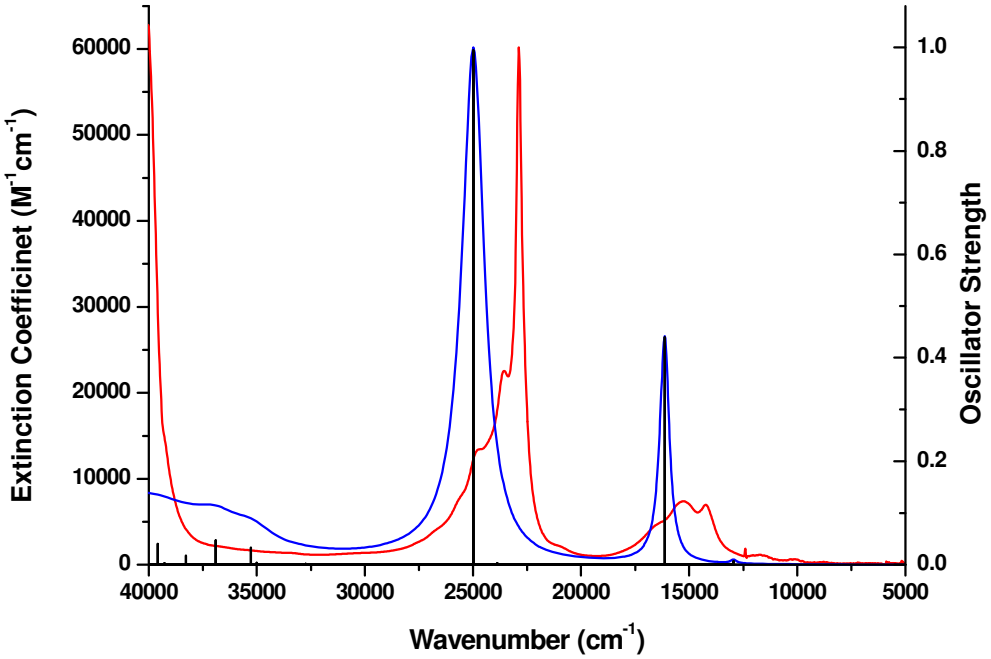

Figure 4.32 Overlay of the experimental UV/Vis/NIR spectrum (red) and the TD-DFT calculated spectrum (blue) of [5,5´-$(CN)_2$-bpy]$^{1-}$. Calculated transitions are shown as black columns

As with the other [X,X´-$(CN)_2$-bpy]$^{1-}$ species the SOMO→LUMO transition can be assigned to a low intensity band of peaks between 11600 - 8000 cm^{-1} in the experimental spectrum. It is noted that this band is blue-shifted compared to the

similar bands observed in the other cyano substistuted bpy compounds. The peaks around 16000 cm^{-1} in the experimental spectrum can be assigned to transitions from the SOMO to higher lying empty π^* orbitals. The highly intense band observed at 22900 cm^{-1} can be assigned to a transition from the HOMO-1→SOMO. This equates to the HOMO→LUMO transition in the 5,5´-$(CN)_2$-bpy species moving to lower energy upon reduction.

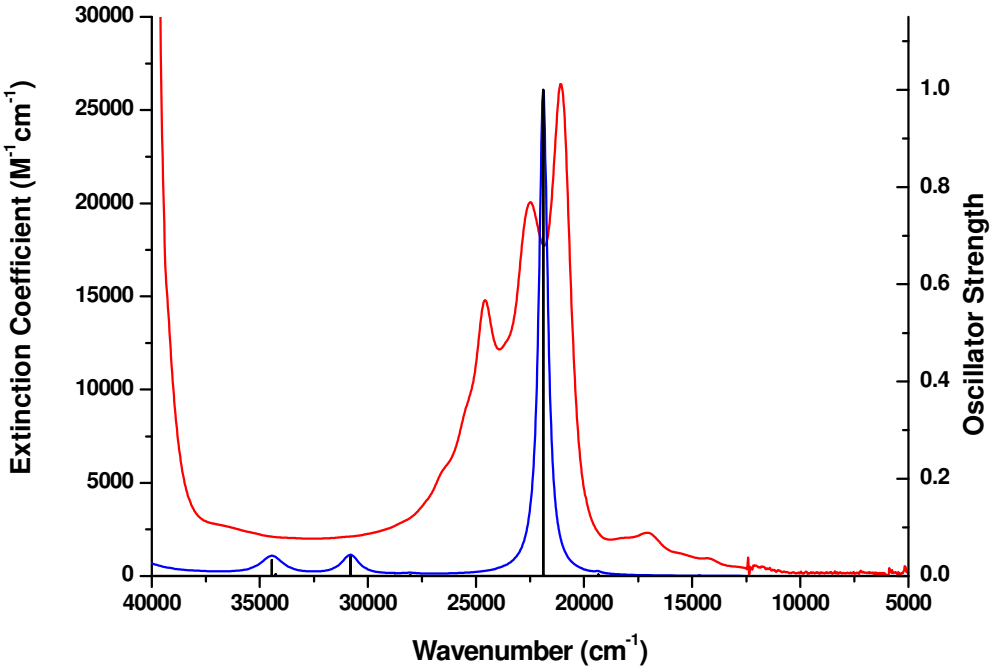

Figure 4.33 Overlay of the experimental UV/Vis/NIR spectrum (red) and the TD-DFT calculated spectrum (blue) of [5,5´-$(CN)_2$-bpy]$^{1-}$. Calculated transitions are shown as black columns

Shown in figure 4.33 is an overlay of the experimental and calculated spectra for the di-reduced [5,5´-$(CN)_2$-bpy]$^{2-}$ species. The overestimation in the energy of the observed transitions is smaller than for the mono-reduced compounds. However, the calculation has still failed to replicate the fine structure observed in the experimental spectrum. The experimental and calculated transitions are given in table 4.10.

The low intensity band at 14200 cm^{-1} in the experimental spectrum can be assigned to the transition from the now doubly occupied SOMO→LUMO. The peak at 16000

cm^{-1} and the band between 24600 - 21100 cm^{-1} in the experimental spectrum can be assigned to transitions from the SOMO to higher lying empty π^* orbitals.

	Experimental		Calculation	
	Wavenumber (cm^{-1})	Extinction Coefficient ($M^{-1}cm^{-1}$)	Wavenumber (cm^{-1})	Osc. Strength
5,5'-$(CN)_2$-bpy	32700	13200	32100	1.0574
$[5,5'\text{-}(CN)_2\text{-bpy}]^{1-}$	24800	11300		
	23600	21300	25000	0.9496
	22900	63800		
	16400	5900		
	15300	9200	16100	0.4195
	14200	8700		
	11600	1000		
	10200	650	12900	0.0068
	8900	200		
$[5,5'\text{-}(CN)_2\text{-bpy}]^{2-}$	24600	14800		
	22500	20100	21900	1.7034
	21100	26400		
	17100	2300	19300	0.0052
	14200	900	14600	0.0007

Table 4.10 Transitions in the experimental and calculated UV/Vis/NIR spectra of 5,5´-$(CN)_2$-bpy, $[5,5'\text{-}(CN)_2\text{-bpy}]^{1-}$ and $[5,5'\text{-}(CN)_2\text{-bpy}]^{2-}$

Calculations can be used in the same way to aid in the assignment of experimental EPR hyperfine coupling constants to specific nuclei in the paramagnetic species under investigation.

Shown in tables 4.11–4.13 are the hyperfine coupling constants calculated for the $[3,3'\text{-}(CN)_2\text{-bpy}]^{1-}$, $[4,4'\text{-}(CN)_2\text{-bpy}]^{1-}$ and $[5,5'\text{-}(CN)_2\text{-bpy}]^{1-}$ species respectively.

$[3,3'\text{-}(CN)_2\text{-bpy}]^{1-}$			
Coupling constant	Experimental	Calculated	Assignment
A(2 x ^{14}N) / G	0.95	0.63	Ring ^{14}N
A(2 x ^{14}N) / G	1.05	0.85	Cyano ^{14}N
A(2 x ^{1}H) / G	2.6	4.73	5,5´ position ^{1}H
A(2 x ^{1}H) / G	1.2	1.17	4,4´ position ^{1}H
A(2 x ^{1}H) / G	-	0.07	6,6´ position ^{1}H

Table 4.11 Experimental and calculated EPR hyperfine coupling constants for $[3,3'\text{-}(CN)_2\text{-bpy}]^{1-}$

$[4,4´\text{-}(CN)_2\text{-bpy}]^{1-}$			
Coupling constant	**Experimental**	**Calculated**	**Assignment**
A(2 x ^{14}N) / G	2.09	2.85	Ring ^{14}N
A(2 x ^{14}N) / G	0.18	0.38	Cyano ^{14}N
A(2 x ^{1}H) / G	7.00	5.78	5,5´ position ^{1}H
A(2 x ^{1}H) / G	0.85	0.94	6,6´ position ^{1}H
A(2 x ^{1}H) / G	-	0.24	3,3´ position ^{1}H

Table 4.12 Experimental and calculated EPR hyperfine coupling constants for $[4,4´\text{-}(CN)_2\text{-bpy}]^{1-}$

$[5,5´\text{-}(CN)_2\text{-bpy}]^{1-}$			
Coupling constant	**Experimental**	**Calculated**	**Assignment**
A(2 x ^{14}N) / G	0.95	0.92	Ring ^{14}N
A(2 x ^{14}N) / G	1.20	0.99	Cyano ^{14}N
A(2 x ^{1}H) / G	1.43	1.35	4,4´ position ^{1}H
A(2 x ^{1}H) / G	1.32	1.27	3,3´ position ^{1}H
A(2 x ^{1}H) / G	0.22	0.35	6,6´ position ^{1}H

Table 4.13 Experimental and calculated EPR hyperfine coupling constants for $[5,5´\text{-}(CN)_2\text{-bpy}]^{1-}$

Comparison of the experimental and calculated coupling constants for the three $[X,X´\text{-}(CN)_2\text{-bpy}]^{1-}$ species indicate that the calculations have been able to effectively replicate the pattern of coupling constants observed experimentally. By comparing the magnitude of the calculated and experimental hyperfine coupling constants it is possible to make assignment of a coupling to specific nuclei.

Through analysis of these calculations it is possible to solve the problem of differentiating the two observed ^{14}N couplings, which is not possible from experimental data alone. For the $[4,4´\text{-}(CN)_2\text{-bpy}]^{1-}$ compound the calculations indicate that the larger of the ^{14}N couplings is due the ring nitrogen atoms rather than nitrogen atoms of the electron withdrawing cyano substituents. This in accordance with what was found when the SOMO of the species was examined. This suggests that while the electron withdrawing substituent affects the electronic character of the molecule the electronic properties are still dominated by the bipyridine ring system.

Examination of the ^{1}H couplings constants indicates that the larger of the two observed couplings is due to the hydrogen atoms in the 5 and 5´ positions of the pyridine ring, while the smaller coupling is due to the hydrogen atoms in the 6 and 6´ positions. The coupling to remaining pair of hydrogen atoms in the 3 and 3´ positions is not observed experimentally and is predicted to be small, with a value of 0.24 G. This is much smaller than the experimental linewidth of 0.42 G so it is unlikely to be detected.

While the pattern of couplings observed for the $[5,5´\text{-}(CN)_2\text{-bpy}]^{1-}$ species follows the same trend as the $[4,4´\text{-}(CN)_2\text{-bpy}]^{1-}$ analogue the distribution of electron density can be seen to be different from examination of the calculations. As with the $[4,4´\text{-}(CN)_2\text{-bpy}]^{1-}$ species the calculations can be used to differentiate between the two ^{14}N couplings. In contrast to what was found for the previous compound the calculations indicate that the larger of the two couplings arises from the cyano group nitrogen nuclei and the smaller from the ring nitrogen nuclei.

The calculations can also be used to assign the ^{1}H coupling constants. The largest of the ^{1}H couplings can be assigned to the hydrogen atoms in the 4 and 4´positions of the bipyridine rings. The second largest of the ^{1}H couplings can be assigned to the hydrogen atom in the 3 and 3´ positions. Assignment of the remaining small ^{1}H coupling can be made to the hydrogen atoms in the 6 and 6´ positions. It is noted that the relative importance of the 3,3´ and 6,6´ positions appear to be inverted from what was observed for the $[4,4´\text{-}(CN)_2\text{-bpy}]^{1-}$ species.

When the calculated coupling constants for the [3,3´-$(CN)_2$-bpy]$^{1-}$ species are examined it can be seen that while the overall pattern of couplings is replicated well, the calculation has significantly overestimated the largest ^{1}H nuclei. This coupling is assigned to the hydrogen atoms in the 5,5´ positions. The smaller ^{1}H coupling has been calculated accurately and there is fairly good agreement with the two ^{14}N couplings. In this species the larger of the two ^{14}N couplings is due to the cyano group nitrogen atoms rather than the ring nitrogen atoms. As with [4,4´-$(CN)_2$-bpy]$^{1-}$ species the calculations have predicted a coupling to a pair of hydrogen atoms that is not observed experimentally. This coupling is attributed to the hydrogen atoms in the 6,6´positions and is predicted to be very small, with a value of 0.07 G. This is considerably smaller than the experimental linewidth of 0.85 G so it is not surprising that it is not detected.

4.5 Conclusion

Investigations into effect of substituting 2,2´-bipyridine with cyano functional groups has indicated that the dicyanobipyridines exhibit properties that are similar to many other substituted bpys previously investigated.[1-4,10] Electrochemical analysis has indicated that substitution with such electron withdrawing groups cause the two one-electron reductions of bpy to move to less negative potentials. UV/Vis/NIR and EPR studies have confirmed that the reduction electrons in each case enter a molecular orbital that is predominantly based on the bpy rings rather than localised to the substituent group.

Electrochemical investigations of the 3,3´-$(CN)_2$-bpy and 5,5´-$(CN)_2$-bpy have shown that both compounds undergo two sequential one-electron reductions. The separation between the first and second reduction, $\Delta E_{½}$, for both complexes suggests that in each case the second reduction is a spin pairing process. This is confirmed by the collapse of the EPR signal upon di-reduction. The 4,4´-$(CN)_2$-bpy compound exhibits only a single one-electron reduction in the available solvent window. Comparison of the reduction potentials indicates that 5,5´-$(CN)_2$-bpy is reduced at significantly less negative potentials than the 3,3´- or 4,4´-substituted analogues. The 4,4´-$(CN)_2$-bpy molecule exhibits the most negative reduction potential. This is in direct contrast to investigations on CO_2Et and NO_2 substituted bpy[1,2], which concluded that substitution at the 3,3´ resulted in the least stabilisation of the reduction electron.

Attempts to evaluate if 4,4´-$(CN)_2$-bpy and 5,5´-$(CN)_2$-bpy fit the previously observed correlations between the *para* Hammett parameter and the first reduction potential have resulted in good quality fits being obtained for both compounds. It is noted that the fit for the 5,5´-$(X)_2$-bpy compounds has a higher R^2 value indicating σ_p is more able to describe the interaction of the resonance and field effects in this these compounds than the 4,4´-$(X)_2$-bpy analogues.

The UV/Vis/NIR spectroelectrochemistry results for the three X,X´-$(CN)_2$-bpy compounds yield spectra for the mono-reduced species that are very similar to that obtained for CO_2Et analogous.[1] Comparison of the spectra of these compounds with the spectrum of $[bpy]^{1-}$ shows that all the spectra contain peaks at similar positions. Therefore it can be inferred that the electronic character of the frontier orbitals of bpy,

3,3´-$(CN)_2$-bpy, 4,4´-$(CN)_2$-bpy and 5,5´-$(CN)_2$-bpy are similar *i.e.* that the MO of the compounds are primarily based on the bpy part of the molecule.

EPR analysis of the three electrogenerated $[X,X´\text{-}(CN)_2\text{-bpy}]^{1-}$ mono-reduced species give rise to spectra that indicate that the reduction electron enters a molecular orbital that is spread over both rings rather than localised on one of the pyridine rings. Coupling to both the ring nitrogen atoms and the CN substituent group nitrogen atoms is observed for all three species.

DFT calculations have enabled the assignment of the observed coupling constants to specific nuclei. This has made it possible to differentiate the coupling to the ring nitrogen atoms and the substituent group nitrogen atoms. These results have indicated that the relative sizes of these couplings are quite different in each case. The $[3,3´\text{-}(CN)_2\text{-bpy}]^{1-}$ and $[5,5´\text{-}(CN)_2\text{-bpy}]^{1-}$ species exhibit a large coupling to the cyano group nitrogen atoms and a much smaller coupling to the ring nitrogen atoms. The inverse is found for the $[4,4´\text{-}(CN)_2\text{-bpy}]^{1-}$ species. This indicates that 3,3´ and 5,5´ analogues experience a greater degree of delocalisation on to the substituent which would account for the greater degree of stabilisation experienced by these species relative to 4,4´-$(CN)_2$-bpy.

4.6 References

1. E. A. M. Geary, K. L. McCall, A. Turner, P. R. Murray, E. J. L. McInnes, L. A. Jack, L. J. Yellowlees, N. Robertson, *Dalton Trans.,* 2008, 3701-3708.

2. P. R. Murray, Ph.D Thesis, University of Edinburgh, 2006.

3. L. Jack, Ph.D Thesis, University of Edinburgh, 2003.

4. S. K. Al-Musharafi, Ph.D Thesis, University of Edinburh, 2006.

5. C. Hansch, A. Leo, R. W. Taft, *Chem. Rev*., 1991, **91**, 165-195.

6. P. N. W. Baxter, J. A. Connor, D. C. Povey, J. D. Wallis, *J. Chem. Soc*., *Chem. Commun*., 1991, **16**, 1135-1137.

7. L. L. Merritt Jr., E. D. Schroeder, *Acta Cryst*., 1956, **9**, 801-804.

8. E. König, S. Kremer, *Chem. Phys. Lett*., 1970, **5**(2), 87-90.

9. A. Göller, U.-W. Grummt, *Chem. Phys. Lett*., 2000, **321**, 399-405.

10. E. J. L. McInnes, R. D. Farley, C. C. Rowlands, A. J. Welch, L. Rovatti, L. J. Yellowlees, *J. Chem. Soc*., *Dalton Trans*., 1999, 4203-4208.

5 Electrochemical and Spectroelectrochemical characterisation of 3,3´-$(CF_3)_2$-bpy, 4,4´-$(CF_3)_2$-bpy and 5,5´-$(CF_3)_2$-bpy

5.1 Introduction

It is of interest to note that of the wide range of substituted bipyridines that have been studied to date,[1-5] no investigation has been conducted into substituents that have an overall electron withdrawing character but have little or no effect on the conjugated π-system. As previously discussed in section 1.2, attempts to quantify the electronic effect on the bipyridine ring system of substitution with electron withdrawing/donating substituents using Hammett parameters has highlighted some deficiencies in the model. This has been attributed to the inability of the Hammett parameters to accurately account for the relative contributions of Field/Inductive and Resonance effects in the bipyridine system.

Previous spectroelectrochemical studies of substituted bipyridines have concluded that the LUMO in each case is located predominantly on the bpy π-system.[1-4] It is therefore of interest to investigate the effect of addition of a substituent that does not contribute to the π-orbitals of the bpy ring system.

The trifluoromethyl substituent has good chemical stability and is a very strong σ-acceptor, making it an ideal candidate for this investigation.[6] Shown in table 5.1 are the Hammett parameters and the corresponding Field/Induction and Resonance

parameters for the CF_3 substituent and a number of electron withdrawing groups that exhibit extensive π-type resonance delocalisation which have been studied previously.

	σ_m	σ_p	F	R
CO_2Et	0.37	0.45	0.34	0.11
CF_3	0.43	0.54	0.38	0.16
CN	0.56	0.66	0.51	0.15
NO_2	0.71	0.78	0.65	0.13

Table 5.1 Hammett parameters, Field/Induction parameters and Resonance parameters for CO_2Et, CF_3, CN and NO_2 substituent groups[7]

Comparison of the F parameters for the four substituents indicates that CF_3 possess a Field/Induction effect of similar magnitude to that of CO_2Et. It is noted that the CF_3 substituent possesses the largest Resonance parameter of the substituents studied to date. Therefore the resonance effects are likely to be significant for ditrifluoromethyl substituted bpys.

The synthesis of 4,4´-$(CF_3)_2$-bpy and 5,5´-$(CF_3)_2$-bpy have been reported previously.[6,8] However studies have concentrated on complexes containing X,X´-$(CF_3)_2$-bpy ligands and detailed electrochemical characterisation of the ligands themselves has not been reported. This chapter therefore details the electrochemical and spectroelectrochemical (UV/Vis/NIR, EPR) characterisation of the ditrifluromethyl substituted bpy ligands, 3,3´-$(CF_3)_2$-bpy, 4,4´-$(CF_3)_2$-bpy and 5,5´-$(CF_3)_2$-bpy to enable comparison with previous work and to determine the importance of resonance stabilisation.

5.2 Crystal Structures

The crystal structures of 4,4´-$(CF_3)_2$-bpy and 5,5´-$(CF_3)_2$-bpy have been determined for the first time in this work. Full crystallographic data for both molecules is given in the appendix.

Shown in figure 5.1 is the crystal structure of 4,4´-$(CF_3)_2$-bpy. The unit cell is monoclinic with a = 11.79 Å, b = 12.69 Å, c = 7.68 Å and β = 102°. The space group is $P2_1/c$ and there are four molecules per unit cell. The average C-C and C-N bond lengths in the pyridine rings are 1.38 Å and 1.34 Å respectively. These bond lengths are slightly shorter than the same bonds observed for bipyridine.[9] The C(2)-C(2´) bond length is 1.49 Å which again is slightly shorter than the equivalent bond in bpy. The two substituted pyridine rings are slightly twisted away from coplanarity, with a N(1)-C(2)-C(2´)-N(1´) torsional angle of 177.8° The resulting angle between the rings planes of 2.2° is only slightly larger than that observed in unsubstituted bpy.

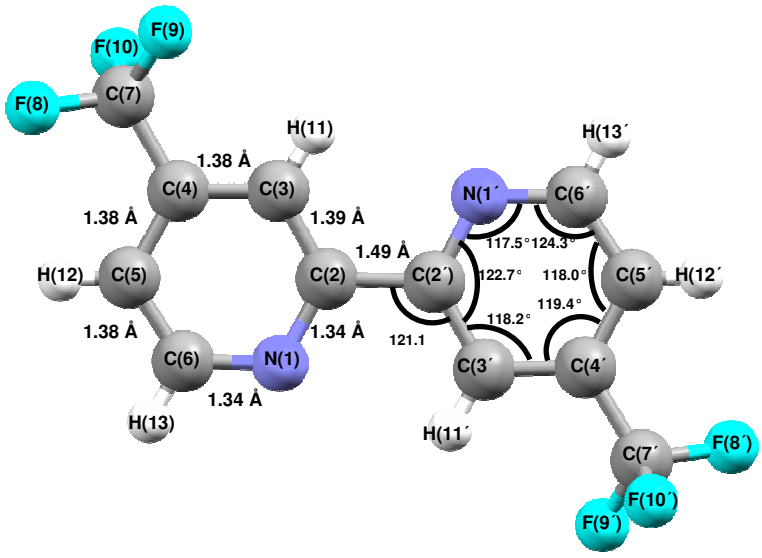

Figure 5.1 Crystal structure of 4,4´-$(CF_3)_2$-bpy

Shown in figure 5.2 is the crystal structure of 5,5´-$(CF_3)_2$-bpy. The unit cell is triclinic with a = 7.19 Å, b = 7.30 Å, c = 11.09 Å, α = 76.4° β = 81.9° and γ = 80.9°. The space group is $P\bar{1}$ and there are two molecules per unit cell. The average C-C and C-N bond lengths in the pyridine rings are 1.39 Å and 1.34 Å respectively. The C-C bond length agrees well with the same bonds observed in bipyridine while the C-N bonds are slightly shorter than for bpy.[9] The C(2)-C(2´) bond length is 1.49 Å which again is slightly shorter than the equivalent bond in bpy. The two substituted pyridine rings are slightly twisted away from coplanarity, with a N(1)-C(2)-C(2´)-N(1´) torsional angle of 172.6° The resulting angle between the rings planes of 7.4° is only slightly larger than that observed in unsubstituted bpy.

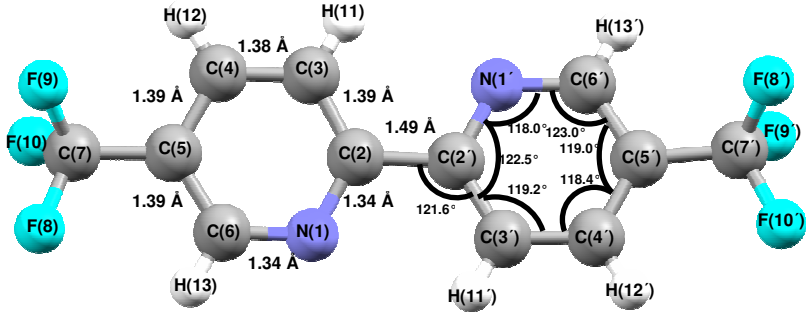

Figure 5.2 Crystal structure of 5,5´-$(CF_3)_2$-bpy

5.3 Electrochemistry

5.3.1 Cyclic Voltammetry

The cyclic voltammogram of 3,3´-$(CF_3)_2$-bpy in 0.1 M [TBA][BF_4]/DMF at 298 K, shown in figure 5.3, exhibits an irreversible reduction at E_{pc} = -1.50 V.

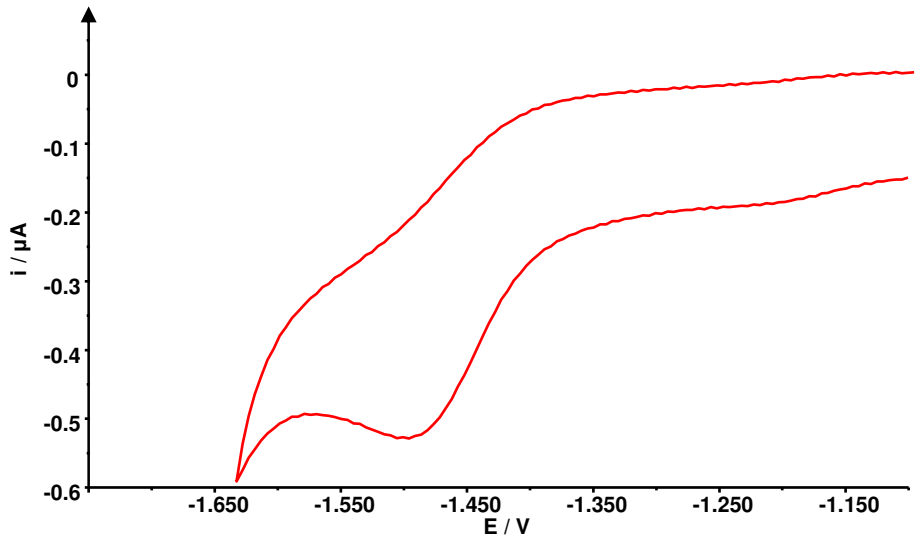

Figure 5.3 Cyclic Voltammogram of 3,3´-$(CF_3)_2$-bpy *vs*. Ag/AgCl in 0.1 M [TBA][BF_4]/DMF at 298 K, ν = 100 mVs^{-1}

The scan rate was increased sequentially from 0.1 Vs^{-1} to 1.0 Vs^{-1} in an attempt to investigate the irreversible nature of the reaction. It was determined that even at the highest scan rate the reaction remained irreversible. This indicates that a rapid decomposition process is occurring following the electron transfer. No further study of this system was attempted.

When the cyclic voltammogram for 4,4´-$(CF_3)_2$-bpy in 0.1 M [TBA][BF_4]/DMF at 298 K was recorded one reversible reduction reaction was observed, see figure 5.4 below. The $E_{½}$ value for this redox couple is -1.52 V. A plot of i_p *vs.* $v^{½}$ for the reduction of 4,4´-$(CF_3)_2$-bpy reveals a linear relationship. This indicates that the reduction is diffusion controlled.

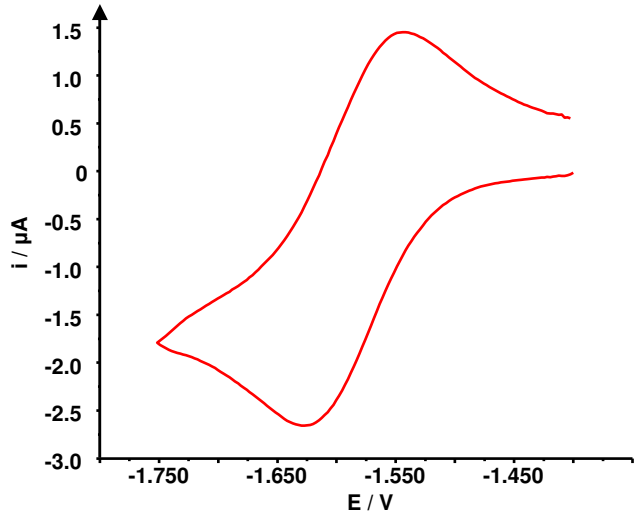

Figure 5.4 Cyclic Voltammogram of 4,4´-$(CF_3)_2$-bpy *vs*. Ag/AgCl in 0.1 M [TBA][BF_4]/DMF at 298 K, ν = 100 mVs^{-1}

The cyclic voltammogram of 5,5´-$(CF_3)_2$-bpy in 0.1 M [TBA][BF_4]/DMF at 298 K, figure 5.5, indicates that it also has one reversible reduction process with an $E_{½}$ value of –1.38 V.

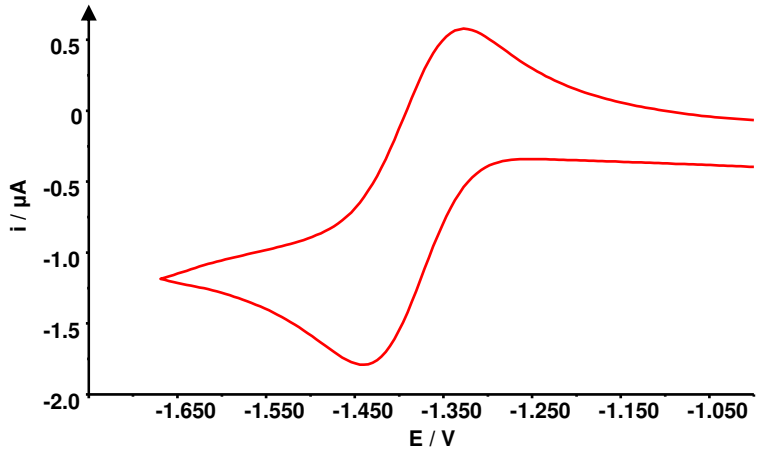

Figure 5.5 Cyclic Voltammogram of 5,5´-$(CF_3)_2$-bpy *vs*. Ag/AgCl in 0.1 M [TBA][BF_4]/DMF at 298 K, ν = 100 mVs^{-1}

The reduction potentials for all of the processes observed in the cyclic voltammetric investigation of the three ditrifluoromethylbipyridine ligands are shown in table 5.2. Comparison of the potentials for the reductions in each of the compounds clearly shows that the 5,5´-$(CF_3)_2$-bpy ligand is reduced at significantly less negative potentials than either the 3,3´ or 4,4´ substituted ligands.

	$E_{½}$ /V
3,3´-$(CF_3)_2$-bpy	**-1.50***
4,4´-$(CF_3)_2$-bpy	**-1.52**
5,5´-$(CF_3)_2$-bpy	**-1.38**

Table 5.2 Half wave reduction potentials for 3,3´-$(CF_3)_2$-bpy, 4,4´-$(CF_3)_2$-bpy and 5,5´-$(CF_3)_2$-bpy. * indicates a irreversible process, E_{pc} value is quoted for this process

Plots of the Hammett parameter $\sigma_{p,}$ *vs*. the first reduction potential of a series of substituted bipyridines including the 4,4´-$(CF_3)_2$-bpy and 5,5´-$(CF_3)_2$-bpy compounds investigated during these studies, are shown in figure 5.6 and figure 5.7, in order to establish if the CF_3 substitution group follows the previously determined correlation observed for the 4,4´-$(X)_2$-bpy and 5,5´-$(X)_2$-bpy ligands (see section 4.2.1).

From figure 5.6 it can be seen that inclusion of the data for 4,4´-$(CF_3)_2$-bpy leads to an improved agreement with the predicted correlation of the reduction potential with σ_p, the R^2 value for the linear fit having increased from 0.8838 in figure 4.5 to 0.8915 in figure 5.6.

Conversely the $E_{½,(1)}$ of the 5,5´-$(CF_3)_2$-bpy ligand gives a poorer agreement with the predicted correlation with σ_p, the linear fit having a R^2 value of 0.9121. This value is reduced slightly from the plot in figure 4.6 but does not represent a marked departure from the previously observed correlation.

Thus the general observation that the half-wave reduction potential for substituted bpys is dependent on σ_p still holds.

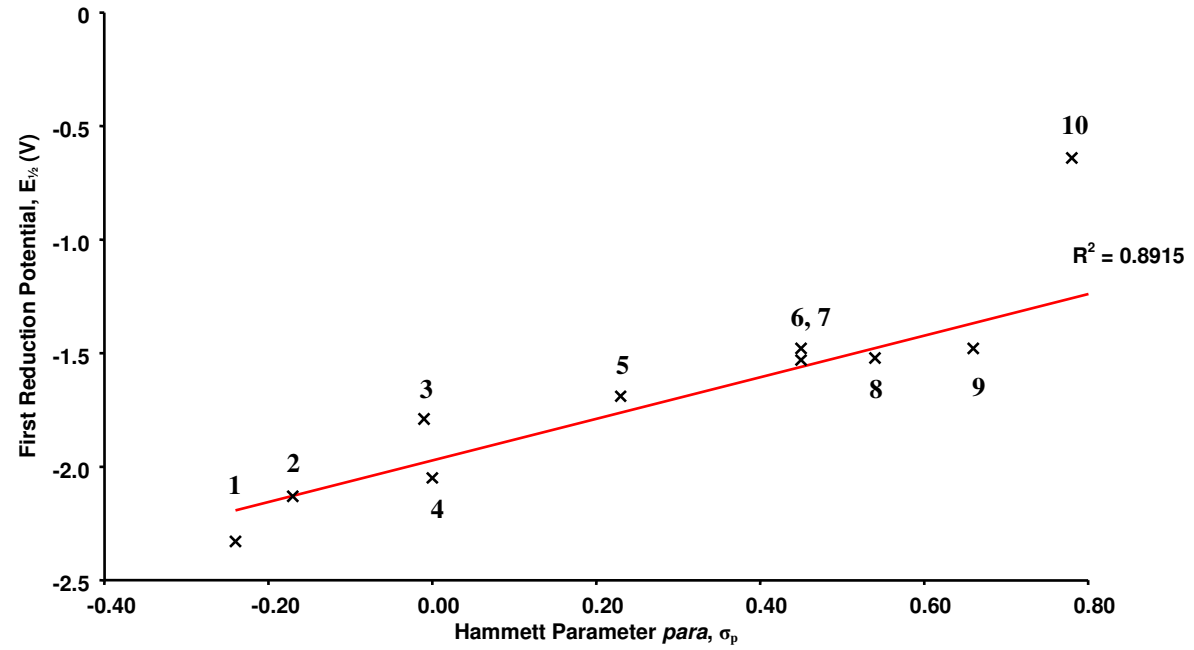

Figure 5.6 Plot of $E_{½}$ of the first reduction of 4,4´-$(X)_2$-bpy *vs. para* Hammett parameter, σ_m of the substituent X, (were X is the substituent under investigation). 1) X= OEt, 2) X = Me, 3) X = Ph, 4) X = H, 5) X = Cl, 6) X = CO_2Me 7) X = CO_2Et, 8) X= CF_3 9) X = CN and 10) X = NO_2 (4,4´-$(NO_2)_2$-bpy data excluded from the linear fit due to the unusual properties of this compound)[2]

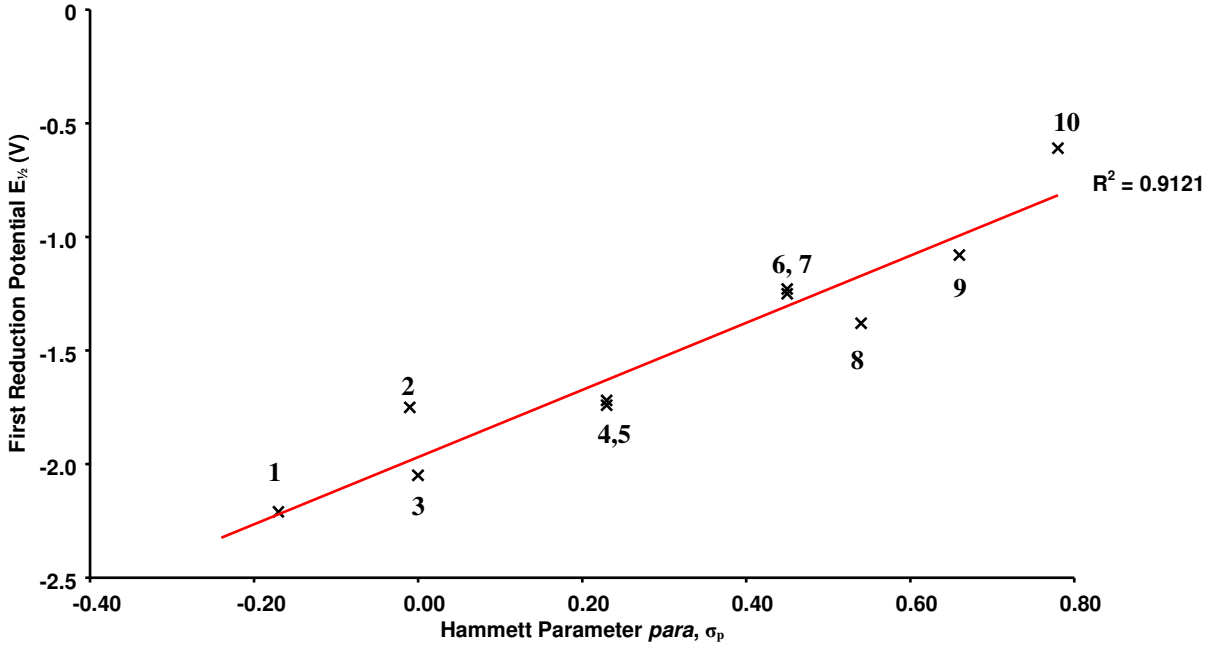

Figure 5.7 Plot of $E_{½}$ of the first reduction of 5,5´-$(X)_2$-bpy *vs. para* Hammett parameter, σ_p of the substituent X, (were X is the substituent under investigation). 1) X= Me, 2) X = Ph, 3) X = H, 4) X = Cl, 5) X = Br, 6) X = CO_2Me, 7) X = CO_2Et 8) X = CF_3 9) X = CN and 10) X = NO_2

5.3.2 Differential Pulse Voltammetry

The differential pulse voltammograms for the three ditrifluoromethyl pro-ligands were also recorded to compare with the results of the cyclic voltammetry experiments. The differential pulse voltammograms for the 4,4´-$(CF_3)_2$-bpy and 5,5´-$(CF_3)_2$-bpy confirmed the findings from the cyclic voltammogram, indicating that both compounds had one reversible reduction at -1.52 V and -1.39 V respectively. The voltammogram for 5,5´-$(CF_3)_2$-bpy is shown below in figure 5.8.

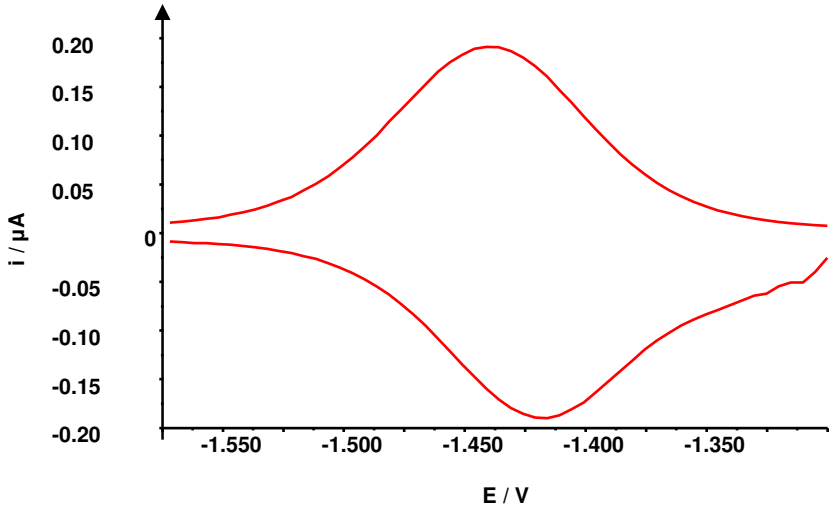

Figure 5.8 Differential Pulse Voltammogram of 5,5´-$(CF_3)_2$-bpy in 0.3M [TBA][BF_4]/DMF at 298 K

When the differential pulse voltammetry of the 3,3´-$(CF_3)_2$-bpy compound was conducted it indicated that the reaction was not irreversible as the CV had suggested, but was in fact a quasi-reversible reduction, figure 5.9. The quasi-reversible peak has $E_{½}$ = -1.46 V.

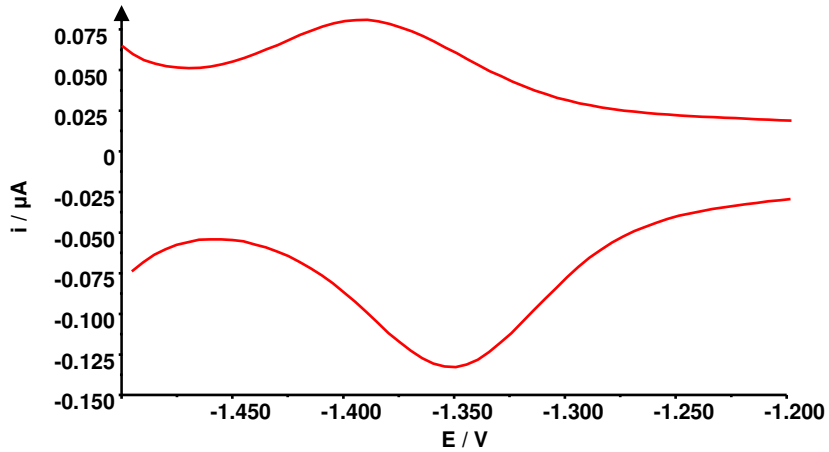

Figure 5.9 Differential Pulse Voltammogram of 3,3´-$(CF_3)_2$-bpy in 0.3M [TBA][BF_4]/DMF at 298 K

5.4 Spectroelectrochemistry

5.4.1 Ultra Violet/Visible/Near Infra-Red Spectroelectrochemistry

The UV/Vis/NIR spectrum of 4,4´-$(CF_3)_2$-bpy in 0.1M [TBA][BF_4]/DMF at 233 K before a potential was applied is shown in figure 5.10. From the spectrum it can be seen that there is one intense transition at approximately 34800 cm^{-1} (ε = 15200 $M^{-1}cm^{-1}$). The peak is assigned to a HOMO-LUMO π-π^* transition.

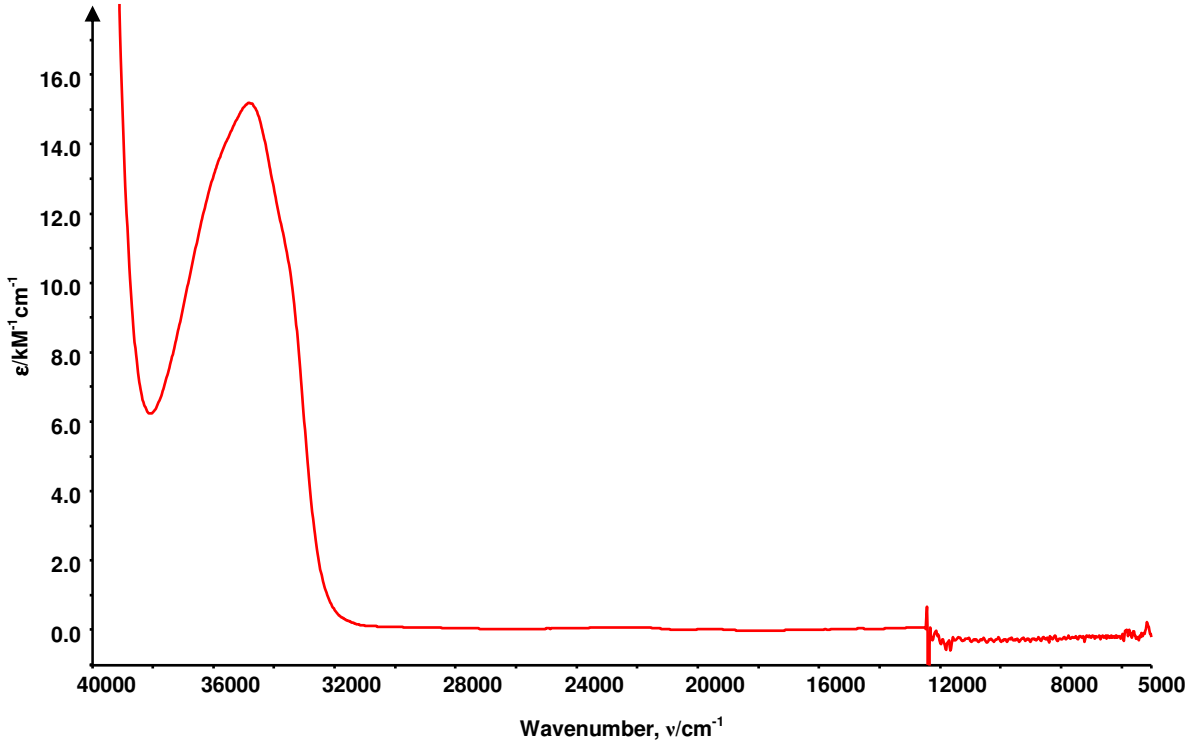

Figure 5.10 UV/Vis/NIR of 4,4´-$(CF_3)_2$-bpy in 0.1 M [TBA][BF_4]/DMF at 233 K

A potential of -1.8 V was then applied to the system to generate the mono-reduced [4,4´-$(CF_3)_2$-bpy]$^{1-}$ species. Figure 5.11 shows the spectrum of the system during the reduction process which proceeded for 110 minutes. By comparing figure 5.10 and 5.11 the changes in the absorption character of the compound can be clearly seen. The intense peak that was present in the initial spectrum has collapsed over the course of the experiment. In addition there are a series of new peaks that have appeared and grown in as the potential is applied and continue to increase until the point of

maximum growth. The position and extinction coefficient of these peaks are given in table 5.3. These bands were assigned to intraligand transitions involving the partially filled lowest energy π^* orbital. When the generation potential was switched back to 0 V the original spectrum was regenerated indicating that the reduction is reversible.

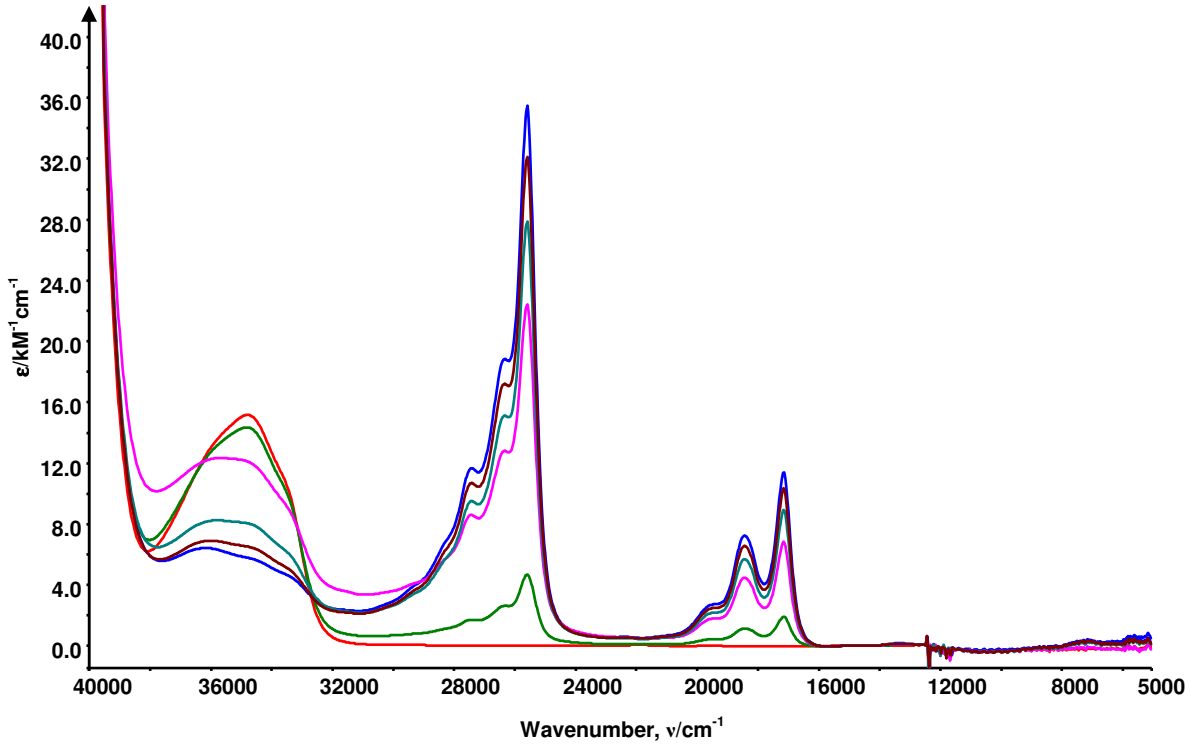

Figure 5.11 UV/Vis/NIR of 4,4´-$(CF_3)_2$-bpy *vs*. Ag/AgCl in 0.1 M [TBA][BF_4]/DMF at 233 K 110 minutes after a potential of 1.8 V *vs*. Ag/AgCl was applied. Initial spectrum red, final spectrum blue

	Wavenumber (cm^{-1})	Extinction Coefficient ($M^{-1}cm^{-1}$)
4,4'-$(CF_3)_2$-bpy	34800	15200
$[4,4'\text{-}(CF3)_2\text{-bpy}]^{1-}$	36100	6400
	29400	3900
	28200	7100
	27400	11700
	26300	18800
	25600	35600
	19600	2700
	18400	7300
	17200	11400
	14900	100
	13400	250
	8600	300
	7200	700
	5500	700

Table 5.3 Peak positions and extinction coefficient for signals in the UV/Vis/NIR spectra of 4,4´-$(CF_3)_2$-bpy and $[4,4'\text{-}(CF_3)_2\text{-bpy}]^{1-}$

Comparison of the spectrum of the $[4,4'\text{-}(CF_3)_2\text{-bpy}]^{1-}$ with the spectral information reported for $[bpy]^{1-}$ by König and Kremer[10] indicates, that like many other substituted bipyridines[1-4], the LUMO of 4,4´-$(CF_3)_2$-bpy is primarily based on the bpy rings with only a minor contribution from the substituent.

The spectrum of 5,5´-$(CF_3)_2$-bpy in 0.1M [TBA][BF_4]/DMF at 233 K is shown in figure 5.12. The spectrum again shows an intense peak at approximately 35500 cm^{-1} (ε = 13500 $M^{-1}cm^{-1}$) with a shoulder at 34700 cm^{-1} (ε = 13100 $M^{-1}cm^{-1}$). This band is assigned to a HOMO-LUMO π-π^* transition.

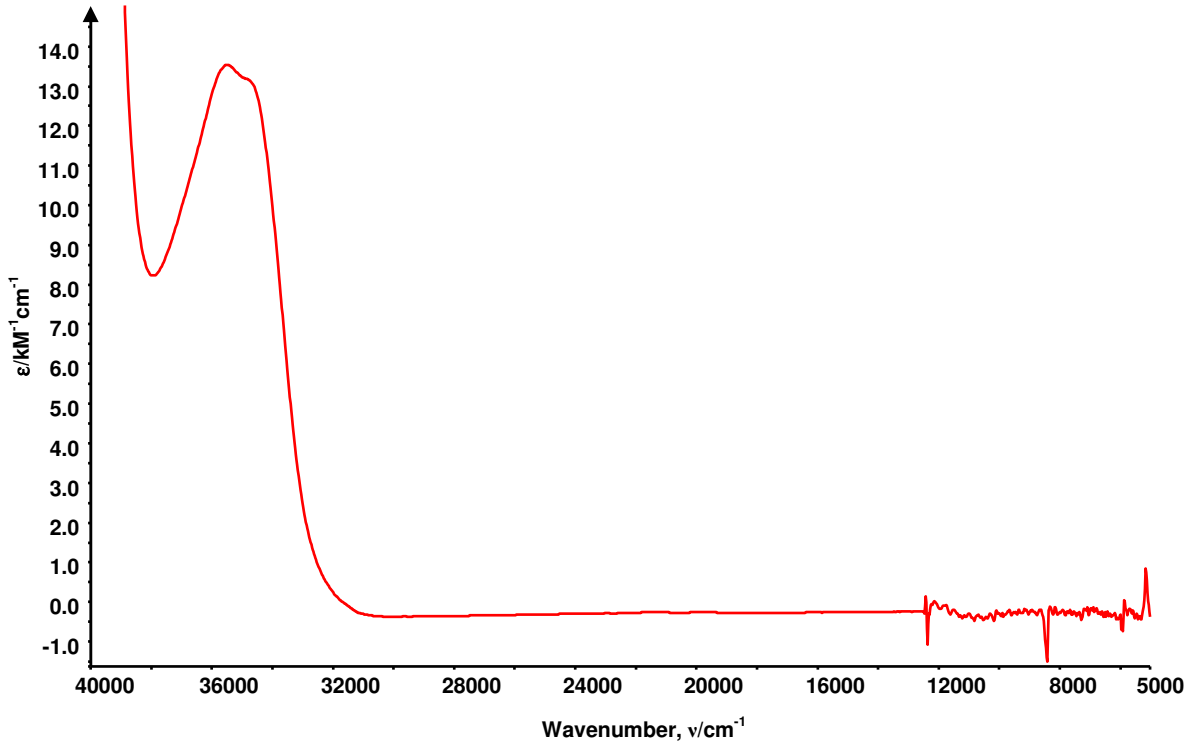

Figure 5.12 UV/Vis/NIR of 5,5´-$(CF_3)_2$-bpy in 0.1 M [TBA][BF_4]/DMF at 233 K

A potential of -1.65 V was then applied to generate the mono-reduced $[5,5'\text{-}(CF_3)_2\text{-bpy}]^{1-}$ species. The spectra collected during the application of the generation potential for 290 minutes is shown in figure 5.13. Comparison of the spectra shows that the peak at 35500 cm^{-1} and its shoulder have decreased in intensity,

while a series of new peaks have grown in during the course of the experiment. The position and extinction coefficient of these peaks is given in table 5.4.

	Wavenumber (cm^{-1})	Extinction Coefficient ($M^{-1}cm^{-1}$)
5,5'-$(CF_3)_2$-bpy	35500 34700	13500 13100
[5,5'-$(CF3)_2$-bpy]$^{1-}$	36500 35600 27800 27100 25800 25100 18000 16900 15200 13600 11300 10100 8900 7500	4700 4800 6000 9700 18200 32400 6100 8100 1200 600 400 475 450 300

Table 5.4 Peak positions and extinction coefficient for signals in the UV/Vis/NIR spectra of 5,5´-$(CF_3)_2$-bpy and [5,5´-$(CF_3)_2$-bpy]$^{1-}$

The fact that the spectral features between 30000 – 5000 cm^{-1} are not present in the non-reduced spectrum and then appear after the generation potential is applied is a clear indicator that these peaks are due to the [5,5´-$(CF_3)_2$-bpy]$^{1-}$ species. The finding is supported by the isosbestic point at 32700 cm^{-1}.

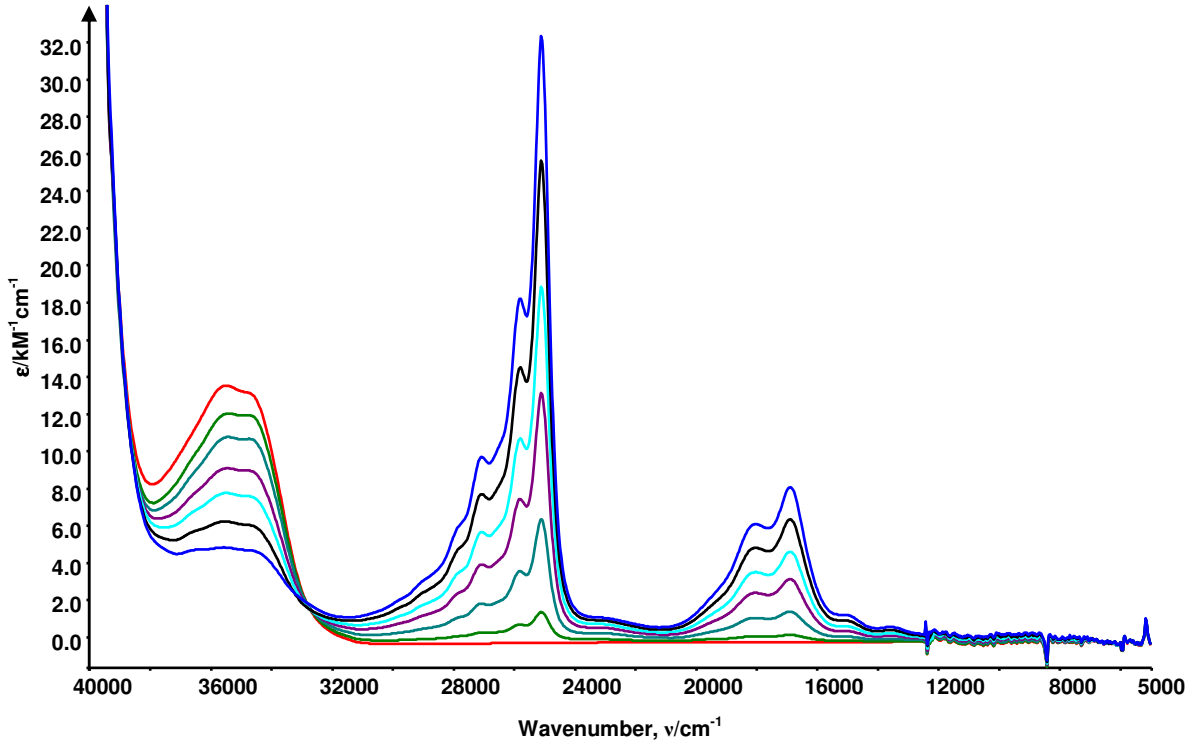

Figure 5.13 UV/Vis/NIR of 5,5´-$(CF_3)_2$-bpy *vs*. Ag/AgCl in 0.1 M [TBA][BF_4]/DMF at 233 K 290 minutes after a potential of 1.65 V *vs*. Ag/AgCl was applied. Initial spectrum red, final spectrum blue

Once again the peaks characteristic of $[bpy]^{1-}$ can be observed,[10] indicating that the LUMO of 5,5´-$(CF_3)_2$-bpy is located predominantly on the bpy rings. These bands were again assigned to intraligand transitions involving semi-occupied lowest energy π^* orbital.

5.4.2 EPR Spectroelectrochemistry

In-situ electrogeneration was used to generate the EPR active mono-reduced species $[4,4´\text{-}(CF_3)_2\text{-bpy}]^{1-}$ and $[5,5´\text{-}(CF_3)_2\text{-bpy}]^{1-}$. A potential of -1.8 V was used to generate the $[4,4´\text{-}(CF_3)_2\text{-bpy}]^{1-}$ species and a potential of -1.65 V was used to generate the $[5,5´\text{-}(CF_3)_2\text{-bpy}]^{1-}$.

The EPR spectrum recorded for the $[4,4´\text{-}(CF_3)_2\text{-bpy}]^{1-}$ species shown in figure 5.14 consists of 13 main peaks with extensive further fine structure. Simulation of the experimental spectrum was achieved by including coupling to a pair of equivalent ^{14}N nuclei, six equivalent ^{19}F nuclei and three pairs of two equivalent ^{1}H nuclei. This pattern of couplings can only be possible if the unpaired electron is delocalised over the entire molecule rather than being localised to one of the CF_3-py rings.

The largest couplings results from coupling to a pair of symmetry related ^{1}H nuclei with a coupling constant of 5.25 G. Assuming that this large coupling arises for the hydrogen nuclei at the 5,5´ positions this observation is consistent with the hypothesis that significant electron density of the bpy based LUMO is located at the 5,5´ positions.[11,12] The couplings to the two ^{14}N nuclei and the six ^{19}F nuclei are of a similar size with coupling constants of 3.03 G and 2.98 G respectively. The remaining two ^{1}H coupling are significantly smaller with coupling constants of 0.99 G and 0.56 G which are tentatively assigned to the ^{1}H nuclei in the 3,3´ and 6,6´ positions.

Specific assignment of these couplings cannot be made from these experimental results alone but previous studies have shown that the ^{1}H nuclei in the 6,6´ positions contribute least to the EPR spectra.[11,12] It is therefore tempting to assign the smaller ^{1}H coupling to the hydrogen nuclei in 6,6´ the positions and the hydrogen nuclei in 3,3´ positions to the 0.99 G coupling.

The EPR spectrum obtained for the $[5,5´\text{-}(CF_3)_2\text{-bpy}]^{1-}$ species is shown figure 5.15, it comprises a septet of quintets with fine structure from additional couplings also observed. Simulation of the experimental spectrum was achieved by considering coupling to a pair of equivalent ^{14}N nuclei, six equivalent ^{19}F nuclei, four equivalent ^{1}H nuclei and a pair of ^{1}H nuclei. Though the overall coupling pattern is similar to that observed for the $[4,4´\text{-}(CF_3)_2\text{-bpy}]^{1-}$ species the size of the coupling constants corresponding to each set of nuclei are wildly different. The largest coupling by far in this spectrum is to the six ^{19}F nuclei resulting in a coupling constant of 13.19 G, leading to the clearly observable septet. The coupling to the ring nitrogen atoms is significantly smaller than that observed for the 4,4´ analogue with a coupling constant of 1.61 G. That a coupling constant of 1.61 G arising from coupling to four equivalent ^{1}H nuclei is observed suggests that a similar amount of electron density is localised at four positions around the bpy ring system. The remaining ^{1}H coupling is much smaller with a coupling constant of 0.52 G. This indicates that there is significantly less electron density localised at these positions. Assignment of the ^{1}H couplings is again not possible from the experimental data alone but comparison with pervious studies on $[5,5´\text{-}(X)_2\text{-bpy}]^{1-}$ compounds suggest that the smallest coupling arises from the ^{1}H nuclei in the 6,6´ positions.

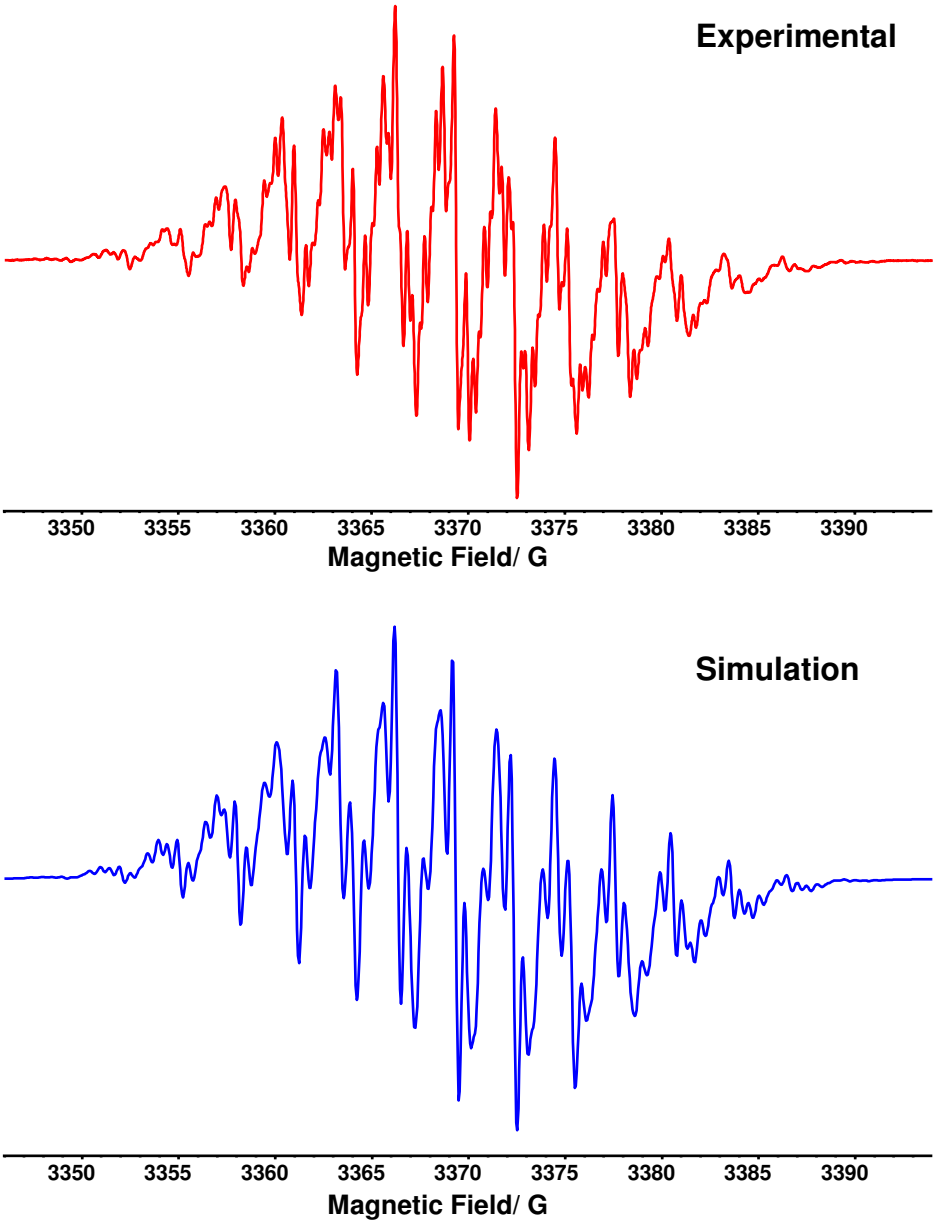

$A_{2\ ^{14}N} = 3.03\ G$

$A_{6\ ^{19}F} = 2.98\ G$

$A_{2\ ^{1}H} = 5.25\ G$

$A_{2\ ^{1}H} = 0.99\ G$

$A_{2\ ^{1}H} = 0.56\ G$

$\Delta H_{pp} = 0.41\ G$

$L/G = 0$

$g_{iso} = 2.00315$

Figure 5.14 Experimental and simulated EPR of $[4,4'\text{-}(CF_3)_2\text{-bpy}]^{1-}$ generated *in-situ* at -1.8 V *vs.* Ag/AgCl at 233 K in 0.1 M [TBA][BF_4]/DMF

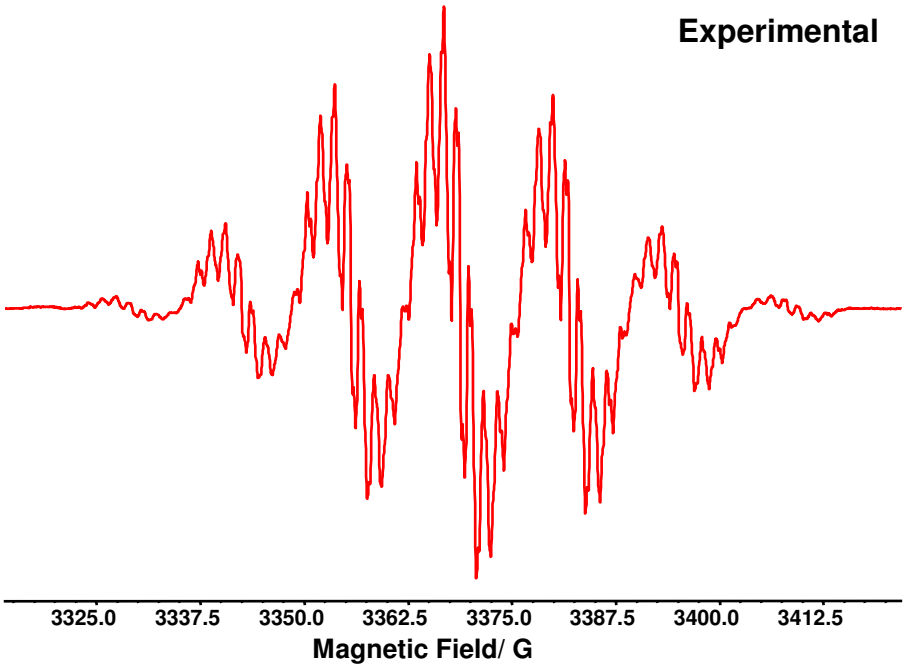

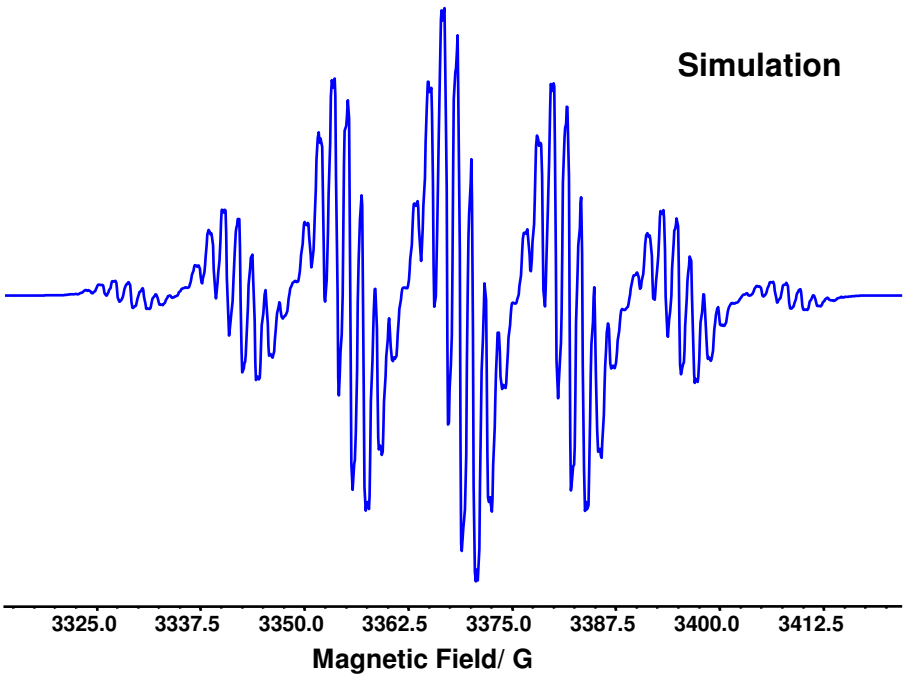

$A_{2\ ^{14}N} = 1.61\,G$

$A_{6\ ^{19}F} = 13.19\,G$

$A_{4\ ^{1}H} = 1.61\,G$

$A_{2\ ^{1}H} = 0.52\,G$

$\Delta H_{pp} = 0.60\,G$

$L/G = 0$

$g_{iso} = 2.0035$

Figure 5.15 Experimental and simulated EPR of $[5,5'\text{-}(CF_3)_2\text{-bpy}]^{1-}$ generated *in-situ* at -1.65 V *vs*. Ag/AgCl at 233 K in 0.1 M $[TBA][BF_4]$/DMF

5.5 Calculations

DFT calculations were undertaken in an attempt to gain a greater understanding of the electronic properties of the X,X´-$(CF_3)_2$-bpy compounds and to aid in the assignment of EPR couplings.

Shown in figure 5.16 and 5.17 are the optimised geometry calculated for 4,4´-$(CF_3)_2$-bpy and 5,5´-$(CF_3)_2$-bpy. By comparison of the calculated structures with the crystal structures discussed previously is section 5.2, it is possible to assess the accuracy of the calculations in predicting the structural properties of the CF_3 substituted bipyridines studied in this work.

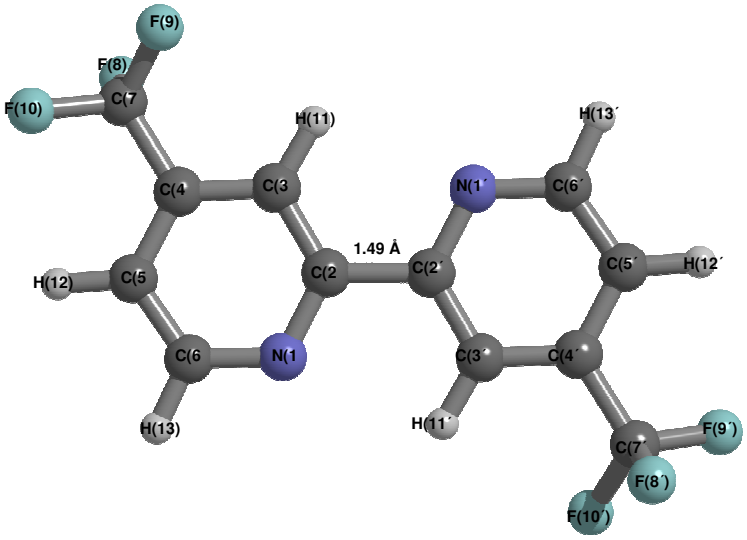

Figure 5.16 Optimised geometry of 4,4´-$(CF_3)_2$-bpy

The overall structural properties of the molecules from their crystal structures have been replicated well but that there are some small discrepancies. In both compounds the pyridine rings are coplanar with the N(1)-C(2)-C(2´)-N(2´) torsional angle reported to be 180°. However in the crystal structure the compounds have been found to be slightly twisted with torsional angles of 177.8° and 172.6° for the 4,4´ and 5,5´

analogues respectively. Comparison of the C(2)-C(2´) bond length between the rings for the two X,X´-$(CF_3)_2$-bpy structures shows that they are approximately 1.49 Å, with variance from crystal structure as little as 0.004 Å. Thus the computational model can be considered to be accurate with the discrepancies resulting from the calculation being run in the gas phase.

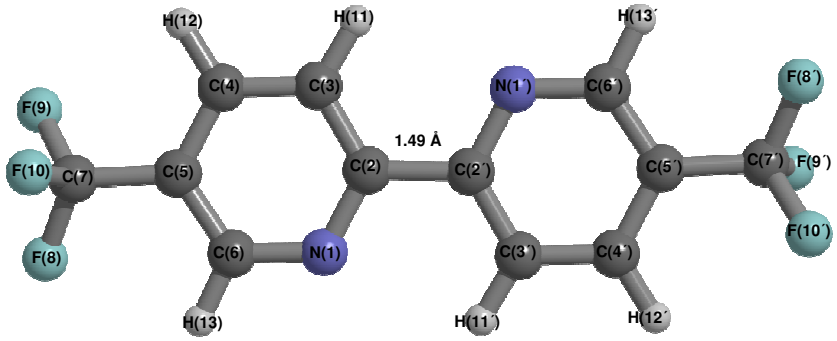

Figure 5.17 Optimised geometry of 4,4´-$(CF_3)_2$-bpy

The optimised geometries calculated for the two ditrifluoromethylbipyridines in their mono-reduced states are shown in figures 5.18 and 5.19. Comparison of these geometries with those calculated for non-reduced species enables examination of the effect of adding an additional electron to the structure of the molecule.

Both molecules do not deviate from the coplanar structure of the non-reduced state. There are some changes observed in the bond lengths of each of the compounds. For $[4,4´\text{-}(CF_3)_2\text{-bpy}]^{1-}$ there is a shortening of the C(2)-C(2´) (-0.050 Å) and lengthening of the N(1)-C(2) (+0.042 Å), C(2)-C(3) (+0.026 Å) and C(4)-C(5) (0.032 Å) bonds. For $[5,5´\text{-}(CF_3)_2\text{-bpy}]^{1-}$ there is a shortening of the C(2)-C(2´) (-0.057 Å), N(1)-C(6) (-0.011 Å) and C(3)-C(4) (-0.016Å) bonds and lengthening of the N(1)-C(2) (+0.038 Å), C(2)-C(3) (0.028 Å), C(4)-C(5) (+0.016 Å) and C(5)-C(6) (+0.011 Å) bonds. The shortening of the inter-ring C(2)-C(2´) bond in the reduced species is indicative of an

increased amount of double bond character and therefore an increased π-conjugation and a favouring of a planar conformation.

Also shown in figure 5.18 and 5.19 are the calculated SOMOs for each of the mono-reduced X,X´-$(CF_3)_2$-bpy compounds. Examination of these orbitals can aid in the interpretation of the experimental results obtained from spectroelectrochemcial investigation of the mono-reduced species.

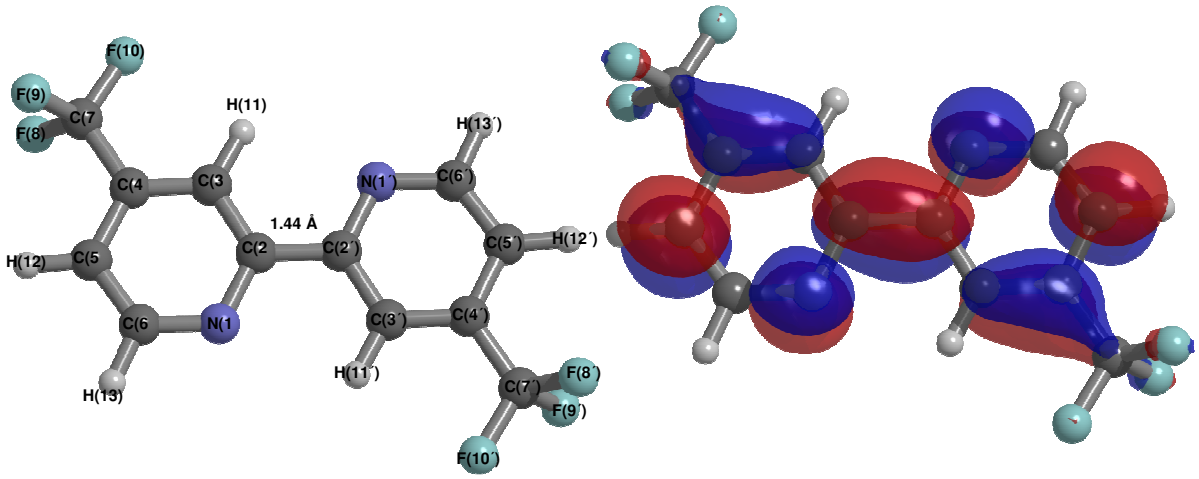

Figure 5.18 Optimised geometry and calculated SOMO of $[4,4´\text{-}(CF_3)_2\text{-bpy}]^{1-}$

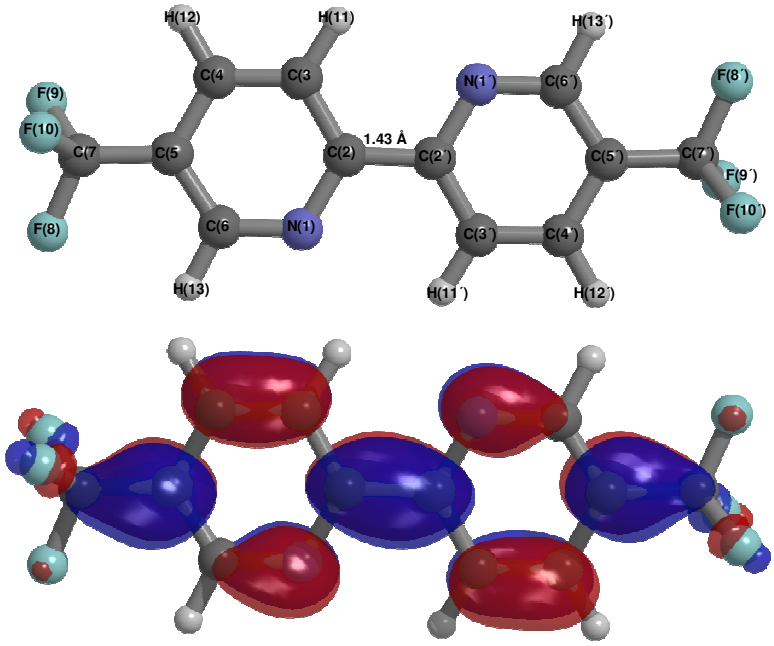

Figure 5.19 Optimised geometry and calculated SOMO of $[5,5´\text{-}(CF_3)_2\text{-bpy}]^{1-}$

Comparison of the orbitals clearly shows that altering the positions of the CF_3 substituents has a significant effect on the distribution of electron density about the bipyridine rings. Given in table 5.5 are the breakdowns of the % occupations by atom for the SOMOs of the two $[X,X'\text{-}(CF_3)_2\text{-bpy}]^{1-}$ species.

$[4,4'\text{-}(CF_3)_2\text{-bpy}]^{1-}$ SOMO	
# Atom	%
N(1)	8.85
C(2)	8.90
C(3)	1.58
C(4)	8.92
C(5)	14.86
C(6)	0.41
C(7)	1.01
F(8)	0.16
F(9)	2.64
F(10)	2.63
H(11)	0.01
H(12)	0.02
H(13)	0.00
N(1′)	8.85
C(2′)	8.90
C(3′)	1.58
C(4′)	8.92
C(5′)	14.86
C(6′)	0.41
C(7′)	1.01
F(8′)	0.16
F(9′)	2.64
F(10′)	2.63
H(11′)	0.01
H(12′)	0.02
H(13′)	0.00

$[5,5'\text{-}(CF_3)_2\text{-bpy}]^{1-}$ SOMO	
# Atom	%
N(1)	5.92
C(2)	10.11
C(3)	3.68
C(4)	5.45
C(5)	14.42
C(6)	1.46
C(7)	2.56
F(8)	0.32
F(9)	3.32
F(10)	2.75
H(11)	0.01
H(12)	0.02
H(13)	0.01
N(1′)	5.92
C(2′)	10.11
C(3′)	3.68
C(4′)	5.44
C(5′)	14.40
C(6′)	1.46
C(7′)	2.55
F(8′)	0.32
F(9′)	3.32
F(10′)	2.74
H(11′)	0.01
H(12′)	0.02
H(13′)	0.01

Table 5.5 The % occupations by atom for the SOMOs of $[4,4'\text{-}(CF_3)_2\text{-bpy}]^{1-}$ and $[5,5'\text{-}(CF_3)_2\text{-bpy}]^{1-}$

Comparison of the SOMOs for the $[X,X'\text{-}(CF_3)_2\text{-bpy}]^{1-}$ species indicates that the ring nitrogen atoms contribute 11.84-17.70%, with the larger contribution observed for the $[4,4'\text{-}(CF_3)_2\text{-bpy}]^{1-}$. It is also of interest to examine how the amount of electron density localised onto the CF_3 substituent is affected by the position of the groups. It is noted that for the $[X,X'\text{-}(CF_3)_2\text{-bpy}]^{1-}$ compounds the substituent atoms contributes

12.88 - 17.88% to the SOMOs, with the larger contribution observed for the 5,5´-$(CF_3)_2$-bpy molecule.

Time-dependent density functional theory (TD-DFT) calculations were conducted in an attempt to gain further information about the UV/Vis/NIR spectroelectrochemical data collected for the ditrifluoromethylbipyridine compounds.

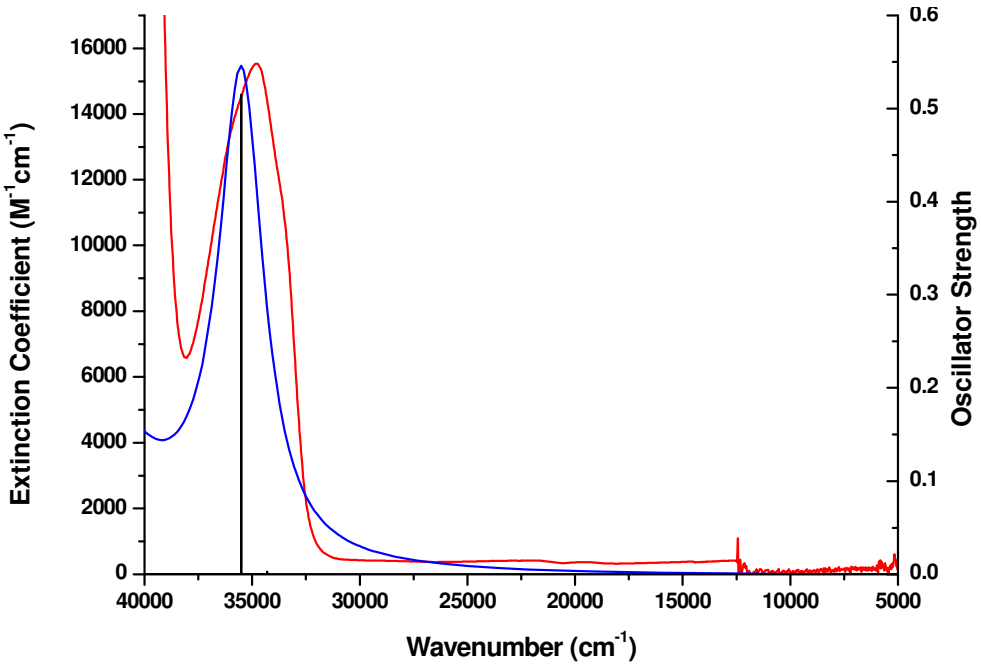

Figure 5.20 Overlay of the experimental UV/Vis/NIR spectrum (red) and the TD-DFT calculated spectrum (blue) of 4,4´-$(CF_3)_2$-bpy. Calculated transitions are shown as black columns

Shown in figure 5.20 is an overlay of the calculated and experimental UV/Vis/NIR spectra of 4,4´-$(CF_3)_2$-bpy.When the spectra are compared it can be seen that the calculated spectrum matches the overall shape of the experimental data very well. The experimental and calculated transitions observed in the UV/Vis/NIR spectrum of 4,4´-$(CF_3)_2$-bpy are reported in table 5.6. Analysis of the transition in the calculated spectrum show that it is due to the HOMO-LUMO transition.

	Wavenumber (cm^{-1})	Extinction Coefficient ($M^{-1}cm^{-1}$)	Wavenumber (cm^{-1})	Osc. Strength
4,4'-$(CF_3)_2$-bpy	**34800**	**15200**	**35000**	**0.5357**
$[4,4'-(CF_3)_2\text{-bpy}]^{1-}$	**36100**	**6400**	**37500**	**0.0326**
	29400	**3900**	**31100**	**0.0106**
	28200	**7100**	**28000**	**0.5251**
	27400	**11700**		
	26300	**18800**		
	25600	**35600**		
	19600	**2700**	**20000**	**0.2026**
	18400	**7300**		
	17200	**11400**		
	14900	**100**	**7200**	**0.0423**
	13400	**250**		
	8600	**300**		
	7200	**700**		
	5500	**700**		

Table 5.6 Transitions in the experimental and calculated UV/Vis/NIR spectra of 4,4´-$(CF_3)_2$-bpy and $[4,4'-(CF_3)_2\text{-bpy}]^{1-}$

Of more interest is the information that can be gained by applying this technique to the more complicated spectrum of the mono-reduced $[4,4'-(CF_3)_2\text{-bpy}]^{1-}$ species. Shown in figure 5.21 is an overlay of the experimental and calculated spectra for this species.

Again comparison of the spectra indicates that the calculated spectrum matches the overall pattern of transitions observed in the experimental spectrum. However, it is noted that the calculation overestimates the energy of many of the transitions. Shown in table 5.6 are the experimental and calculated transitions observed in the UV/Vis/NIR spectrum of the $[4,4'-(CF_3)_2\text{-bpy}]^{1-}$ species.

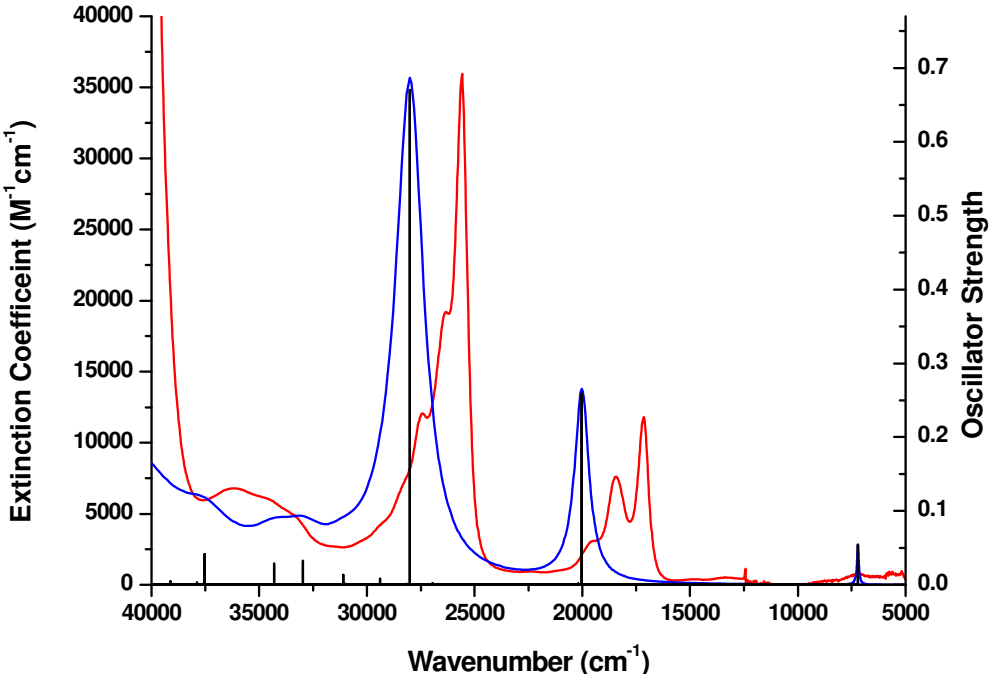

Figure 5.21 Overlay of the experimental UV/Vis/NIR spectrum (red) and the TD-DFT calculated spectrum (blue) of [4,4´-$(CF_3)_2$-bpy]$^{1-}$. Calculated transitions are shown as black columns

Though the overall structure features of the experimental spectrum are reproduced accurately by the calculation it has failed to replicate the fine structure observed in some of the experimental peaks. This is possibly due to these features arising from vibrational coupling effects which cannot be accounted for in the TD-DFT calculation.

Analysis of the composition of the transitions in the calculated spectrum allows for the assignment of the bands observed in the experimental spectrum. It is of interest to note that the SOMO→LUMO transition can be assigned to the very low intensity band of peaks between 14900 - 5700 cm^{-1} in the experimental spectrum. The first features in the experimental spectrum with any significant intensity are the bands around 18000 cm^{-1}. These features can be attributed to transitions from the SOMO to higher lying empty π^* orbitals. The intense band observed at 25600 cm^{-1} can be assigned to a transition from the HOMO-1→SOMO. This equates to the

HOMO→LUMO transition in the 4,4´-$(CF_3)_2$-bpy species moving to lower energy upon reduction. The high energy bands at 36100 cm^{-1} and 29400 cm^{-1} can be assigned to transitions from the SOMO to very high energy π^* orbitals.

A similar approach can be adopted for the analysis of the spectra of the 5,5´-$(CF_3)_2$-bpy. Shown in figure 5.22 is an overlay of the calculated and experimental UV/Vis/NIR spectra. The experimental and calculated transitions observed in the UV/Vis/NIR spectrum are reported in table 5.7.

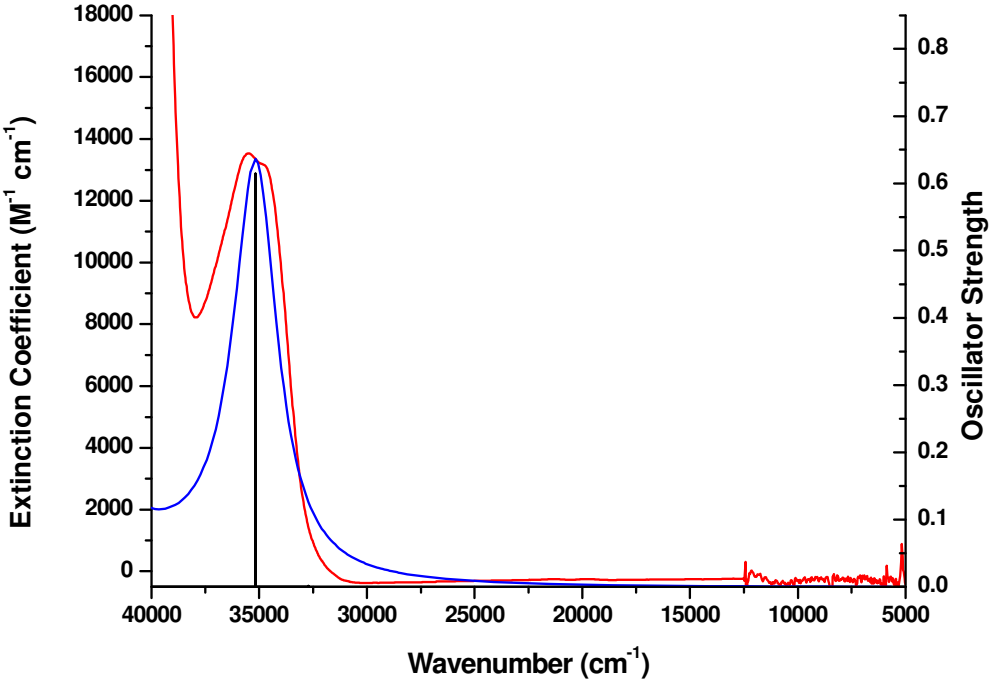

Figure 5.22 Overlay of the experimental UV/Vis/NIR spectrum (red) and the TD-DFT calculated spectrum (blue) of 5,5´-$(CF_3)_2$-bpy. Calculated transitions are shown as black columns

Analysis of the calculated spectrum shows that the lowest energy transition is due to the HOMO-LUMO transition. It is noted that the doublet feature in the experimental spectrum is not replicated in the calculated spectrum.

Shown in figure 5.23 is an overlay of the experimental and calculated spectra for the mono-reduced $[5,5´\text{-}(CF_3)_2\text{-bpy}]^{1-}$ species. As was found for $[4,4´\text{-}(CF_3)_2\text{-bpy}]^{1-}$

species, the calculation overestimates the energy of many of the observed transitions and has failed to replicate the fine structure observed in some of the experimental peaks. The experimental and calculated transitions are given in table 5.7.

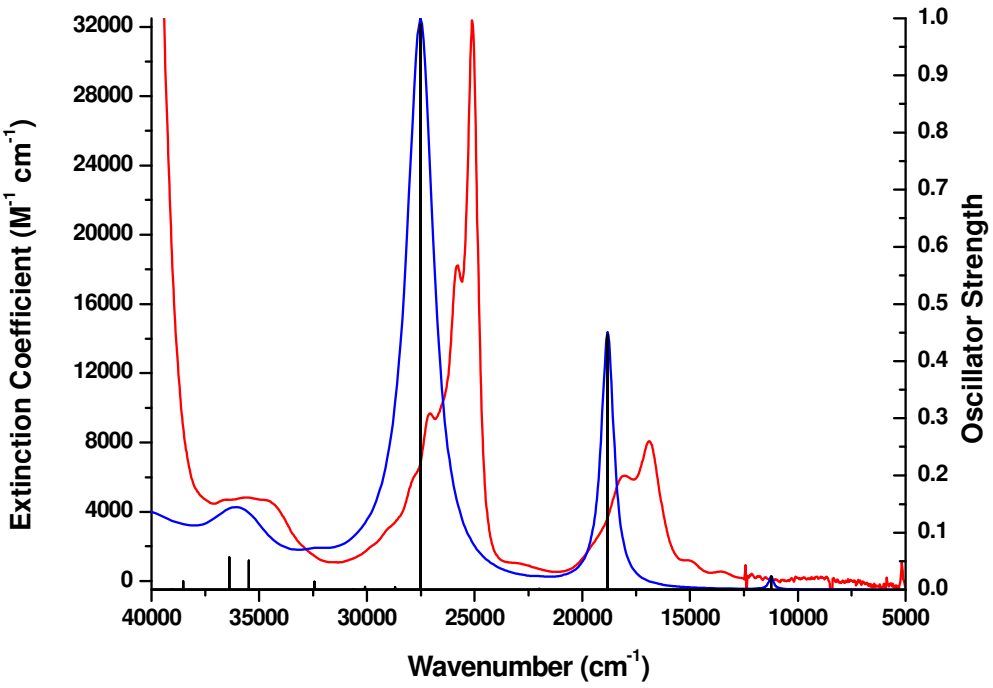

Figure 5.23 Overlay of the experimental UV/Vis/NIR spectrum (red) and the TD-DFT calculated spectrum (blue) of [5,5´-$(CF_3)_2$-bpy]$^{1-}$. Calculated transitions are shown as black columns

Analysis of the composition of the transitions in the calculated spectrum allows for the assignment of the bands observed in the experimental spectrum. Once again the SOMO→LUMO transition can be assigned to the very low intensity band of peaks between 13600 - 7500 cm^{-1} in the experimental spectrum. The features between 18000 – 15200 cm^{-1} in the experimental spectrum can be attributed to transitions from the SOMO to higher lying empty π^* orbitals. The intense band observed at 25100 cm^{-1} can be assigned to a transition from the HOMO-1→SOMO. This equates to the HOMO→LUMO transition in the 5,5´-$(CF_3)_2$-bpy species moving to lower energy upon reduction. The high energy bands at 36500 cm^{-1} and 35600 cm^{-1} can be assigned to transitions from the SOMO to very high energy π^* orbitals.

	Experimental		Calculation	
	Wavenumber (cm^{-1})	Extinction Coefficient ($M^{-1}cm^{-1}$)	Wavenumber (cm^{-1})	Osc. Strength
5,5'-$(CF_3)_2$-bpy	35500 34700	13500 13100	35200	0.7023
$[5,5'\text{-}(CF_3)_2\text{-bpy}]^{1-}$	36500 35600	4700 4800	36400 35500	0.0395 0.0355
	27800 27100 25800 25100	6000 9700 18200 32400	27500	0.6839
	18000 16900 15200	6100 8100 1200	18800	0.3084
	13600 11300 10100 8900 7500	600 400 475 450 300	11200	0.0159

Table 5.7 Transitions in the experimental and calculated UV/Vis/NIR spectra of 5,5´-$(CF_3)_2$-bpy and $[5,5\text{´-}(CN)_2\text{-bpy}]^{1-}$

Calculations can be used in the same way to aid in the assignment of experimental EPR hyperfine coupling constants to specific nuclei in the paramagnetic species under investigation.

Shown in tables 5.8 and 5.9 are the hyperfine coupling constants calculated for the $[4,4\text{´-}(CF_3)_2\text{-bpy}]^{1-}$ and $[5,5\text{´-}(CF_3)_2\text{-bpy}]^{1-}$ species respectively.

$[4,4\text{´-}(CF_3)_2\text{-bpy}]^{1-}$			
Coupling constant	Experimental	Calculated	Assignment
A(2 x ^{14}N) / G	3.03	2.53	Ring ^{14}N
A(2 x ^{19}F) / G	2.98	2.81	CF_3 ^{19}F
A(2 x ^{1}H) / G	5.25	6.00	5,5´ position ^{1}H
A(2 x ^{1}H) / G	0.99	0.98	6,6´ position ^{1}H
A(2x ^{1}H) / G	0.56	0.48	3,3´ position ^{1}H

Table 5.8 Experimental and calculated EPR hyperfine coupling constants for $[4,4\text{´-}(CF_3)_2\text{-bpy}]^{1-}$

$[5,5'\text{-}(CF_3)_2\text{-bpy}]^{1-}$			
Coupling constant	**Experimental**	**Calculated**	**Assignment**
A(2 x ^{14}N) / G	**1.61**	**1.26**	**Ring ^{14}N**
A(2 x ^{19}F) / G	**13.19**	**16.65**	**CF_3 ^{19}F**
A(4 x ^{1}H) / G	**1.61**	**1.36**	**4,4´ position ^{1}H**
		1.29	**3,3´ position ^{1}H**
A(2 x ^{1}H) / G	**0.52**	**0.18**	**6,6´ position ^{1}H**

Table 5.9 Experimental and calculated EPR hyperfine coupling constants for $[5,5'\text{-}(CF_3)_2\text{-bpy}]^{1-}$

Comparison of the experimental and calculated coupling constants for the $[4,4'\text{-}(CF_3)_2\text{-bpy}]^{1-}$ and $[5,5'\text{-}(CF_3)_2\text{-bpy}]^{1-}$ species indicate that the calculations have been able to effectively replicate the pattern of coupling constants observed experimentally. By comparing the magnitude of the calculated and experimental hyperfine coupling constants it is possible to make assignment of coupling to specific nuclei.

Through analysis of these calculations it is possible to assign the observed ^{1}H couplings, which is not possible from experimental data alone. For the $[4,4'\text{-}(CF_3)_2\text{-bpy}]^{1-}$ compound the calculations indicate that the largest of the ^{1}H couplings is due the hydrogen atoms in the 5 and 5´ positions of the pyridine rings. The ^{1}H coupling of 0.99 G can be assigned to the hydrogen atoms in the 6 and 6´ positions. The remaining ^{1}H coupling can be assigned to the pair of hydrogen atoms in the 3 and 3´ positions

While the pattern of couplings observed for the $[5,5'\text{-}(CF_3)_2\text{-bpy}]^{1-}$ species follows the same trend as the $[4,4'\text{-}(CF_3)_2\text{-bpy}]^{1-}$ analogue the distribution of electron density can be seen to be different from examination of the calculations. As with the $[4,4'\text{-}(CF_3)_2\text{-bpy}]^{1-}$ species the calculations can be used to assign the two observed ^{1}H

couplings constants. The coupling of 1.61 G to four equivalent ^{1}H nuclei can be assigned to the hydrogen atoms in the 3,3´ and 4,4´positions of the bipyridine rings. The remaining ^{1}H couplings can be assigned to the hydrogen atoms in the 6,6´ positions. It is noted that the relative importance of the 3,3´ and 6,6´ positions appear to be inverted from what was observed for the $[4,4´\text{-}(CF_3)_2\text{-bpy}]^{1-}$ species. In addition the coupling to the ring nitrogen atoms is approximately twice as large in the 4,4´ substituted bpy compared to the 5,5´-CF_3-bpy analogue.

5.6 Conclusion

Electrochemical and spectroelectrochemical investigation of the trifluoroemthyl disubstituted bipyridines studied in this work have determined that the CF_3 substituent exhibit properties that are similar to many previously investigated substituted bpys.[1-4] Electrochemical analysis has indicated that substitution with the CF_3 group causes the first reduction to move to less negative potential, relative to unsubstituted bpy, in line with the prediction from the correlation with the *para* Hammett parameter. UV/Vis/NIR and EPR studies have confirmed that the reduction electrons in each case enter a molecular orbital that is predominantly based on the bpy rings rather than localised to the substituent group.

Electrochemical investiagtions of the three X,X´-$(CF_3)_2$-bpy molecules have shown that all three compounds undergo a single one-electron reduction in the available solvent window. It is noted that the reduction process observed for 3,3´-$(CF_3)_2$-bpy is irreversible on the CV timescale. Comparison of the reduction potentials indicates that 5,5´-$(CF_3)_2$-bpy is reduced at significantly less negative potentials than the 3,3´- or

4,4´-substituted analogues. The 4,4´-$(CF_3)_2$-bpy molecule exhibits the most negative reduction potential. This is in agreement with the investigations on CN substituted bpys reported elsewhere in this work.

Attempts to evaluate if 4,4´-$(CF_3)_2$-bpy and 5,5´-$(CF_3)_2$-bpy fit the previously observed correlations between the *para* Hammett parameter and the first reduction potential have resulted in good quality fits being obtained for both compounds. This indicates that resonance effects of the CF_3 substituent can be effectively modelled despite the different nature of the resonance interaction. Once again the fit for the 5,5´-$(X)_2$-bpy compounds has been found to give a higher R^2 value indicating σ_p is more able to describe the interaction of the resonance and field effects in this these compounds than the 4,4´-$(X)_2$-bpy analogues.

The UV/Vis/NIR spectroelectrochemistry results for the two X,X´-$(CF_3)_2$-bpy compounds with reversible electrochemistry yield spectra for the mono-reduced species that are very similar to the spectrum obtained for $[bpy]^{1-}$. Therefore it can be inferred that the electronic character of the frontier orbitals of bpy, 4,4´-$(CF_3)_2$-bpy and 5,5´-$(CF_3)_2$-bpy are similar *i.e.* that the MO of the compounds are primarily based on the bpy part of the molecule.

EPR analysis of the paramagnetic $[4,4´\text{-}(CF_3)_2\text{-bpy}]^{1-}$ and $[5,5´\text{-}(CF_3)_2\text{-bpy}]^{1-}$ mono-reduced species give rise to spectra that indicate that the reduction electron enters a molecular orbital that is spread over both rings rather than localised on one of the pyridine rings. Comparison of the ^{19}F coupling arising from the CF_3 groups in the

two compounds indicates that the coupling constant in the 5,5´ analogue is more than four times as large as that observed for $[4,4´\text{-}(CF_3)_2\text{-bpy}]^{1-}$. In addition the largest observable coupling in the $[4,4´\text{-}(CF_3)_2\text{-bpy}]^{1-}$ species is due to the a pair of ^1H nuclei. These results clearly demonstrate the greater contribution of the 5,5´ positions to the electronic structure of the bpy π-system.

It is also noted that the ^{14}N coupling due to the ring nitrogen atoms in $[4,4´\text{-}(CF_3)_2\text{-bpy}]^{1-}$ is more than twice as large than the equivalent coupling in $[5,5´\text{-}(CF_3)_2\text{-bpy}]^{1-}$. These results are in line with what has been found by Geary for CO_2Et substituted bpys[1] and the CN substituted bpys studied in chapter 4. This indicates the greater importance that the ring nitrogen atoms have in determining the electronic properties of 4,4´-substituted bpys.

DFT calculations have enabled the assignment of the observed coupling constants to specific nuclei. This has made it possible to differentiate the couplings arising from the pairs of equivalent ^1H nuclei spaced around the rings. The large ^1H coupling observed for the $[4,4´\text{-}(CF_3)_2\text{-bpy}]^{1-}$ species can be assigned to the hydrogen atoms in the 5,5´ positions, supporting the theory that these positions are the most electronically important with respect to substitution.

5.7 References

1. E. A. M. Geary, K. L. McCall, A. Turner, P. R. Murray, E. J. L. McInnes, L. A. Jack, L. J. Yellowlees, N. Robertson, *Dalton Trans.,* 2008, 3701-3708.

2. L. Jack, Ph.D Thesis, University of Edinburgh, 2003.

3. S. K. Al-Musharafi, Ph.D Thesis, University of Edinburh, 2006.

4. E. J. L. McInnes, R. D. Farley, C. C. Rowlands, A. J. Welch, L. Rovatti, L. J. Yellowlees, *J. Chem. Soc*., *Dalton Trans*., 1999, 4203-4208.

5. P. R. Murray, Ph.D Thesis, University of Edinburgh, 2006.

6. M. Furue, K. Maruyama, T. Oguni, M. Naiki, M. Kamachi, *Inorg. Chem*., 1992, **31**, 3792-3795.

7. C. Hansch, A. Leo, R. W. Taft, *Chem. Rev*., 1991, **91**, 165-195.

8. S. A. McFarland, F. S. Lee, K. A. W. Y. Cheng, F. L. Cozens, N. P. Schepp, *J. Am. Chem. Soc*., 2005, **127**, 7065-7070.

9. L. L. Merritt Jr., E. D. Schroeder, *Acta Cryst*., 1956, **9**, 801-804.

10. E. König, S. Kremer, *Chem. Phys. Lett*., 1970, **5**(2), 87-90.

11. T. Takeshita, N. Hirota, *J. Am. Chem. Soc*., 1971, **93**, 6421-6429.

12. J. Boersma, A. Mackor, J. G. Noltes, *J. Organomet. Chem*., 1975, **99**, 337-341.

6 Solvent Effects on the Electrochemical and Spectroelectrochemical properties of 4-CN-py and 5,5´-$(CN)_2$-bpy

6.1 Introduction

The motivation behind this study was to investigate the effects of altering the solvent on the electrochemical and spectroelectrochemical properties of cyano substituted polypyridines and to compare the findings to those for other substituted polypyridines studied previously. To this end electrochemical and spectroelectrochemical studies were carried out on the 4-CN-py and 5,5´-$(CN)_2$-bpy pro-ligands in a number of solvent systems.

Previous studies into the effect of solvent on the electronic properties of substituted py and bpy compounds have shown that the half-wave potential for the reduction processes observed for these compounds varies with the solvent system used. Moorcraft found for the X-NO_2-py and X-$COMe_2$-py ligands that the reduction potentials were significantly affected by the choice of solvent but that no correlation could be drawn between the observed potentials and a number of empirical parameters of the solvents used.[1] Investigation of NO_2 substituted bpy compounds by Murray[2] and Al-Musharafi[3] have found a strong linear correlation between the half-wave potentials for the reduction process of 5,5´-$(NO_2)_2$-bpy and 4-NO_2-bpy and the solvent acceptor number. Conversely when Al-Musharafi studied 4,4´-$(NO_2)_2$-bpy and 4-NO_2-4´-Cl-bpy it was discovered that these ligands do exhibit a dependence on the solvent but no correlation with solvent acceptor number was observed.[3] Al-Musharafi

also investigated the 6,6´-$(Cl)_2$-bpy ligand and found that reduction of this compound showed no solvent dependence.[3] This study considers the effect of solvent on the electronic properties of 4-CN-py and 5,5´-$(CN)_2$-bpy. The solvents used and their acceptor number (AN)[4] are presented in table 6.1.

Solvent	AN
THF	8.0
Ethyl Acetate	9.3
Acetone	12.4
Pyridine	14.2
DMF	16.0
MeCN	18.9
DMSO	19.3

Table 6.1 Solvent used during solvent effects study and their acceptor number

6.2 Electrochemistry

6.2.1 Cyclic Voltammetry

The solvent study re-examined the cyclic voltammogram of 4-CN-py in 0.3 M [TBA][BF_4]/DMF. Full characterisation of the ligand in this solvent has been described previously in section 3.2. This solvent was chosen to be investigated first as it represents the middle of the acceptor number range studied. When the ligand was examined in 0.3 M [TBA][BF_4]/THF, the cyclic voltammogram revealed one reversible reduction process at -1.77 V. This is significantly more negative than the process observed in the DMF system, $|E_{½,THF} - E_{½,DMF}| = 110$ mV.

The third solvent system investigated was 0.3 M [TBA][BF_4]/DMSO, a solvent at the high end of the acceptor number range. When the cyclic voltammogram was conducted it was found to also have a reversible one-electron reduction. The $E_{½}$ of this process was found to be -1.60 V. The cyclic voltammograms for the THF, DMF and DMSO systems are shown in figure 6.1 below.

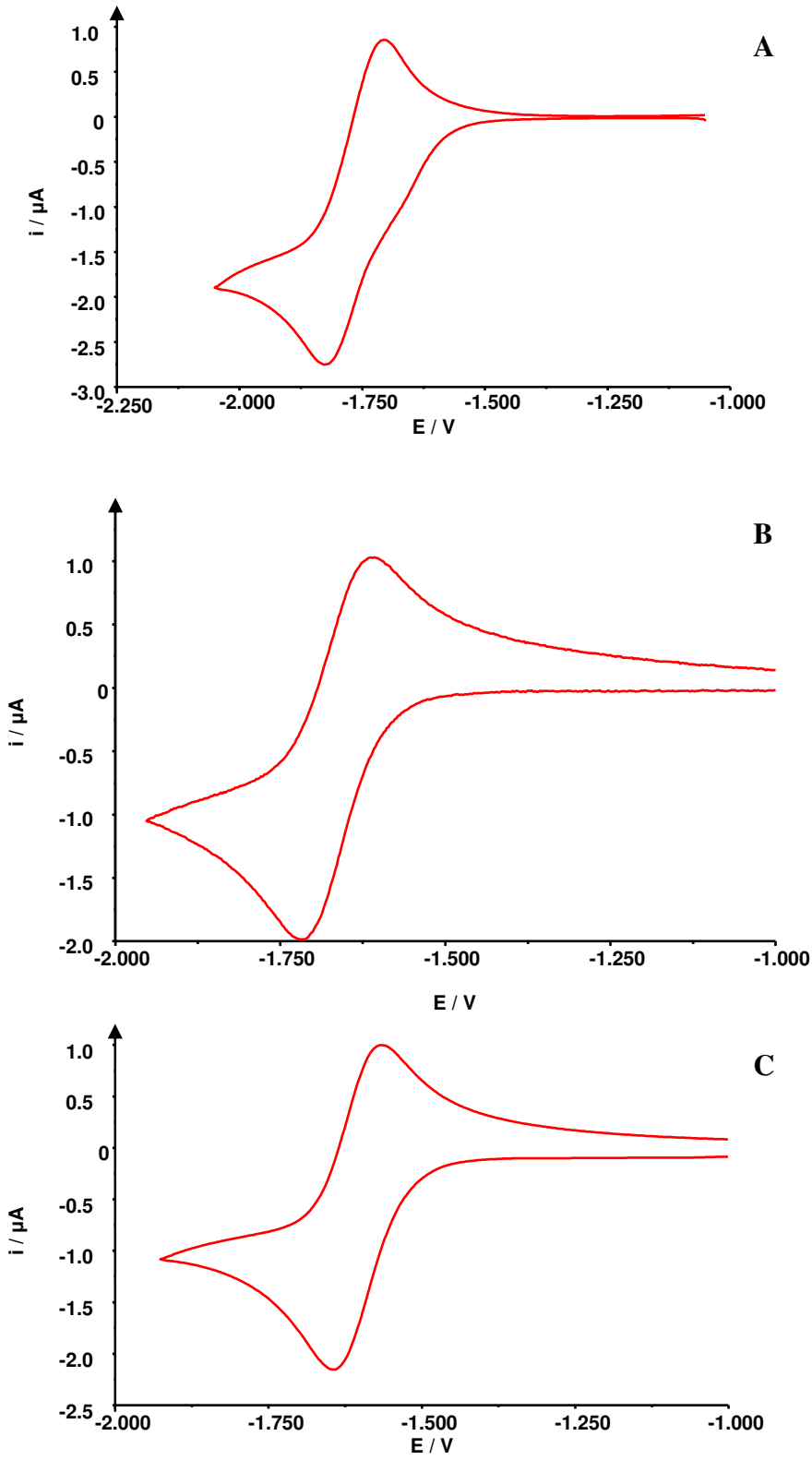

Figure 6.1 Cyclic Voltammograms of 4-CN-py *vs.* Ag/AgCl in 0.3 M [TBA] [BF_4]/THF (A), DMF (B), DMSO (C) at 298 K

The study was then expanded to the full range of solvents. The $E_{½}$ values of all of systems investigated are shown in table 6.2. Comparison of these results clearly

shows that the solvent has a significant effect on the electrochemical behaviour of 4-CN-py. In low acceptor number solvents (THF, ethyl acetate) the reduction process is moved to more negative potential with respect to the DMF system. At high end of the acceptor number range (MeCN, DMSO) the reduction peak is moved to less negative potential with respect to the DMF system.

Unlike the other solvent systems used in this study the cyclic voltamogram of 4-CN-py in acetone comprises an irreversible reduction process at a scan rate of 0.1 Vs^{-1}. Upon increasing the scan rate the reduction becomes quasi-reversible, figure 6.2. It is not understood at this time why 4-CN-py has an irreversible reduction process in acetone.

Solvent	AN	$E_{½}$ (V)
DMSO	19.3	-1.60
MeCN	18.9	-1.67
DMF	16	-1.66
Pyridine	14.2	-1.70
Acetone	12.4	-
Ethyl Acetate	9.3	-1.79
THF	8.0	-1.77

Table 6.2 $E_{½}$ values for the reduction of 4-CN-py *vs.* Ag/AgCl as determined from cyclic voltammetry in varying solvents as 298 K (electrolyte = 0.3 M [TBA][BF_4])

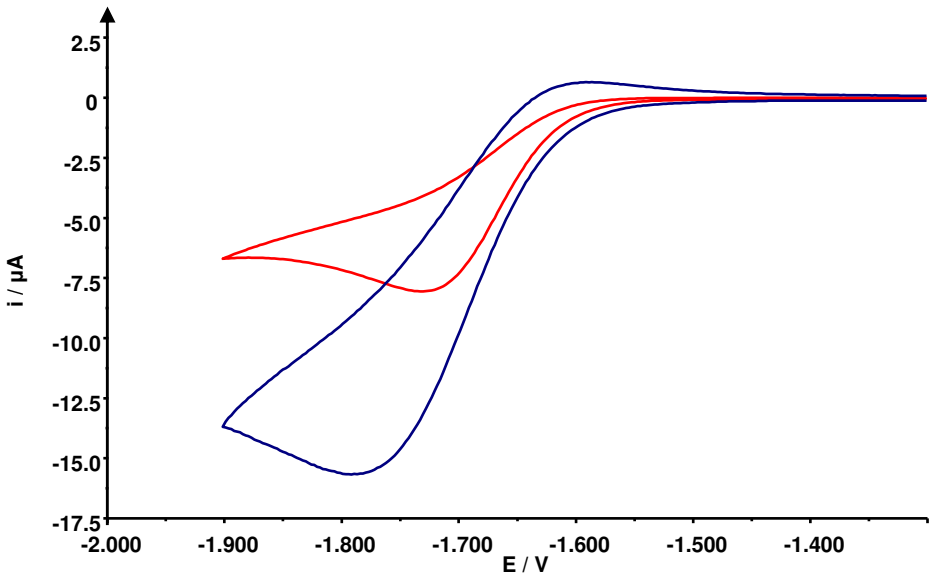

Figure 6.2 Cyclic Voltammogram of 4-CN-py *vs.* Ag/AgCl in 0.3 M [TBA][BF_4]/Acetone at scan rates of 0.1 Vs^{-1} (red) and 1.0 Vs^{-1} (blue) at 298 K

When the full range of data for the 4-CN-py is compared a clear trend can be observed. As the acceptor number of the solvent increases the reversible one electron reduction of 4-CN-py moves to less negative potentials. The acceptor number of the solvent is a measure of the ability of the solvent to accept a pair of electrons and therefore is also a measure of its Lewis Acidity. As has been previously discussed in section 3.3.2 EPR analysis of the $[4\text{-CN-py}]^{1-}$ species has indicated that a significant amount of electron density is localised on the CN substituent of the reduced species. Solvents with higher acceptor numbers will be more effective at surrounding and stabilising the negatively charged cyano moiety of the reduced molecule. This results in the mono-reduced species being more stable in higher acceptor number solvents. The increased stability of the reduced species will cause a decrease in the potential required to generate them and thus $E_{½}$ will become less negative.

As in the solvent study of 4-CN-py the electrochemical study of 5,5´-$(CN)_2$-bpy was started by re-examining the cyclic voltammogram of the ligand in 0.3 M [TBA][BF_4]/DMF. Full characterisation of the ligand in this solvent system is discussed in section 4.2.

This was followed by investigating 5,5´-$(CN)_2$-bpy in 0.3 M [TBA][BF_4]/THF. The cylic voltammogram for 5,5´-$(CN)_2$-bpy revealed two reversible reductions. The $E_{½}$ values for these processes are $E_{½,(1)}$ = -1.14 V and $E_{½,(2)}$ = -1.66 V, leading to a $\Delta E_{½}$ value of 520 mV. These two processes are at significantly more negative potentials than those observed in the DMF system. The first and second reductions are shifted by 60 mV and 50 mV respectively when compared to the corresponding processes in the DMF system. The $\Delta E_{½}$ between the two reductions is slightly smaller in the THF

than in DMF. In addition to the two reversible reduction processes observed there is an anodic peak at -1.61 V. It is suggested that this is a daughter product peak from the breakdown of a small amount of the di-reduced species. Comparison of the peak heights for the two reduction processes indicates that the second peak is slightly smaller than the first thereby supporting this theory. Increasing the scan rate or decreasing the temperature causes this peak to disappear, indicating that the decomposition is relatively slow.

The 0.3 M [TBA][BF_4]/DMSO system was investigated next to determine the compounds response in a high acceptor number solvent. When the cyclic voltammogram was conducted it was found to also have two reversible one-electron reductions. The $E_{½}$ values for these processes are $E_{½,(1)}$ = -1.05 V and $E_{½,(2)}$ = -1.53 V. This results in a $\Delta E_{½}$ value of 480 mV. In comparison to the THF system these peaks are moved to significantly less negative potentials than those in the DMF system. The first and second reduction processes are shifted by 30 mV and 80 mV respectively. The $\Delta E_{½}$ value between the two reductions is also significantly smaller in the DMSO system, with the difference between the two processes being 50 mV smaller than in DMSO compared to the DMF system. The cyclic voltammograms for the THF, DMF and DMSO systems are shown in figure 6.3.

The study was then expanded to the full range of solvents. The $E_{½}$ values of all the systems investigated are shown in table 6.3. When all of these results are compared it can be clearly seen that the solvent has a measurable effect on the electrochemical properties of 5,5´-$(CN)_2$-bpy. In solvents with a low acceptor number (THF, ethyl acetate) the reduction peaks are moved to more negative potentials with respect to the

DMF system. In high acceptor number solvents (MeCN, DMSO) the reduction peaks are moved to less negative potentials with respect to the DMF system.

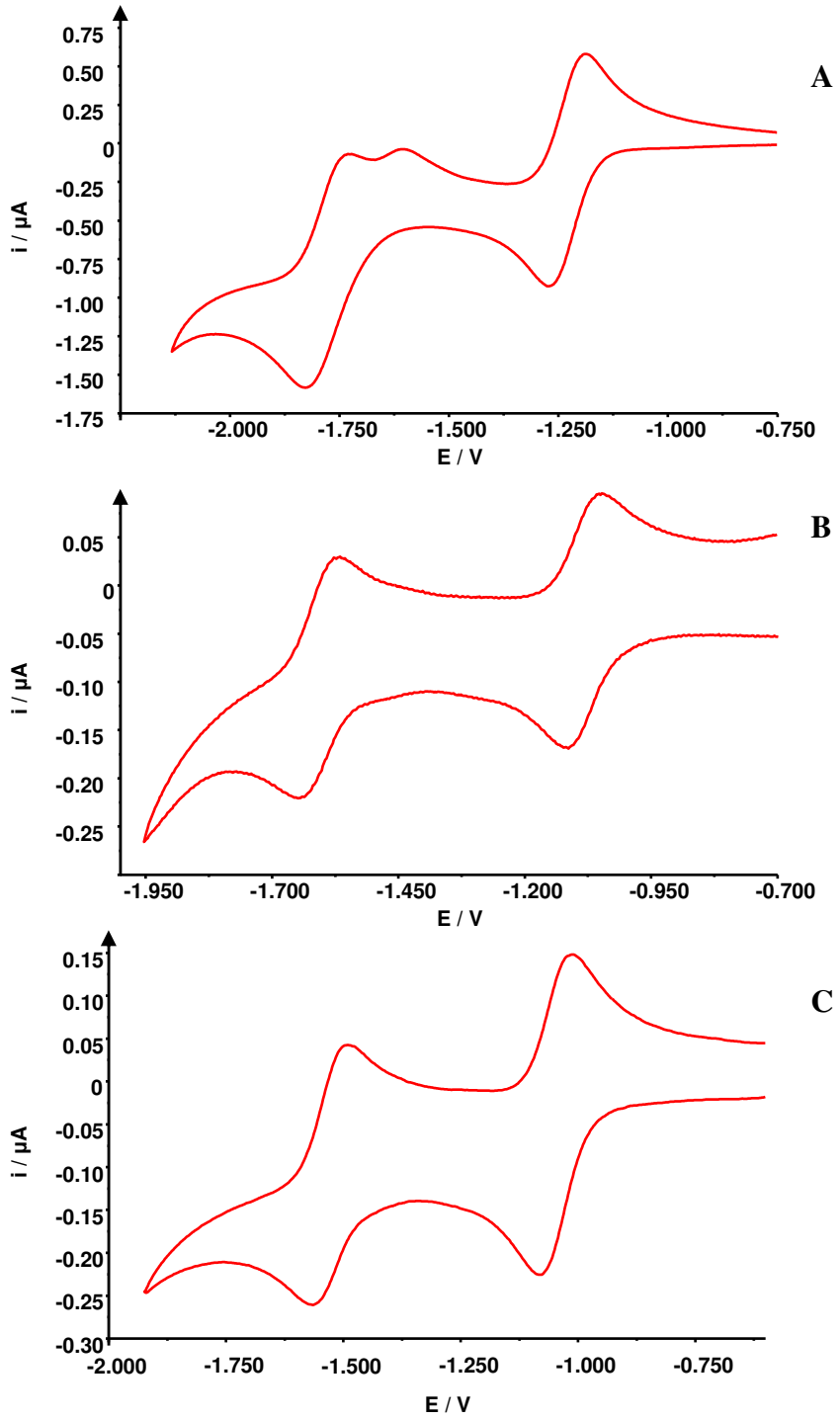

Figure 6.3 Cyclic Voltammograms of 5,5´-$(CN)_2$-bpy *vs.* Ag/AgCl in 0.3 M [TBA][BF_4]/THF (A), DMF (B), DMSO (C) at 298 K

Solvent	AN	$E_{½,(1)}$ (V)	$E_{½,(2)}$ (V)	$\Delta E_{½}$ (V)
DMSO	19.3	-1.05	-1.53	0.48
MeCN	18.9	-1.11	-1.56	0.45
DMF	16.0	-1.08	-1.61	0.53
Pyridine	14.2	-1.12	-1.59	0.47
Acetone	12.4	-1.13	-1.64	0.51
Ethyl Acetate	9.3	-1.17	-1.68	0.51
THF	8.0	-1.14	-1.66	0.52

Table 6.3 $E_{½}$ values for the reduction of 5,5´-$(CN)_2$-bpy *vs*. Ag/AgCl as determined from cyclic voltammetry in varying solvents as 298 K (electrolyte = 0.3 M [TBA][BF_4])

When the full range of data is compared a clear trend can be observed. As the acceptor number of the solvent increases the two reductions of 5,5´-$(CN)_2$-bpy move to less negative potentials. Comparison of the $\Delta E_{½}$ values from the different solvent systems does not yield as strong a correlation with the solvent acceptor number. However there is some evidence that as the solvent acceptor number increases the separation between the two reduction processes decreases. The variance in the $\Delta E_{½}$ values for the two reductions in the range of solvents used in this study is 80 mV, indicating that the solvent does have a significant effect.

6.2.2 Differential Pulse Voltammetry

The differential pulse voltammograms for 4-CN-py in the full range of solvents were also recorded to confirm the findings of the cyclic voltammetry experiments. 4-CN-py was found to have one reversible reduction process in all solvent systems studied. The $E_{½}$ values for these systems are shown below in table 6.4.

No.	Solvent	AN	$E_{½}$ (V)
1	THF	8.0	-1.77
2	Ethyl Acetate	9.3	-1.78
3	Acetone	12.4	-1.67
4	Pyridine	14.2	-1.70
5	DMF	16.0	-1.67
6	Ethyl Acetate	9.3	-1.66
7	DMSO	19.3	-1.62

Table 6.4 $E_{½}$ values for the reduction of 4-(CN)-py *vs*. Ag/AgCl as determined from DPV in varying solvents as 298 K (electrolyte = 0.3 M [TBA][BF_4]). Numbering scheme refers to data points in figure 6.4

Comparison of the results from the DPV experiments for these systems confirms the findings from the cyclic voltammetry that the reduction reaction in 4-CN-py moves to less negative potentials as the solvent acceptor number increases. Thus the half-wave potential for the one-electron reduction of 4-CN-py to $[4\text{-CN-py}]^{1-}$ may be shifted by 160 mV simply by changing the solvent. An attempt to determine a correlation between the $E_{½}$ value and the solvent acceptor number has been made and the plot is shown in figure 6.4. A linear correlation can be drawn with the fit having a R^2 value of 0.8435.

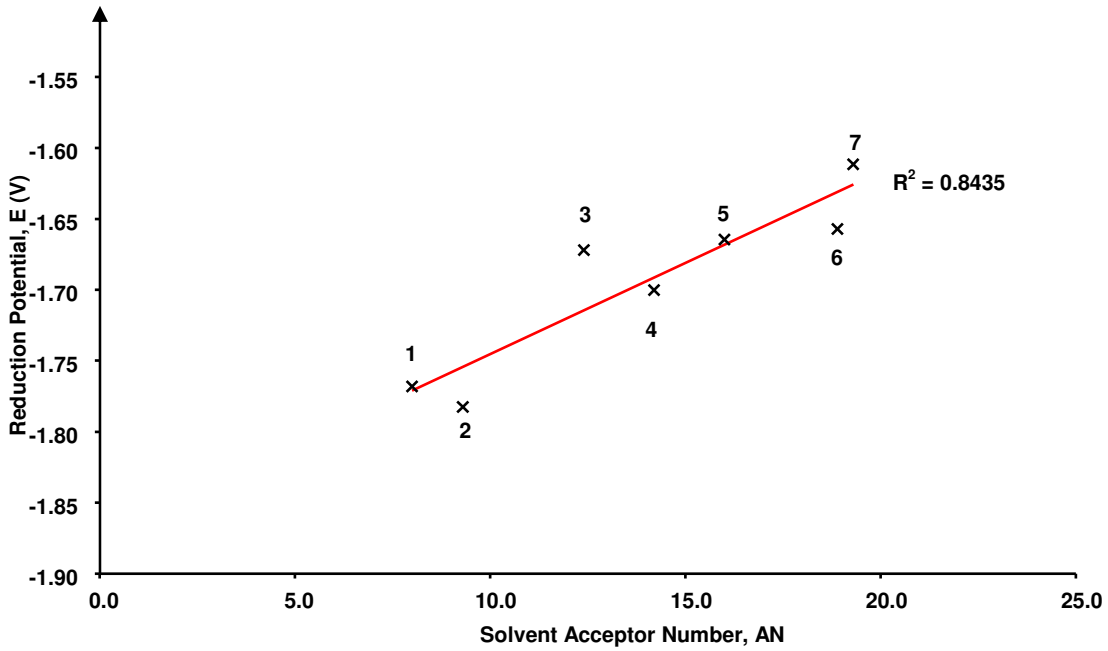

Figure 6.4 $E_{½}$ (from differential pulse) *vs.* solvent acceptor number for the reduction of 4-CN-py in a range of solvents (electrolyte = 0.3 M [TBA][BF_4]). For point numbering scheme see Table 7.4

As with the 4-CN-py ligand the differential pulse voltammetry of 5,5´-$(CN)_2$-bpy in the full range of solvents studied was conducted. The differential pulse voltammograms for all of the solvent systems studied indicated that the 5,5´-$(CN)_2$-bpy had two reversible one electron reductions. The $E_{½}$ values for these systems along with the $\Delta E_{½}$ values are shown table 6.5.

No.	Solvent	AN	$E_{½p1}$ (V)	$E_{½p2}$ (V)	$\Delta E_{½}$ (V)
1	THF	8.0	-1.18	-1.72	0.54
2	Ethyl Acetate	9.3	-1.16	-1.67	0.51
3	Acetone	12.4	-1.12	-1.65	0.53
4	Pyridine	14.2	-1.12	-1.60	0.48
5	DMF	16.0	-1.09	-1.61	0.52
6	MeCN	18.9	-1.11	-1.56	0.45
7	DMSO	19.3	-1.06	-1.54	0.48

Table 6.5 $E_{½}$ values for the reduction of 5,5´-$(CN)_2$-bpy *vs.* Ag/AgCl as determined from DPV in varying solvents as 298 K (electrolyte = 0.3 M [TBA][BF_4]). Numbering scheme refers to data points in figure 6.5

Comparison of the results from the differential pulse voltammograms for these systems confirms the findings from the cyclic voltammetry in that the two reduction reactions in 5,5´-$(CN)_2$-bpy become less negative as the solvent acceptor number increases. Plots of $E_{½}$ *vs.* AN for both of the redox processes are shown in figure 6.5.

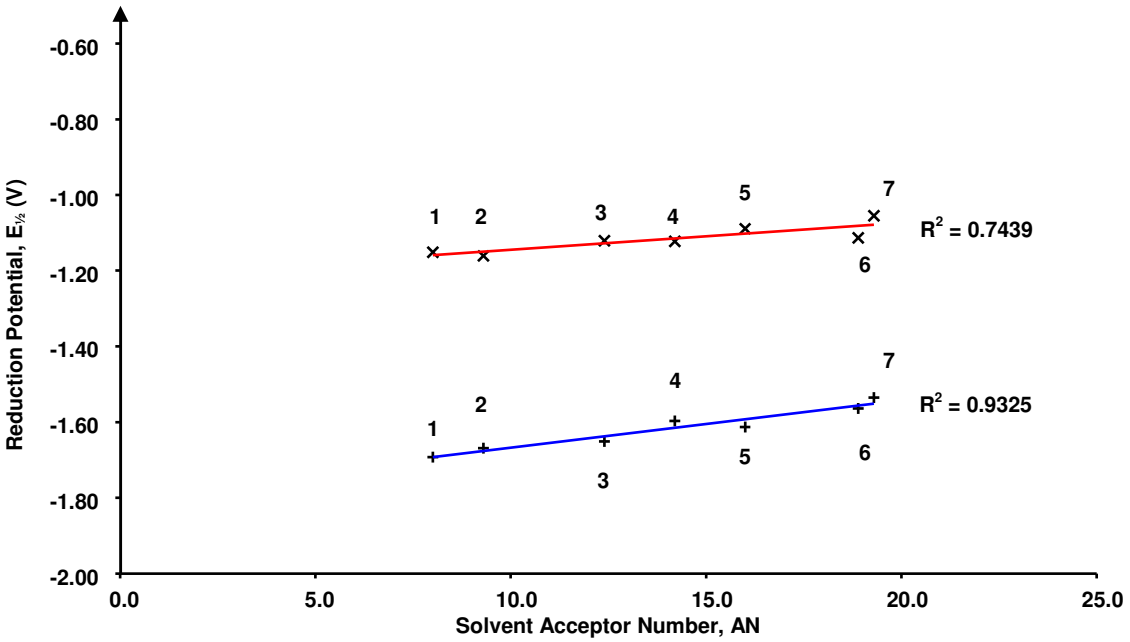

Figure 6.5 $E_{½}$ (from differential pulse) *vs.* solvent acceptor number for the 1st (red) and 2nd (blue) reductions of 5,5´-$(CN)_2$-bpy in a range of solvents (electrolyte = 0.3 M [TBA][BF_4]). For point numbering scheme see Table 6.5

These plots indicate that for both reductions there are linear relationships with R^2 = 0.7439 and R^2 = 0.9325 for the first and second reduction respectively. It is also observed that the fit for the second reduction has a steeper gradient and therefore is more affected by the nature of the solvent. This can be rationalised by considering that the stabilising effect of the solvent will be increased for a more highly charged molecule. Thus the di-reduced species will experience a greater effect than the mono-reduced species.

When the $\Delta E_{½}$ values for the different solvent systems obtained from the DPV experiments are compared a correlation between the solvent acceptor number and the separation between the two reductions peaks ($\Delta E_{½}$) in 5,5´-$(CN)_2$-bpy can be observed. A plot of $\Delta E_{½}$ *vs.* solvent acceptor number is shown in figure 6.6. This plot indicates that there is an approximately linear relationship however the fit has a rather low R^2 value of 0.5149. It is believed that due to the greater stabilization effect experienced by the di-reduced species the $E_{½}$ value for this species will decrease more rapidly than the mono-reduced resulting in the decrease in $\Delta E_{½}$ at higher acceptor number. From extrapolation of the plot it can be estimated that the peaks will completely overlap, i.e. $\Delta E_{½}$ = 0, at an acceptor number of approximately 103.5, however there is no known solvent with an acceptor number of this value.

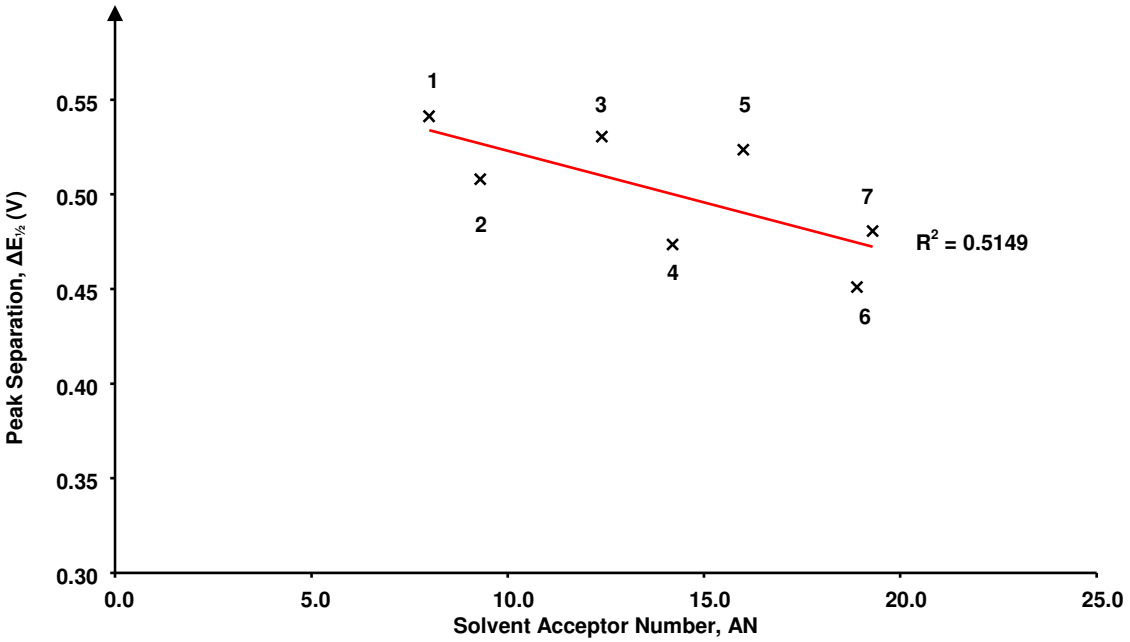

Figure 6.6 Plot of the separation in half-wave potential of the 1st and 2nd reduction of 5,5´-$(CN)_2$-bpy against solvent acceptor number. For data point numbering scheme see Table 7.5

In comparison when Murray investigated the effect of solvent on the electrochemistry of 5,5´-$(NO_2)_2$-bpy it was discovered that the separation between the two observable reversible reduction processes have a dramatic solvent dependence.[2] In low acceptor number solvents such as THF two distinct $1e^-$ reduction processes are observed. In DMF the two peaks have begun to overlap such that the second reduction appears as a shoulder. Investigation of the compound in DCM (AN = 20.4) showed only one observable reversible $2e^-$ reduction process. This difference in behaviour between the substituted bpys can be rationalised by considering the fact that more electron density will be drawn onto the more electronegative NO_2 groups than the CN groups. Therefore the solvent molecules will be able to coordinate and stabilise the NO_2 substituted bpy more effectively leading to greater observable solvent effects.

6.3 EPR Spectroelectrochemistry

As was found previously for the DMF solvent system (see section 4.3.2) the EPR of 5,5´-$(CN)_2$-bpy in the full range of solvents studied was found to give no signal, thus

confirming that it must be diamagnetic. *In-situ* electrogeneration was used to generate the EPR active $[5,5´\text{-}(CN)_2\text{-bpy}]^{1-}$ species. A potential of -1.5 V was used for all the systems with the exception of the THF system where a voltage of -2.0 V was used. This potential used in the THF system is large enough to also generate the di-reduced $[5,5´\text{-}(CN)_2\text{-bpy}]^{2-}$ species. However this large over-potential is required to decrease the timescale of the experiment to a manageable level. The EPR spectra collected for 5,5´-$(CN)_2$-bpy in THF and DMSO are shown in figure 6.6 and 6.7 respectively. The spectrum for the DMF system had been shown previously in figure 4.18.

It was necessary to record the EPR spectrum of $[5,5´\text{-}(CN)_2\text{-bpy}]^{1-}$ in DMSO at 298 K due to the high melting point of the solvent. This temperature remains close to the freezing limit of DMSO leading to an increase in viscosity of the sample solution. This causes the molecules of the sample species to tumble less effectively, resulting in the broader less resolved peaks observed in the spectrum of $[5,5´\text{-}(CN)_2\text{-bpy}]^{1-}$ in DMSO when compared to the spectra collected for the other solvent systems used.

The pattern of observable hyperfine coupling constants for all the systems studied were the same as those expected for the DMF system. The values determined by simulation for these couplings in each system investigated is shown in table 6.6.

No	Solvent	AN	$A_2{}^{14}N$	$A_2{}^{14}N$	$A_2{}^{1}H$	$A_2{}^{1}H$	$A_2{}^{1}H$	H_{pp}	g_{iso}
1	THF	8	1.4	0.95	1.22	0.91	-	0.35	2.00335
2	Acetone	12.4	1.365	0.96	1.23	0.92	0.205	0.5	2.00250
3	Pyridine	14.2	1.34	0.94	1.28	0.95	0.195	0.35	2.00169
4	DMF	16	1.3	0.9	1.47	1.03	0.2	0.4	2.00305
5	MeCN	18.9	1.31	0.89	1.435	1.035	0.135	0.35	2.00435
6	DMSO	19.3	1.28	0.89	1.43	1.06	0.135	0.4	2.00360

Table 6.6 EPR data for $[5,5´\text{-}(CN)_2\text{-bpy}]^{1-}$ in a range of solvents at 233 K (electrolyte = 0.3 M [TBA][BF_4])

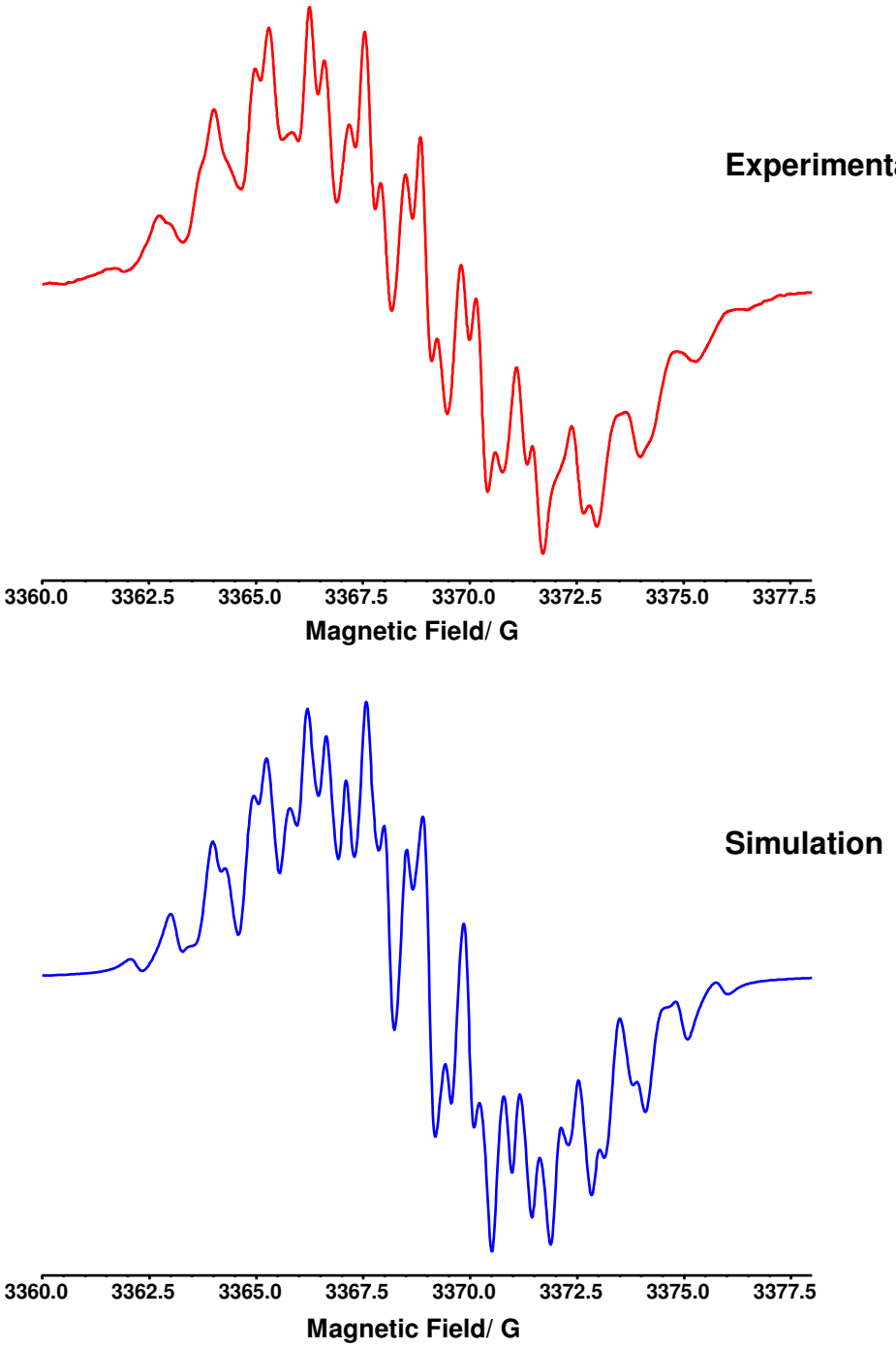

$A_{2\ ^{14}N} = 1.400$
$A_{2\ ^{14}N} = 0.950$
$A_{2\ ^{1}H} = 1.220$
$A_{2\ ^{1}H} = 0.910$
$\Delta H_{pp} = 0.40$
$L/G = 0$
$g_{iso} = 2.00360$

Figure 6.7 Experimental and simulated EPR of $[5,5'\text{-}(CN)_2\text{-bpy}]^{1-}$ generated *in-situ* at -2.0 V vs. Ag/AgCl at 233 K in 0.1 M $[TBA][BF_4]$/THF

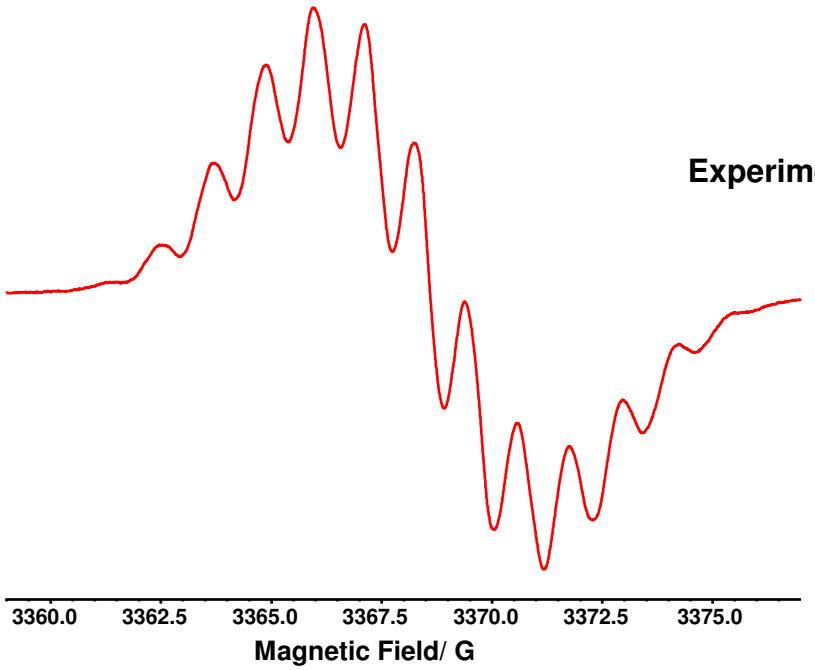

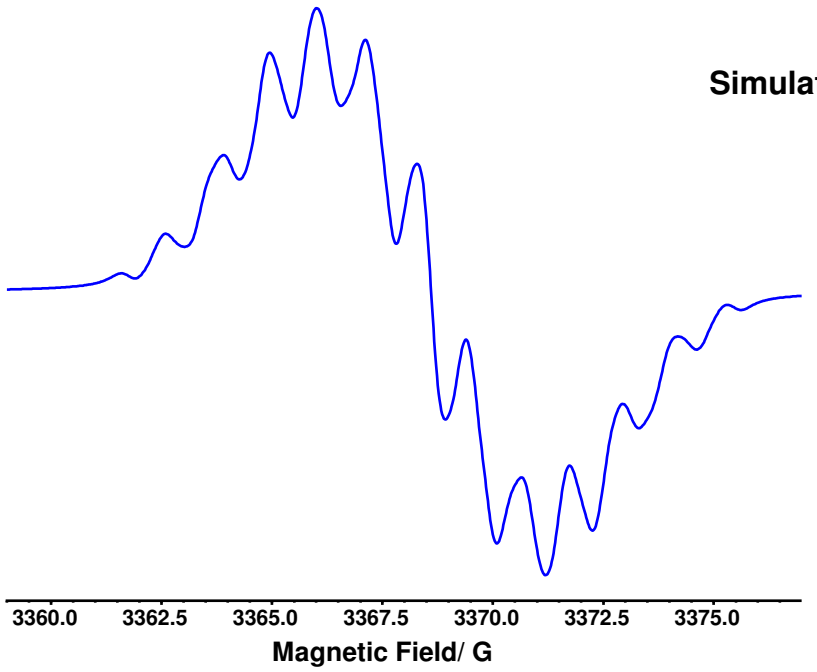

$A_{2\ ^{14}N} = 1.280$
$A_{2\ ^{14}N} = 0.890$
$A_{2\ ^{1}H} = 1.430$
$A_{2\ ^{1}H} = 1.060$
$A_{2\ ^{1}H} = 0.135$
$\Delta H_{pp} = 0.40$
$L/G = 0$
$g_{iso} = 2.00360$

Figure 6.8 Experimental and simulated EPR of $[5,5'\text{-}(CN)_2\text{-bpy}]^{1-}$ generated *in-situ* at -1.5 V vs. Ag/AgCl at 298 K in 0.1 M $[TBA][BF_4]$/DMSO

Comparison of the values from the coupling constants across the full range of solvents shows evidence that the magnitude of the coupling constant is dependent on the solvent acceptor number. Murray observed that the EPR spectroelectrochemical results for $[5,5´\text{-}(NO)_2\text{-bpy}]^{1-}$ were solvent dependent but could draw no quantitative correlation with a number of empirical solvent parameters, including the acceptor number.[2] It was noted that changing the solvent system resulted in the spectra recorded for $[5,5´\text{-}(NO)_2\text{-bpy}]^{1-}$ being visibly different.

The coupling to the ^{14}N nuclei in the NO_2 groups was found to be more affected by changes in the solvent than the coupling to the ^{1}H nuclei in the rings. For all the observable couplings it was seen that larger couplings arose in higher acceptor number solvents. Murray theorised that solvents with a higher acceptor number stabilise the e^- density on the NO_2 groups to a greater extent than the ^{1}H nuclei of the rings, thus leading to the observed trend, as the hyperfine coupling constant is directly proportional to the electron density. It was expected that a similar effect would be observed for the solvent studies of $[5,5´\text{-}(CN)_2\text{-bpy}]^{1-}$ in this investigation.

When the EPR spectra of $[5,5´\text{-}(CN)_2\text{-bpy}]^{1-}$ in the six solvent systems studied were compared it was found that the overall structure was very similar. Each contains a ^{14}N coupling and a ^{1}H coupling of approximately 1.3 G and smaller ^{14}N and ^{1}H couplings of approximately 0.9 G, with most of the spectra also exhibiting a further ^{1}H coupling of 0.2 G. These similarities indicate that the $[5,5´\text{-}(CN)_2\text{-bpy}]^{1-}$ species has the same basic electronic structure in all the solvent systems. Changing the solvent therefore has the effect of fine tuning the magnitude of the coupling constants, rather than resulting in large scale changes in the pattern of observable coupling constants.

Examination of the results indicates a correlation between all the observable coupling constants and the solvent acceptor number. As the acceptor number of the solvent increases the value of the two ^{14}N coupling constants decreases. The linear fits for the two data series gives good R^2 values of 0.9105 and 0.7639, see figure 6.9. Conversely the two larger ^{1}H coupling constants increase as the acceptor number increases. Again both of the linear fits of these data series have good R^2 values of 0.7341 and 0.8544, see figure 6.10. The remaining smallest ^{1}H coupling constant decreases with increasing solvent acceptor number, also giving a linear fit with a good R^2 value of 0.8450, see figure 6.10.

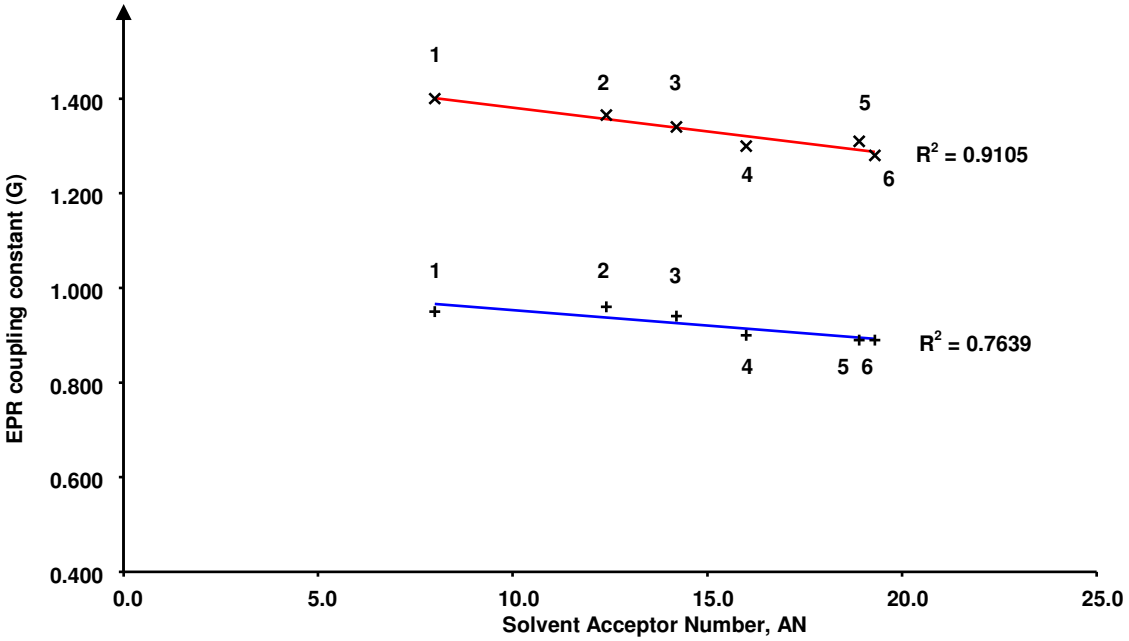

Figure 6.9 Plot of the EPR coupling constants for the two pairs of ^{14}N nuclei of 5,5´-$(CN)_2$-bpy against solvent acceptor number. For data point numbering scheme see Table 6.6

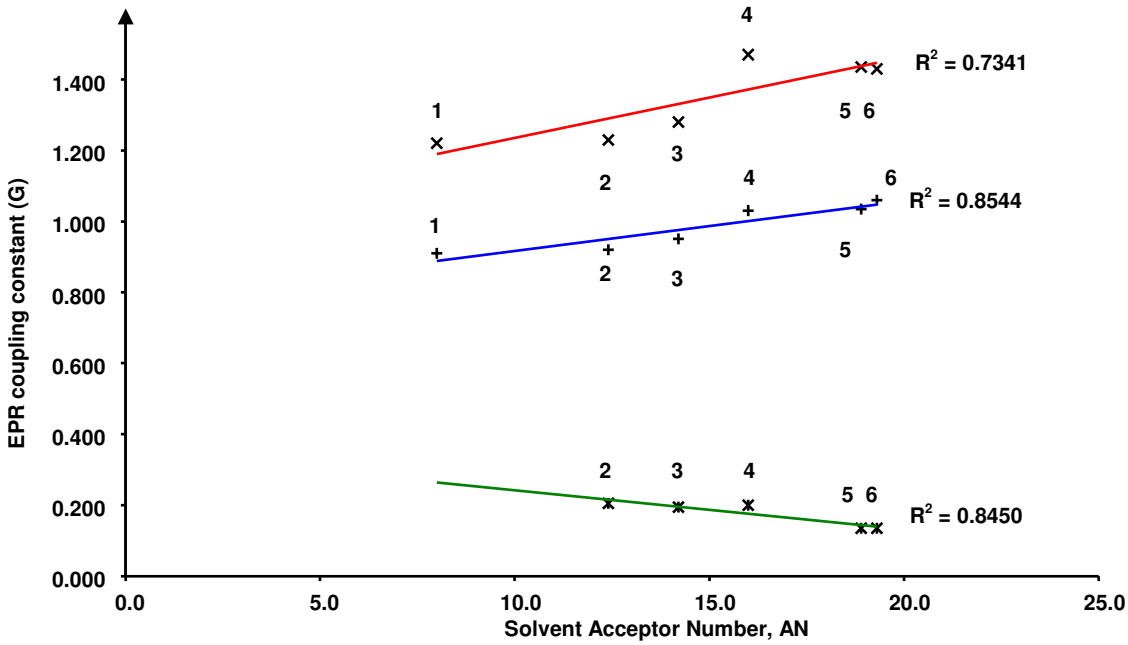

Figure 6.10 Plot of the EPR coupling constants for the three pairs of ^{1}H nuclei of 5,5´-$(CN)_2$-bpy against solvent acceptor number. For data point numbering scheme see Table 6.6

6.4 Conclusion

It has been determined in this study that the solvent has an effect on the electrochemical properties of the cyano substituted ligands studied. As the acceptor number of the solvent increases the one-electron reduction process of 4-CN-py become less negative. The variance in the $E_{½}$ value for the one-electron reduction of 4-CN-py in the range of solvents used in this study is 160 mV. This effect arises from the solvents with higher acceptor number and therefore greater acidic character being able to more effectively stabilise the negatively charged species, thus making the addition of the reduction electron to the 4-CN-py molecule easier.

For the 5,5´-$(CN)_2$-bpy ligand as the acceptor number of the solvent increases the two one electron reductions become less negative. In addition there is also evidence of a weak correlation between the solvent acceptor number and the separation between the

two reduction peaks. It was tentatively asserted that as the solvent acceptor number increased the separation between the two reduction peaks decreased.

This effect arises from the solvent with higher acceptor number and therefore greater acidic character being able to more effectively stabilise the negatively charged species. The di-reduced species with its higher negative charge will attract the acidic solvent more and it will experience greater stabilisation affect than the mono-reduced species.

The stabilisation effect experienced by the 5,5´-$(CN)_2$-bpy system is not as pronounced as the one determined for the 5,5´-$(NO_2)_2$-bpy system investigated by Murray.[2] This is due to a difference in the reduction reaction mechanism. Murray has theorised that the reduction mechanism of 5,5´-$(NO_2)_2$-bpy involves addition of the reduction electron to a molecular orbital localised on the NO_2 substituent groups with little delocalisation to the bpy rings. In contrast the evidence collected from this study suggests that the reduction mechanism of 5,5´-$(CN)_2$-bpy involves addition of the reduction electron to a molecular orbital that is not localised to the CN substituent but is spread across the entire molecule.

Investigation of the EPR spectroscopy of [5,5´-$(CN)_2$-bpy]$^{1-}$ in the range of solvents used has shown evidence that the experimentally determined EPR coupling constants are dependent on the acceptor number of the solvent. Comparison with previous work by Murray[2] on the solvent dependence of the EPR coupling constants of [5,5´-$(NO_2)_2$-bpy]$^{1-}$ indicates evidence of a stronger correlation between the solvent AN and the EPR coupling constants for the [5,5´-$(CN)_2$-bpy]$^{1-}$ species investigated in

this work. These findings support the theory that the mechanism of reduction for the two ligands is different.

The spectra of $[5,5´\text{-}(NO_2)_2\text{-bpy}]^{1-}$ show a large change in the magnitude of the ^{14}N coupling constant that was assigned to the NO_2 groups but a much smaller change in the ^{1}H coupling observable in all the spectra. This suggests that the solvent is interacting with a molecular orbital that is localised at the highly electronegative NO_2 groups.

In comparison the spectra of $[5,5´\text{-}(CN)_2\text{-bpy}]^{1-}$ show much smaller changes in the magnitude of the coupling constants than those observed in $[5,5´\text{-}(NO_2)_2\text{-bpy}]^{1-}$. However coupling to all possible spin active nuclei is observed, suggesting the solvent is interacting with a molecular orbital spread across the entire ring system rather than localised at the CN substitution groups.

Examination of the results shows some evidence of a trend between the two ^{14}N coupling constants and the solvent acceptor number. As the acceptor number increases the coupling constants decrease. In addition a correlation is observed for the two larger ^{1}H coupling constants determined for the $[5,5´\text{-}(CN)_2\text{-bpy}]^{1-}$ species. In contrast to the effect seen for the ^{14}N couplings, as the solvent acceptor number increases the magnitude of the ^{1}H coupling constants also increase. This suggests that higher acceptor number solvents can cause a smearing out of the e^- density in the molecule away from the more electronegative nitrogen atoms, thus allowing for the unpaired electron to interact more strongly with the ^{1}H nuclei of the rings.

6.5 References

1. L. P. Moorcraft, Ph.D Thesis, University of Edinburgh, 2008.
2. P. R. Murray, Ph.D Thesis, University of Edinburgh, 2006.
3. S. K. Al-Musharafi, Ph.D Thesis, University of Edinburh, 2006.
4. V. Gutmann, *The Donor-Acceptor Aproach to Molecular Interactions*, plenum Press, New York, 1978.

7 Electrochemical and Spectroelectrochemical Characterisation Of $[Pt(X,X'\text{-}(CN)_2\text{-}bpy)Cl_2]$, $[Fe(II)(X,X'\text{-}(CN)_2\text{-}bpy)_3][BF_4]_2$ and $[Fe(II)(X,X'\text{-}(CF_3)_2\text{-}bpy)_3][BF_4]_2$ complexes

7.1 Introduction

Derivatised 2,2´-bipyridine, bpy, molecules have found much use as ligands in complexes with a large number of transition metals.[1-12] The nature and position of substituent groups on the ligands can be varied with relative ease.[13-18] Through controlled manipulation of the ligand set around the metal centre it is possible to tune physical properties of a complex such as redox potentials, absorption maxima and energies and lifetimes of excited states.[9,10,12,19]

As described in detail in section 1.2, 4,4´-derivatives of bpy have been the most extensively investigated, due in part to the fact that there are simpler synthetic routes to their preparation, but also because upon complexation ligands with substitution groups in these positions do not experience steric hindrance effects, unlike the corresponding 3,3´ and 6,6´ analogues.[1,20]

Most studies of bpy transition metal complexes have involved tris-bpy complexes with pseudo-octahedral geometry.[2,11] A lesser number of square-planar complexes have also been investigated.[21-26] Two classes of bpy complex that have been examined in this work are Pt(II) bpy dichloride complexes and Fe(II) tris-bpy complexes.

Square-planar Pt(II) bipyridine coordination complexes have been studied for their unusual redox, spectroscopic and photophysical properties.[20,27-32] More recently these complexes have seen renewed interest with investigations into their potential use in the area of dye-sensitised solar cells (DSSCs).[33-37] A highly desirable property of metal complexes for such applications is the presence of long-lived excited states which usually exhibit good charge separation. An accurate model of the electronic structure of these complexes could help in the design of future useful materials. Spectroelectrochemical techniques offer an ideal way of probing the electronic properties of the HOMO and LUMO of such metal complexes.

When the redox character of a series of [Pt(4,4´-X_2-bpy)Cl_2] complexes (where X = NH_2, OEt, Me, H, Ph, Cl or CO_2Me) was investigated by McInnes *et al* it was found that the first reduction potential had a linear dependence on the Hammett parameter of the substitution group.[12] An extensive search of current literature yields electrochemical data for a number of [Pt(3,3´-$(X)_2$-bpy)Cl_2][37,39,40] and [Pt(5,5´-$(X)_2$-bpy)Cl_2][37,40,41,42] complexes as well as data for [Pt(4,4´-$(CO_2Et)_2$-bpy)Cl_2].[37] The electrochemical data for all the known systems have been collated and are reported in table 7.1, table 7.2 and table 7.3 for the 3,3´, 4,4´ and 5,5´ complexes respectively. All redox potentials reported have been adjusted relative to the Ag/AgCl reference used in this work.

Substituent X	σ_m	[Pt(3,3´-$(X)_2$-bpy)Cl_2]			Ref.
		$E_{½,(1)}$ / V	$E_{½,(2)}$ / V	$E_{½,(1)}$ - $E_{½,(2)}$ / mV	
H	0.00	-1.06	-1.79	730	38
CO_2Me	0.37	-0.61	-1.26	650	39
CO_2Et	0.37	-0.61	-1.27	660	37
NO_2	0.71	-0.44	-0.88	440	40

Table 7.1 Half wave reduction potentials for a series of [Pt(3,3´-$(X)_2$-bpy)Cl_2] complexes *vs*. Ag/AgCl (Where X = H, CO_2Me, CO_2Et and NO_2)

Substituent X	σ_p	[Pt(4,4´-(X)$_2$-bpy)Cl$_2$]			Ref.
		$E_{½,(1)}$ / V	$E_{½,(2)}$ / V	$E_{½,(1)} - E_{½,(2)}$ / mV	
NH_2	-0.66	-1.53	-	-	12
OEt	-0.24	-1.23	-1.86	630	12
Me	-0.17	-1.16	-1.92*	760	12
Ph	-0.01	-1.01	-1.62	610	38
H	0.00	-1.06	-1.79	730	12
Cl	0.23	-0.83	-1.56*	730	12
CO_2Me	0.45	-0.67	-1.25	580	12
CO_2Et	0.45	-0.67	-1.25	580	37

Table 7.2 Half wave reduction potentials for a series of [Pt(4,4´-(X)$_2$-bpy)Cl$_2$] complexes *vs*. Ag/AgCl (Where X = NH_2, OEt, Me, H, Cl, Ph, CO_2Me, CO_2Et and NO_2). * Indicates an irreversible process, E_{pc} value is quoted for this process

Substituent X	σ_m	[Pt(5,5´-(X)$_2$-bpy)Cl$_2$]			Ref.
		$E_{½,(1)}$ / V	$E_{½,(2)}$ / V	$E_{½,(1)} - E_{½,(2)}$ / mV	
Me	-0.07	-1.17	-1.82	650	41
H	0.00	-1.06	-1.79	730	38
Ph	0.06	-0.93	-1.51	580	42
Cl	0.37	-0.80	-	-	42
CO_2Me	0.37	-0.52	-1.01	490	41
CO_2Et	0.37	-0.53	-1.03	500	37
Br	0.39	-0.83	-	-	42
NO_2	0.71	-0.18	-0.32	140	40

Table 7.3 Half wave reduction potentials for a series of [Pt(5,5´-(X)$_2$-bpy)Cl$_2$] complexes *vs*. Ag/AgCl (Where X = Me, H, Ph, Cl, CO_2Me, CO_2Et, Br and NO_2)

Plots of the first and second reduction potentials for the [Pt(X)$_2$-bpy)Cl$_2$] complexes, where X is the substituent in the 3,3´, 4,4´ and 5,5´positions *vs*. the relevant Hammett parameter have been drawn up, figures 7.1 – 7.3. These plots indicate that for each of the complexes a linear correlation exists between the electron withdrawing/donating nature of the substituent group and the reduction potential. It can be seen that electron donating substitution groups destabilise the LUMO of the complex compared to unsubstituted 2,2´-bipyridine.

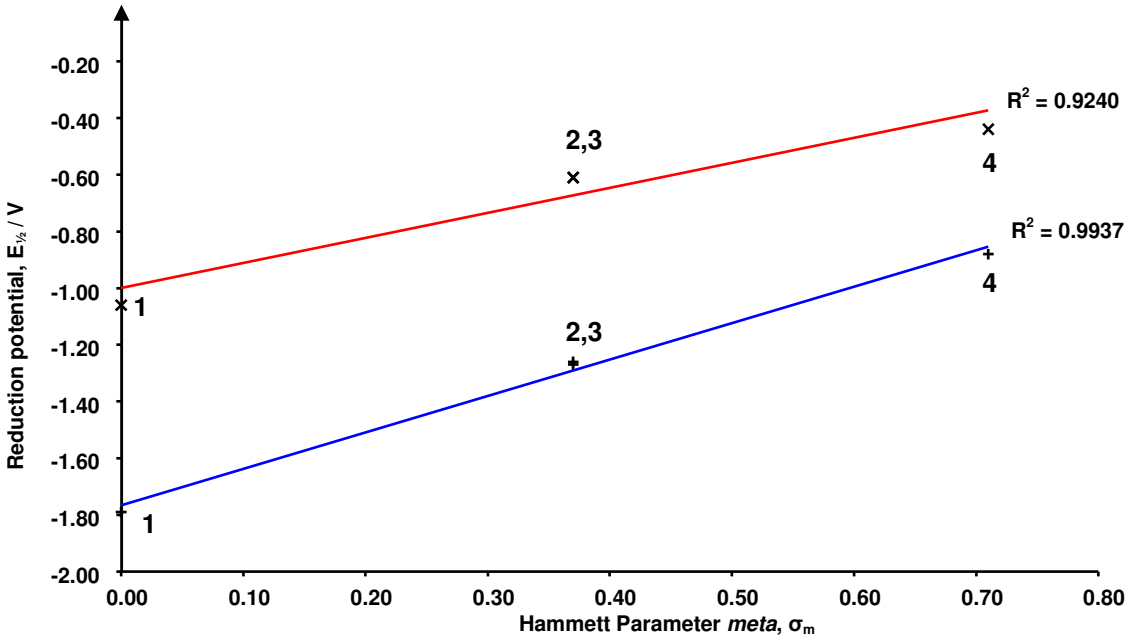

Figure 7.1 Plot of $E_{½}$ of the first (red) and second (blue) reduction of [Pt(3,3´-$(X)_2$-bpy)Cl_2] *vs. meta* Hammett parameter, σ_m of the substituent X, (where X is the substituent under investigation). 1) X= H, 2) X = CO_2Me, 3) X = CO_2Et, 4) X = NO_2

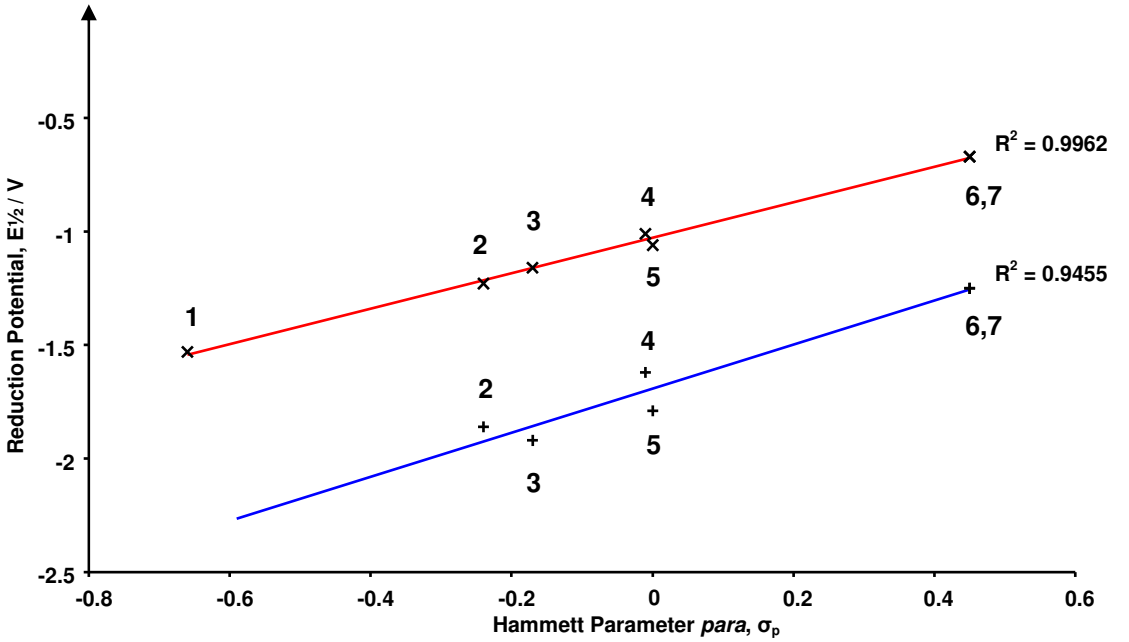

Figure 7.2 Plot of $E_{½}$ of the first (red) and second (blue) reduction of [Pt(4,4´-$(X)_2$-bpy)Cl_2] *vs. para* Hammett parameter, σ_p of the substituent X, (where X is the substituent under investigation). 1) X= NH_2, 2) X = OEt, 3) X = Me, 4) X = Ph, 5) X = H, 6) X = CO_2Me, 7) X = CO_2Et

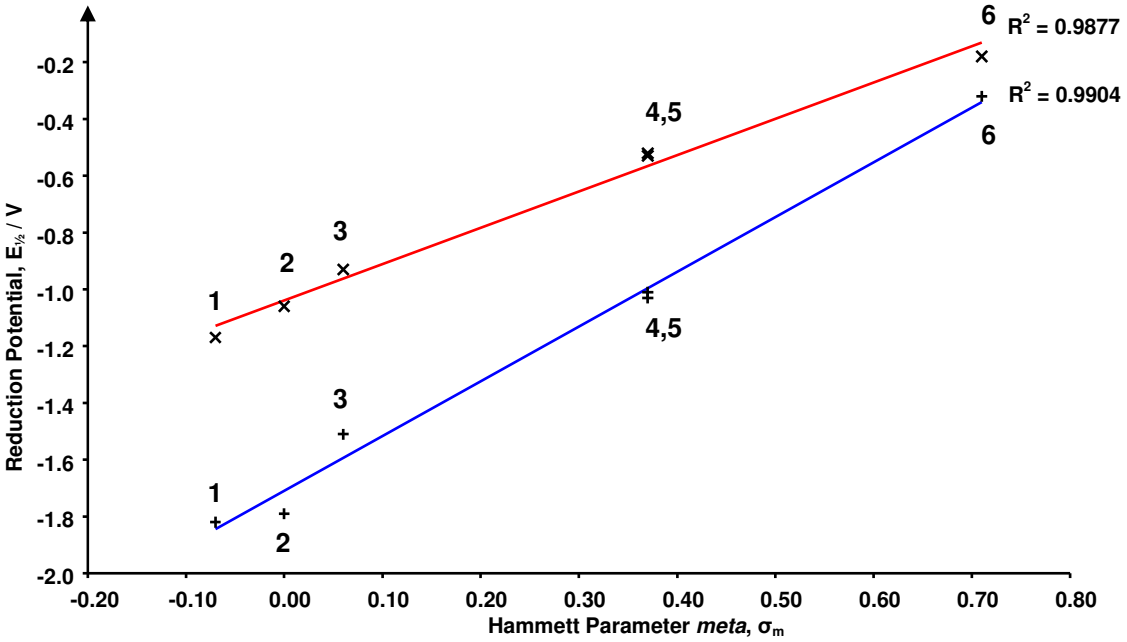

Figure 7.3 Plot of $E_{½}$ of the first (red) and second (blue) reduction of [Pt(5,5´-$(X)_2$-bpy)Cl_2] *vs. meta* Hammett parameter, σ_m of the substituent X, (where X is the substituent under investigation). 1) X= Me, 2) X = H, 3) X = Ph, 4) X = CO_2Me, 5) X = CO_2Et, 6) X = NO_2

McInnes and co-workers have also conducted *in situ* UV/Vis and EPR spectroelectrochemical studies on a series of [Pt(4,4´-(X_2)-bpy)Cl_2] complexes (where X = NH_2, OEt, Me, H, Ph, Cl or CO_2Me) and have shown that the LUMO of the complex is predominantly ligand-based.[12] The Pt metal centre contribution was determined to between 7-12% to the SOMO of the mono-reduced [Pt(4,4´-(X_2)-bpy)Cl_2]$^{1-}$ complex and arises from contribution of the $5d_{yz}$ and $6p_z$ orbitals (the principle axes are defined as shown in figure 7.4). Similar investigation by Jack[41] and Murray[40] on analogous [Pt(5,5´-(X_2)-bpy)Cl_2]$^{1-}$ complexes have determined the Pt metal contribution to be in the range of 2.3-12.6%.

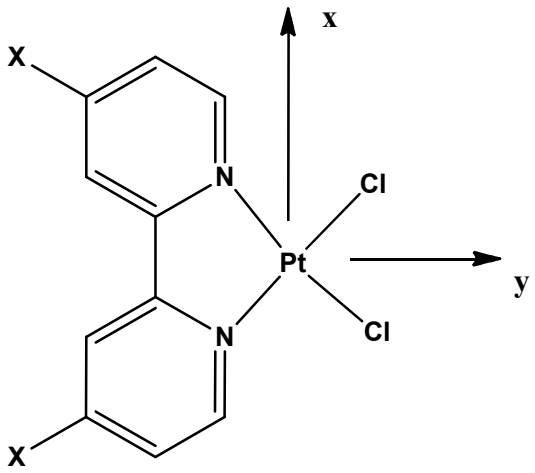

Figure 7.4 Structure and principle axes of $[Pt(4,4´\text{-}(X_2)\text{-bpy})Cl_2]^{1-}$, the z axis is perpendicular to the plane of the molecule

As mentioned earlier, more commonly studied bpy compounds are tris-bpy complexes of the form $[M(X_2\text{-bpy})_3]^{n+}$, with pseudo-octahedral geometry.[2-11] Tris-bpy complexes have been used as photoredox catalysts[11,43] and chemilinescence sensors.[44] Complexes with this type of coordination sphere are represented in this work by the Fe(II) complexes with the general formula $[Fe(II)(X_2\text{-bpy})_3][BF_4]_2$, where X = CN or CF_3 in either the 4,4´ or 5,5´ positions.

In comparison to the Pt complexes discussed above, there is limited electrochemical data in the literature for complexes of the form $[Fe(II)(4,4´\text{-}(X_2)\text{-bpy})_3]^{2+}$.[10,45,46] In addition the redox properties of only one 5,5´ analogue has been reported.[9] Electrochemical studies of the Fe(II) and analogous transition metals tris-bpy complexes have shown that these compounds all undergo three closely spaced one-electron reductions. Spectroelectrochemical experiments have determined that these three reductions involve the sequential addition of an electron to the lowest energy unoccupied π^* orbital of each of the bipyridine ligands.[9,10]

The aim of this chapter is to demonstrate the ability of the CN and CF_3 substituted bpy ligands investigated to form metal complexes analogous to those reported in the literature.[9,10,12] The electrochemical properties of these complexes were studied to determine if they fit with the previously observed trends for the Pt(II) complexes and to see if a similar trend can be observed for the Fe(II) complexes. Two complexes ($[Pt(3,3´\text{-}(CN)_2\text{-bpy})Cl_2]$ and $[Fe(II)(4,4´\text{-}(CF_3)\text{-bpy})_3][BF_4]_2$) have been chosen for use as spectroelectrochemical case studies of complexes with these types of ligands.

7.2 Synthesis

Complexes of the form $[Pt(X,X´\text{-}(CN)_2\text{-bpy})Cl_2]$ (where X,X´ = 3,3´ and 5,5´) were prepared by dissolving the appropriate ligand in acetonitrile which was then added to an equimolar amount of $K_2[PtCl_4]$ dissolved in H_2O. The combined solution was heated to reflux and the resulting precipitate filtered. The products were confirmed by CHN analysis as given in section 2.1.

The Fe complexes were prepared by adding the appropriate ligand to a solution of $Fe(II)(BF_4)_2$ in acetonitrile. Addition of diethyl ether resulted in precipitation of the desired product. The syntheses were confirmed by CHN analysis, as given in section 2.1.

7.3 Electrochemistry

7.3.1 [Pt(X,X´-$(CN)_2$-bpy)Cl_2] complexes

7.3.1.1 Cyclic Voltammetry

The cyclic voltammogram of [Pt(3,3´-$(CN)_2$-bpy)Cl_2] in 0.1 M [TBA][BF_4]/DMF at 298 K, shown in figure 7.5, exhibits one-electron reversible reductions at $E_{½,(1)}$ = -0.41 V and $E_{½,(2)}$ = -1.06 V. A plot of i_p *vs.* $v^{½}$ gives a linear relationship for both processes, indicating that both electron transfer processes are diffusion controlled.

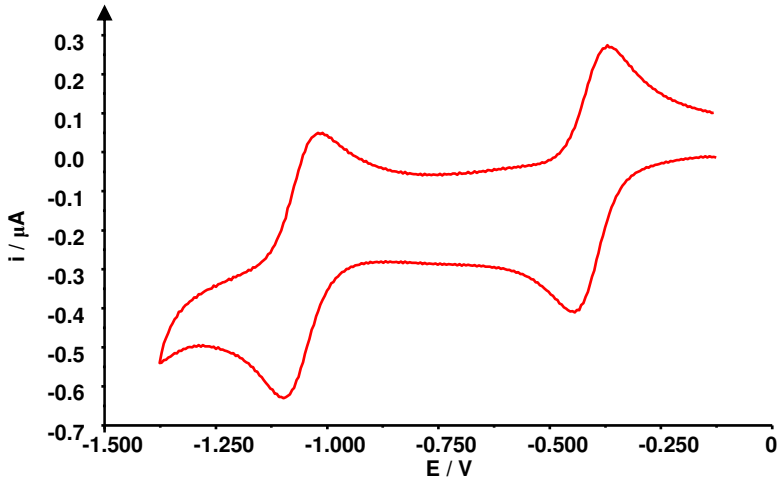

Figure 7.5 Cyclic Voltammogram of [Pt(3,3´-$(CN)_2$-bpy)Cl_2] *vs.* Ag/AgCl in 0.1 M [TBA][BF_4]/DMF at 298 K, ν = 100 mVs^{-1}

The two one-electron reductions processes of [Pt(3,3´-$(CN)_2$-bpy)Cl_2] are assigned to the sequential reductions of the 3,3´-$(CN)_2$-bpy ligand. The separation between the two redox processes, $\Delta E_{½}$, was found to be 650 mV. A value of this size indicates that the second reduction is a spin pairing processes.

When the cyclic voltammogram of [Pt(5,5´-$(CN)_2$-bpy)Cl_2] in 0.1 M [TBA][BF_4]/DMF at 298 K was conducted two reversible reductions at $E_{½,1}$ = -0.35 V and $E_{½,2}$ = -0.90 V were observed, shown in figure 7.6. Plots of i_p *vs.* $v^{½}$ for both

redox processes observed give linear relationships. This indicates that both redox processes are diffusion controlled.

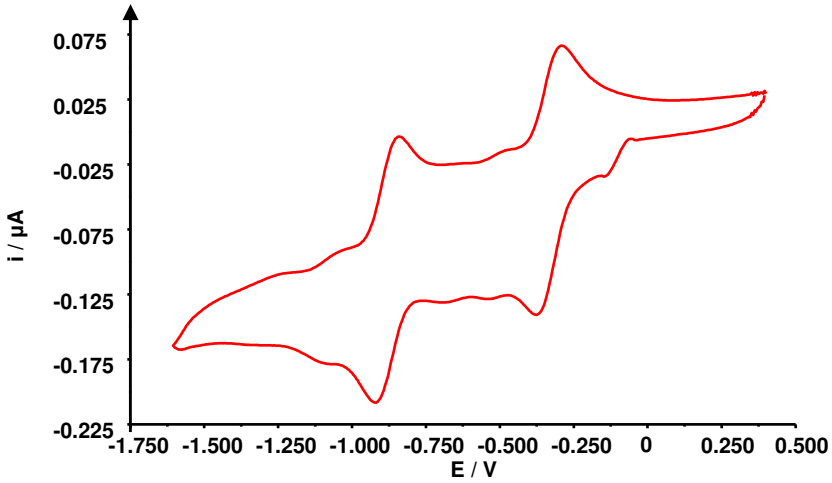

Figure 7.6 Cyclic Voltammogram of [Pt(5,5´-$(CN)_2$-bpy)Cl_2] *vs*. Ag/AgCl in 0.1 M [TBA][BF_4]/DMF at 298 K, ν = 100 mVs^{-1}

The separation between the two reduction reactions in [Pt(5,5´-$(CN)_2$-bpy)Cl_2], $\Delta E_{½}$, was found to be 550 mV. Again a value of this size indicates that the second reduction is a spin pairing process.

Attempts to synthesis the [Pt(4,4´-$(CN)_2$-bpy)Cl_2] analogue were unsuccessful. This is rather surprising giving the number of other [Pt(4,4´-$(X)_2$-bpy)Cl_2] complexes that have been reported in the literature.[12,38,39]

The two Pt complexes studied both exhibit easier (less negative potential) reductions than the equivalent free ligands, $E_{½,(1)}$ = -0.41 V and $E_{½,(2)}$ = -1.06 V cf. $E_{½,(1)}$ = -1.34 V and $E_{½,(2)}$ = -1.97 V for 3,3´-$(CN)_2$-bpy and $E_{½,(1)}$ = -0.35 V and $E_{½,(2)}$ = -0.90 V cf. $E_{½,(1)}$ = -1.08 V and $E_{½,(2)}$ = -1.61 V for 5,5´-$(CN)_2$-bpy. This shift may be attributed to the electronic influence of the Pt^{2+} metal centre.

It is also noted that two additional reduction processes are observed in the cyclic voltammogram of [Pt(5,5´-$(CN)_2$-bpy)Cl_2], with $E_{½,1}$ = -0.53 V and $E_{½,2}$ = -1.09 V, Both are significantly less negative than the free ligand reduction processes. It is suggested that these peaks are due to a secondary kinetically unfavoured product. One possibility is a complex where the dicyanobipyridine is coordinated to the metal centre via the CN group; another could be the substitution of one or both chloride ligands for H_2O or CH_3CN. All attempts to purify the Pt complex were unsuccessful.

The reduction potentials observed during the cyclic voltammetric investigation of the two dicyanobipyridine Pt complexes are shown in table 7.4. An attempt has been made to estimate the first and second reduction potentials of the analogous [Pt(4,4´-$(CN)_2$-bpy)Cl_2] complex. This was achieved by extrapolating the data from the plot of the para Hammett parameter, σ_p *vs*. the first and second reduction potentials of the known [Pt(4,4´-$(X)_2$-bpy)Cl_2] complexes listed in table 7.2 (figure 7.2). Substitution of the CN group Hammett parameter (σ_p = 0.66) into the straight line equations for the two linear fits yields the estimated values shown in table 7.4.

Comparison of the potentials for the first reduction in each of the compounds clearly shows that the [Pt(5,5´-$(CN)_2$-bpy)Cl_2] complex is the most easily reduced. This is in line with the results for the methyl and ethyl ester complexes, table 7.5 and table 7.6 respectively. The second reduction potentials also exhibit a pattern that matches that seen for the ester complexes. The [Pt(5,5´-$(CN)_2$-bpy)Cl_2]$^{1-}$ complex is reduced at significantly less negative potential than either the 3,3´ or 4,4´ analogues. In contrast to what is seen for the first reduction, the second reduction of [Pt(3,3´-$(CN)_2$-bpy)Cl_2] and [Pt(4,4´-$(CN)_2$-bpy)Cl_2] are predicted to occur at very

similar potentials. This indicates that the $[Pt(3,3'\text{-}(CN)_2\text{-}bpy)Cl_2]^{1-}$ and $[Pt(4,4'\text{-}(CN)_2\text{-}bpy)Cl_2]^{1-}$ species must be stabilised to a similar degree with respect to the addition of a second electron to the SOMO of the complex.

	$E_{½,(1)}$ / V	$E_{½,(2)}$ / V	$E_{½,(1)} - E_{½,(2)}$ / mV
$[Pt(3,3'\text{-}(CN)_2\text{-}bpy)Cl_2]$	**-0.41**	**-1.06**	**650**
$[Pt(4,4'\text{-}(CN)_2\text{-}bpy)Cl_2]$	**-0.51***	**-1.05***	**540**
$[Pt(5,5'\text{-}(CN)_2\text{-}bpy)Cl_2]$	**-0.35**	**-0.90**	**550**

Table 7.4 Half wave reduction potentials for $[Pt(3,3'\text{-}(CN)_2\text{-}bpy)Cl_2]$, $[Pt(4,4'\text{-}(CN)_2\text{-}bpy)Cl_2]$ and $[Pt(5,5'\text{-}(CN)_2\text{-}bpy)Cl_2]$ *vs*. Ag/AgCl. * Indicates values estimated from figure 7.2

	$E_{½,(1)}$ / V	$E_{½,(2)}$ / V	$E_{½,(1)} - E_{½,(2)}$ / mV	Ref.
$[Pt(3,3'\text{-}(CO_2Me)_2\text{-}bpy)Cl_2]$	**-0.61**	**-1.26**	**650**	**39**
$[Pt(4,4'\text{-}(CO_2Me)_2\text{-}bpy)Cl_2]$	**-0.67**	**-1.25**	**580**	**12**
$[Pt(5,5'\text{-}(CO_2Me)_2\text{-}bpy)Cl_2]$	**-0.52**	**-1.01**	**490**	**41**

Table 7.5 Half wave reduction potentials for $[Pt(3,3'\text{-}(CO_2Me)_2\text{-}bpy)Cl_2]$, $[Pt(4,4'\text{-}(CO_2Me)_2\text{-}bpy)Cl_2]$ and $[Pt(5,5'\text{-}(CO_2Me)_2\text{-}bpy)Cl_2]$ *vs*. Ag/AgCl

	$E_{½,(1)}$ / V	$E_{½,(2)}$ / V	$E_{½,(1)} - E_{½,(2)}$ / mV	Ref.
$[Pt(3,3'\text{-}(CO_2Et)_2\text{-}bpy)Cl_2]$	**-0.61**	**-1.27**	**660**	**37**
$[Pt(4,4'\text{-}(CO_2Et)_2\text{-}bpy)Cl_2]$	**-0.67**	**-1.25**	**580**	**37**
$[Pt(5,5'\text{-}(CO_2Et)_2\text{-}bpy)Cl_2]$	**-0.53**	**-1.03**	**500**	**37**

Table 7.6 Half wave reduction potentials for $[Pt(3,3'\text{-}(CO_2Et)_2\text{-}bpy)Cl_2]$, $[Pt(4,4'\text{-}(CO_2Et)_2\text{-}bpy)Cl_2]$ and $[Pt(5,5'\text{-}(CO_2Et)_2\text{-}bpy)Cl_2]$ *vs*. Ag/AgCl

Revised plots of the *meta* Hammett parameter *vs*. the first and second reduction potential of the known $[Pt(3,3'\text{-}(X)_2\text{-}bpy)Cl_2]$ and $[Pt(5,5'\text{-}(X)_2\text{-}bpy)Cl_2]$ complexes including the dicyanobipyridine complexes investigated in these studies are shown in figure 7.7 and figure 7.8 in order to determine if the cyano substitution group follows the correlation previously observed (see section 7.1).

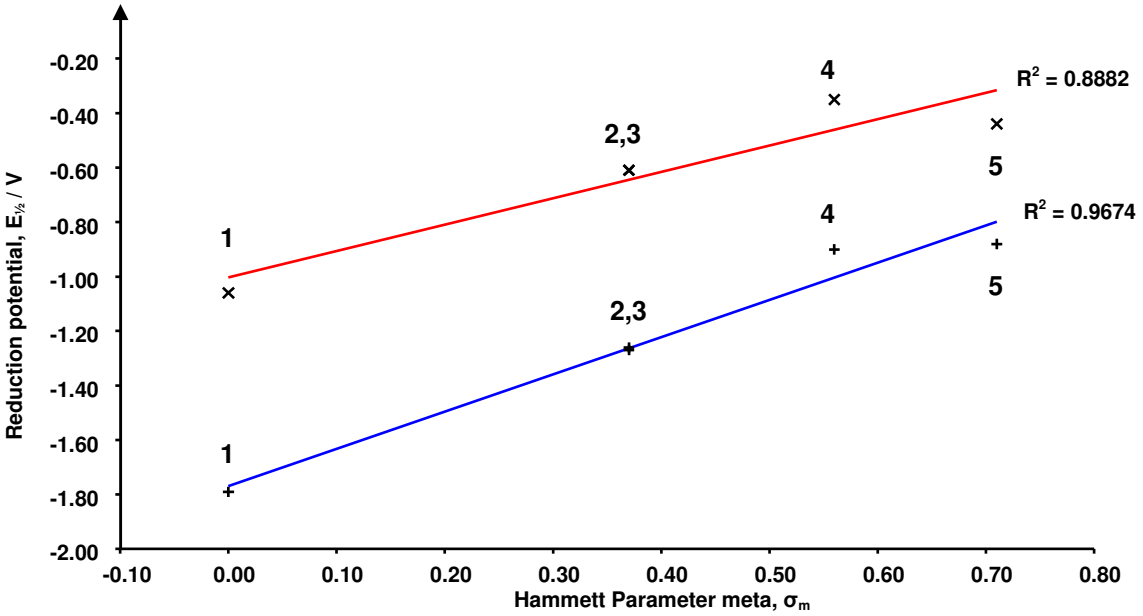

Figure 7.7 Plot of $E_{½}$ of the first (red) and second (blue) reduction of [Pt(3,3´-$(X)_2$-bpy)Cl_2] *vs.* meta Hammett parameter, σ_m of the substituent X, (were X is the substituent under investigation). 1) X= H, 2) X = CO_2Me, 3) X = CO_2Et, 4) X = CN, 5) X = NO_2

From figure 7.7 it can be seen that $E_{½,(1)}$ and $E_{½,(2)}$ of the [Pt(3,3´-$(CN)_2$-bpy)Cl_2] complex give a fairly good agreement with the predicted correlation with σ_m, the linear fits having R^2 values of 0.8882 and 0.9674 for the first and second reduction respectively. These values are reduced slightly from the plot in figure 7.1 but do not represent a marked departure from the previously observed correlation.

As for the 3,3´ analogue, the $E_{½,(1)}$ and $E_{½,(2)}$ of the [Pt(5,5´-$(CN)_2$-bpy)Cl_2] complex also give a good agreement with the predicted correlation with σ_m, the linear fits having R^2 values of 0.9823 and 0.9120 for the first and second reduction respectively. Once again the values in this plot are reduced from the previous correlation plot, figure 7.3, with only a slight deviation for the first reduction but a much more marked change for the second reduction from 0.9904 in figure 7.3 to 0.9120 in figure 7.8. The observed reduction potential for [Pt(5,5´-$(CN)_2$-bpy)Cl_2]$^{1-}$ is significantly more negative than predicted by this correlation, suggesting that the cyano groups play less

of a role in stabilising the $[Pt(5,5'\text{-}(CN)_2\text{-}bpy)Cl_2]^{2-}$ species compared to the substitution groups of the other known $[Pt(5,5'\text{-}(X)_2\text{-}bpy)Cl_2]^{2-}$ complexes.

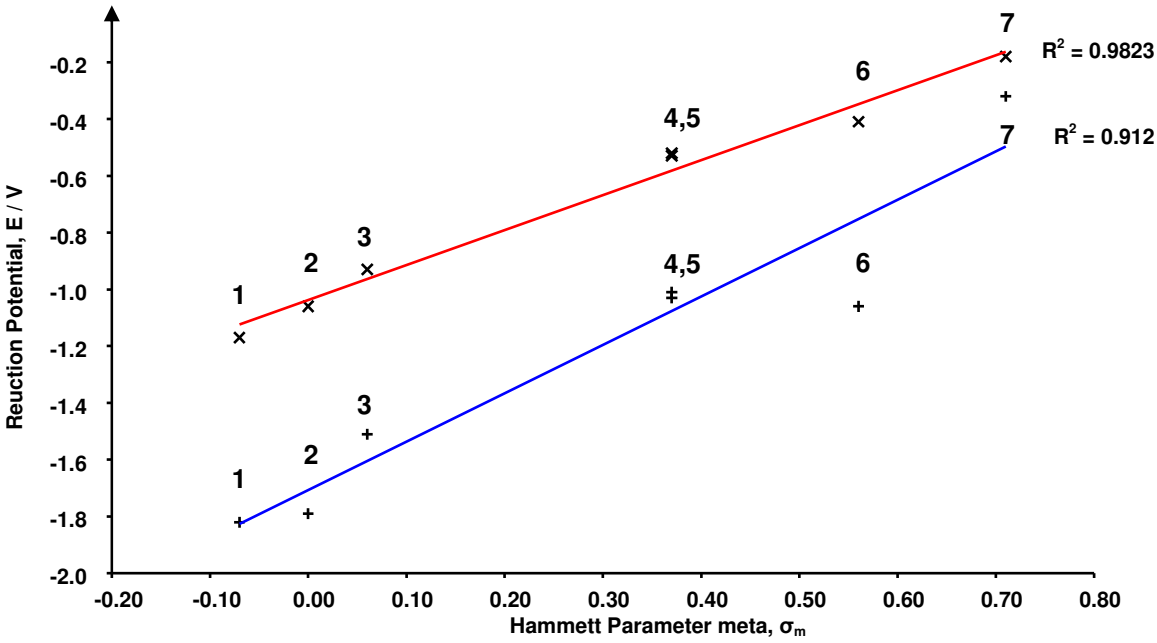

Figure 7.8 Plot of $E_{½}$ of the first (red) and second (blue) reduction of $[Pt(5,5'\text{-}(X)_2\text{-}bpy)Cl_2]$ *vs.* meta Hammett parameter, σ_m of the substituent X, (were X is the substituent under investigation). 1) X= Me, 2) X = H, 3) X = Ph, 4) X = CO_2Me, 5) X = CO_2Et, 6) X = CN, 7) X =NO_2

7.3.1.2 Differential Pulse

The differential pulse voltammograms of the two Pt complexes under investigation were also recorded to corroborate the findings from the CV investigation. The differential pulse voltammogram of $[Pt(3,3'\text{-}(CN)_2\text{-}bpy)Cl_2]$, figure 7.9, confirmed the findings from the cyclic voltammetry experiments, indicating that the complex had two reversible reduction processes at $E_{½,(1)}$ = -0.41 V and $E_{½,(2)}$ = -1.06 V respectively.

When the differential pulse voltammetry of the $[Pt(5,5'\text{-}(CN)_2\text{-}bpy)Cl_2]$ complex was conducted it showed four reversible reduction process, figure 7.10. The two strong signals at $E_{½,(1)}$ = -0.36 V and $E_{½,(3)}$ = -0.90 V correspond to the major peaks in the CV and the two much weaker signals at $E_{½,(2)}$ = -0.53 V and $E_{½,(4)}$ = -1.09 V

correspond to the less well resolved peaks in the CV. Examination of the peak heights clearly show that peaks 1 and 3 are related and peaks 2 and 4 related. A comparison of the separation between the two reductions for each pair of peaks showed that $\Delta E_{½,(1\text{-}3)}$ = 540 mV and $\Delta E_{½,(2\text{-}4)}$ = 560 mV, indicating that they are similar types of processes. It is likely that these pairs of processes are all 5,5´-$(CN)_2$-bpy ligand based reductions with the potentials varying due to the mode of coordination to the metal centre or the nature of the ancillary ligands.

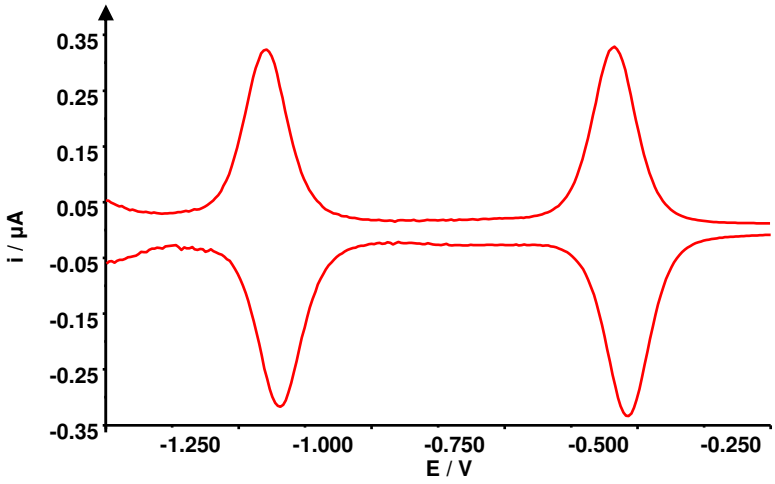

Figure 7.9 Differential Pulse Voltammogram of $[Pt(3,3´\text{-}(CN)_2\text{-}bpy)_3][BF_4]_2$ *vs.* Ag/AgCl in 0.1 M [TBA][BF_4]/DMF at 298 K

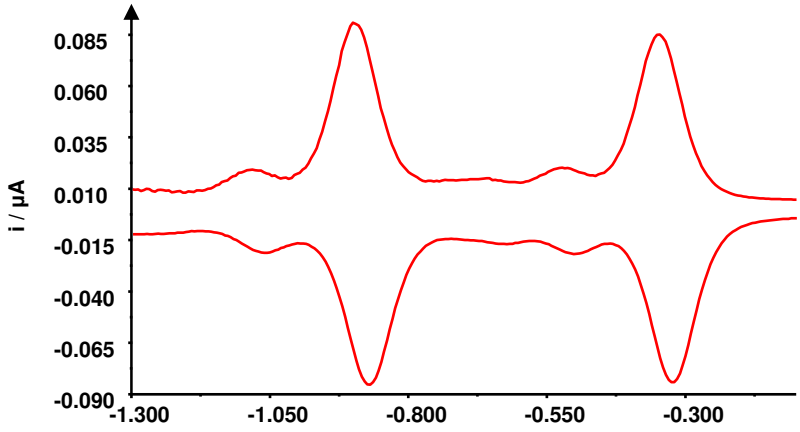

Figure 7.10 Differential Pulse Voltammogram of $[Pt(5,5´\text{-}(CN)_2\text{-}bpy)_3][BF_4]_2$ *vs.* Ag/AgCl in 0.1 M [TBA][BF_4]/DMF at 298 K

7.3.2 [Fe(II)(X,X´-$(CN)_2$-bpy)$_3$][BF_4]$_2$ complexes

7.3.2.1 Cyclic Voltammetry

When the cyclic voltammogram of [Fe(II)(5,5´-$(CN)_2$-bpy)$_3$][BF_4]$_2$ 0.1 M [TBA][BF_4]/MeCN at 298 K was conducted reversible reductions at $E_{½\,(1)}$ = -0.40 V, $E_{½,(2)}$ = -0.51 V, $E_{½,(3)}$ = -0.65 V, $E_{½,(4)}$ = -0.92 V, $E_{½,(5)}$ = -1.10 V, $E_{½,(6)}$ = -1.24 V and $E_{½,(7)}$ = -1.50 V were observed, shown in figure 7.11. In addition a reversible oxidation peak was observed at E_{pa} = 1.76 V.

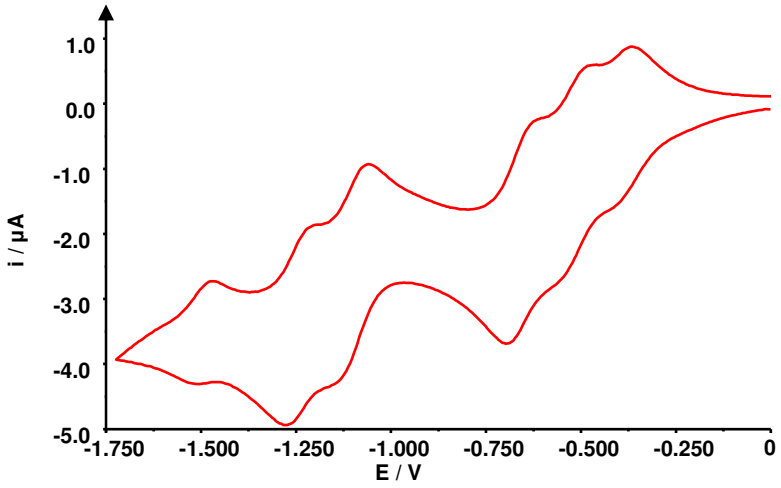

Figure 7.11 Cyclic Voltammogram of [Fe(II)(5,5´-$(CN)_2$-bpy)$_3$][BF_4]$_2$ *vs*. Ag/AgCl in 0.1 M [TBA][BF_4]/MeCN at 298 K, ν = 100 mVs^{-1}

Attempts to synthesise the [Fe(II)(4,4´-$(CN)_2$-bpy)$_3$][BF_4]$_2$ analogue were unsuccessful. Given the number of [Fe(II)(4,4´-$(X)_2$-bpy)$_3$] complexes reported in the literature[10] it was rather unexpected that it was not possible to isolate the Fe complex of this ligand. This is in line with the attempts to synthesise the Pt complex of this ligand discussed previously in section 7.3.1.1.

7.3.2.2 Differential Pulse Voltammetry

When the differential pulse voltammetry of [Fe(II)(5,5´-$(CN)_2$-bpy)$_3$][BF_4]$_2$ complex was conducted it showed six reversible reductions at $E_{½,(1)}$ = -0.41 V, $E_{½,(2)}$ = -0.49 V,

$E_{½,(3)}$ = -0.66 V, $E_{½,(4)}$ = -0.92, $E_{½,(5)}$ = -1.10 V and $E_{½,(6)}$ = -1.24 V and one quasi-reversible reduction at $E_{½,(7)}$ = -1.50 V. In addition there was a reversible oxidation at $E_{½}$ = 1.71 V.

7.3.3 [Fe(II)(X,X´-$(CF_3)_2$-bpy)$_3$][BF_4]$_2$ complexes

7.3.3.1 Cyclic Voltammetry

The cyclic voltammogram of [Fe(II)(4,4´-$(CF_3)_2$-bpy)$_3$][BF_4]$_2$ in 0.1 M [TBA][BF_4]/MeCN at 298 K, shown in figure 7.12, exhibits three reversible reductions at $E_{½,(1)}$ = -0.66 V, $E_{½,(2)}$ = -0.83 V and $E_{½,(3)}$ = -1.03 V. In addition there is a reversible oxidation observed at $E_{½}$ = 1.67 V. All the observed redox-processes are of the same height and all involve one-electron.

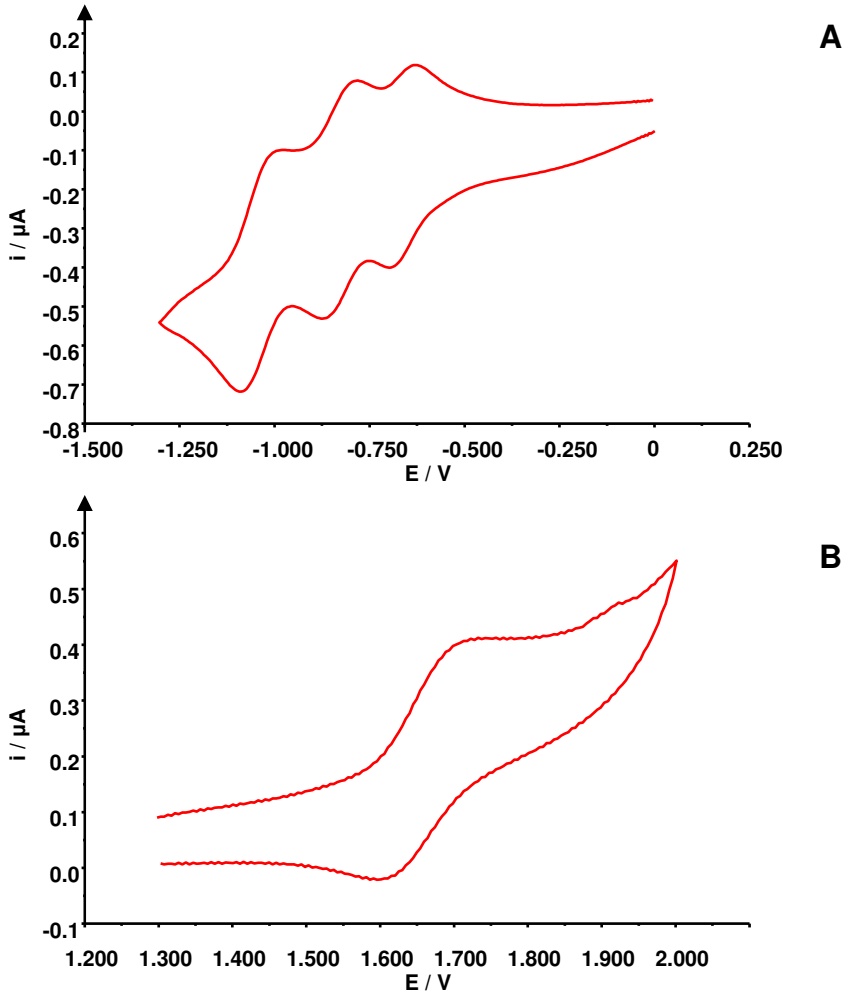

Figure 7.12 Cyclic Voltammogram of [Fe(II)(4,4´-$(CF_3)_2$-bpy)$_3$][BF_4]$_2$ *vs.* Ag/AgCl in 0.1 M [TBA][BF_4]/MeCN at 298 K, v = 100 mVs^{-1}. A) negative V features, B) positive V feature

The three one-electron reductions processes of [Fe(II)(4,4´-$(CF_3)_2$-bpy)$_3$][BF_4]$_2$ are assigned to the sequential reductions of the three 4,4´-$(CF_3)_2$-bpy ligands as observed and assigned for other tris-bipyridiyl transition metal complexes.[9,10] The oxidation process is assigned to the oxidation of the Fe(II) metal centre to Fe(III).

When the cyclic voltammogram of [Fe(II)(5,5´-$(CF_3)_2$-bpy)$_3$][BF_4]$_2$ in 0.1 M [TBA][BF_4]/MeCN was conducted three reversible reductions at $E_{½,(1)}$ = -0.56 V $E_{½,(2)}$ = -0.71 V and $E_{½,(3)}$ = -0.88 V were observed, shown in figure 7.13. In addition there is an irreversible oxidation at 1.52 V.

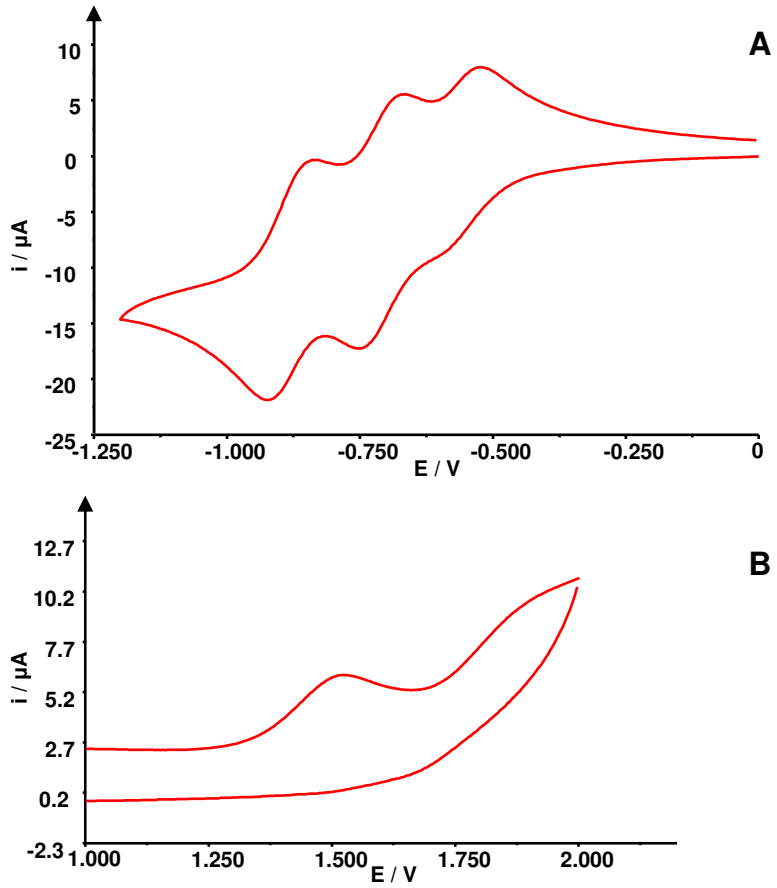

Figure 7.13 Cyclic Voltammogram of [Fe(II)(5,5´-$(CF_3)_2$-bpy)$_3$][BF_4]$_2$ *vs*. Ag/AgCl in 0.1 M [TBA][BF_4]/DMF at 298 K, ν = 100 mVs^{-1}. A) negative V features, B) positive V features

As with the 4,4´ analogue the three one-electron reductions processes of [Fe(II)(5,5´-$(CF_3)_2$-bpy)$_3$][BF_4]$_2$ are assigned to the sequential reductions of the three

5,5´-$(CF_3)_2$-bpy ligands. The oxidation process is assigned to the oxidation of the Fe(II) metal centre to Fe(III).

The complex was not infinitely stable in MeCN as observed by the collapse of the cyclic voltammetric signal after 10 minutes. This therefore meant that further spectroelectrochemical study was not possible. However it is interesting to note that once again the 5,5´- analogue is easier to reduce than the 4,4´- as discussed previously in section 7.3.1.1.

Comparison of the redox behaviour of 4,4´ derivatised bpy ligands on Fe are given in table 7.7 and a plot of reduction potential *vs*. Hammett parameter is shown in figure 7.14. This plot indicates that the data for CF_3 analogue fits the observed trend. A similar table and figure for the 5,5´ results are shown in table 7.8 and figure 7.15 and fit the same trend.

Substituent X	σ_p	$[Fe(4,4´-(X)_2-bpy)_3]^{2+}$				Ref.
		Oxidation	Reduction			
		$E_{½}$ / V	$E_{½,(1)}$ / V	$E_{½,(2)}$ / V	$E_{½,(3)}$ / V	
Me	-0.17	0.90	-1.47	-1.66	-1.91	46
Ph	-0.01	-	-1.24	-1.41	-1.62	10
H	0.00	1.26	-1.08	-1.26	-1.44	45
CO_2Et	0.45	-	-0.85	-1.02	-1.23	10
CF_3	0.54	1.67	-0.66	-0.83	-1.03	-

Table 7.7 Half wave oxidation potential and half wave reduction potentials for a series of $[Fe(II)(4,4´-(X)_2-bpy)_3]^{2+}$ complexes *vs*. Ag/AgCl (Were X = Me, Ph, H, CO_2Et and CF_3)

Substituent X	σ_m	$[Fe(5,5´-(X)_2-bpy)_3]^{2+}$							Ref.
		Oxidation	Reduction						
		$E_{½}$ / V	$E_{½,(1)}$ / V	$E_{½,(2)}$ / V	$E_{½,(3)}$ / V	$E_{½,(4)}$ / V	$E_{½,(5)}$ / V	$E_{½,(6)}$ / V	
H	0.00	1.35	-1.08	-1.26	-1.44	-	-	-	45
CO_2Et	0.37	-	-0.69	-0.80	-0.96	-1.37	-1.52	-1.76*	9
CF_3	0.43	1.52	-0.56	-0.71	-0.88	-	-	-	-
CN	0.56	1.71†	-0.40	-0.49	-0.66	-0.92	-1.10	-1.24	-

Table 7.8 Half wave oxidation potential and half wave reduction potentials for a series of $[Fe(II)(5,5´-(X)_2-bpy)_3]^{2+}$ complexes *vs*. Ag/AgCl (Were X = Me, Ph, H, CO_2Et and CF_3). * Indicates an irreversible process, E_{pc} value is quoted for this process. † Value taken from DP

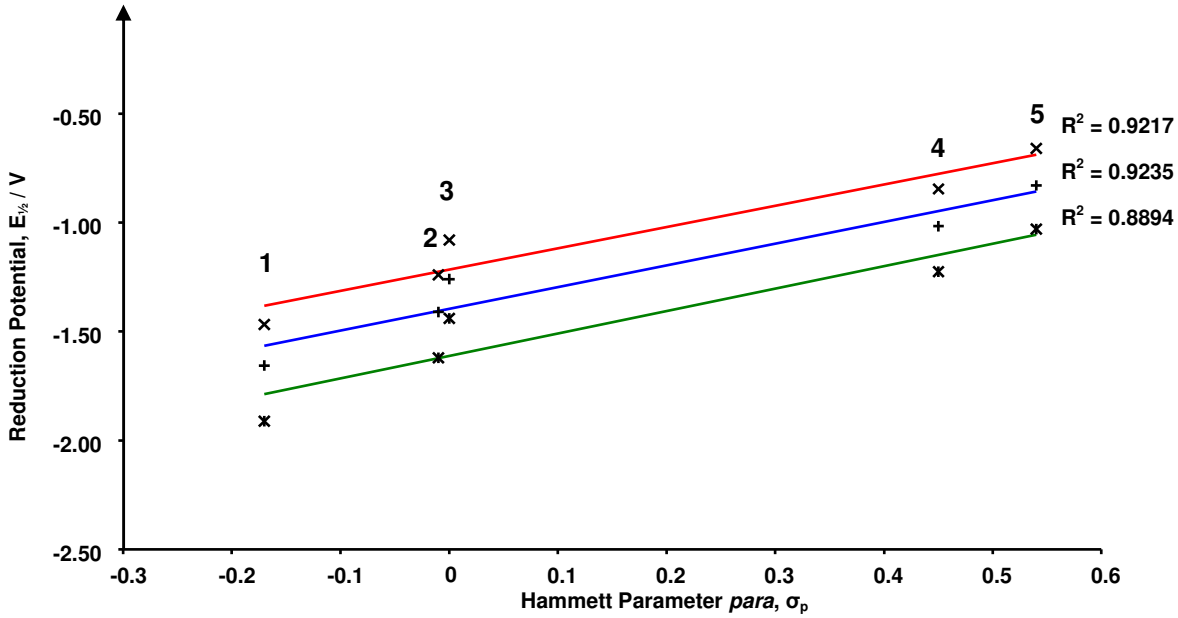

Figure 7.14 Plot of $E_{½}$ of the first (✖, red), second (✚, blue) and third (✱, green) reduction of $[Fe(II)(4,4´\text{-}(X)_2\text{-}bpy)_3]^{2+}$ *vs. para* Hammett parameter, σ_p of the substituent X, (were X is the substituent under investigation). 1) X= Me, 2) X = Ph, 3) X = H, 4) X =CO_2Et, 5) X = CF_3

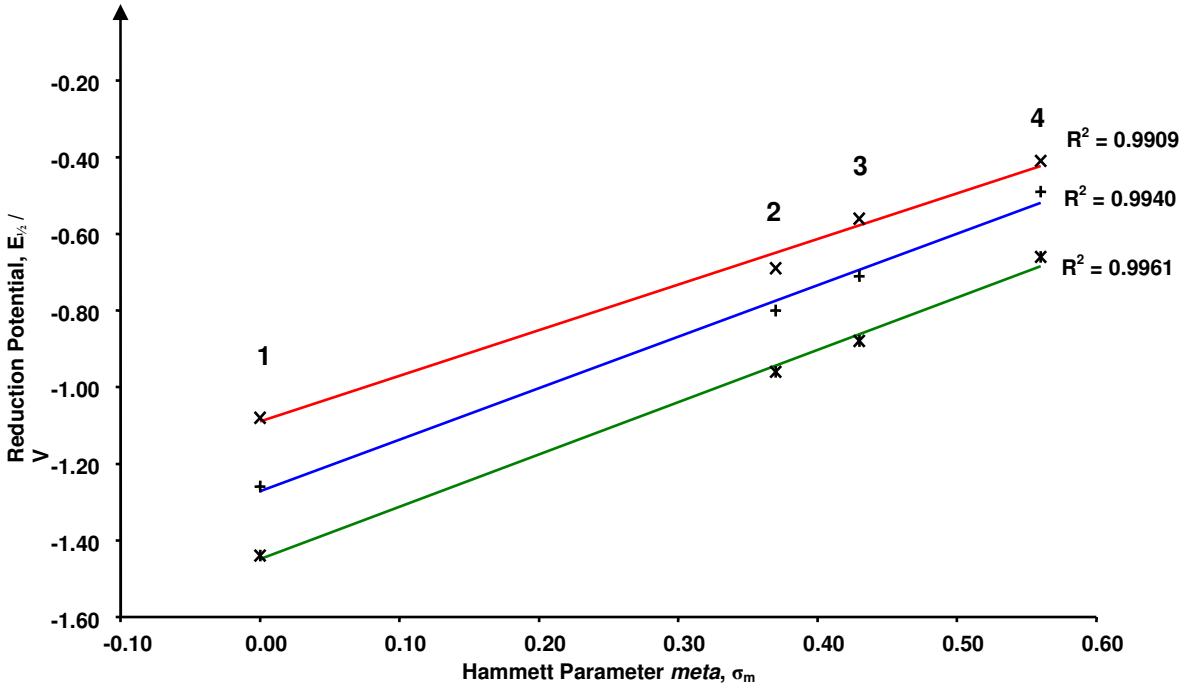

Figure 7.15 Plot of $E_{½}$ of the first (✖, red), second (✚, blue) and third (✱, green) reduction of $[Fe(II)(5,5´\text{-}(X)_2\text{-}bpy)_3]^{2+}$ *vs. meta* Hammett parameter, σ_p of the substituent X, (were X is the substituent under investigation). 1) X= H, 2) X = CO_2Et, 3) X = CF_3, 4) X = CN

7.4 Spectroelectrochemistry

7.4.1 [Pt(3,3´-$(CN)_2$-bpy)Cl_2]

7.4.1.1 UV/Vis/NIR Spectroelectrochemistry

The UV/Vis/NIR spectrum of [Pt(3,3´-$(CN)_2$-bpy)Cl_2] in 0.1 M [TBA][BF_4]/DMF at 233 K before a potential is applied is shown in figure 7.16. The spectrum has three absorption band features. Their positions and extinction coefficients are given in table 7.9. The bands at 35800 cm^{-1} (ε = 9800 $M^{-1}cm^{-1}$) and 33200 cm^{-1} (ε = 11500 $M^{-1}cm^{-1}$) are assigned intra-ligand π-π* transitions. The band at 22900 cm^{-1} (ε = 2100 $M^{-1}cm^{-1}$) is assigned to a Pt^{2+}-bpy π* MLCT transition in agreement with other Pt-bpy containing complexes.[12,38,39]

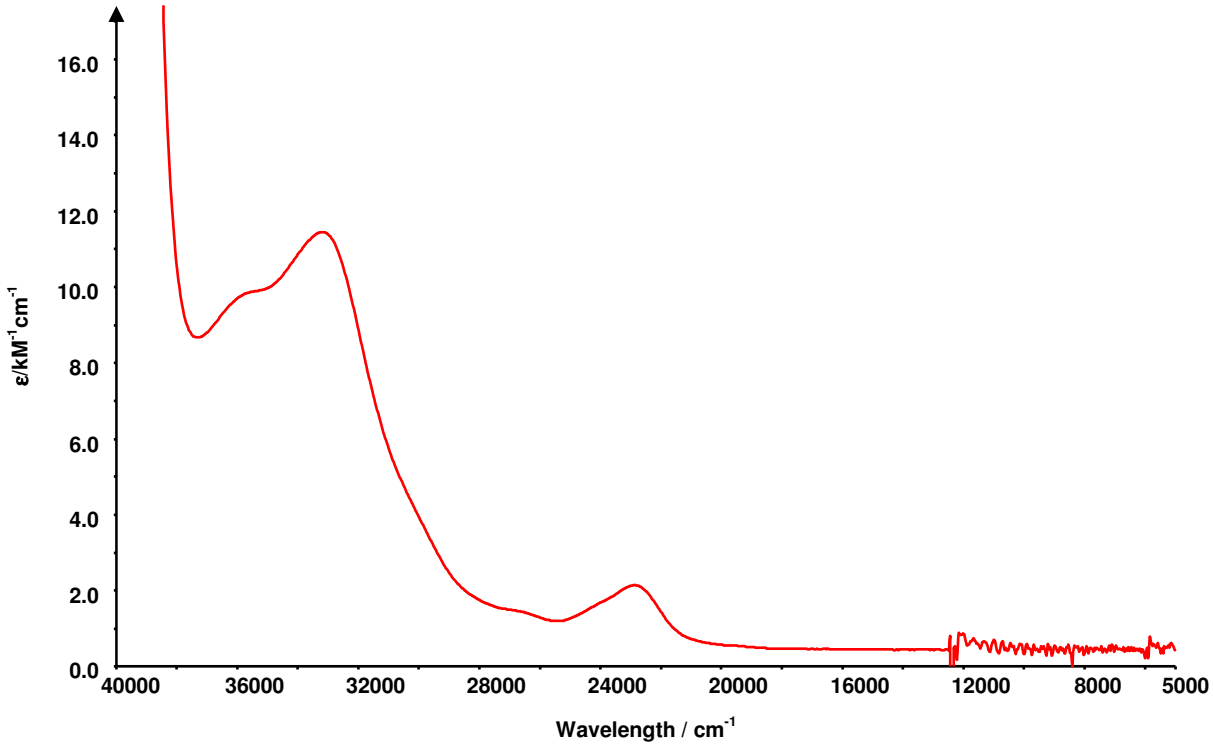

Figure 7.16 UV/Vis/NIR of [Pt(3,3´-$(CN)_2$-bpy)Cl_2] in 0.1 M [TBA][BF_4]/DMF at 233 K.

A potential of -0.7 V was then applied to generate the mono-reduced [Pt(3,3´-$(CN)_2$-bpy)Cl_2]$^{1-}$ species. The spectra collected during the application of the generation potential (150 minutes) is shown in figure 7.17. The final spectrum of

$[Pt(3,3´\text{-}(CN)_2\text{-}bpy)Cl_2]^{1-}$ is very different to that of the starting material and is characterised by the new peaks between 28000 cm^{-1} and 16000 cm^{-1}.

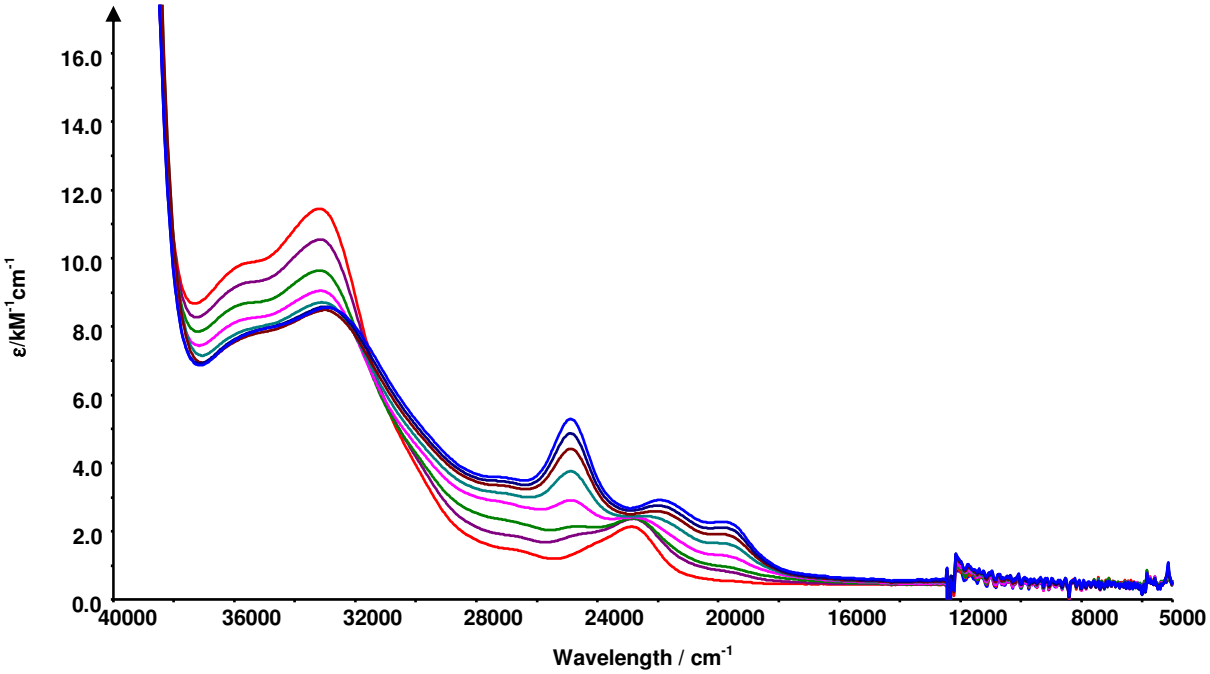

Figure 7.17 UV/Vis/NIR of $[Pt(3,3´\text{-}(CN)_2\text{-}bpy)Cl_2]$ in 0.1 M $[TBA][BF_4]$/DMF at 233 K 150 minutes after a potential of -0.7 V *vs*. Ag/AgCl was applied. Initial spectrum (red), Final spectrum (blue)

The position and extinction coefficients of the peaks are given in table 7.10. The peaks at 24900 cm^{-1}, 21900 cm^{-1} and 19800 cm^{-1} are not in the initial scan before the application of the generation potential and continue to increase in intensity until the point of maximum growth. This is a clear indication that these peaks correspond to the $[Pt(3,3´\text{-}(CN)_2\text{-}bpy)Cl_2]^{1-}$ species. It is also noted that there is an isosbestic point at 31600 cm^{-1} indicating a clean conversion of the neutral starting material to the monoanion. When the generation potential was switched back to 0 V the original spectrum was regenerated indicating that the reduction is reversible.

Assignment of the absorption bands to specific electronic transitions is given in table 7.10. Comparison of the spectrum of $[Pt(3,3´\text{-}(CN)_2\text{-}bpy)Cl_2]^{1-}$ with the spectrum of

$[3,3´\text{-}(CN)_2\text{-bpy}]^{1-}$ indicates a very similar pattern of transitions. In the spectrum of mono-reduced $[3,3´\text{-}(CN)_2\text{-bpy}]^{1-}$ the transitions must be assigned to intraligand charge transfers involving the π and π^* orbitals. Since similar features are observed in the spectrum of $[Pt(3,3´\text{-}(CN)_2\text{-bpy})Cl_2]^{1-}$ similar electronic transitions are assumed to give rise to the absorption bands. This indicates that the reduction electron enters an orbital that is primarily based on the $3,3´\text{-}(CN)_2$-bpy ligand. Thus the mono-reduced complex can be more formally written as $[Pt(II)(3,3´\text{-}(CN)_2\text{-bpy})^{1-}Cl_2]^{1-}$. This is in accordance with the findings of previous investigations into the spectral properties of $[Pt(3,3´\text{-}(X)_2\text{-bpy})Cl_2]^{1-}$ complexes.[37,38,40]

Substituent X	σ_m	$[Pt(3,3'\text{-}(X)_2\text{-bpy})Cl_2]$		Ref.
		π-π^* ν / cm^{-1} (ε / $M^{-1}cm^{-1}$)	MLCT ν / cm^{-1} (ε / $M^{-1}cm^{-1}$)	
H	0.00	32000 (11900) 30800 (12800)	25000 (4500)	38
CO_2Et	0.37	33900 (14700) 29800 (5100)	26900 (1700) 23200 (2700)	37
CN	0.56	35800 (9800) 33200 (11500)	22900 (2100)	-
NO_2	0.71	34000 (10000)	21400 (2900)	40

Table 7.9 Peak positions and extinction coefficient for signals in the UV/Vis/NIR spectra of a series of $[Pt(3,3´\text{-}(X)_2\text{-bpy})Cl_2]$ complexes (where X = H, CO_2Et, CN and NO_2)

Substituent X	σ_m	$[Pt(3,3'\text{-}(X)_2\text{-bpy})Cl_2]^{1-}$		Ref.
		Intra-ligand ν / cm^{-1} (ε / $M^{-1}cm^{-1}$)	MLCT ν / cm^{-1} (ε / $M^{-1}cm^{-1}$)	
H	0.00	27900 (17200) 21600 (5400) 20100 (10000) 11200 (2100)	23900 (8100)	38
CO_2Et	0.37	33200 (15400) 22100 (7200) 20400 (5800)	24400 (9800)	37
CN	0.56	35200 (7900) 32900 (8600) 21900 (2900) 19800 (2300)	24900 (5300)	-
NO_2	0.71	32000 (17900) 21000 (4600) 11000 (3200)	26900 (6500)	40

Table 7.10 Peak positions and extinction coefficient for signals in the UV/Vis/NIR spectra of a series of $[Pt(3,3'\text{-}(X)_2\text{-bpy})Cl_2]^{1-}$ complexes (where X = H, CO_2Et, CN and NO_2)

7.4.1.2 EPR Spectroelectrochemistry

In-situ electrogeneration was used to generate the EPR active mono-reduced species $[Pt(3,3'\text{-}(CN)_2\text{-bpy})Cl_2]^{1-}$. A potential of -0.8 V was applied to a solution of $[Pt(3,3'\text{-}(CN)_2\text{-bpy})Cl_2]$ in 0.1 M $[TBA][BF_4]$/DMF at 233K to generate the desired redox product.

The EPR spectrum recorded for the $[Pt(3,3'\text{-}(CN)_2\text{-bpy})Cl_2]^{1-}$ species shown in figure 7.18 consists of three main peaks. Simulation of the experimental spectrum was achieved by including coupling to a single Pt nucleus. Coupling to an I = ½ ^{195}Pt nucleus gives rise to the two smaller intensity peaks while the greater intensity central peak arises from the molecules that contain one of the five I = 0 isotopes of Pt that comprise approximately 66% of the natural abundance. No coupling to nuclei of the ligands is observed but this may be due to the broad nature of the peaks, given that the signals have a linewidth of 17.0 G. Attempts to further resolve the spectrum were

unsuccessful. The observed hyperfine coupling constant to ^{195}Pt of 50.0 G is in agreement with other mono-reduced bpy derivatives of Pt.[37,38,40]

A comparison of the ^{195}Pt couplings of a series of $[Pt(3,3´\text{-}(X)_2\text{-bpy})Cl_2]^{1-}$ complexes is given in table 7.11 It can been seen that as the electron withdrawing nature of the substitution group increases the magnitude of the coupling constant decreases. Therefore more electron density must be drawn away from the metal centre and onto the $[3,3´\text{-}(X)_2\text{-bpy}]^{1-}$ ligand.

Substituent X	$[Pt(3,3´\text{-}(X)_2\text{-bpy})Cl_2]^{1-}$		Ref.
	g_{iso}	A_{iso} ^{195}Pt / cm^{-1}	
H	1.99800	54.0×10^{-4}	38
CO_2Et	1.99750	42.2×10^{-4}	37
CN	1.99465	46.6×10^{-4}	-
NO_2	2.00374	20.1×10^{-4}	40

Table 7.11 EPR g_{iso} and ^{195}Pt hyperfine coupling constants for a series of $[Pt(3,3´\text{-}(X)_2\text{-bpy})Cl_2]^{1-}$ complexes (were X = H, CO_2Et, CN and NO_2)

On cooling the EPR sample to 173 K a rhombic spectrum was obtained for the $[Pt(3,3´\text{-}(CN)_2\text{-bpy})Cl_2]^{1-}$ species. The experimental and simulated spectra are shown in figure 7.19. The g values and hyperfine coupling constants determined from simulation of this spectrum are given in table 7.13. The average of $g_{xx} + g_{yy} + g_{zz}$ is in good agreement with the g_{iso} value from the solution phase spectrum. Coupling is observed to the ^{195}Pt nucleus for each of the g-components but no further splitting to ligand nuclei was resolved. It is noted that the ^{195}Pt hyperfine splitting about the high-field g_{zz} component (A_{zz}) is not resolved in the spectrum and the magnitude of A_{zz} is estimated to have an uncertainty of $\pm 5 \times 10^{-4}$ cm^{-1}.

Previous studies have shown that the SOMO in related complexes is of b_2 symmetry, assuming C_{2v} point symmetry, with metal contributions to the SOMO consisting of $5d_{yz}$ and $6p_z$ contributions.[12,38] The principle axes are defined as shown in figure 7.4. The contribution of these orbitals to the SOMO can be determined following Reiger's methodology[47] using equation 7.1-7.3.

$$\mathbf{A_{xx} = A_s - (4/7)P_d a^2 - (2/5)P_p b^2} \qquad \textbf{Equation 7.1}$$

$$\mathbf{A_{yy} = A_s - (2/7)P_d a^2 - (2/5)P_p b^2} \qquad \textbf{Equation 7.2}$$

$$\mathbf{A_{zz} = A_s + (2/7)P_d a^2 + (4/5)P_p b^2} \qquad \textbf{Equation 7.3}$$

The parameters a^2 and b^2 are respectively the contribution of $5d_{yz}$ and the $6p_z$ to the SOMO, P_d and P_p are the electron nuclear dipolar coupling parameters for platinum 5d and 6p electrons respectively and A_s is the isotropic Fermi contact term. Using the values P_d = 549 x 10^{-4} cm^{-1} and P_p = 402 x 10^{-4} cm^{-1}, calculated assuming a $5d^8$ configuration, values for a^2 and b^2 can be determined, see table 7.12.

X	σ_m	$[Pt(3,3'\text{-}(X)_2\text{-bpy})Cl_2]^{1-}$			Ref.
		$\%5d_{yz}$	$\%6p_z$	Total %Pt	
H	0.00	5.1	7.5	12.6	12
CO_2Et	0.37	3.4	5.0	8.4	37
CN	0.56	3.0	1.7	4.7	-
NO_2	0.71	0.7	0.7	1.4	40

Table 7.12 Platinum $5d_{yz}$ and $6p_z$ admixtures to the SOMO of $[Pt(3,3'\text{-}(X)_2\text{-bpy})Cl_2]^{1-}$ (were X = H, CO_2Et, CN and NO_2)

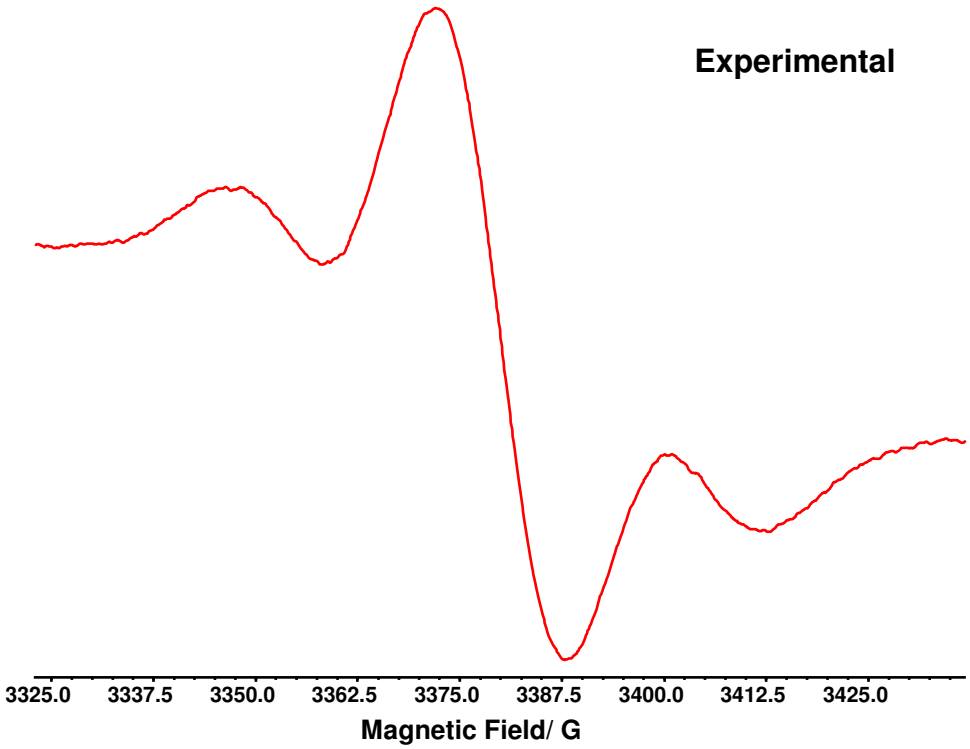

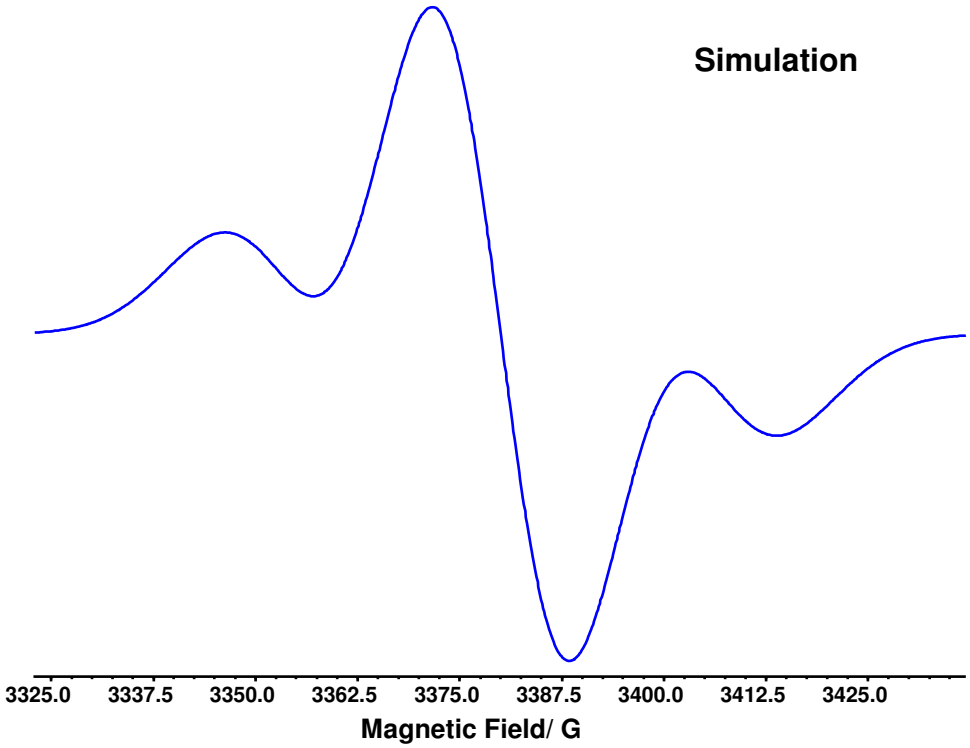

$A_{1^{195}Pt} = 50.0$

$\Delta H_{pp} = 18.5$

$L/G = 1$

$g_{iso} = 1.99465$

Figure 7.18 Experimental and simulated EPR of $[Pt(3,3'\text{-}(CN)_2\text{-bpy})Cl_2]^{1-}$ generated *in-situ* at -0.8 V vs. Ag/AgCl at 233 K in 0.1 M $[TBA][BF_4]$/DMF

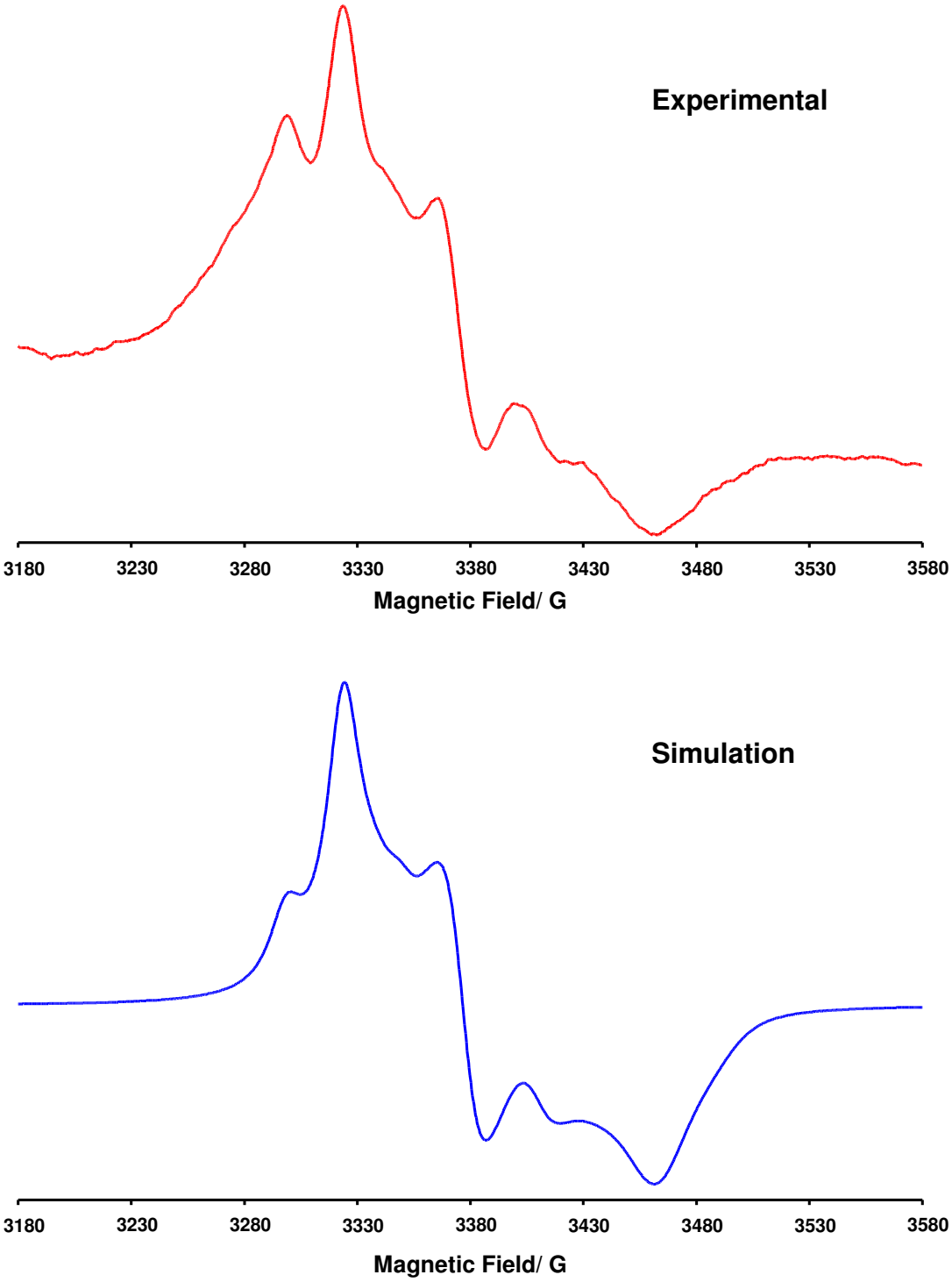

Figure 7.19 Experimental and simulated EPR of $[Pt(3,3'-(CN)_2-bpy)Cl_2]^{1-}$ generated *in-situ* at -0.8 V vs. Ag/AgCl at 173 K in 0.1 M $[TBA][BF_4]$/DMF

$[Pt(3,3'-(CN)_2-bpy)Cl_2]^{1-}$							
g_{iso}	g_{yy}	g_{xx}	g_{zz}	A_{iso} /cm^{-1}	A_{yy} /cm^{-1}	A_{xx} /cm^{-1}	A_{zz} /cm^{-1}
1.995	2.031	1.999	1.949	46.6×10^{-4}	48.0×10^{-4}	62.0×10^{-4}	40.0×10^{-4}

Table 7.13 Isotropic and Anisotropic EPR parameters for $[Pt(3,3'-(CN)_2-bpy)Cl_2]^{1-}$ in 0.1 M $[TBA][BF_4]$/DMF

Shown in table 7.12 are the contributions from the Pt metal $5d_{yz}$ and $6p_z$ orbtials to the SOMO for a series of $[Pt(3,3´\text{-}(X)_2\text{-bpy})Cl_2]^{1-}$ complexes. The total metal contribution to the SOMO is in the range of 1.4-12.6% indicating that in each case the orbital is predominantly ligand based. These results confirm the findings from the UV/Vis/NIR spectroelectrochemical studies that the reduction electron is located primarily on the bpy rings.

A plot of the total metal contribution to the SOMO for the $[Pt(3,3´\text{-}(X)_2\text{-bpy})Cl_2]^{1-}$ complexes *vs*. the *meta* Hammett parameter of the substituent is shown in figure 7.20. The plot indicates that there is a linear correlation between the electron withdrawing nature of the substituent and the degree of admixture of the metal $5d_{yz}$ and $6p_z$ orbitals to the SOMO. It can be seen that as the electron withdrawing nature of the substituent increases the contribution of the Pt metal to the SOMO decreases. These results are in line with those reported for known $[Pt(5,5´\text{-}(X)_2\text{-bpy})Cl_2]^{1-}$ complexes, table 7.14.

X	σ_m	$[Pt(5,5'\text{-}(X)_2\text{-bpy})Cl_2]^{1-}$			Ref.
		$\%5d_{yz}$	$\%6p_z$	Total %Pt	
Me	-0.07	6.0%	6.4%	12.4%	41
H	0.00	5.1%	7.5%	12.6%	12
CO_2Me	0.37	3.8%	5.8%	9.6%	41
CO_2Et	0.37	3.8%	4.6%	8.4%	41
NO_2	0.71	2.2%	0.1%	2.3%	40

Table 7.14 Platinum $5d_{yz}$ and $6p_z$ admixtures to the SOMO of $[Pt(5,5´\text{-}(X)_2\text{-bpy})Cl_2]^{1-}$ (were X = Me, H, CO_2Me, CO_2Et and NO_2)

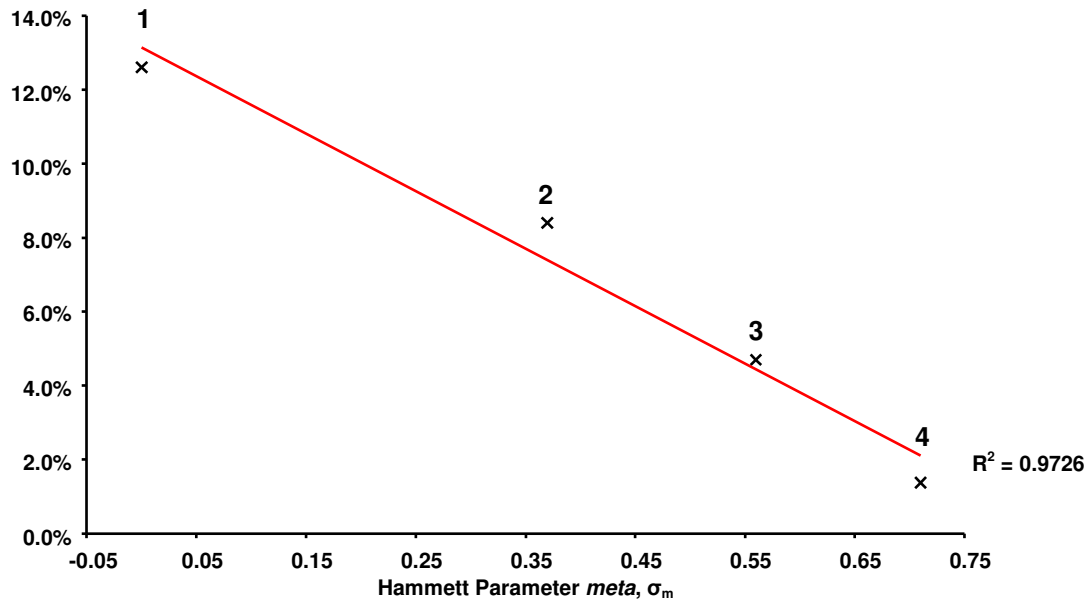

Figure 7.20 Plot of the total Pt metal % contribution to the SOMO of $[Pt(3,3'\text{-}(X)_2\text{-bpy})Cl_2]^{1-}$ *vs.* *meta* Hammett parameter, σ_m of the substituent X, (were X is the substituent under investigation). 1) X= H, 2) X = CO_2Et, 3) X = CN, 4) X = NO_2

7.4.2 $[Fe(II)(4,4'\text{-}(CF_3)_2\text{-bpy})][BF_4]_2$

7.4.2.1 UV/Vis/NIR Spectroelectrochemistry

The UV/Vis/NIR spectrum of $[Fe(II)(4,4'\text{-}(CF_3)_2\text{-bpy})_3][BF_4]_2$ in 0.1 M $[TBA][BF_4]$/MeCN at 233 K before a potential is applied is shown in figure 7.21. The spectrum has three main absorption bands. The positions of the absorption peaks and extinction coefficients are given in table 7.15. The peaks at 33800 cm^{-1} (ε = 37000 $M^{-1}cm^{-1}$) and 32600 cm^{-1} (ε = 36800 $M^{-1}cm^{-1}$) are assigned to intra-ligand π-π^* transitions. The peaks at 20300 cm^{-1} (ε = 7900 $M^{-1}cm^{-1}$) and 18800 cm^{-1} (ε = 10400 $M^{-1}cm^{-1}$) are assigned to a Fe^{2+}-bpy π^* MLCT transition. The peak at 27600 cm^{-1} (ε = 7700 $M^{-1}cm^{-1}$) is also assigned to a MLCT transition. This MLCT is assigned to transitions from Fe^{2+} metal centre to a higher lying ligand π^* orbital. These assignments are in agreement with previous studies of tris-bpy complexes of Fe(II).[9,10,45]

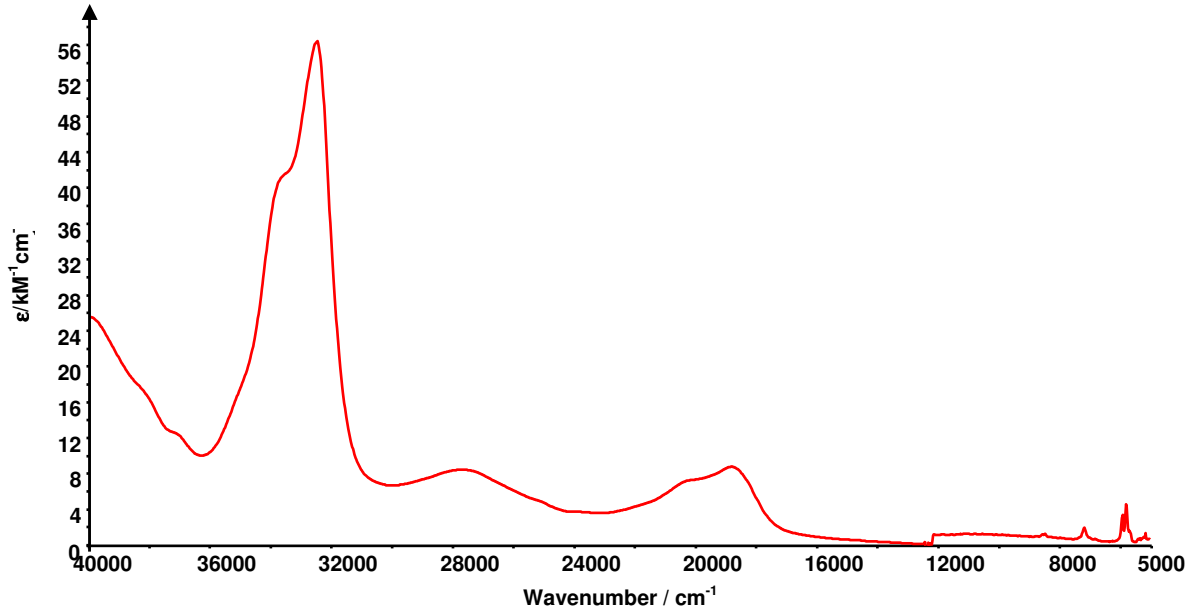

Figure 7.21 UV/Vis/NIR of [Fe(II)(4,4´-$(CF_3)_2$-bpy)][BF_4]$_2$ in 0.1 M [TBA][BF_4]/MeCN at 233 K.

A potential of -0.8 V was then applied to the system in an attempt to generate the mono-reduced species of the [Fe(II)(4,4´-$(CF_3)_2$-bpy)$_3$]$^{2+}$ complex. The spectra collected during the application of the generation potential for 90 minutes are shown in figure 7.22. The initial peaks have decreased in intensity and a series of new peaks have grown in during the course of the experiment.

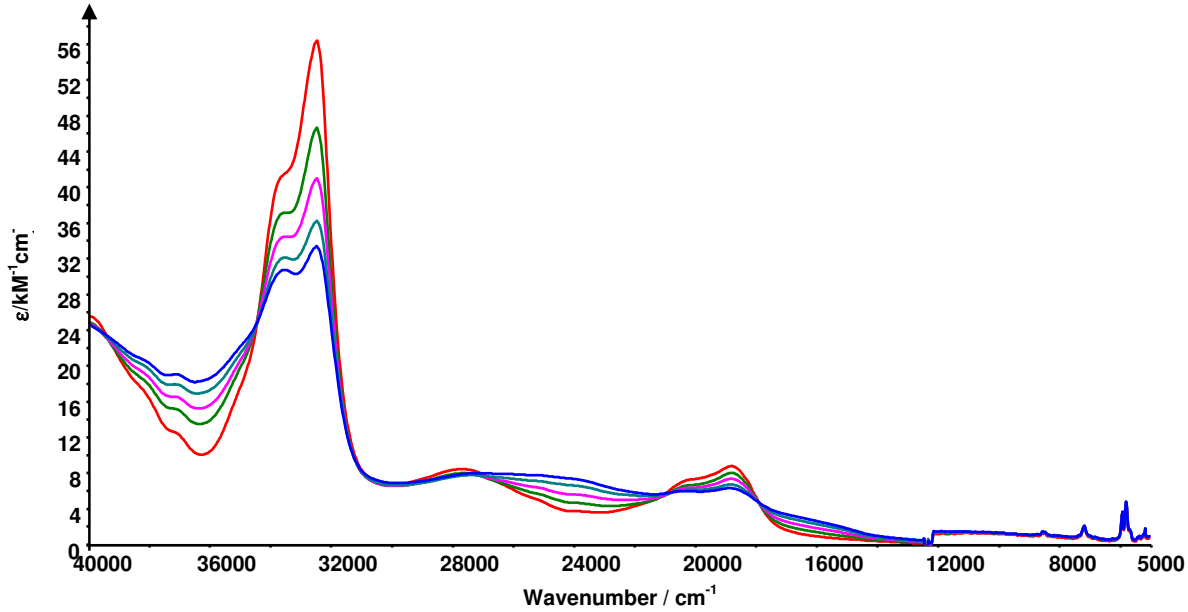

Figure 7.22 UV/Vis/NIR of [Fe(II)(4,4´-$(CF_3)_2$-bpy)][BF_4]$_2$ in 0.1 M [TBA][BF_4]/DMF at 233 K 90 minutes after a potential of -0.8 V *vs*. Ag/AgCl was applied. Initial spectrum (red), Final spectrum (blue)

The position and extinction coefficients of the peaks are given in table 7.16. The peaks at 24500 cm^{-1}, 16500 cm^{-1} and 10700 cm^{-1} are not in the initial scan before the application of the generation potential and continue to increase in intensity until the point of maximum growth. This is a clear indication that these peaks correspond to a $[Fe(II)(4,4´\text{-}(CF_3)_2\text{-}bpy)_3]^{n+}$ reduction product. It is also noted that there are isosbestic points at 34500 cm^{-1}, 27100 cm^{-1}, 21000 cm^{-1} and 18000 cm^{-1} indicating a clean conversion of the neutral starting material.

Upon mono-reduction of the $[Fe(II)(4,4´\text{-}(CF_3)_2\text{-}bpy)_3]^{2+}$ complex the high energy $\pi\text{-}\pi^*$ transition peaks decrease in intensity as does the MCLT band at 18800 cm^{-1}. Broad featureless absorptions are also observed around 24500 cm^{-1} and 16500 cm^{-1}.

Comparison with the spectrum of $[4,4´\text{-}(CF_3)_2\text{-}bpy]^{1-}$ indicates a very similar pattern of intra-ligand transitions to those observed. Thus the spectrum of $[Fe(II)(4,4´\text{-}(CF_3)_2\text{-}bpy)_3]^{1+}$ exhibits features (at 27100 cm^{-1}, 24500 cm^{-1}, 16500 cm^{-1} and 10700 cm^{-1}) that are consistent with the presence of mono-reduced $[4,4´\text{-}(CF_3)_2\text{-}bpy]^{1-}$ as well as features due to ligand in the non-reduced state (at 33500 cm^{-1}, 32500 cm^{-1}, 20300 cm^{-1} and 18900 cm^{-1}). This indicates that the reduction electron enters an orbital that is primarily based on one of the $4,4´\text{-}(CF_3)_2$-bpy ligands. Thus the mono-reduced complex can be more formally written as $[Fe(II)(4,4´\text{-}(CF_3)_2\text{-}bpy)_2(4,4´\text{-}(CF_3)_2\text{-}bpy)^{1-}]^{1+}$.

Substituent X	σ_p	$[Fe(II)(4,4'\text{-}(X)_2\text{-}bpy)_3]^{2+}$		Ref.
		π-π* transitions ν / cm^{-1} (ε / $M^{-1}cm^{-1}$)	MLCT transitions ν / cm^{-1} (ε / $M^{-1}cm^{-1}$)	
H	0.00	32900 (58000)	19200 (11200)	45
CO_2Et	0.45	32700 (≈50400) 31500 (65000)	25600 (12000) 20000 (≈12500) 18400 (16000)	10
CF_3	0.54	33600 (41000) 32500 (56500)	27600 (8500) 20200 (7300) 18800 (8800)	-

Table 7.15 Peak positions and extinction coefficient for signals in the UV/Vis/NIR spectra of a series of $[Fe(II)(4,4'\text{-}(X)_2\text{-}bpy)_3]^{2+}$ complexes (were X = H, CO_2Et and CF_3)

Substituent X	σ_p	$[Fe(II)(4,4'\text{-}(X)_2\text{-}bpy)_2(4,4'\text{-}(X)_2\text{-}bpy)^{1-}{}_1]^{1+}$			Ref.
		Bpy π-π* ν / cm^{-1} (ε / $M^{-1}cm^{-1}$)	Bpy^{1-} Intra-ligand ν / cm^{-1} (ε / $M^{-1}cm^{-1}$)	MLCT ν / cm^{-1} (ε / $M^{-1}cm^{-1}$)	
H	0	32700 (39500)	27400 (12200) 18300 (10200) 10700 (2700)	19500 (≈9000)	45
CO_2Et	0.45	31300 (40000)	27900 (≈14500) 26400 (15000) 20100 (8000) 18600 (11000) 8000 (2500) 6500 (4000)	23000 (12000) 16200 (10000)	9
CF_3	0.54	33500 (30700) 32500 (33400)	27100 (8000) 25000 (7700) 16500 (3000) 10700 (1300)	20300 (6000) 18900 (6300)	-

Table 7.16 Peak positions and extinction coefficient for signals in the UV/Vis/NIR spectra of a series of $[Fe(II)(4,4'\text{-}(X)_2\text{-}bpy)_2(4,4'\text{-}(X)_2\text{-}bpy)^{1-}{}_1]^{1+}$ complexes (were X = H, CO_2Et and CF_3)

7.4.2.2 EPR Spectroelectrochemistry

In-situ electrogeneration was used to generate the EPR active mono-reduced species $[Fe(4,4'\text{-}(CF_3)_2\text{-}bpy)_3]^{1+}$. A potential of -1.0 V was applied to a solution of $[Fe(II)(4,4'\text{-}(CF_3)_2\text{-}bpy)_3][BF_4]_2$ in 0.1 M [TBA][BF_4]/MeCN at 233K to generate the desired mono-reduced product.

The EPR spectrum recorded for the $[Fe(4,4´\text{-}(CF_3)_2\text{-bpy})_3]^{1+}$ species at 233 K is shown in figure 7.23. The spectrum consists of a single peak broad peak. Simulation of the experimental spectrum yields $g_{iso} = 1.992$. A value of this size indicates that the reduction electron enters an orbital that has significant ligand character. This supports the finding from the UV/Vis/NIR study that the reduction electron is localised on one of the 4,4´-$(CF_3)_2$-bpy ligands. However, no coupling is observed to the ligand nuclei due to the broad nature of the peak, 26 G. Attempts to further resolve the spectrum were unsuccessful.

When the temperature of the sample was varied a temperature-dependent line broadening is effect was observed. An increase in temperature resulted in the increase in the linewidth and an overall broadening of the spectrum. This is in accordance with the findings of DeArmond *et al*. for analogous $[Fe(II)(4,4´\text{-}(X)_2\text{-bpy})_3]^{1+}$ complexes (where X= H and Me).[46,48]

DeArmond et al. proposed that this line broadening effect arises from an interligand electron hopping mechanism that occurs at a rate comparable to the EPR time scale.[48] The electron hopping processes can be treated as pseudo spin-rotational coupling. The electron which is localised on one of the three ligand rings can hop to either of the two neutral rings, thus simulating a 120° molecular rotation. Note that the electron hopping only occurs on the same coordination compound and does not occur between two different complexes.

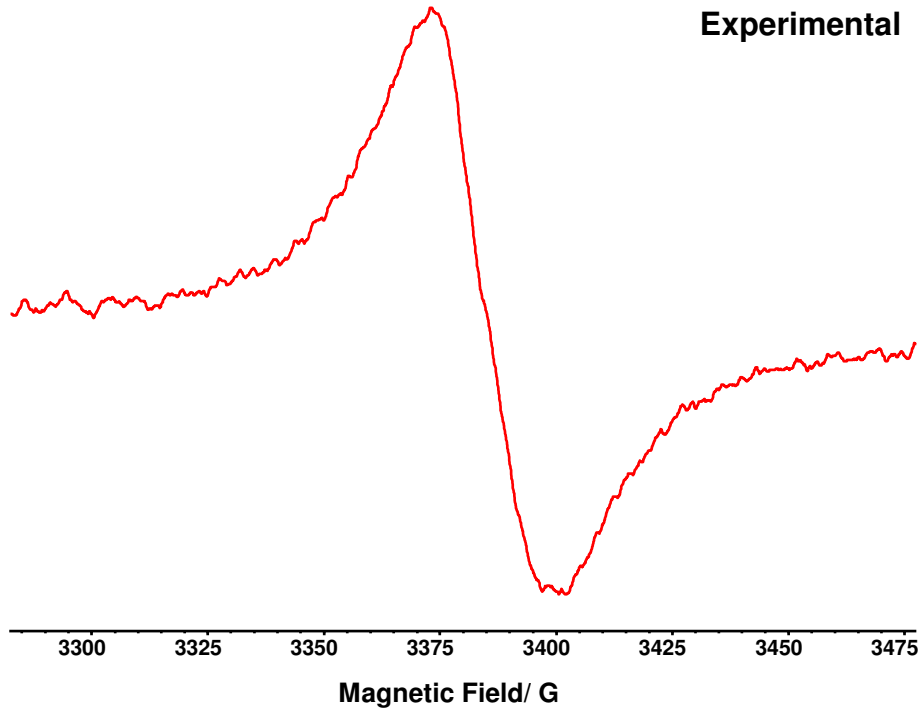

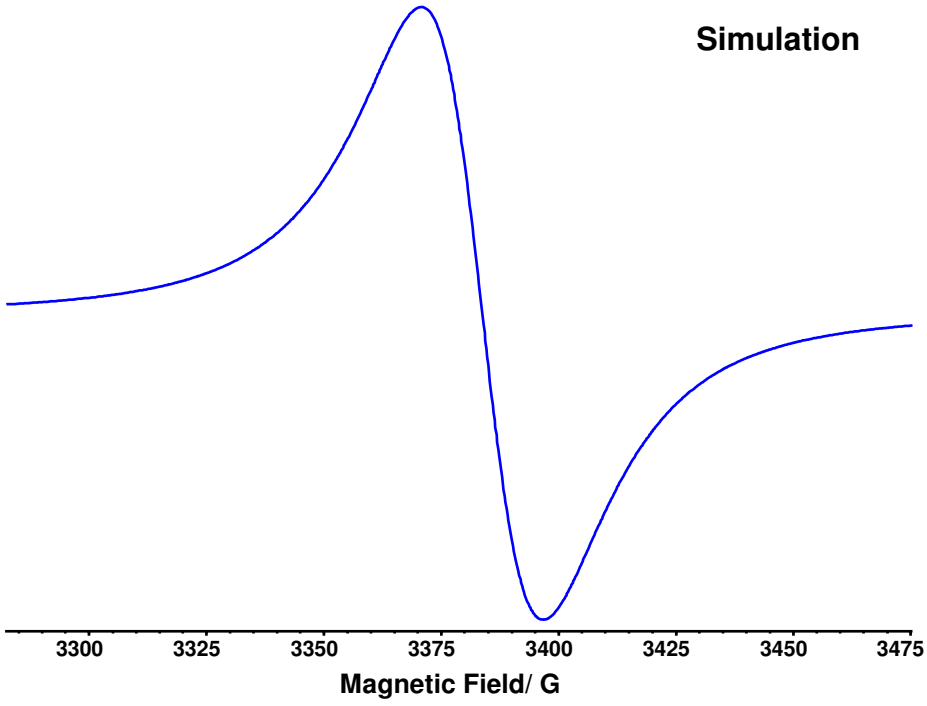

$$\Delta H_{pp} = 26.0\ G$$
$$L/G = 1$$
$$g_{iso} = 1.99245$$

Figure 7.23 Experimental and simulated EPR of $[Fe(II)(4,4'\text{-}(CF_3)_2\text{-}bpy)_3]^{1+}$ generated *in-situ* at -1.0 V *vs*. Ag/AgCl at 233 K in 0.1 M $[TBA][BF_4]$/MeCN

By analogy to a normal spin-rotational coupling DeArmond *et al*. were able to formulate an Arrhenius expression relating the spin-spin relaxation time (T_2) to the temperature.[48] Therefore a plot of $\ln(1/T_2)$ *vs*. 1/T should be linear with the activation barrier to hopping given by the slope. Such a plot for $[Fe(II)(4,4´\text{-}(CF_3)_2\text{-}bpy)_3]^{1+}$ is shown in figure 7.24. The activation energy obtained is reported in table 7.17 along with the data for the analogous $[Fe(II)(4,4´\text{-}(X)_2\text{-}bpy)_3]^{1+}$ complexes investigated by DeArmond *et al*.[46.48]

Comparison of the results for the three complexes shows that all have similar activation energies. Further data on related compounds is necessary before any trends can be indentified.

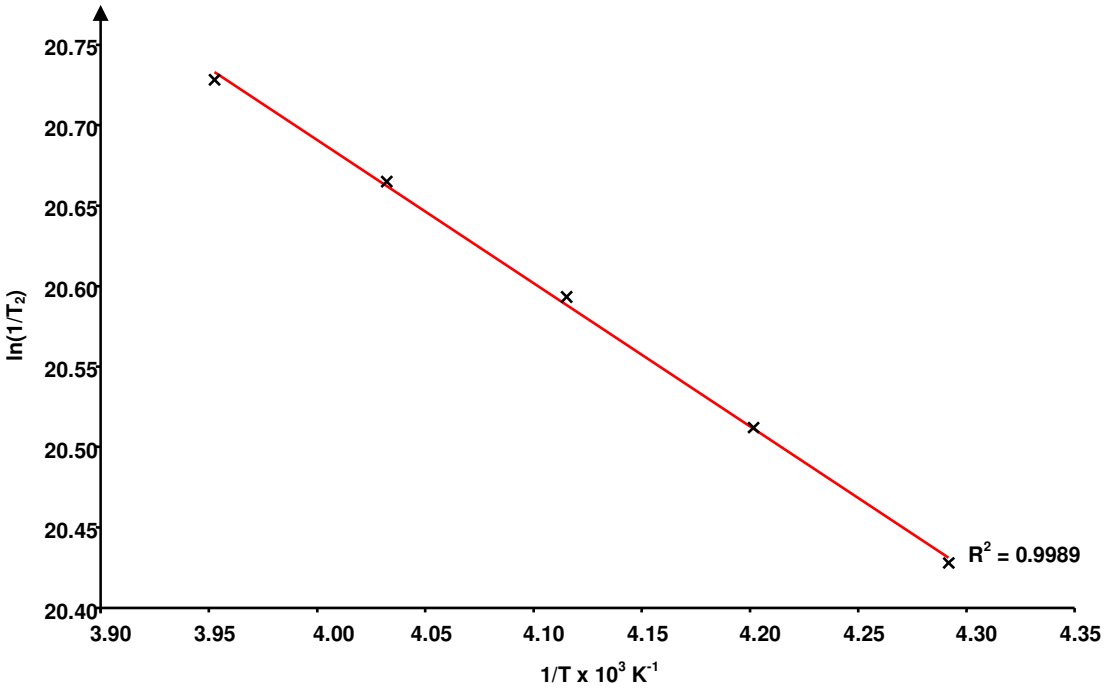

Figure 7.24 Arrhenius plot of $\ln(1/T_2)$ *vs*. 1/T for $[Fe(II)(4,4´\text{-}(CF_3)_2\text{-}bpy)_3]^{1+}$ in 0.1 M $[TBA][BF_4]$/MeCN

$[Fe(4,4´\text{-}(X)_2\text{-}bpy)_3]^{1+}$			
Substituent X	σ_p	E_a /cm^{-1}	**Ref.**
Me	**-0.17**	**820±20**	**46**
H	**0**	**960±50**	**48**
CF_3	**0.54**	**890±40**	**-**

Table 3.17 Activation Barriers for electron hopping in $[Fe(II)(4,4´\text{-}(X)_2\text{-}bpy)_3]^{1+}$ (where X = Me, H and CF_3

7.5 Conclusion

The cyano and trifluoromethyl disubstituted bipyridine molecules investigated in this work have been successfully bound to Pt(II) and Fe(II) metal centres, demonstrating their ability to act as ligands to transition metals. Electrochemical analysis has indicated that all the complexes exhibit ligand-based reduction processes and, in the case of the Fe(II) complexes, metal based oxidations. UV/Vis/NIR and EPR studies have confirmed that the reduction electron in each case enters a molecular orbital that is predominantly based on a bpy ligand.

Electrochemical investigations of the complexes $[Pt(3,3´\text{-}(CN)_2\text{-}bpy)Cl_2]$ and $[Pt(5,5´\text{-}(CN)_2\text{-}bpy)Cl_2]$ have shown that both complexes undergo two sequential one-electron reductions. The separation between the first and second reduction, $\Delta E_{½}$, for both complexes suggests that in each case the second reduction is a spin pairing process. This is confirmed by the collapse of the EPR signal upon di-reduction.

Estimated values for the first and second reduction of $[Pt(4,4´\text{-}(CN)_2\text{-}bpy)Cl_2]$ have been determined by extrapolation from a plot of the *para* Hammett parameter *vs*. the reduction potentials for a series of known $[Pt(4,4´\text{-}(X)_2\text{-}bpy)Cl_2]$ complexes[37-39] (where X = NH_2, Me, H, Ph, OEt, Cl, CO_2Me and CO_2Et).

Comparison of the reduction potentials for the three [Pt(X,X´-$(CN)_2$-bpy)Cl_2] complexes has indicated that the 5,5´ analogue is the most stabilised in both the non-reduced and mono-reduced states. While the 4,4´ analogue is the least stabilised in the non-reduced state. In the mono-reduced state the 3,3´ and 4,4´ analogues have been found to have very similar stability with respect to the addition of another reduction electron. These finding are in accordance for the results reported for the analogous methyl ester and ethyl ester complexes.[37,39]

UV/Vis/NIR investigations of [Pt(3,3´-$(CN)_2$-bpy)Cl_2] has indicated that the complex has two high energy π-π^* transitions and a Pt(II)-π^* MLCT transition at lower energy. Upon reduction to the mono-reduced [Pt(3,3´-$(CN)_2$-bpy)Cl_2]$^{1-}$ species the high energy π-π^* transitions decrease in intensity and move to lower energy and a series of new π-π^* transitions grow in between approximately 22000 – 20000 cm^{-1}. Comparison with the spectrum of [3,3´-$(CN)_2$-bpy]$^{1-}$ shows a similar pattern on π-π^* transitions indicating that the SOMO of the complex is primarily ligand based. In addition in the mono-reduced [Pt(3,3´-$(CN)_2$-bpy)Cl_2]$^{1-}$ species the MLCT transition increases in intensity and moves to higher energy.

Solution phase EPR investigations of [Pt(3,3´-$(CN)_2$-bpy)Cl_2]$^{1-}$ species have yielded a spectrum that exhibits a large platinum coupling of 50.0 G. This indicates that the SOMO of the complex must have a significant degree of Pt metal character. No ligand nuclei couplings were observed but this is likely due to the very broad nature of the spectrum.

Upon cooling the EPR sample to a frozen glass the spectrum became rhombic, with each of the g components exhibiting coupling to the ^{195}Pt nucleus. This enabled calculation of the contributions of the Pt metal $5d_{yz}$ and $6p_z$ orbitals to the SOMO of $[Pt(3,3´\text{-}(CN)_2\text{-bpy})Cl_2]^{1-}$ at 3.0% and 1.7% respectively. This confirms the findings from the UV/Vis/NIR investigations that the reduction electron enters an orbital that is predominantly ligand based.

Electrochemical investigations of the complexes $[Fe(II)(4,4´\text{-}(CF_3)_2\text{-bpy})_3]^{2+}$ and $[Fe(II)(5,5´\text{-}(CF_3)_2\text{-bpy})_3]^{2+}$ have shown that both complexes undergo three sequential one-electron reductions. These reduction processes have been assigned to the sequential reduction of the bpy ligands in accordance with the findings for other tris-bipyridyl transition metal complexes.[9,10] In addition both complexes exhibit an oxidation process, which is attributed to the oxidation of the Fe(II) metal centre to Fe(III).

Comparison of the reduction potentials for the two $[Fe(II)(X,X´\text{-}(CF_3)_2\text{-bpy})_3]^{2+}$ complexes has indicated that the 5,5´- analogue is the most stabilised in all the observed redox states. These finding are in accordance for the results reported for the analogous ethyl ester complexes.[9,10]

UV/Vis/NIR investigations of $[Fe(II)(4,4´\text{-}(CF_3)_2\text{-bpy})_3]^{2+}$ have shown that bands attributed to both the neutral $4,4´\text{-}(CF_3)_2\text{-bpy}$ ligand and the mono-reduced $[4,4´\text{-}(CF_3)_2\text{-bpy}]^{1-}$ species can be identified in the spectrum of $[Fe(II)(4,4´\text{-}(CF_3)_2\text{-bpy})_3]^{1+}$. This indicates that reduction electron eneters a molecular orbital that is located predominantly on one of the $4,4´\text{-}(CF_3)_2\text{-bpy}$ ligands.

The solution EPR spectrum of the $[Fe(II)(4,4´\text{-}(CF_3)_2\text{-}bpy)_3]^{1+}$ species consist of a single broad peak with a g_{iso} value close to that of the free electron. This is indicative of the unpaired electron being in a molecular orbital that has significant ligand character, supporting the finds from the UV/Vis/NIR studies.

In addition the EPR spectrum was found to exhibit a temperature-dependent line broadening effect. This phenomenon has been attributed to the reduction electron hopping from an orbital based on a $[4,4´\text{-}(CF_3)_2\text{-}bpy]^{1-}$ ligand to one of the remaining neutral ligands. These results are in line with the findings for other tris-bipyridyl transition metal complexes.[46,48]

7.6 References

1. D. C. Craig, H. A. Goodwin, D. Onggo, *Aust. J. Chem.*, 1988, **41**, 1157-1169.

2. J. A. Connor, C. Overton, N.E. Murr, *J. Organomet. Chem.*, 1984, **277**, 277-284.

3. P. N. W. Baxter, J. A. Conner, *J. Organomet. Chem.*, 1988, **355**, 193-196.

4. L. A. Worl, R. Duesing, P. Chen, L. D. Ciana, T. J. Meyer, *J. Chem. Soc., Dalton Trans.*, 1991, 849-859.

5. M. A. Weiner and A. Basu, *Inorg. Chem.*, 1980, **19**, 2797-2800.

6. A. Basu, M. A. Weiner, T. C. Strekas and H. D. Gafney, *Inorg. Chem.*, 1982, **21**, 1085-1092.

7. A. Basu, H. D. Gafney and T. C. Strekas, *Inorg. Chem.*, 1982, **21**, 2231-2235.

8. S. Anderson, E. C. Constable, K. R. Seddon, J. E. Turp, J. E. Baggott and M. J. Pilling, *J. Chem. Soc., Dalton Trans.*, 1985, 2247-2261.

9. R. J. Donohoe, C. D. Tait, M. K. De Armond and D. W. Wertz, *J. Phys. Chem.*, 1986, **90**, 3923, 3927-3930.

10. R. J. Donohoe, C. D. Tait, M. K. DeArmond, D. W. Wertz, *J. Phys. Chem.*, 1986, 90, 3923-3926.

11. M. Furue, K. Maruyama, T. Oguni, M. Naiki and M. Kamachi, *Inorg. Chem.*, 1992, **31**, 3792-3795.

12. E. J. L. McInnes, R. D. Farley, C. C. Rowlands, A. J. Welch, L. Rovatti, L. J. Yellowlees, *J. Chem. Soc., Dalton Trans.*, 1999, 4203-4208.

13. F. H. Case, *J. Am. Chem. Soc.*, 1946, **68**, 2574-2577.

14. G. Maerker and F. H. Case, *J. Am. Chem. Soc.*, 1958, **80**, 2745-2748.

15. W. H. F. Sasse and C. P. Whittle, *J. Chem. Soc.*, 1961, 1347-1350.

16. C. P. Whittle, *J. Heterocycl. Chem.*, 1977, **14**, 191-194.

17. K. D. Bos, J. G. Kraaijkamp and J. G. Noltes, *Synth. Commun.*, 1979, **9**, 497-504.

18. D. Wenkert and R. B. Woodward, *J. Org. Chem.*, 1983, **8**, 283-289.

19. S. D. Cummings, R. Eisenberg, *J. Am. Chem. Soc.*, 1996, **118**, 1949-1960.

20. V. M. Miskowski, V. H. Holding, C.-M. Che and Y. Wang, *Inorg. Chem.*, 1993, **32**, 2518-2524.

21. G.-F. Ran, X.Y. Xu, L.S. Ling, Z.K. He, Y. Zeng, *Wuhan Huagong Xueyuan Xuebao*, 2000, **22(2)**, 8-10

22. S. S. Kamath, V. Uma, T. S. Srivastava, *Inorganica. Chimica. Acta*. 1989, **161(1)**, 49-56.

23. Y. Q. Wang, W. H. Bi, X. Li, R. Cao, *Acta. Crystallographica*, *Sec. E*: *Structure Reports Online*, 2004, **E60(6)**, m876-m877.

24. S. Wang, Z. Peng, Z. Qin, *Wuji Huaxue Xuebao*, 1994, **10(2)**, 115-19.

25. G. Muller, J. Sales, J. Vinaixa, J. Organomet. Chem. 1984, **273(2)**, 255-61.

26. M. A. Ivanov, M. V. Puzyk, T. A. Tkacheva, K. P. Balashev, *Russ. J. Gen. Chem.*, 2006, **76(2)**, 165-169.

27. P. M. Gidney, R. D. Gillard and B. T. Heaton, *J. Chem. Soc.*, *Dalton Trans.*, 1973, 132-134.

28. D. L. Webb and L. A. Rossiello, *Inorg. Chem.*, 1971, **10**, 2213-2218.

29. V. M. Miskowski and V. H. Holding, *Inorg. Chem.*, 1989, **28**, 1529-1533.

30. R. Ballardini, M. T. Gandolfi, L. Prodi, M. Ciano, V. Balzani, F. H. Kohnke, H. Shahrini-Zavareh, N. Spencer and J. F. Stoddart, *J. Am. Chem. Soc.*, 1989, **111**, 7072-7078.

31. C.-M. Che, K.-T. Wan, L.-Y. He, C.-K. Poon and V. W.-W. Yam, *J. Chem. Soc.*, *Chem. Commun.*, 1989, 943-944.

32. J. Biedermann, M. Walfahrer and G. Gliemann, *J. Lumin.*, 1987, **37**, 323-329.

33. E. A. M. Geary, N. Hirata, J. Clifford, J. R. Durrant, S. Parsons, A. Dawson, L. J. Yellowlees, N. Robertson, *Dalton Trans.*, 2003, 3757-3762.

34. A. Islam, H. Sugihara, K. Hara, L. Pratap Singh, R. Katoh, M. Yanagida, Y. Takahashi, S. Murata and H. Arakawa, *New J. Chem.*, 2000, **24**, 343-345.

35. A. Islam, H. Sugihara, K. Hara, L. P. Singh, R. Katoh, M. Yanagida, Y. Takahashi, S. Murata, H. Arakawa and G. Fujihashi, *Inorg. Chem.*, 2001, **40**, 5371-5380.

36. E. A. M. Geary, L. J. Yellowlees, L. A. Jack, I. D. H. Oswald, S. Parsons, N. Hirata, J. R. Durrant, N. Robertson, *Inorg. Chem.*, 2005, **44**, 242-250.

37. E. A. M. Geary, K. L. McCall, A. Turner, P. R. Murray, E. J. L. McInnes, L. A. Jack, L. J. Yellowlees, N. Robertson, *Dalton Trans.,* 2008, 3701-3708.

38. D. Collison, F. E. Mabbs, E. J. I. McInnes, K. J. Taylor, A. J. Welch and L. J. Yellowlees, *J. Chem. Soc*., *Dalton Trans*., 1996, 329-334.

39. L. Yang, F. L. Wimmer, S. Wimmer, J. Zhao, P. S. Braterman, *J. Organomet. Chem.*, 1996, 525, 1-8.

40. P. R. Murray, Ph.D Thesis, University of Edinburgh, 2006.

41. L. Jack, Ph.D Thesis, University of Edinburgh, 2003.

42. S. K. Al-Musharafi, Ph.D Thesis, University of Edinburh, 2006.

43. K. Zeitler, *Angew. Chem. Int. Ed.* 2009, **48**, 9785 – 9789.

44. R. Pyati, M. M.Richter, *Annu. Rep. Prog. Chem., Sect. C*, 2007, **103**, 12–78.

45. P. S. Braterman, J. Song, R. D. Peacock, *Inorg. Chem.*, 1992, **31(4)**, 555-559.

46. D. E. Morris, K. W. Hanck, M. K. DeArmond, *J. Am. Chem. Soc*. 1983, **105(10)**, 3032-3038.

47. P. H. Rieger, *J. Magn. Reson*. 1997, **124**, 140-146.

48. A. G. Motten, K. Hanck, M. K. De Armond, *Chem*. *Phys*. *Lett*., 1981, **79(3)**, 541-546.

8 Conclusions and Future Work

The electrochemical and spectroelectrochemical properties of the CN and CF_3 disubstituted bipyridines have been found to follow the general trends observed for other substituted bipyrdines previously investigated. Electrochemical analysis has indicated that substitution with these groups result in the first reduction moving to less negative potential, relative to unsubstituted bpy, in line with the prediction for such electron withdrawing functional groups. UV/Vis/NIR and EPR studies have confirmed that the reduction electrons in each case enter a molecular orbital that is predominantly based on the bpy rings rather than localised to the substituent group.

It has been determined that the electronic character of the substituted bpy molecules is highly dependent on the position of the substituent group. Investigation of the electrochemical properties of X,X´-$(CN)_2$-bpy (where X,X´ = 3,3´, 4,4´ or 5,5´) have determined that substitution at the 3,3´ and 5,5´ positions result in two reversible one-electron reductions being observed, while substitution at the 4,4´ position gives only a single reversible reduction in the available solvent window. Equivalent investigations on the X,X´-$(CF_3)_2$-bpy compounds (where X,X´ = 3,3´, 4,4´ or 5,5´) indicate that the 4,4´ and 5,5´ analogues posses a single reversible reduction, while the reduction process in 3,3´-$(CF_3)_2$-bpy is irreversible on the CV timescale.

Comparison of the reduction potentials for the X,X´-$(CN)_2$-bpy and X,X´-$(CF_3)_2$-bpy substituted bipyridines indicates that the relative ease of reduction follows the order 5,5´ > 3,3´ > 4,4´. This is in direct contrast to investigations on CO_2Et and NO_2

substituted bpy, which concluded that substitution at the 3,3´ resulted in the least stabilisation of the reduction electron.

Attempts to evaluate if 4,4´-$(X)_2$-bpy compounds studied in this work fit the previously observed correlations between the *para* Hammett parameter, σ_p and the first reduction potential has resulted in a good quality linear fit being obtained. In contrast when correlation between the *meta* Hammett parameter, σ_m and the first reduction potentials of the 5,5´-$(X)_2$-bpy, reported by Jack, was evaluated it was found to give a poor fit. This has been attributed to the inability of the Hammett parameters to accurately account for the relative contributions of Field/Inductive and Resonance effects in the bipyridine system. A much improved correlation was found between the reduction potential for the 5,5´-$(X)_2$-bpy molecules and the *para* Hammett parameter.

It is noted that the linear fit for the 5,5´-$(X)_2$-bpy compounds with the *para* Hammett parameter has a higher R^2 value indicating σ_p can more accurately describe the interaction of the resonance and field/induction effects in this these compounds than the 4,4´-$(X)_2$-bpy analogues. While the correlation with the *para* Hammett parameter is sufficiently good to qualitatively predict the effect that substitution with a given functional group will have upon the electrochemical properties of the bpy system a more accurate Hammett parameter could be developed to describe the interactions of a substituent with the bipyridine ring system. It is proposed that these Hammett parameters, $\sigma_{X,X´}$, would follow the general form given in equation 8.1, where $\alpha_{X,X´}$ and $\beta_{X,X´}$ are the weighting coefficients for the Field/Induction and Resonance parameters when the substituents are in the positions X,X´ of the bipyridine ring.

$$\sigma_{X,X'} = \alpha_{X,X'}F + \beta_{X,X'}R \qquad \textbf{Equation 8.1}$$

To enable the development of these Hammett parameters it would be of interest to investigate as wide a range of substituent groups as possible. One possible substituent for investigation is the fluoro group. This group has a small σ_p resulting from the combination of a highly positive Field/Induction parameter and a strongly negative Resonance parameter. It would be of interest to study which properties dominates the electronic character of the substituent in various positions around the bipyridine rings.

The UV/Vis/NIR spectroelectrochemistry investigations of the CN and CF_3 substituted bipyridines have yielded spectra for the mono-reduced species that are very similar to the spectrum obtained for $[bpy]^{1-}$. Therefore it can be inferred that the electronic character of the frontier orbitals of the X,X´-$(CN)_2$-bpy and X,X´-$(CF_3)_2$-bpy compounds are similar to that of unsubstituted bpy. Therefore the LUMO of the CN and CF_3 substituted bipyridines are predominantly located on the bpy rings of the molecule with only a small contribution from the substituents.

EPR analysis of the paramagnetic $[X,X'\text{-}(CN)_2\text{-bpy}]^{1-}$ (where X,X´ = 3,3´, 4,4´ and 5,5´) and $[X,X'\text{-}(CF_3)_2\text{-bpy}]^{1-}$ (where X,X´ = 4,4´ and 5,5´) mono-reduced species give rise to spectra that indicate that for all of these molecules the reduction electron enters a molecular orbital that is spread over both rings rather than localised on one of the pyridine rings. Comparison of the ^{19}F couplings in spectra of $[4,4'\text{-}(CF_3)_2\text{-bpy}]^{1-}$ and $[5,5'\text{-}(CF_3)_2\text{-bpy}]^{1-}$ show clear evidence of the greater contribution of the 5,5´ positions to the electronic structure of the bpy π-system.

DFT calculations have enabled the assignment of the observed coupling constants to specific nuclei. In the cyano substituted bpys this has made it possible to differentiate the coupling to the ring nitrogen atoms and the substituent group nitrogen atom. The $[3,3´\text{-}(CN)_2\text{-bpy}]^{1-}$ and $[5,5´\text{-}(CN)_2\text{-bpy}]^{1-}$ species exhibit a large coupling to the cyano group nitrogen atoms and a much smaller coupling to the ring nitrogen atoms. The inverse is found for the $[4,4´\text{-}(CN)_2\text{-bpy}]^{1-}$ species. This indicates that 3,3´ and 5,5´ analogues experience a greater degree of delocalisation on to the substituent which would account for the greater degree of stabilisation of the reduced species experienced by these compounds relative to $4,4´\text{-}(CN)_2\text{-bpy}$.

These findings could be verified by enriching the nitrogen atoms in the cyano groups so that they are ^{15}N (I= ½) as apposed to predominant natural abundance of ^{14}N (I= 1). This would result in a 1:2:1 triplet splitting pattern for the coupling arsing from the cyano group nitrogen atoms compared to a 1:2:3:2:1 quintet splitting pattern for the ^{14}N nuclei in the pyridine ring.

It has been determined in this study that the solvent has an effect on the electrochemical properties of the CN substituted compounds studied. As the acceptor number of the solvent increases the observed reduction processes of 4-CN-py and $5,5´\text{-}(CN)_2\text{-bpy}$ become less negative. This effect arises from the solvents with higher acceptor number and therefore greater acidic character being able to more effectively stabilise the negatively charged species.

Investigation of the EPR spectroscopy of $[5,5´\text{-}(CN)_2\text{-bpy}]^{1-}$ in the range of solvents used has shown evidence that the experimentally determined EPR coupling constants

are dependent on the acceptor number of the solvent. Changes are observed in all the coupling constants, suggesting the solvent is interacting with a molecular orbital spread across the entire ring system rather than localised at the CN substitution groups.

The X,X´-$(CN)_2$-bpy and X,X´-$(CF_3)_2$-bpy molecules investigated in this work have been successfully bound to Pt(II) and Fe(II) metal centres, demonstrating their ability to act as ligands to transition metals. Electrochemical analysis has indicated that all the complexes exhibit ligand-based reduction processes and, in the case of the Fe(II) complexes, metal based oxidations. UV/Vis/NIR and EPR studies have confirmed that the reduction electron in each case enters a molecular orbital that is predominantly based on a bpy ligand.

Comparison of the reduction potentials for the three [Pt(X,X´-$(CN)_2$-bpy)Cl_2] complexes has indicated that the 5,5´ analogue is the most stabilised in both the non-reduced and mono-reduced states. While the 4,4´ analogue is the least stabilised in the non-reduced state. In the mono-reduced state the 3,3´ and 4,4´ analogues have been found to have very similar stability with respect to the addition of another reduction electron. These finding are in accordance for the results reported for the analogous methyl and ethyl ester complexes.

The contributions of the Pt metal $5d_{yz}$ and $6p_z$ orbitals to the SOMO of the $[Pt(3,3´\text{-}(CN)_2\text{-bpy})Cl_2]^{1-}$ complex have been calculated at 3.0% and 1.7% respectively. This confirms the findings from the UV/Vis/NIR investigations that the reduction electron enters an orbital that is predominantly ligand based.

Electrochemical investigations of the complexes $[Fe(II)(4,4´\text{-}(CF_3)_2\text{-}bpy)_3]^{2+}$ and $[Fe(II)(5,5´\text{-}(CF_3)_2\text{-}bpy)_3]^{2+}$ have shown that both complexes undergo three sequential one-electron reductions. These reduction processes have been assigned to the sequential reduction of the bpy ligands in accordance with the findings for other tris-bipyridyl transition metal complexes. In addition both complexes exhibit an oxidation process, which is attributed to the oxidation of the Fe(II) metal centre to Fe(III).

Comparison of the reduction potentials for the two $[Fe(II)(X,X´\text{-}(CF_3)_2\text{-}bpy)_3]^{2+}$ complexes has indicated that the 5,5´- analogue is the most stabilised in all the observed redox states. These finding are in accordance for the results reported for the analogous ethyl ester complexes.

The solution EPR spectrum of the $[Fe(II)(4,4´\text{-}(CF_3)_2\text{-}bpy)_3]^{1+}$ species has been found to exhibit a temperature-dependent line broadening effect. This phenomenon has been attributed to the reduction electron hopping from an orbital based on a $[4,4´\text{-}(CF_3)_2\text{-}bpy]^{1-}$ ligand to one of the remaining neutral ligands. These results are in line with the findings for other tris-bipyridyl transition metal complexes. EPR studies of other $[Fe(II)(4,4´\text{-}(X)_2\text{-}bpy)_3]^{1+}$ species will help to determine if a correlation exists between the energy barrier to electron hopping and the nature of substituent.

Appendix

Crystal structure data for 4,4´-$(CF_3)_2$-bpy

Experimental parameters	
Empirical formula	$C_{12}H_6F_6N_2$
Formula weight	292.19
Wavelength, Å	0.71073
Temperature, K	150(2)
Crystal system	Monoclinic
Space group	P 21/c
Unit cell dimensions	
a (Å)	11.7866(6)
b (Å)	12.6868(5)
c (Å)	7.6838(3)
α (°)	90
β (°)	102.006(4)
γ (°)	90
V ($Å^3$)	1123.86(8)
Number of reflections for cell parameters	1705 ($3^o < \theta < 17.5^o$)
Z	4
Density (calc.) ($Mg\ m^{-3)}$	1.727
Absorption coefficient (mm^{-1})	0.174
F(000)	584
Crystal description	colourless plate
Crystal size (mm)	0.45 x 0.20 x 0.06
Instrument	Bruker Smart Apex CCD
θ range for data collection (°)	2.39-26.40
Index ranges	-14<=h<=14 -15<=k<=15 -9<=l<=9
Reflections collected	7381
Independent reflections	2303 [R(int) = 0.0423]
Scan type	ω scans
Absorption correction	Semi-empirical from equivalents (Tmin= 0.7693, Tmax=0.9914)
Solution	direct (Shelxs Sheldrick)
Refinement type	Full-matrix least-squares on F^2
Program used for refinement	SHELXL-97
Data / restraints / parameters	2303/ 0/ 181
Goodness-of-fit on F^2	1.186
Conventional R [F>4σ(F)]	R1 = 0.0782 [1661 data]
Rw	0.1574
Final maximum Δ/σ	0
Weighting scheme	calc $w=1/[\sigma^2(Fo^2)+(0.0347P)^2+1.4784P]$ where $P=(Fo^2+2Fc^2)/3$
Largest peak $e.Å^{-3}$	0.307
Largest hole $e.Å^{-3}$	-0.207

Bond lengths / Å	
C(1)-N(2)	1.339(4)
C(1)-C(6)	1.389(4)
C(1)-C(7)	1.485(4)
N(2)-C(3)	1.337(4)
C(3)-C(4)	1.376(5)
C(3)-H(3)	0.9500
C(4)-C(5)	1.382(5)
C(4)-H(4)	0.9500
C(5)-C(6)	1.380(5)
C(5)-C(51)	1.502(5)
C(51)-F(52)	1.325(4)
C(51)-F(51)	1.335(4)
C(51)-F(53)	1.338(4)
C(6)-H(6)	0.9500
C(7)-N(8)	1.336(4)
C(7)-C(12)	1.394(5)
N(8)-C(9)	1.333(4)
C(9)-C(10)	1.378(5)
C(9)-H(9)	0.9500
C(10)-C(11)	1.374(5)
C(10)-H(10)	0.9500
C(11)-C(12)	1.395(5)
C(11)-C(111)	1.497(5)
C(111)-F(111)	1.313(4)
C(111)-F(112)	1.322(4)
C(111)-F(113)	1.329(4)
C(12)-H(12)	0.9500

Bond angles / º	
N(2)-C(1)-C(6)	122.7(3)
N(2)-C(1)-C(7)	117.1(3)
C(6)-C(1)-C(7)	120.2(3)
C(3)-N(2)-C(1)	117.5(3)
N(2)-C(3)-C(4)	124.0(3)
N(2)-C(3)-H(3)	118.0
C(4)-C(3)-H(3)	118
C(3)-C(4)-C(5)	117.9(3)
C(3)-C(4)-H(4)	121.1
C(5)-C(4)-H(4)	121.1
C(6)-C(5)-C(4)	119.5(3)
C(6)-C(5)-C(51)	119.9(3)
C(4)-C(5)-C(51)	120.5(3)
F(52)-C(51)-F(51)	106.8(3)
F(52)-C(51)-F(53)	106.6(3)
F(51)-C(51)-F(53)	106.6(3)
F(52)-C(51)-C(5)	112.6(3)
F(51)-C(51)-C(5)	111.6(3)
F(53)-C(51)-C(5)	112.3(3)
C(5)-C(6)-C(1)	118.5(3)
C(5)-C(6)-H(6)	120.7
C(1)-C(6)-H(6)	120.7
N(8)-C(7)-C(12)	122.6(3)
N(8)-C(7)-C(1)	116.3(3)
C(12)-C(7)-C(1)	121.1(3)
C(9)-N(8)-C(7)	117.5(3)
N(8)-C(9)-C(10)	124.3(3)
N(8)-C(9)-H(9)	117.9
C(10)-C(9)-H(9)	117.9
C(11)-C(10)-C(9)	118.0(3)
C(11)-C(10)-H(10)	121.0
C(9)-C(10)-H(10)	121.0
C(10)-C(11)-C(12)	119.3(3)
C(10)-C(11)-C(111)	120.8(3)
C(12)-C(11)-C(111)	119.9(3)
F(111)-C(111)-F(112)	107.5(3)
F(111)-C(111)-F(113)	105.8(3)
F(112)-C(111)-F(113)	105.5(3)
F(111)-C(111)-C(11)	112.5(3)
F(112)-C(111)-C(11)	112.9(3)
F(113)-C(111)-C(11)	112.1(3)
C(7)-C(12)-C(11)	118.3(3)
C(7)-C(12)-H(12)	120.9
C(11)-C(12)-H(12)	120.9

Atomic coordinates ($x10^4$)			
	x	y	z
C(1)	9327(3)	2363(3)	1801(4)
N(2)	9574(2)	1337(2)	1697(4)
C(3)	10633(3)	1085(3)	1465(5)
C(4)	11479(3)	1812(3)	1344(5)
C(5)	11208(3)	2868(3)	1436(4)
C(51)	12108(3)	3700(3)	1389(5)
F(51)	12651(2)	3980(2)	3026(3)
F(52)	11659(2)	4571(2)	572(3)
F(53)	12929(2)	3373(2)	544(3)
C(6)	10118(3)	3154(3)	1658(4)
C(7)	8151(3)	2636(3)	2075(4)
N(8)	7934(2)	3661(2)	2235(4)
C(9)	6877(3)	3930(3)	2448(5)
C(10)	6006(3)	3220(3)	2535(5)
C(11)	6239(3)	2166(3)	2398(5)
C(111)	5325(3)	1354(3)	2449(5)
F(111)	4755(2)	1089(3)	854(3)
F(112)	5747(2)	480(2)	3275(4)
F(113)	4529(2)	1695(2)	3312(4)
C(12)	7331(3)	1855(3)	2157(4)

Hydrogen coordinates ($x10^4$)			
	x	y	z
H(3)	10812	359	1377
H(4)	12226	1596	1201
H(6)	9912	3875	1712
H(9)	6715	4658	2546
H(10)	5266	3452	2686
H(12)	7512	1132	2051

Crystal structure data for 5,5´-$(CF_3)_2$-bpy

Experimental parameters	
Empirical formula	C12 H6 F6 N2
Formula weight	292.19
Wavelength	0.71073 A
Temperature	150(2) K
Crystal system	Triclinic
Space group	P -1
Unit cell dimensions	
a (Å)	7.1939(8)
b (Å)	7.3021(8)
c (Å)	11.0924(13)
α (º)	76.352(7)
β (°)	81.933(7)
γ(°)	80.879(7)
V ($Å^3$)	555.85(11)
Number of reflections for cell	3377 (2.8845° < θ < 26.387°)
Z	2
Density (calc) (Mg m^3)	1.746
Absorption coefficient (mm^{-1})	0.176
F(000)	292
Crystal description	colourless plate
Crystal size (mm)	0.84 x 0.34 x 0.08
Instrument	Bruker Smart Apex CCD
Theta range for data collection	2.88° to 26.41°
Index ranges	-8<=h<=8 -9<=k<=9 -13<=l<=13
Reflections collected	6052
Independent reflections	2270 [R(int) = 0.0235]
Scan type	φ and ω scans
Absorption correction	Semi-empirical from equivalents (Tmin= 0.8581, Tmax=0.9839)
Solution	direct (Shelxs Sheldrick)
Refinement type	Full-matrix least-squares on F^2
Program used for refinement	SHELXL-97
Data / restraints / parameters	2270/ 0/ 181
Goodness-of-fit on F^2	1.155
Conventional R [F>4sigma(F)]	R1 = 0.0495 [2072 data]
Rw	0.127
Final maximum Δ/σ	0.003
Weighting scheme	calc $w=1/[\sigma^2(Fo^2)+(0.0511P)^2+0.3755P]$ where $P=(Fo^2+2Fc^2)/3$
Largest diff. peak and hole e.$Å^{-3}$	0.220 and -0.392

Bond lengths / Å	
F(1)-C(31)	1.340(2)
N(1)-C(2)	1.333(3)
N(1)-C(6)	1.342(2)
F(2)-C(31)	1.334(2)
C(2)-C(3)	1.388(3)
C(2)-H(2)	0.9500
F(3)-C(31)	1.337(3)
C(3)-C(4)	1.385(3)
C(3)-C(31)	1.498(3)
F(4)-C(101)	1.331(2)
C(4)-C(5)	1.380(3)
C(4)-H(4)	0.9500
F(5)-C(101)	1.337(2)
C(5)-C(6)	1.394(3)
C(5)-H(5)	0.9500
F(6)-C(101)	1.340(2)
C(6)-C(7)	1.488(3)
C(7)-N(8)	1.340(3)
C(7)-C(12)	1.392(3)
N(8)-C(9)	1.336(3)
C(9)-C(10)	1.387(3)
C(9)-H(9)	0.9500
C(10)-C(11)	1.387(3)
C(10)-C(101)	1.499(3)
C(11)-C(12)	1.376(3)
C(11)-H(11)	0.9500
C(12)-H(12)	0.9500

Bond angles / º	
C(2)-N(1)-C(6)	117.96(17)
N(1)-C(2)-C(3)	123.04(19)
N(1)-C(2)-H(2)	118.5
C(3)-C(2)-H(2)	118.5
C(4)-C(3)-C(2)	118.96(18)
C(4)-C(3)-C(31)	122.53(18)
C(2)-C(3)-C(31)	118.50(18)
C(5)-C(4)-C(3)	118.44(18)
C(5)-C(4)-H(4)	120.8
C(3)-C(4)-H(4)	120.8
C(4)-C(5)-C(6)	119.16(18)
C(4)-C(5)-H(5)	120.4
C(6)-C(5)-H(5)	120.4
N(1)-C(6)-C(5)	122.44(18)
N(1)-C(6)-C(7)	115.91(16)
C(5)-C(6)-C(7)	121.64(17)
N(8)-C(7)-C(12)	122.91(18)
N(8)-C(7)-C(6)	116.95(17)
C(12)-C(7)-C(6)	120.12(18)
C(9)-N(8)-C(7)	117.77(16)
N(8)-C(9)-C(10)	122.90(18)
N(8)-C(9)-H(9)	118.6
C(10)-C(9)-H(9)	118.6
C(11)-C(10)-C(9)	118.86(18)
C(11)-C(10)-C(101)	119.65(17)
C(9)-C(10)-C(101)	121.49(18)
C(12)-C(11)-C(10)	118.80(18)
C(12)-C(11)-H(11)	120.6
C(10)-C(11)-H(11)	120.6
C(11)-C(12)-C(7)	118.74(19)
C(11)-C(12)-H(12)	120.6
C(7)-C(12)-H(12)	120.6
F(2)-C(31)-F(3)	106.29(18)
F(2)-C(31)-F(1)	106.86(17)
F(3)-C(31)-F(1)	106.65(17)
F(2)-C(31)-C(3)	112.21(17)
F(3)-C(31)-C(3)	112.02(17)
F(1)-C(31)-C(3)	112.40(17)
F(4)-C(101)-F(5)	107.08(17)
F(4)-C(101)-F(6)	106.86(17)
F(5)-C(101)-F(6)	106.01(16)
F(4)-C(101)-C(10)	112.87(16)
F(5)-C(101)-C(10)	111.68(17)
F(6)-C(101)-C(10)	111.94(17)

Atomic coordinates ($x10^4$)			
	x	y	z
F(1)	8492(2)	8248(2)	13869(1)
N(1)	8424(2)	7162(3)	9821(2)
F(2)	10641(2)	6141(2)	13287(1)
C(2)	9331(3)	7278(3)	10764(2)
F(3)	10740(2)	9082(2)	12450(1)
C(3)	8400(3)	7623(3)	11888(2)
F(4)	857(2)	7697(2)	6051(1)
C(4)	6439(3)	7844(3)	12050(2)
F(5)	3286(2)	8531(2)	4803(1)
C(5)	5488(3)	7715(3)	11082(2)
F(6)	3031(2)	5582(2)	5508(1)
C(6)	6525(3)	7384(3)	9977(2)
C(7)	5579(3)	7293(3)	8887(2)
N(8)	3697(2)	7292(2)	9065(2)
C(9)	2815(3)	7281(3)	8085(2)
C(10)	3760(3)	7275(3)	6906(2)
C(11)	5710(3)	7249(3)	6735(2)
C(12)	6636(3)	7254(3)	7739(2)
C(31)	9562(3)	7771(3)	12872(2)
C(101)	2723(3)	7275(3)	5824(2)

Hydrogen coordinates ($x10^4$)			
	x	y	z
H(2)	10676	7116	10662
H(4)	5765	8079	12810
H(5)	4144	7851	11168
H(9)	1482	7278	8200
H(11)	6394	7229	5940
H(12)	7972	7231	7650

Courses and conference attended

- Inorganic section seminar and colloquia
- The 41st Annual International meeting of the ESR group of the RSC, London, 2008
- 4th European EPR Federation summer school in Advanced Techniques in EPR, St Andrews, 2008
- EaStCHEM Graduate School Course: Introduction to Computational Chemistry, 2008